Polarization-Sensitive Optical Coherence Tomography to Study Diffusion of Plasmonic Gold Nanorods – a Novel Tool for Optical Bioimaging

Raghav K. Chhetri

A dissertation submitted to the faculty of the University of North Carolina at Chapel Hill in partial fulfillment of the requirements for the degree of Doctor of Philosophy in the Department of Physics and Astronomy.

Chapel Hill
2013

Approved by:

Amy L. Oldenburg

Christian Iliadis

Michael R. Falvo

Otto Zhou

Rene Lopez

Abstract

RAGHAV K. CHHETRI: Polarization-Sensitive Optical Coherence Tomography to Study Diffusion of Plasmonic Gold Nanorods – a Novel Tool for Optical Bioimaging
(Under the direction of Amy L. Oldenburg)

Optical Coherence Tomography (OCT) is an imaging tool that performs micron-resolution, non-invasive, cross-sectional imaging by measuring the echoes of backscattered light. In this thesis, a custom-designed polarization-sensitive OCT (PS-OCT) system is discussed, which is implemented in using plasmonic gold nanorods (GNRs) as diffusion probes. PS-OCT imaging is undertaken in Newtonian fluids and validation of rotational and translational diffusion of GNRs with the Stokes-Einstein relation is presented via analysis of the autocorrelations of the OCT signals. Diffusion of GNRs in non-Newtonian fluids is also studied and the frequency-dependent viscoelasticity is also explored using generalized Stokes-Einstein relation. Furthermore, diffusion of GNRs in the "correlation length $\geq$ probe" regime is discussed in low concentration polymer solutions. Biological samples such as porous extracellular matrix (ECM) and *in vitro* mucus are explored using PEGylated GNRs as diffusion probes with PS-OCT imaging. The diffusion of GNRs was found to be sensitive to changes in the ECM induced either by ECM-remodeling fibroblasts or by changes in the ECM concentration. In mucus, the diffusion of GNRs was observed to be slowed down by less than 7-fold compared to the solvent, suggesting that the GNRs are able to readily navigate between the mucus mesh and avoid being readily trapped, thereby illustrating the potential GNRs hold in drug-delivery across the mucus barrier to the epithelial layers in lung airways. The capability of OCT to map diffusing GNRs and speckle fluctuations resulting from other motile activities in biological samples is also presented. A longitudinal study of mam-

mary epithelial cells cultured in 3D with fibroblasts, to study normal and pre-malignant architectural cues, carried out using the custom-designed OCT system is also presented in detail. The integration of PS-OCT imaging with the measurement of diffusing GNRs in biological samples enables OCT to perform functional imaging to supplement its excellent structural imaging capability. This thesis presents a platform for extending the reach of OCT imaging to the exciting fields of microrheology and bio-rheology, which holds tremendous promise in the assessment of micro- and nano- scale viscoelasticity of biological samples using GNRs as probes.

Dedicated to my family & friends.

Acknowledgements

I feel truly fortunate to have the blessing, good wishes, love, support and encouragement from my family. Without the solid foundation they laid for me, this work won't be possible. Thank you so much! My warmest thanks to my better half, Lachhita Neupane, for always being there to support me, providing apt humor on stressful grad-school days to lighten me up, and helping me to see the forest for the trees.

I'd like to acknowledge the guidance, supervision, and support of my advisor Dr. Amy L. Oldenburg throughout my time in the Coherence Imaging Laboratory. I'd like to thank her for giving me the opportunity to work in her group, which exposed me to the exciting field of biomedical optics. I'm grateful to all present and former members of the group, whom I have had the opportunity to interact with and learn from. I would like to thank Dr. Joseph B. Tracy in the Department of Material Science and Engineering at North Carolina State University for synthesizing and providing several batches of gold nanorods, and also for timely advice, guidance, and suggestions to research queries. It was my pleasure to collaborate with Dr. Tracy's group and I'd like to thank his group members, Krystian A. Kozek, Aaron C. Johnston-Peck, and Wei-Chen Wu, for their contribution in synthesizing and characterizing the gold nanorods. I am also indebted to the University of North Carolina Cystic Fibrosis and Pulmonary Research and Treatment Center, particularly David B. Hill and Brian Button for culturing and providing mucus samples, *in vitro* hBE cultures, and also engaging in helpful discussions on mucus rheology. Thanks also to Dr. Michael Rubinstein and Liheng Cai for many

helpful discussions on polymer physics and mucus rheology. I would also like to thank Dr. Melissa Troester in the UNC Gillings School of Public Health and her research group for providing cells for the breast cancer study, their assistance in establishing protocols for cell cultures in 2D and 3D, and numerous insightful discussions on our collaborative research on breast cancer pre-malignancy.

I would also like to thank Timothy O'Brien in the Computer Integrated Systems for Microscopy and Manipulation (CISMM) at UNC, Chapel Hill for allowing me to use his lab space for cell cultures, his insights to biology-related queries, and his willingness to help at all times. Thanks are also due to Amanda C. Sullivan, Zachary F. Phillips, and Jason M. Cooper for their contributions in several research projects, and I am grateful for the opportunity to work with & mentor such outstanding undergraduate students. I am also indebted to the faculty members who helped me understand the fundamentals of physics during my time as a graduate student. I feel fortunate to have had excellent faculty members to learn from, which include Yue Wu, Charles R. Evans, Jonahan Engel, Laura Mersini-Houghton, Jainping Lu, Otto Zhou, Dmitri Khveshchenko, the late Eugen Merzbacher, Michael Rubinstein, Caterina Gallippi, and Daniel J. Gauthier (Fitzpatrick Institute for photonics) during my time at UNC, Chapel Hill. I'd also like to acknowledge my Masters and PhD committee members, Rene Lopez, Otto Zhou, Yue Wu, Michael R. Falvo, Christian Iliadis, and Amy L. Oldenburg, for their role in helping me set my research goals and guidance in achieving them.

My gratitude also goes to the 2010 Nano-biophotonics Summer School at the University of Illinois, Urbana-Champaign for piquing my interest in the field of biomedical optics. In particular, I am indebted to Gabriel Popescu, Stephen Boppart, and Samir Sayegh for their continued encouragement and suggestions beyond the confines of the summer school. I would also like to thank the Center for Biomedical OCT Research at Massachusetts General Hospital and Harvard Medical School for providing me the

opportunity to learn the principles, functionality, and clinical relevance of various OCT systems.

Lastly, I'd like to acknowledge my fellow Tarheels in the Department of Physics and Astronomy at UNC Chapel Hill and the good friends I have made outside the department for their support and encouragement at various junctures in my graduate-student-life. I am also indebted to my officemates, Brian Pohl and Michael Good in particular, for engaging in discussions on important scientific problems in their fields and beyond, and also for their unparalleled office humor.

Table of Contents

List of Tables

List of Figures

List of Abbreviations

CF	Cystic Fibrosis
COPD	Chronic Obstructive Pulmonary Disease
CTAB	Cetyltrimethylammonium Bromide
DCIS	Ductal Carcinoma *in situ*
DLS	Dynamic Light Scattering
DWS	Diffusing Wave Spectrsocopy
ECM	Extracullular Matrix
FD-OCT	Fourier Domain Optical Coherence Tomography
FWHM	Full Width at Half Maximum
GNRs	Gold Nanorods
GSER	Generalized Stokes-Einstein Relation
hBE	Human Tracheo-bronchial-epithelial
LCI	Low Coherence Interferometry
LSPR	Longitudinal Surface Plasmon Resonance
MEC	Mammary Epithelial Cells
MNPs	Magnetic Nanoparticles
MSD	Mean Squared Displacement
NA	Numerical Aperture
OCE	Optical Coherence Elastography

OCT	Optical Coherence Tomography
OPD	Optical Path Length Difference
PEG	Poly-ethylene Glycol
PEO	Poly-ethylene Oxide
PSF	Point Spread Function
PS-OCT	Polarization Sensitive Optical Coherence Tomography
QWP	Quarter Wave Plate
RMF	Reduction Mammoplasty Fibroblasts
SD-OCT	Spectral Domain Optical Coherence Tomography
SLS	Static Light Scattering
SNR	Signal to Noise Ratio
SPR	Surface Plasmon Resonance
SS-OCT	Swept Source Optical Coherence Tomography
TD-OCT	Time Domain Optical Coherence Tomography

Chapter 1

Introduction

1.1 Motivation

Light scattering is a fascinating phenomenon, the consequences of which are both perplexing and insightful, and has caught the imagination of scientists across the entire discipline of science. Recent developments in optical bioimaging are unraveling the ease and flexibility light scattering affords in studying complex biological systems non-invasively and yet with ultrahigh resolution. Optical Coherence Tomography (OCT) is an example of such a recently established optical bioimaging tool. OCT implements a low coherence, infra-red light source with an interferometer, which enables depth-sectioning of samples by only allowing coherent backscattering of light from various depths in the sample to interfere with the unaltered light beam backscattered from a reference mirror. OCT has been established as a powerful research and diagnostic tool in various fields such as cardiology, pulmonology, urology, oncology, and most notably, opthalmology. With the advent of faster acquisition tools and rapid improvements in laser sources, the imaging capability of OCT will inevitably approach and possibly exceed traditional optical imaging modalities.

The potential of integrating functional imaging with the structural imaging capa-

bility of OCT makes it even more appealing in biomedical studies. The integration of functional imaging is explored in this thesis via the design of a custom polarization-sensitive OCT (PS-OCT) system, which exploits the polarization dependent optical scattering property of plasmonic gold nanorods (GNRs), and enables the study of their diffusion in biological fluids such as mucus, and soft gels such as collagen I & Matrigel. The ability to not only image structural cues but also non-invasively probe the viscoelastic properties of such biological fluids and soft solids via the diffusion of nanosized probes, such as GNRs, presents an immense opportunity in understanding the micro- and nano- scale rheology of bioiogical samples. Moreover, the knowledge of micro- and nano- scale diffusion of cylindrical probes such as GNRs sheds light on the diffusion of various nanoscopic objects (such as viruses, pathogens, toxins *etc.*) encountered in biological studies. This thesis aims to supplement the excellent and real-time visualization of biological features afforded by OCT with an extension of its applications to the growing fields of microrheology and bio-rheology.

1.2 Thesis contributions

In this thesis, I discuss the polarization dependent and high albedo of plasmon resonant GNRs combined with the imaging modality of OCT to investigate micro- and nano- scale diffusion. Development of a custom polarization-sensitive OCT (PS-OCT) system is discussed in this thesis followed by a method to probe the rotational and translational diffusion of GNRs. This work establishes the capability of OCT to image in two orthogonal polarization channels, and extends its functionality beyond structural imaging by allowing measurement of the diffusion of GNRs.

Unlike conventional micron-sized and spherical-shaped diffusion probes used in Dynamic Light Scattering (DLS), we use GNRs, which offer three main advantages – 1. Due to their nanoscale size, their diffusion is dictated by the nanoscale rheology of the

fluid, which the micron-sized probes are unable to sense. 2. GNRs depict plasmon resonance due to the oscillation of their conduction band electrons which increases the radiative properties of the GNRs. This makes GNRs an excellent choice as efficient light scatterers. 3. GNRs are optically anisotropic *i.e.,* they scatter light in a polarization-dependent manner. This enables us to probe their rotational diffusion in addition to translational diffusion using light scattering.

Additionally, we employ OCT to probe the diffusion of GNRs, which offers two major advantages over traditional DLS techniques – 1. OCT allows diffusion to be depth-resolved within a heterogeneous sample. 2. OCT efficiently rejects multiple scattering from turbid samples and thus enables investigation of probe diffusion in highly scattering samples.

1.3 Thesis outline

Chapter 2 begins by discussing the fundamentals of dynamic light scattering and how the Brownian motion of structurally isotropic as well as anisotropic probes can be characterized from the scattered light. The motivation for using low coherence interferometry (LCI) to study Brownian motion is presented in this chapter, making way for the discussion of optical coherence tomography (OCT), an LCI-based technique, in the next chapter.

Chapter 3 first gives an overview of the principle of OCT through the discussion of time-domain OCT (TD-OCT) technique. The working principle of spectral domain OCT (SD-OCT) is then briefly reviewed, and various parameters associated with the performance of OCT systems are also discussed. The design and development of a custom PS-OCT system is described next. Characterization of the PS-OCT system, image acquisition and processing are also presented in this chapter.

Chapter 4 establishes the motivation for our choice of GNRs as diffusion probes for

use with OCT. The experimental methods including GNRs number density estimation, data acquisition, and data analysis to relate OCT signals to diffusion coefficients are presented in this chapter.

Chapter 5 delves into the experimental method of studying Brownian motion using OCT. It starts out by validating rotational diffusion of GNRs in Newtownian fluids with the Stokes-Einstein relation. Depth-resolving rotational diffusion to infer viscosity within a single sample using the established method is also discussed. Next, the method is extended to translational diffusion of GNRs, and a simultaneous measurement of rotational and translational diffusion of GNRs over a range of viscosities is discussed. This chapter further explores the diffusion of GNRs in non-Newtonian fluids such as polymer solutions, and explores the nanoscale viscoelasticity probed by the GNRs.

Chapter 6 is dedicated to the biological study of the diffusion of GNRs in biologically relevant tissue-mimicking matrices (collagen I, Matrigel) and fluids (mucus), and culminates with an in-depth imaging study of mammary epithelial-fibroblast 3D cultures carried out using the custom-built OCT system.

Lastly, chapter 7 summarizes the utility of the imaging modality of OCT and the proposed method of probing nano- and micro- scale diffusion using GNRs with OCT. It also explores the potential impacts of this thesis in the fields of bio-rheology and functional OCT imaging.

Chapter 2

Light scattering and Brownian motion

2.1 Light scattering

Naturally occurring colors such as the bright blue sky, a majestic view of the horizon during sunrise and sunset, and arching rainbows after a misty rain shower, have long captured the imagination of humankind. Mankind's quest to understand such natural phenomena has today grown into the enormous field of light scattering, and has led to profound applications in various scientific disciplines.

Light is electromagnetic radiation spanning the frequency range from infrared (frequency of $\sim 10^{13}$ Hz) to ultra-violet (frequency of $\sim 10^{17}$ Hz). Visible light is the range of electromagnetic spectrum over which our human eyes are sensitive (wavelength range of $\sim$400 nm to $\sim$750 nm). Light can be characterized by its frequency (related to the wavelength via the speed of light), state of polarization and the direction of propagation. The phenomenon of light scattering is a result of heterogeneity in the medium, whether on the molecular scale or on the scale of larger molecular aggregates that result in a spatial distribution of the refractive index. The basic process underlying scattering is the absorption of the incident electromagnetic radiation by the molecules in the obstacle which sets the electric charges in the molecule in an oscillatory motion, and as a con-

sequence of the oscillating electric charges, electromagnetic radiation is emitted (since accelerating electric charges radiate energy), which we call radiation scattered by the obstacle. The intrinsic properties of the scattered radiation can be different than that of the incident radiation. For the purpose of this thesis, we will limit ourselves to *elastic* scattering in which the frequency of the scattered radiation is the same as that of the incident radiation.

The strength of scattering is dependent primarily on polarizability of the scatterers, the number of scatterers, and the size of the scatterers. When the scatterers are non-interacting and are sufficiently small compared to the wavelength of light (λ_o), they can be considered point-dipole oscillators of the incident radiation (Figure 2.1). This was first described by Lord Rayleigh in the late 1800s and today bears his name: Rayleigh scattering. In the regime of Rayleigh scattering, the scattered intensity is observed to be inversely proportional to λ_o^4, and the scattering is observed to have insignificant angular dependence. However, as the particle size approaches or exceeds the wavelength of light, it can no longer be treated as a single dipole oscillator. The simplest approach then would be to treat a single particle as an assembly of many dipole scatterers each of which gives rise to Rayleigh scattering. Although the size of the scatterers plays a critical role in the treatise of light scattering, the scatterers' shapes dictate the overall scattering as well and so does the polarization state of the incident beam. This fact is exploited in chapter 4 where scattering from GNRs is discussed.

The study of scattering media isn't limited to the methods of light scattering, as there are numerous other scattering methods which have their own merits. For instance, X-ray and neutron scattering, due to their small wavelength, are able to probe smaller structures (on the order of a few angstroms). In comparison, due to significantly longer wavelengths compared to X-ray and neutron scattering, light is suitable for probing larger structures (on the order of nanometers and microns). Actually, the past 50

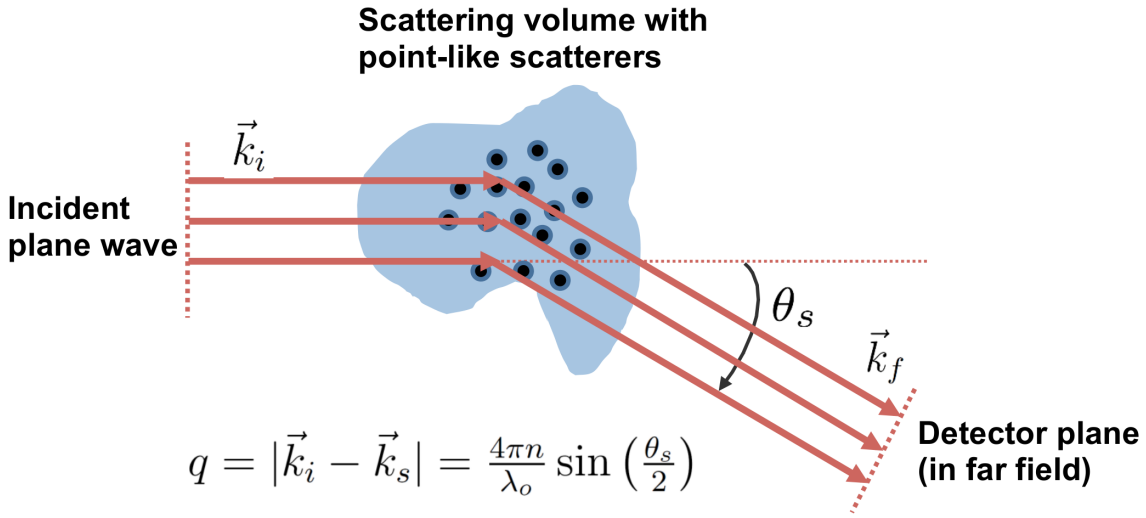

Figure 2.1: Point-like scatterers in the scattering volume are irradiated by a plane wave (incident wave vector, k_i), and the scattered beam is collected at an angle θ_s (scattering wave vector, k_s).

years has brought about various light scattering-based advancements in the characterization of macromolecules, polymers and colloids. Unlike X-ray and neutron scattering, light scattering techniques are non-invasive & non-ionizing, which is a critical advantage especially considering biomedical applications. Also, the availability of laser sources, which provide collimated (spatially coherent) and temporally coherent light, presents an additional advantage over other scattering methods.

A typical light scattering experiment consists of three basic units: a light source, a scattering medium, and a detector. In our discussion of light scattering, we are restricting ourselves to a scattering medium consisting of a dilute ensemble of particles, so the total scattering signal is the composite of the scattering from all particles within the illumination volume of the light source. Techniques based on light scattering rely on analyzing this composite scattered field to retrace the nature or the behavior of particles that are responsible for the scattering of light. A wealth of information about the scattering medium, such as particle size and distribution, particle shape, molar mass,

diffusion coefficients, and relaxation times of statistical fluctuations, can be extracted from suitable analysis of the scattered light. Light scattering techniques can be broadly categorized into two subgroups: static (classic) light scattering (SLS) and, dynamic (quasi-static) light scattering. In static light scattering, the time-averaged intensity of scattered light is measured as a function of the scattering angle, and parameters such as weight-averaged molar mass and radius of gyration of aggregates can be extracted by following a Rayleigh-Debye-Zimm formalism [1, 2]. In dynamic light scattering, the quantity of interest is the temporal intensity fluctuation scattered light, and the typical parameters that can be derived are the hydrodynamic size, and the diffusion coefficients of the particles. Dynamic light scattering is discussed in more detail in the following section.

2.2 Dynamic light scattering

Dynamic light scattering (DLS) deals with the analysis of intensity fluctuations of scattered light which can then be related to the underlying dynamics of the scattering medium. DLS is the technique behind various commercial light scattering based particle-sizers. A monochromatic laser source irradiates a dilute solution containing the particles to be characterized. The scattered field fluctuates due to the stochastic motion of the scatterers and this signal is collected by various detection schemes. With *a priori* knowledge of the solvent, the analysis of this temporal signal is used to infer the hydrodynamic size and size distribution of the particles. Alternatively, using probes of known size, shape, and low polydispersity, the physical property of the solvent such as viscosity in case of Newtonian fluids and viscoelasticity in case of non-Newtonian fluids can be elucidated from the measured diffusion coefficients of the probes.

To understand the analysis involved in DLS experiments, let's start by considering a plane electromagnetic wave (E_i) of wavelength λ_o coherently illuminating the scatterers

in the sample. In complex notation, the incident field is represented as:

$$\vec{E_i}(\vec{r},t) = E_o\, e^{i\vec{k_i}\cdot\vec{r}} e^{-i\omega_o t}\, \hat{E}_o \tag{2.1}$$

where $\vec{k_i}$ is the incident wave vector, ω_o is the frequency of the incident light, E_o is the amplitude of the incident electric field, and $\hat{E}_o$ a unit vector that represents the direction of the electric field.

A detector in the far-field positioned at an angle θ_s collects the beam scattered from the sample as shown in figure 2.1. Due to the difference in path lengths traversed by light scattered from different scatterers, interference results in the detector-plane. The overall scattered field at the detector (E_s) positioned at $\vec{r}$ is thus a superposition of the fields radiating at the angle θ_s from all N scatterers (assuming dilute suspensions) in their respective positions $\vec{r}_j$ within the scattering volume, and is given by:

$$E_s(\vec{r},t) = \sum_{j=1}^{N} A_j\, e^{i\vec{q}\cdot\vec{r}_j}\, E_o\, e^{-i\omega_o t} \tag{2.2}$$

where $\vec{q} = \vec{k_i} - \vec{k_s}$ is the scattering vector with $|\vec{q}| = \frac{4\pi n \sin(\theta_s/2)}{\lambda_o}$ (n is the refractive index of the medium), and A_j is the amplitude of the field scattered by the j^{th} particle. A_j has the form of a spherical wave in the far-field limit, depends on the difference in dipole polarizability between the particle and the medium, volume of the scattering particle, and is independent of the position of the scatterer [3, 4].

The argument of the first exponent, $(\vec{q}\cdot\vec{r}_j)$, in equation (2.2) represents the phase due to each scattering event, and the summation over all j scatterers results in a cumulative phase which is dependent on the relative position of the scatterers in the scattering volume. Thus, as the particles move randomly, the phase of the scattered field from each scatterer changes, and the overall scattered field (equation (2.2)) depicts a temporal fluctuation. The temporally variant scattered field E_s is stochastic in nature for

scatterers under Brownian motion. To extract useful information from this stochastic variable, autocorrelation functions are implemented, which have long been in use in noise and stochastic theories [5]. The autocorrelation represents the self-similarity between a signal and its delayed counterpart, and at a fundamental level, elucidates underlying physical processes such as Brownian motion, flow, chemical reactions, or other temporal processes present in the system [6, 7]. The particular case of scatterers in Brownian motion is the focus in this thesis and is discussed in section 2.3.

The autocorrelation can be computed for E_s, which is called the first-order field autocorrelation $G^{(1)}(\tau)$:

$$G^{(1)}(\tau) = \langle E_s^*(t)\, E_s(t+\tau)\rangle = \lim_{T\to\infty} \int_{-T/2}^{T/2} E_s^*(t)\, E_s(t+\tau)\; dt \tag{2.3}$$

where $\langle \dots \rangle$ represents ensemble-averaging (equal to time-averaging for an ergodic system), T is the overall observation time, and τ is the lag time. The value of τ ranges from 0 (no lag) to T (total observation time). The autocorrelation function of a temporally varying signal with zero mean value starts out from maximum correlation at $\tau = 0$ and eventually decays to a state of no correlation at long lag ($\tau \to \infty$).

Experimentally, the quantity measured by the detector in a scattering experiment (Figure 2.1) is the intensity rather than the electric field. Thus, similar to the first-order autocorrelation function, the second-order intensity autocorrelation function is defined as:

$$G^{(2)}(\tau) = \langle I_{det}(t)\, I_{det}(t+\tau)\rangle = \lim_{T\to\infty} \int_{-T/2}^{T/2} I_{det}(t)\, I_{det}(t+\tau)\; dt \tag{2.4}$$

where

$$I_{det} = \begin{cases} I_s = |E_s|^2 & \text{Homodyne (scattered beam detected)} \\ |E_s + E_{ref}|^2 & \text{Heterodyne (scattered beam mixed with a reference beam)} \end{cases}$$

In practice, the $T \to \infty$ requirement in the definition of an autocorrelation isn't satisfied in any experiment, and thus the intensity autocorrelations computed are only approximations to the true intensity autocorrelation given in equation (2.4). This approximation improves as T becomes much longer compared to the autocorrelation decay-time. Secondly, actual data in a DLS experiment isn't a continuous function as in the definition of the autocorrelation. The data consists of a discrete string of numbers,

$$\{I_{det}(\Delta t), I_{det}(2\Delta t), \ldots, I_{det}((N-1)\Delta t), I_{det}(N\Delta t)\},$$

collected by the detector by integrating the intensity signal over a small sampling time (Δt) throughout the entire duration of study (T). The autocorrelation is then computed by sequentially sliding and multiplying the string of intensity signals with itself before summing the result into a new sequence of numbers. This resulting sequence of numbers,

$$\{A_c(\tau = -(N-1)\Delta t), \ldots, A_c(\tau = -\Delta t), A_c(\tau = 0), A_c(\tau = \Delta t), \ldots, A_c(\tau = (N-1)\Delta t)\},$$

is the approximation to $G^{(2)}(\tau)$, which is a symmetric function about $A_c(\tau = 0)$ and thus its first-half can be ignored without loss of information. Graphically, each autocorrelation point $A_c(\tau)$ represents the area after multiplication of the signal with its time-lagged self (lagged by τ) (Figure 2.2). The rate at which the intensity autocorrelation decays indicates the rate of fluctuation of $I_{det}(t)$. Rapid fluctuations indicate that high frequency components are present whereas slow fluctuations indicate that low frequency components are present. Instead of analyzing the intensity fluctuation in time-domain, a similar analysis can thus be performed in frequency-domain by computing the power spectrum of $I_{det}(t)$. Experimentally, replacing the detector in a DLS setup by a spectrum analyzer directly facilitates analysis via power spectrum. Analysis via autocorrelation or via power spectrum both relay the same information and the choice usually depends

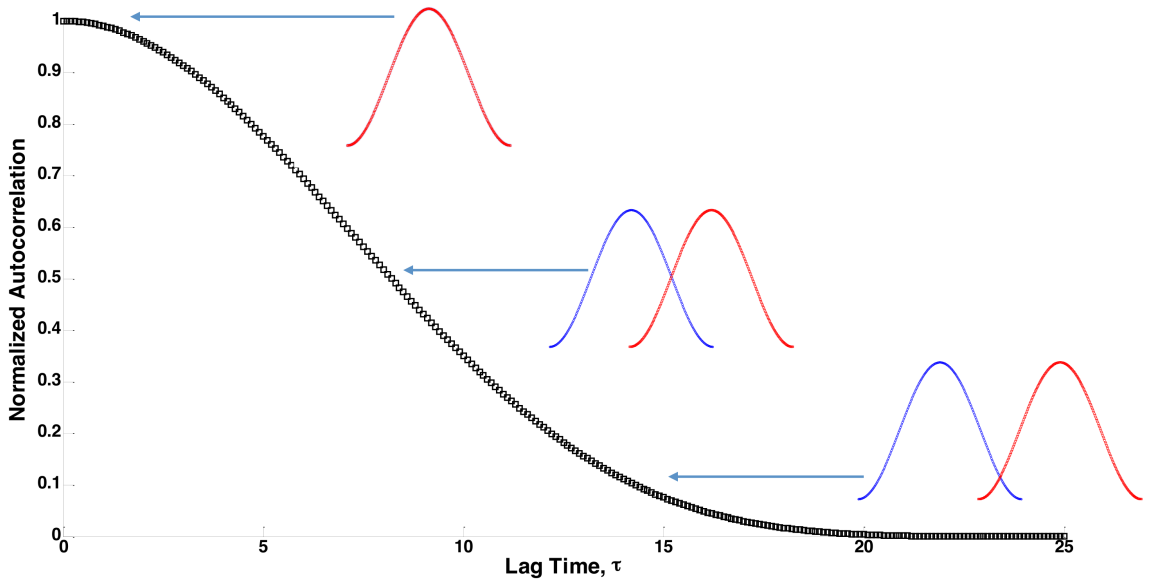

Figure 2.2: Autocorrelation of $\sin^2(x)$ function is shown as an example. Initially, when there is no lag ($\tau = 0$), the function and its sliding counterpart overlap entirely and this represents a state of maximum correlation. The correlation decreases with an increase in time-lag between the original function and its time-lagged self, which eventually decays to zero (state of no correlation). Note: Autocorrelation function is shown only for the positive time lags; the negative time lag values are symmetric across $\tau = 0$).

on the experimental setup. In fact, the power spectrum and autocorrelation are related by a Fourier transform according to Wiener-Khinchin theorem [8].

The first-order field autocorrelation and the second-order intensity autocorrelation are related to each other when the random variables involved are Gaussian (*i.e.,* the frequency distribution of the random variables is a bell-shaped curve symmetric about its mean). In a **homodyne** detection scheme where the scattered light from the sample is detected directly and the photon count rate or the photocurrent in the detector is used to generate an approximation to $G^{(2)}(\tau)$, the first-order and second-order autocorrelations are related by **homodyne Siegert relationship** [3, 9]:

$$G^{(2)}(\tau) = \langle I_{det} \rangle^2 + \left| G^{(1)}(\tau) \right|^2 \tag{2.5}$$

Typically, in DLS experiments using a **homodyne** detection scheme, a modified Siegert relation, using the normalized versions $g^{(1)}(\tau)$ & $g^{(2)}(\tau)$ of $G^{(1)}(\tau)$ & $G^{(2)}(\tau)$ respectively, is used, as follows:

$$g^{(2)}(\tau) = 1 + \beta \left| g^{(1)}(\tau) \right|^2 \tag{2.6}$$

where

$$g^{(1)}(\tau) = \frac{G^{(1)}(\tau)}{\langle I_{det} \rangle}$$

$$g^{(2)}(\tau) = \frac{G^{(2)}(\tau)}{\langle I_{det} \rangle^2}$$

In equation (2.6), β is an experimental unitless parameter of order unity.

Commercial DLS equipments to characterize particle size and diffusion coefficients almost exclusively operate under the homodyne detection scheme, especially due to the simplicity of the optical setup involved. However, the heterodyne detection scheme is equally capable of reproducing the same information. Unlike the homodyne detection scheme, the heterodyne detection scheme is also sensitive to forced mobility of the particles in the system, which is needed for measurements in the fields of light scattering velocimetry [10] and electrophoretic light scattering [11, 12]. More importantly, the methods developed for heterodyne schemes lend themselves directly to heterodyne-based techniques such as OCT, which is the direction pursued in this thesis. Thus, in the following subsection, we'll take a closer look at the heterodyne detection scheme and establish some useful relations.

2.2.1 Heterodyne detection scheme

In a heterodyne detection scheme, the scattered light I_s is mixed with a portion of the unscattered reference beam I_{ref}. Under the following conditions, (i) $I_{ref} \gg I_s$, (ii) fluctuations in the reference field E_{ref} are negligible compared to those in the scattered sample field E_s, and (iii) E_{ref} and E_s are statistically independent, the first-order and

second-order autocorrelations are related by **heterodyne Siegert relationship** [3, 9]:

$$G^{(2)}(\tau) = \langle I_{ref} \rangle^2 + 2I_{ref}\, \mathbf{Re}\left[G^{(1)}(\tau)\, e^{i\omega_o \tau}\right] \tag{2.7}$$

where $G^{(1)}(\tau)$ is the first-order autocorrelation of the sample electric field given by equation (2.3), and **Re** indicates the real part. From equation (2.7), we see that the quantity computed from intensity measurements, $G^{(2)}(\tau)$, can be directly related to the real part of $G^{(1)}(\tau)$, a quantity that describes the underlying physical processes responsible for the scattering fluctuation.

It is important to note that fluctuation of the intensity from its average, represented by $\delta I_{det}(t) = I_{det}(t) - \langle I_{det}(t) \rangle$, relays the same temporal information as intensity autocorrelation. The two are related as follows [9]:

$$G^{(2)}(\tau) = \langle I_{det} \rangle^2 + \langle \delta I_{det}(t)\, \delta I_{det}(t+\tau) \rangle \tag{2.8}$$

The autocorrelation of intensity fluctuation has a simpler structure than the autocorrelation of intensity as only the time-variant part is present in the former. Using the autocorrelation of intensity fluctuation especially simplifies the analysis in the context of the heterodyne detection scheme. Note that for $I_{ref} \gg I_s$, $\langle I_{det} \rangle^2$ in equation (2.8) can be replaced by $\langle I_{ref} \rangle^2$, so from equations (2.7) and (2.8), we get the following:

$$\langle \delta I_{det}(t)\, \delta I_{det}(t+\tau) \rangle = 2I_{ref}\, \mathbf{Re}\left[G^{(1)}(\tau)\, e^{i\omega_o \tau}\right] \tag{2.9}$$

In equation (2.9), we see a simple and direct relationship between a computed quantity from measured intensity fluctuations, on the left-hand side, and the quantity that underpins the physical processes, on the right-hand side. For further simplification, let $g^{(2)}(\tau)$ represent the normalized autocorrelation of heterodyne intensity fluctuation such that

its values range between 0 and 1; similarly, let $g^{(1)}(\tau)$ be the normalized autocorrelation of the sample field (*i.e.,* normalized version of $G^{(1)}(\tau)$) and for simplicity, we'll drop the $e^{i\omega_o\tau}$ term since it always cancels with $e^{-i\omega_o\tau}$ when $G^{(1)}(\tau)$ is written out using the complex form of electric fields (see equation 2.25). Then, from equation (2.9), it is clear that:

$$g^{(2)}(\tau) = \mathbf{Re}\left[g^{(1)}(\tau)\right] \tag{2.10}$$

Thus, in the heterodyne detection scheme, the normalized intensity fluctuation autocorrelation $g^{(2)}(\tau)$ is directly related to the real part of the normalized first-order sample field autocorrelation $g^{(1)}(\tau)$, a quantity that relates to the physical processes underpinning the intensity fluctuation such as Brownian motion which is discussed in section 2.3. So, from equation (2.10), it is clear that in the heterodyne detection scheme, $g^{(1)}(\tau)$ is an experimentally determined quantity via the measurement of intensity fluctuation.

Having established the utility of autocorrelation functions in analyzing temporal intensity fluctuations in DLS experiments, we now turn our attention to a particular case of particles diffusing in fluids under Brownian motion. The diffusion coefficients of the particles can be directly related to the first-order field autocorrelations, which is discussed in detail in the next section.

2.3 Brownian motion and diffusion

Following the motion of particles diffused in fluids for some time t under an optical microscope, one notices that their motion is quite erratic due to the random collisions with the molecules in the solvent (particles typically 50μm and smaller are considered for the erratic motion to be noticeably clear). This random jiggling motion is called Brownian motion, named after the Scottish naturalist Robert Brown who investigated pollen grains under a microscope in 1827. Diffusion, one of several naturally-occurring

transport phenomena, and Brownian motion are synonymous concepts. To see how this motion is related to time t, lets consider the Brownian motion of a particle in one dimension for simplicity. The displacement of the particle (from its initial position) at each instant can be considered as a random step from its previous position as follows:

$$x(t) = x(t-\tau) \pm \epsilon \tag{2.11}$$

where ϵ is the random step the particle takes between time $(t-\tau)$ and t, and the probability that the particle moves to the right is equal to the probability it moves to the left. Thus the first moment of $x(t)$, given by $\langle x(t) \rangle$ (average displacement of the particle), is insufficient to describe its motion as this quantity is zero. Thus, to quantify this motion, the second moment of $x(t)$ needs to be used:

$$\left\langle x^2(t) \right\rangle = \left\langle x^2(t-\tau) \right\rangle \pm \langle 2\, x(t-\tau)\, \epsilon \rangle + \left\langle \epsilon^2 \right\rangle \tag{2.12}$$

The second term in equation (2.12) averages to zero (since $\langle x(t-\tau) \rangle = 0$) and applying this equation iteratively all the way back to the first step of motion at $t = 0$ (where $x(0) = 0$), we have:

$$\left\langle x^2(t) \right\rangle = n(t)\epsilon^2 \tag{2.13}$$

The mean squared displacement of the particle at time t, $\langle \Delta x^2(t) \rangle = \langle |x(t) - x(0)|^2 \rangle$, is thus given by the number of time steps $n(t)$ times the square of the random step ϵ^2. Compared to the case of ballistic motion where $\langle \Delta x^2(t) \rangle$ scales with displacement as $n^2(t)$, we see that the $\langle \Delta x^2(t) \rangle$ scales linearly with $n(t)$, when the step-wise displacements are random. This is a defining feature that separates diffusive motion from ballistic motion.

In 3D, the mean squared displacement $\langle \Delta r^2(t) \rangle$ can be considered as a summation of the independent mean squared displacements in x, y and z, *i.e.,* $\langle \Delta r^2(t) \rangle = \langle \Delta x^2(t) \rangle +$

$\langle \Delta y^2(t) \rangle + \langle \Delta z^2(t) \rangle$. Thus, in 3D, we get:

$$\left\langle \Delta r^2(t) \right\rangle = 3n(t)\epsilon^2 \tag{2.14}$$

Since τ is the time-step, the number of time steps $n(t) = t/\tau$. So, we have:

$$\left\langle \Delta r^2(t) \right\rangle = 3\frac{t}{\tau}\epsilon^2 = 6D_T\, t \tag{2.15}$$

where $D_T = \frac{\epsilon^2}{2\tau}$ is the translational diffusion coefficient quantifying the Brownian motion.

According to the Einstein relation, the translational diffusion coefficient of a particle is a thermodynamic property which is inversely proportional to the frictional drag experienced by the particle at thermodynamic equilibrium:

$$D_T = \frac{k_B T}{\zeta} \tag{2.16}$$

where k_B is the Boltzmann constant, T is the temperature in Kelvin, and ζ is the frictional constant for the particle ($1/\zeta$ is called the mobility). From the Stokes approximation, for a spherical particle of radius a under no-slip boundary condition and low Reynolds number (*i.e.,* viscous forces dominant over inertial forces), the frictional constant is given by, $\zeta = 6\pi\eta a$. Thus, for a spherical particle, using the Stokes approximation and the Einstein equation, we get:

$$D_T = \frac{k_B T}{6\pi\eta a} \tag{2.17}$$

Thus, we see that a physical property of the fluid (viscosity, η) is directly related to the thermal property of the particle (diffusivity, D_T) via the Einstein equation and the Stokes approximation.

Particles diffusing in solutions also undergo rotational motion in much the same way

as translational motion. Following a similar statistical treatment as the translational case, the mean squared angular displacement $\langle \Delta\Phi^2(\tau) \rangle$ is also seen to be linearly related to time t through rotational diffusion coefficient D_R, as follows:

$$\left\langle \Delta\Phi^2(\tau) \right\rangle = 2ND_R\,t \tag{2.18}$$

where N is the number of angular degrees of freedom for the particle's rotational motion.

Debye extended the Einstein formalism of establishing translation diffusion through frictional drag to the case of rotational diffusion through rotational frictional drag ζ_R:

$$D_R = \frac{k_B T}{\zeta_R} \tag{2.19}$$

For a sphere, the rotational frictional drag is given by the Stokes approximation, $\zeta_R = 8\pi\eta a^3$). Thus, we have:

$$D_R = \frac{k_B T}{8\pi\eta a^3} \tag{2.20}$$

From equation (2.20), we see that rotational diffusion is inversely proportional to the cube of particle radius. So, larger particles rotate significantly more slowly compared to smaller particles.

For a rigid cylindrical-shaped particle (length L, and width d), the translational frictional drag ζ and rotational frictional drag ζ_R can be approximated as [13]:

$$\zeta = \frac{3\pi\eta L}{\left[\ln\left(\frac{L}{d}\right) + \gamma\right]}$$

$$\zeta_R = \frac{\pi\eta L^3}{3\left[\ln\left(\frac{L}{d}\right) + \gamma_R\right]} \tag{2.21}$$

where, γ and γ_R are correction factors introduced to account for the end-effect. For rigid rods in the range $2 < L/d < 20$, these factors were estimated as second-order

polynomials in d/L, the coefficients of which were approximated by numerically fitting the data [14]:

$$\gamma = 0.312 + 0.565\left(\frac{d}{L}\right) - 0.100\left(\frac{d}{L}\right)^2$$

$$\gamma_R = -0.662 + 0.917\left(\frac{d}{L}\right) - 0.050\left(\frac{d}{L}\right)^2 \tag{2.22}$$

Using equations (2.21) and (2.22) for a rigid rod, the Stokes-Einstein relations for translational and rotational diffusion are:

$$D_T = \frac{k_B T}{3\pi\eta L}\left[\ln\left(\frac{L}{d}\right) + 0.312 + 0.565\left(\frac{d}{L}\right) - 0.100\left(\frac{d}{L}\right)^2\right]$$

$$D_R = \frac{3k_B T}{\pi\eta L^3}\left[\ln\left(\frac{L}{d}\right) - 0.662 + 0.917\left(\frac{d}{L}\right) - 0.050\left(\frac{d}{L}\right)^2\right] \tag{2.23}$$

Note that translational diffusion of rigid rods are relatively less susceptible to slight variations in lengths of the rods. This can be seen from equation (2.23), in which D_R is inversely proportional to L^3, whereas D_T is inversely proportional to L only. Thus, a slight change in the length of a rigid rod amounts to a comparatively smaller change in D_T than in D_R.

So far, we have established the Stokes-Einstein relations for spherical and rod-like scatterers, which relates viscosity, a rheological property, to diffusivity, a thermal property. Next, we'll establish a relationship between the diffusion coefficients and the autocorrelation functions.

2.3.1 Autocorrelation and diffusion coefficients

To elucidate the relationship between the autocorrelation and the rotational and translation motion of the particles, lets start with the definition of the first-order field

autocorrelation $G^{(1)}(\tau)$ from equation (2.3):

$$G^{(1)}(\tau) = \langle E_s^*(t)\, E_s(t+\tau)\rangle = \langle E_s^*(0)\, E_s(\tau)\rangle \tag{2.24}$$

For a stationary random process (*i.e.,* independent of the exact time point of the measurement), the second equality in the above equation follows. Next, substituting the scattered field from equation (2.2) into equation (2.24), we get:

$$G^{(1)}(\tau) = \sum_{j=1}^{N}\sum_{k=1}^{N} \left\langle A_j^*(0)A_k(\tau)\right\rangle \left\langle e^{i\vec{q}\cdot[\vec{r}_j(\tau)-\vec{r}_k(0)]}\right\rangle E_o^2\, e^{-i\omega_o\tau} \tag{2.25}$$

In the above equation, the rotational and translation motion of the particles are assumed to be independent (strictly speaking, the rotational motion is independent of translational motion, whereas the translational motion is coupled to the rotational motion. This coupling is significant in 2D whereas it is weak in 3D [15]). Additionally, assuming that each particle in the ensemble has the same statistical behavior and their motions are uncorrelated (fair assumption in the dilute regime), $G^{(1)}(\tau)$ is further simplified to:

$$G^{(1)}(\tau) = N\ \langle A^*(0)A(\tau)\rangle \left\langle e^{i\vec{q}\cdot\vec{\Delta r}(\tau)}\right\rangle E_o^2\, e^{-i\omega_o\tau} \tag{2.26}$$

where $\vec{\Delta r}\,(\tau) = [\vec{r}\,(\tau) - \vec{r}(0)]$ is the displacement of the scatterer within a short time τ. Note that $A(\tau)$ is the amplitude of the field scattered by the particles and depends on their polarizabilities α, which has a tensorial form. For a particle small compared to the wavelength of light and whose polarizability is constant in all its spatial configuration (i.e. optically isotropic scatterer), $\langle A^*(0)A(\tau)\rangle$ reduces to a constant $\left\langle |A|^2\right\rangle$. On the other hand, for an optically anisotropic scatterer whose polarizability varies depending on its spatial configuration, $\langle A^*(0)A(\tau)\rangle$ contributes a polarizability-correlation term, $\langle \alpha^*(0)\alpha(\tau)\rangle$. This polarizability-correlation term is linked directly to the rotational mo-

tion of the particle and thus constitutes a rotationally variant term. The translationally variant term in the first order autocorrelation is present in the $\left\langle e^{i\vec{q}\cdot\vec{\Delta r}(\tau)} \right\rangle$ term, which is known as the self-intermediate scattering function, and is given by $e^{-q^2\left\langle \Delta r^2(\tau)\right\rangle/6}$ [9], where $\langle \Delta r^2(\tau) \rangle$ is the mean squared displacement of the scattering particles. Thus, we see that the first-order field autocorrelation function is proportional to the product of correlation functions for rotational and translational motion, and is given by:

$$G^{(1)}(\tau) = \begin{cases} N' e^{-q^2\left\langle \Delta r^2(\tau)\right\rangle/6}\, e^{-i\omega_o \tau} & \text{Isotropic scatterers} \\ N' \left\langle \alpha^*(0)\alpha(\tau) \right\rangle e^{-q^2\left\langle \Delta r^2(\tau)\right\rangle/6}\, e^{-i\omega_o \tau} & \text{Anisotropic scatterers} \end{cases} \tag{2.27}$$

where all constant terms are accumulated into a single constant N'.

Now, we are one step closer to relating an experimentally evaluated quantity, $g^{(1)}(\tau)$, to Brownian motion. We'll treat the case of optically isotropic particles and optically anisotropic particles separately in the next two sections. It is important to note that not all spherical particles are optically isotropic and neither are all structurally aniostropic particles optically anisotropic. Recent advances in nanomaterial synthesis has enabled scientists to synthesize spherical particles that have optical anisotropy [16]. And, a good majority of bacteria and biological macromolecules aren't optically anisotropic despite their structural anisotropy [17].

2.3.2 Optically isotropic scatterers

For an optically isotropic scatterer, from equations (2.27), we have:

$$G^{(1)}(\tau) = N' e^{-q^2\left\langle \Delta r^2(\tau)\right\rangle/6}\, e^{-i\omega_o \tau} \tag{2.28}$$

Normalizing the above autocorrelation, and also dropping the $e^{-i\omega_o\tau}$ term, the normalized first order field autocorrelation becomes:

$$g^{(1)}(\tau) = e^{-q^2\left\langle\Delta r^2(\tau)\right\rangle/6} = e^{-q^2 D_T\,\tau} \tag{2.29}$$

where the second equality follows from equation (2.15). Thus, $g^{(1)}(\tau)$ is directly related to mean squared displacement $\langle\Delta r^2(\tau)\rangle$ and translational diffusion coefficient D_T of the particle undergoing Brownian motion. As we saw earlier, under the no-slip boundary condition for Stokes's drag, the translational diffusion coefficient for a spherical probe of radius a is given by equation (2.17). So, D_T can be extracted from the experimentally evaluated $g^{(1)}(\tau)$, and using equation (2.17), the viscosity of the solvent η can be estimated from the measured D_T for a known size of the diffusing particles. Alternatively, knowing the viscosity of the solvent, the size of the diffusing probes can be estimated from the measured D_T, as in commercial DLS systems.

2.3.3 Optically anisotropic scatterers

For an optically anisotropic scatterer, from equation (2.27), we have:

$$G^{(1)}(\tau) = N'\,\langle\alpha^*(0)\alpha(\tau)\rangle\,e^{-q^2\left\langle\Delta r^2(\tau)\right\rangle/6}\,e^{-i\omega_o\tau} \tag{2.30}$$

$$= N'\,\langle\alpha^*(0)\alpha(\tau)\rangle\,e^{-q^2 D_T\,\tau}\,e^{-i\omega_o\tau}$$

Firstly, similar to the case of optically isotropic scatterers, we see that their mean squared displacement $\langle\Delta r^2(\tau)\rangle$ and thus translational diffusion D_T are directly related to an experimentally evaluated quantity, $G^{(1)}(\tau)$. More importantly, $\langle\alpha^*(0)\alpha(\tau)\rangle$, the polarizability correlation term, gives information about the tumbling of optically anisotropic scatterers. As light of a certain polarization state impinges on such a scatterer, it in-

duces a dipole moment, the magnitude and direction of oscillation of which depends on the orientation of the scatterer. And, since particles under Brownian motion continually reorient themselves due to random collisions with the solvent molecules, the magnitude and direction of the induced dipole also fluctuates. This fluctuation of the dipole moment is evident in the change in the state of polarization and the electric field strength of the scattered light emitted by the induced dipole.

When linearly polarized light impinges on an ensemble of optically anisotropic rod-like particles, and the same polarization of the scattered field is detected (co-polarized), the polarizability correlation in equation (2.27) takes on the following form [3, 9]:

$$\langle \alpha^*(0)\alpha(\tau)\rangle = \left[\alpha_o^2 + \frac{4}{45}\beta_o^2 e^{-6D_R\tau}\right] \tag{2.31}$$

On the other hand, when an orthogonal polarization of the scattered field is detected (cross-polarized), the polarizability correlation in equation (2.27) takes on the following form [3, 9]:

$$\langle \alpha^*(0)\alpha(\tau)\rangle = \frac{1}{15}\beta_o^2 e^{-6D_R\tau} \tag{2.32}$$

where D_R is the rotational diffusion coefficient of the scattering particles, $\alpha_o = \frac{\left(\alpha_{||}+2\alpha_\perp\right)}{3}$ and $\beta_o = \left(\alpha_{||} - \alpha_\perp\right)$ are called the mean polarizability and anisotropy respectively. $\alpha_{||}$ and $\alpha_\perp$ signify the components of the polarizability tensor along the long and short axes of the rod respectively, as shown in figure 2.3. Thus, from equation (2.30), the associated first-order field autocorrelations for co-polarized and cross-polarized components are given by:

$$G^{(1)}_{HH}(\tau) = N'\left[\alpha_o^2 + \frac{4}{45}\beta_o^2\, e^{-6D_R\tau}\right] e^{-q^2 D_T\,\tau}\, e^{-i\omega_o\tau}$$

$$G^{(1)}_{HV}(\tau) = N'\frac{1}{15}\beta_o^2\, e^{-6D_R\tau} e^{-q^2 D_T\,\tau}\, e^{-i\omega_o\tau} \tag{2.33}$$

In $G^{(1)}_{ij}(\tau)$, the first index (i) and the second index (j) indicate the polarization of the

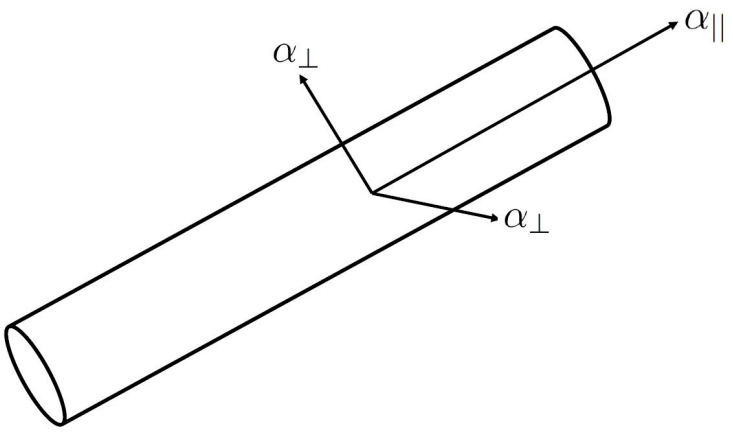

Figure 2.3: Components of polarizability tensors along the long and short axes of an optically anisotropic rod.

incident and detected light respectively. Thus, we see that the translational diffusion coefficient and rotational diffusion coefficient are embedded in the experimentally evaluated quantity, $G^{(1)}(\tau)$.

Normalizing the above autocorrelations by the initial value at zero lag ($\tau = 0$), and also dropping the $e^{-i\omega_o\tau}$ term, the normalized first order field autocorrelations are given by:

$$g^{(1)}_{HH}(\tau) = \left(\frac{45\alpha_o^2}{45\alpha_o^2 + 4\beta_o^2}\right) e^{-q^2 D_T \tau} + \left(\frac{4\beta_o^2}{45\alpha_o^2 + 4\beta_o^2}\right) e^{-6D_R\tau}\, e^{-q^2 D_T \tau}$$

$$g^{(1)}_{HV}(\tau) = e^{-6D_R\tau} e^{-q^2 D_T \tau} \tag{2.34}$$

Besides DLS [18], rotational and translational diffusion of micro- and nano- sized anisotropic scatterers, including GNRs, have also been studied using digital video microscopy [15], confocal microscopy [19], single-particle tracking [20], and holographic video microscopy [21], among others. Anisotropic scatterers are interesting as they more closely resemble the translational and rotational diffusion of various nanoscopic biological objects (*e.g.* viruses, pathogens, toxins *etc.*) whose diffusion isn't quite captured by spherical probes. In this thesis, we consider the diffusion of plasmonic GNRs,

which additionally offers further simplification of expressions in equation (2.34), as will be considered in chapter 4.

2.4 Motivation for Optical Coherence Tomography

DLS has been used for a wide range of practical applications where the optical density in the scattering medium is low and as such, the probing beam essentially undergoes single scattering from the scattering centers in the medium. However, in highly scattering media, traditional DLS systems fail to characterize the properties of the samples due to multiple scattering of the optical beam. When multiple scattering is dominant, an extension of DLS called diffusing wave spectroscopy (DWS) is employed, which assumes diffusive propagation of light through the optically turbid media [17, 22]. DWS has been successfully used to study probe motion in highly concentrated colloids and polymer solutions. However, many systems of practical interest aren't optically diffusive and thus cannot be characterized by DWS techniques. Thus, neither traditional DLS nor DWS cover the regime in which the dynamic systems of interest scatter the optical beam more than once but not sufficiently multiple times.

For many light scattering experiments, a coherent beam of light produced by lasers has been the favorable source due to properties such as high degree of collimation and high beam intensity. Recently developed light sources such as femtosecond lasers, and superluminescent diodes additionally may provide a broad spectrum (*i.e.,* a narrow temporal coherence length). Thus, unlike temporally coherent light sources, broadband sources are able to produce interference only over a limited temporal range due to their narrow temporal coherence length (Figure 2.4). This lack of interference can be utilized as a useful thing when the goal is to path-length resolve the scattering volume while suppressing multiple scattering of the optical radiation.

Interferometry allows the measurement of the magnitude and echo time delay of

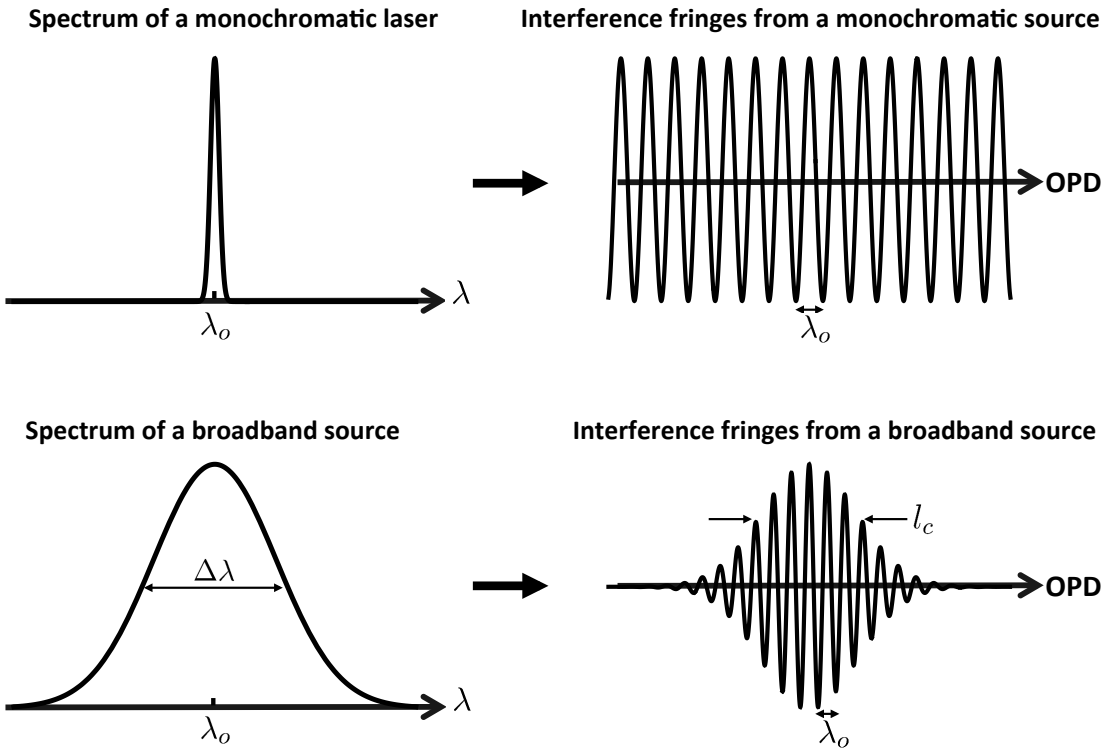

Figure 2.4: A monochromatic spectrum from a typical laser has a narrow bandwidth centered around the central wavelength λ_o. Such coherent sources can form an interference pattern over a long range of optical path length difference (OPD) between the interfering beams in the interferometer; as such, they have a long coherence length. Broadband sources have a large bandwidth $\Delta\lambda$ centered around the central wavelength λ_o. Such sources depict interference over a limited range of OPD between the interfering beams, and thus have limited coherence length (l_c). The interference fringe spacing is λ_o in both cases when plotted against OPD.

backscattered light by superposition with a reference field, providing high sensitivity. Additionally, performing interferometry with a light source with low temporal coherence allows single scattering from a localized volume (the coherence volume) to be analyzed, which is the concept behind the technique called low coherence interferometry (LCI) [23, 24, 25]. LCI has been successfully used to measure particle dynamics as well as resolve spatial variations in Brownian diffusion coefficients within highly scattering me-

dia [26]. LCI has also been shown as a viable alternative to DLS/DWS techniques for microrheological analysis of high concentration polymer solutions [27].

Techniques that are capable of characterizing particle diffusion non-invasively in highly heterogeneous samples such as biological soft tissues and biological fluids are highly desirable in biomedicine today. OCT, which is a non-invasive, micron-resolution imaging modality based on LCI, sits in a favorable position to fulfill this need in biological studies. Studying particle diffusion using OCT extends its functionality beyond architectural imaging of biological soft tissues and opens doors for analysis of particle dynamics in rich biological samples, which holds enormous potential in enhancing our understanding of mechanisms of drug delivery, disease progression, disease pathogenesis, as well as micro- and nano- scale tissue properties. The motivation of this thesis is thus to establish OCT as a viable tool to study dynamics of nano-scale probes (GNRs to be precise), and also to exploit the depth-gating capability offered by low coherence illumination to study heterogeneous samples that presently hold immense interest in the field of biomedicine.

Chapter 3

Optical Coherence Tomography system development

3.1 Optical Coherence Tomography

Optical Coherence Tomography (OCT) is an interferometric technique that performs non-invasive, micron resolution, cross-sectional imaging of biological tissues up to depths of a few millimeters by measuring the echoes of backscattered light [28]. OCT enables real time, *in situ* visualization of tissue microstructures without the need to remove and process specimens, and has tremendous potential for use in clinical settings in guiding surgical and microsurgical procedures, in imaging pristine tissues whose excision isn't possible for use with traditional biopsy-based methods, and in three dimensional reconstruction of *in situ* pathology. Although the limiting factor for OCT imaging is the penetration depth, this limitation is mitigated by integration with fiber optic components such as catheters and endoscopes for real-time *in vivo* imaging of internal structures [29]. OCT has had significant clinical impact in opthalmology [30] and has also found applications in cardiology [31], pulmonology [32], urology [33], neurosurgery [34], gastroenterology [35, 36], and oncology [37, 38], among others.

OCT performs cross-sectional imaging by measuring the magnitude and echo time delay of light scattered from internal microstructures in tissues. An OCT depth-scan

(axial-scan, A-scan, or z-scan) measures the backscattering as a function of depth in a sample. Cross-sectional images are generated by performing a series of axial scans at sequential transverse positions to generate a two-dimensional map (B-scan) of reflection sites in the sample. Additionally, three dimensional datasets representing the volumetric optical backscattering profile of the sample can be generated by raster scanning the imaging beam to acquire sequential B-mode images (Figure 3.1).

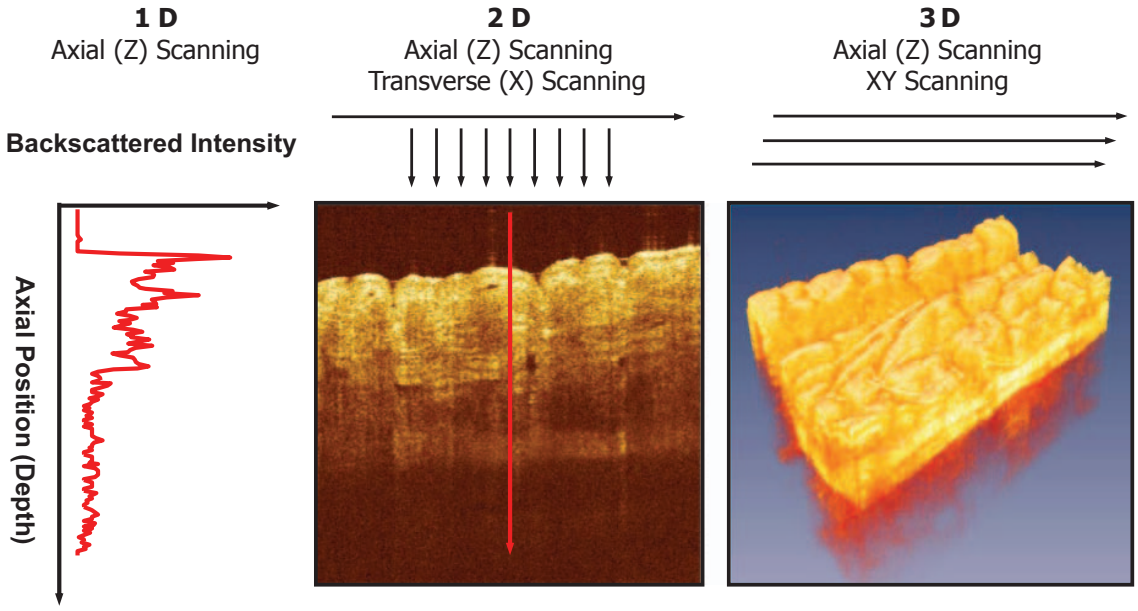

Figure 3.1: Cross-sectional images generated in OCT by measuring the magnitude and echo time delay of light. An axial scan (z-scan) measures backscattered intensity versus depth in the sample. Laterally adjacent depth-scans are used to obtain a two dimensional map of reflection sites (B-mode). Three dimensional data sets are generated by raster scanning a series of B-scans. Figure printed from Optical Coherence Tomography Technology and Applications (2008) [39], pg. 2, Introduction to OCT, J. Fujimoto and W. Drexler, **Copyright** ©Springer-Verlag Berlin Heidelberg 2008, with kind permission of Springer Science+Business Media.

OCT is analogous to ultrasound imaging since both techniques measure backscattering of an incident wave. As the name suggests, ultrasound uses acoustic waves whereas OCT uses optical waves, typically in the near-infrared region, to probe the biological sample. Depending on the varying optical (in OCT) or acoustic properties (in ultra-

sound) of structures in the sample, the incident field is backscattered differently. The locations of these structures are then ascertained by measuring the echo time it takes for light or sound to return from different depths. The fundamental difference between OCT and ultrasound becomes clear when we consider the speeds at which light (3×10^8 m/s) and sound (1500 m/s) propagate. In ultrasound, measurement of distances with a 100 μm resolution (typical resolution in ultrasound) requires a time resolution of $\sim$70 ns which is within the reach of modern electronic detectors. However, in OCT, measurement of distance with a 3 μm resolution (typical axial resolution in OCT) requires time resolution of $\sim$10 fs [39]. Such a timescale doesn't allow for direct electronic detection and thus interferometry is used in OCT for detection of light backscattered from the sample.

OCT is performed in the near-infrared region of the optical spectrum. This choice is motivated by the presence of a "biological window" between the wavelengths of 800 nm and 1300 nm where the cumulative optical attenuation due to absorption from melanin, haemoglobin, and water present in biological tissues reaches a minimum [40, 41, 42]. Additionally, due to high anisotropy parameter ($g = 0.80 - 0.95$) for near-infrared radiation in tissues, optical radiation in this region experiences highly forward-directed scattering [43], thereby allowing deep tissue imaging.

OCT was first conceived as a time-domain system (Time Domain OCT, TD-OCT) in which the interferogram is collected by rapidly changing the optical path length between the sample and reference beams in a Michelson interferometer [28]. Although TD-OCT has been successfully employed to investigate many types of biological samples, its limiting factors have been the lack of optical phase stability, and the speed of data acquisition which is limited by the the scanning speed of the interferometer reference arm. These limitations of TD-OCT are overcome by systems working in the Fourier domain (Fourier Domain OCT, FD-OCT), in which the scanning of the reference arm

is obviated, and the depth-ranging of the sample is made possible by an analysis of the spectral components of the collected interferogram [44]. FD-OCT has been performed in the following two configurations: Spectral Domain OCT (SD-OCT) in which the collected interferogram in split into its frequency components by a diffraction grating and the resulting spectral interferogram is collected using a line-scan camera [45, 46], and Swept Source OCT (SS-OCT), in which the frequency of the optical source is rapidly swept periodically through the entire optical bandwidth [47, 48]. At present, SS-OCT systems are more compact and boast rapid scanning capability compared to SD-OCT systems and are popular in the 1300 nm wavelength range. On the other hand, SD-OCT has been the choice for researchers whose applications require greater optical phase stability, and also are dominant systems in the 800 nm wavelength range. Novel light sources and photodetectors for OCT imaging are continually being improved upon, and with this evolution in light sources and detectors, both SS-OCT and SD-OCT systems should overcome their individual shortcomings and achieve faster acquisition, higher resolution, and sensitivity in the near future. In the following subsections, we'll discuss TD-OCT and SD-OCT before discussing the design of a polarization sensitive SD-OCT system.

3.1.1 Time domain OCT

Figure 3.2 depicts a standard time domain OCT system (TD-OCT) consisting of a low coherence source and a Michelson interferometer. The working principle of TD-OCT is based on LCI, and thus interference fringes occur if the optical path lengths of the sample beam and the reference beam coincide within the coherence length (l_c). The coherence length signifies the spatial extent along the beam axis over which the electric field of the propagating beam is significantly correlated, and is related to correlation time τ_c by $l_c = c\tau_c$ (c is the speed of light). The correlation time τ_c is given by the full-

width-half-maximum (FWHM) of the electric field autocorrelation function. Thus, given a beam with a Gaussian power spectral density, its Fourier transform, which according to Wiener-Khinchin theorem is the autocorrelation of the electric field, is also Gaussian (since the Fourier transform of a Gaussian function is also a Gaussian). The broader the FWHM of the power spectral density, the narrower the FWHM of the autocorrelation function is. In other words, a broader optical spectrum results in a short coherence time τ_c and thus a shorter coherence length l_c. The coherence length for a Gaussian source with a central wavelength λ_o and a spectral bandwidth of $\Delta\lambda$ is given by [39]:

$$l_c = \frac{2\ln(2)}{\pi}\frac{\lambda_o^2}{\Delta\lambda} \tag{3.1}$$

The two optical beams in an interferometer are coherent with each other when their optical path length difference (OPD) $\leq l_c$.

In TD-OCT, the reference optical path length is changed periodically with respect to a fixed sample optical path length as depicted in figure 3.2. The backscattered sample beam coherently interferes with the reference beam only when their OPD is within the coherence length l_c of the source. This allows OCT to depth-range the sample, which is referred to as *coherence gating*. So, the axial resolution of the OCT system is determined by the coherence length of the source. The backscattered sample beam and the reference beam interfere coherently and are subsequently detected by a photodetector. The photocurrent $i(t)$ produced by the photodetector is given by:

$$i(t) = \rho\left(\frac{P_s}{2}\right)\left\langle|E_s + E_r|^2\right\rangle \tag{3.2}$$

where $\rho = \left(\frac{\eta e}{h\nu}\right)$ is the detector responsivity, η is the efficiency of the detector to convert photons to electrons (quantum efficiency), h is the Planck's constant, e is the electronic charge, ν is the mean optical frequency of the beam, P_s is the incident power in the

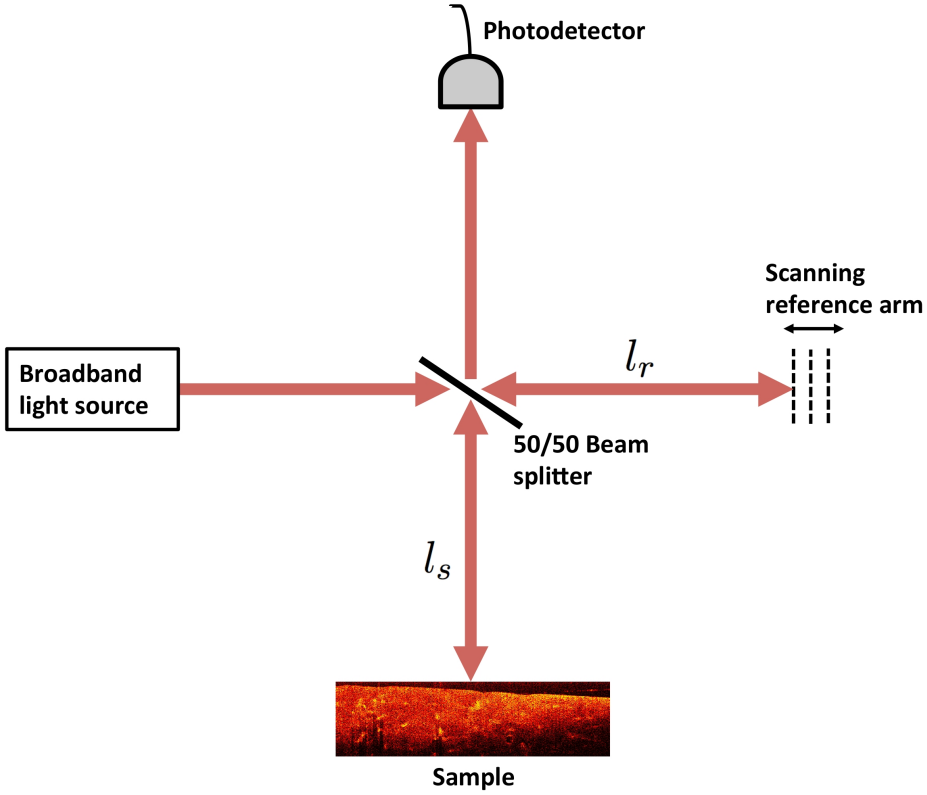

Figure 3.2: A TD-OCT system consisting of a low coherence light source, Michelson interferometer, and a photodetector. Optical path length difference (OPD) is introduced by periodic scanning of the reference arm. OPD $= 2n(l_r - l_s)$, where n is the refractive index (assuming that the reference arm is refractive index matched with the sample arm).

sample arm (which is also the reference power, assuming the interferometer beam splitter is 50/50), E_r is the electric field of the backreflected reference beam, E_s is the electric field of the backscattered sample beam, and $\langle \cdots \rangle$ is the time averaging over the exposure time of the detector. Writing the backscattered sample and reference electric fields in complex notation, we have the following:

$$E_s(t) = a_s\, e^{i2k_s l_s} e^{-i\omega_o t}$$

$$E_r(t) = a_r\, e^{i2k_r l_r} e^{-i\omega_o t} \tag{3.3}$$

where a_s and a_r are the amplitudes of the backscattered sample and reference electric fields respectively, k_s and k_r denote the propagation wave-vector of the sample and reference beams respectively, ω_o denotes the optical angular frequency, and l_r and l_s denote the length of the reference and sample arms.

Substituting E_r and E_s from equation (3.3) into equation (3.2), and assuming $k_s = k_r = k_o$, we get the following:

$$i(t) = \rho \left(\frac{P_s}{2} \right) \left(a_r^2 + a_s^2 + 2a_r a_s \cos[2k_o(l_s - l_r(t))] \right) \tag{3.4}$$

Without the constant prefix in the detected photocurrent above, the detected signal (let $I_D(t)$) can be written as:

$$I_D(t) = a_r^2 + a_s^2 + 2a_r a_s \cos[2k_o(l_s - l_r(t))] \tag{3.5}$$

The first two terms in equation (3.5) are DC-terms (time-invariant terms) whereas the last term with the cosine is the AC-signal (*i.e.,* it is the interference term), which is the signal of interest.

Our treatment of the interference above considered a monochromatic source for simplicity. For a low coherence light source with a bandwidth of Δk (assumed to be a Gaussian), we can extend the simple treatment presented above by considering the electric field of the low coherence source as a superposition of monochromatic waves of various frequencies, in which case the detected signal is given by [39]:

$$I_D(t) = a_r^2 + a_s^2 + 2a_r a_s \, e^{-(l_s - l_r(t))^2 \Delta k^2} \cos[2k_o(l_s - l_r(t))] \tag{3.6}$$

As the relative OPD between the two arms changes (due to the scanning of the reference path length $l_r(t)$), the cosine in the AC-signal is seen to oscillate, which is thus the

interference term:

$$I_{AC}(t) = 2a_r a_s \, e^{-(l_s - l_r(t))^2 \Delta k^2} \cos[2k_o(l_s - l_r(t))] \tag{3.7}$$

The exponential term in the AC-signal, which is equal to the inverse Fourier transform of a Gaussian source spectral density, is the envelope (Gaussian shaped) of the interference term. This envelope term $e^{-(l_s - l_r(t))^2 \Delta k^2}$ is the coherence function that determines the axial spread of the interference term, and is thus also termed the axial Point Spread Function (PSF). It is this envelope term that allows coherence gating at resolution limited by l_c. Therefore, as the reference mirror is scanned axially, the amplitude of the sample electric field a_s is depth-resolved, and this constitutes a single A-scan in TD-OCT.

The lateral scan to produce cross-sectional (B-mode) images is performed by scanning the imaging beam across the sample. The lateral resolution of the B-mode OCT image is determined by the diffraction limited focal spot of the Gaussian imaging beam (Δx) and is given by [8]:

$$\Delta x = 1.22 \, \frac{f \lambda_o}{d} \tag{3.8}$$

where f is the focal length of the imaging lens, λ_o is the central wavelength of the Gaussian imaging beam, and d is the spot size of the beam on the imaging lens. So, a fine transverse resolution can be obtained by using a lens with higher numerical aperture (NA) that focuses the imaging beam to a smaller spot size $\left[NA = \sin\left(\tan^{-1}\left(\frac{d}{2f} \right) \right) \right]$. However, the transverse resolution is also related to the confocal parameter or depth of focus (b) of the Gaussian beam, given by [8]:

$$b = \frac{\pi \Delta x^2}{2\lambda_o} \tag{3.9}$$

Thus, although using a high NA lens increases the transverse resolution (*i.e.,* smaller

Δx), it results in a decrease in the depth of focus, which limits the depth of imaging. So, depending on the experimental purpose, whether it is optical coherence microscopy with ultra-high axial resolution or regular cross-sectional optical coherence tomographic imaging, a proper choice of an imaging lens with a suitable NA needs to be made. More importantly, the axial resolution is decoupled from transverse resolution, which is unique to OCT imaging and is in sharp contrast to imaging modalities such as optical microscopy.

The generation of an OCT image from the detected signal involves several steps. First, the depth-scanned AC-signal $I_{AC}(z,t)$ is isolated from $I_D(z,t)$ by reference subtraction (also, assuming $a_r >> a_s$). Secondly, an analytic continuation of the real AC-signal is performed to generate a complex analytic signal, $\tilde{S}(z,t)$ [49, 50]:

$$\tilde{S}(z,t) = A(z,t)e^{i\phi(z,t)} \tag{3.10}$$

where $A(z,t)$ and $\phi(z,t)$ are the amplitude and phase of the complex analytic signal. Typically, the absolute value of $\tilde{S}(z,t)$ is taken to get $A(z,t)$, which is mapped in the log scale (logarithmic transformation compresses the dynamic range and preserves the visual details in the lower intensity values), and this represents a single A-scan in a structural OCT image. The phase $\phi(z,t)$, extracted during the complex analytic continuation of $I_{AC}(z,t)$, is sensitive to the OPD, and is used in phase sensitive measurements to quantify axial motion in the sample [49, 51]. Due to motion artifacts from inherent scanning of the reference arm in TD-OCT, $\phi(z,t)$ isn't as stable as in SD-OCT. In addition to phase stability, SD-OCT also offers a much faster operation and increased sensitivity, as is to be discussed in the next subsection.

3.1.2 Spectral domain OCT

Unlike TD-OCT, the reference arm is held stationary and all optical echoes from the sample are measured simultaneously in SD-OCT. The backscattered sample and reference beams are split into their frequency components by a diffraction grating and detected by a linescan camera in a spectrometer. Let's consider the backreflected spectral reference and sample field (from a single scatterer at z):

$$E_r(k,t) = a_r\, e^{i2kl_r} e^{-i\omega_o t}$$

$$E_s(k,t) = a_s(z)\, e^{i2kl_s}\, e^{-i\omega_o t} \tag{3.11}$$

where $a_s(z)$ contains the backscattered sample information. Using the expressions for $E_s(k)$ for scatterers at various depths in the sample and $E_r(k)$ for the reference field (suppressing the temporal $e^{-i\omega_o t}$ part for convenience), the spectral interferogram detected in the spectrometer can then be written as:

$$I(k) = S(k) \left| a_r\, e^{i2kl_r} + \int_0^\infty a_s(z)\, e^{i2k[l_r + n(z)z]}\, dz \right|^2 \tag{3.12}$$

$$I(k) = S(k) \left[a_r^2 + 2\, a_r \int_0^\infty a_s(z) \cos[2kn(z)z]\, dz + \int_0^\infty\!\!\int_0^\infty a_s(z) a_s(z') e^{-i2kn(z)(z-z')}\, dz\, dz' \right]$$

where $S(k)$ is the power spectrum of the source (expression for $S(k)$ is given in equation (3.15)), depths z, z' are defined from the $z = 0$ plane, and $n(z)$ is the refractive index. The first term, called the reference term ($I_{ref} = S(k)a_r^2$), can be measured directly by blocking the sample arm and thus eliminated by subtracting it from $I(k)$. The depth information of the sample is present in the second term in equation (3.12), as scattering from depth z in the sample is seen to be encoded in spatial frequency $2n(z)z$ of the cosine function. Thus, deeper scattering events are seen to result in higher encoded frequency. Using $\hat{a}_s(z)$ as a symmetric version of $a_s(z)$ across the reference plane *i.e.,*

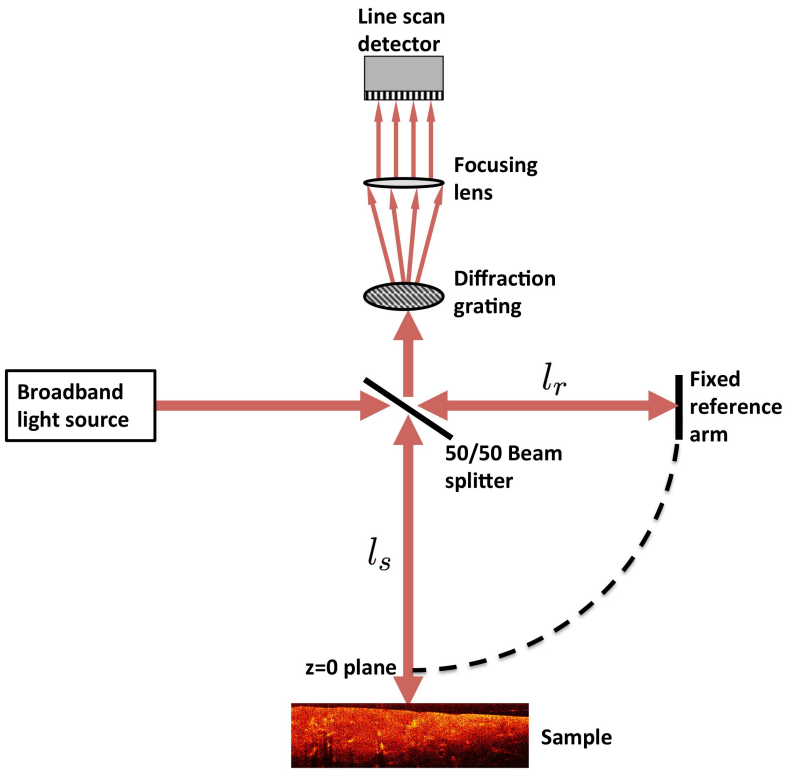

Figure 3.3: An SD-OCT system consisting of a low coherence light source, Michelson interferometer, and a dispersive spectrometer which is comprised of a diffraction grating, focusing lens and a line scan camera. The $z = 0$ plane (reference plane) corresponds to a distance of l_r from the beam splitter such that $l_s = l_r + n(z)z$; z is defined from the $z = 0$ plane, and $n(z)$ is the refractive index ($n(z) = 1$ in the air, and $n(z) = n_{sample}$ inside the sample).

$\hat{a}_s(z) = a_s(-z) + a_s(z)$ (a fair extension, since $a_s(z) = 0$ for z outside the sample), the resultant spectral interferogram can be cast in the form of Fourier transforms:

$$I(k) - I_{ref}(k) = S(k)\left[a_r \int_{-\infty}^{\infty} \hat{a}_s(z)\, e^{-i2kn(z)z}\, dz + \frac{1}{4}\int_{-\infty}^{\infty} \mathbf{R}[\hat{a}_s(z)]\, e^{-i2kn(z)z}\, dz\right] \quad (3.13)$$

$$\text{or, } I(k) - I_{ref}(k) = S(k)\left[a_r\, \mathbf{FT}\left[\hat{a}_s(z)\right] + \frac{1}{4}\, \mathbf{FT}\left[\mathbf{R}[\hat{a}_s(z)]\right]\right]$$

where **FT** denotes the Fourier transform and **R** denotes the autocorrelation function. Thus, performing an inverse Fourier transform, we get:

$$\mathbf{FT}^{-1}[I(k) - I_{ref}(k)] = \mathbf{FT}^{-1}[S(k)] \otimes \left[a_r \hat{a}_s(z) + \frac{1}{4}\mathbf{R}[\hat{a}_s(z)] \right] \tag{3.14}$$

where $\mathbf{FT}^{-1}$ is the inverse Fourier transform, and $\otimes$ indicates a convolution. Note that the Gaussian spectral density function $S(k)$ and its inverse Fourier transform are given by:

$$S(k) = \frac{1}{\Delta k \sqrt{\pi}} e^{-\left[\frac{k-k_o}{\Delta k}\right]^2} \longleftrightarrow \mathbf{FT}^{-1}[S(k)] = e^{-(n(z)z)^2 \Delta k^2} \tag{3.15}$$

Similar to equation (3.6) earlier in TD-OCT, the $e^{-(n(z)z)^2\Delta k^2}$ term is the coherence function (also called the correlogram). In equation (3.14), the first term containing $\hat{a}_s(z)$ has the backscattered depth information of the sample. Thus, the correlogram determines the spread of backscattered interference signal $\hat{a}_s(z)$ at each scattering point along the axial direction, thereby performing coherence gating. The autocorrelation term $\mathbf{R}[\hat{a}_s(z)]$ is due to interference of fields from various depths of the sample. This term is centered around the reference plane ($z = 0$) and typically has negligible contributions at longer depths (strongly correlated at $z = 0$, and decays rapidly for longer z-lags). Thus, the autocorrelation term $\mathbf{R}[\hat{a}_s(z)]$ can be separated from the coherence-gated backscattered interference term, $e^{-(n(z)z)^2\Delta k^2} \otimes \hat{a}_s(z)$, by intentionally keeping the reference plane outside the sample (as shown in figure 3.3), and by keeping $E_s << E_r$. The coherence-gated backscattered interference term is symmetric across the reference plane due to the inverse Fourier transform involved, and thus its conjugate in $z < 0$ can be ignored in post-processing without loss of useful information. The resulting term, $e^{-(n(z)z)^2\Delta k^2} \otimes a_s(z)$, is the SD-OCT axial signal, $\tilde{S}(z)$:

$$\tilde{S}(z) = \mathbf{FT}^{-1}[I(k) - I_{ref}(k)] \approx e^{-(n(z)z)^2\Delta k^2} \otimes a_s(z) \tag{3.16}$$

Additionally, unlike in TD-OCT where complex analytic continuation of the real AC-signal (equation (3.10)) is implemented to get the signal's phase, the SD-OCT signal is already in complex form due to the inverse Fourier transform (thus of the form, $\tilde{S}(z) = A(z)e^{i\phi(z)}$, where $A(z)$ and $\phi(z)$ are the amplitude and phase of the complex SD-OCT signal). In SD-OCT, the low frequency end of the spectral interferogram $I(k)$ results from scatterers at shorter optical path lengths in the sample, and similarly high frequencies result from waves originating from longer optical path length in the sample (i.e. scatterers deep in the sample). Shortening the reference arm thus has the effect of increasing the encoding frequency of the spectral interferogram. However, the linescan detector used to detect the spectral interferogram has a limited spectral resolution, and the highest frequency that can be detected is limited by the Nyquist criterion, according to which the sampling frequency of the linescan array has to be at least twice as large as the largest frequency to be detected. Thus, the imaging depth that can be measured in SD-OCT is determined by the ability of the detector to measure high frequencies, and is limited by Nyquist frequency. The measuring range of the detector is given by [45, 52]:

$$z_{max} = \frac{N\,\lambda_{min}\lambda_{max}}{4\,n\,(\lambda_{max} - \lambda_{min})} \tag{3.17}$$

where $[\lambda_{min}, \lambda_{max}]$ is the detector's spectral range, N is the number of detector pixels, and n is the refractive index of the sample.

The axial and lateral resolutions are given by the same expressions as in TD-OCT (equations (3.1) and (3.8)). Compared to TD-OCT, SD-OCT presents an enhancement in acquisition speed, improvement in phase sensitivity, and additionally, an improvement in the detection sensitivity (signal-to-noise ratio (SNR) for a perfect reflector). The expression for SNR in TD-OCT, assuming shot-noise limited detection, is given by [53]:

$$\mathrm{SNR}_{\text{TD-OCT}} = \frac{\rho R_s P_s}{2eB} \tag{3.18}$$

where ρ is the detector responsivity, R_s is the sample reflectivity, P_s is the power in the sample arm, e is the electron charge, and B is the electronic bandwidth. B is a product of the number of interference fringes occurring on the linescan camera during each A-scan, camera linerate (number of A-scans/sec), and fractional bandwidth of the light impinging on the detector [54]:

$$B = \left(\frac{z_{max}}{\lambda_o/2}\right)\left(\frac{1}{\Delta t}\right)\left(\frac{\Delta\lambda}{\lambda_o}\right) \tag{3.19}$$

where Δt is the time it takes to acquire a single A-scan, and other symbols have their predefined meanings. In SDOCT, all optical echoes from the sample are measured simultaneously and as a result, an improvement of the SNR by a factor of $N/2$ over the SNR in TD-OCT is obtained (N is the number of detector pixels, and the factor of $1/2$ is from redundant data in the positive and negative path delays across reference plane generated in SD-OCT due to the inverse Fourier transform) [54]:

$$\mathrm{SNR}_{\text{SD-OCT}} = \left(\frac{N}{2}\right)\left(\frac{\rho R_s P_s}{2eB}\right) \tag{3.20}$$

Thus far, we have discussed important parameters that define the performance of an SD-OCT system such as axial and lateral resolutions, depth of focus, depth-scan range, and sensitivity. In the next subsection, we'll discuss the design of a custom polarization sensitive OCT (PS-OCT) system operating in the spectral domain.

3.2 Design of spectral domain PS-OCT system

The custom-designed spectral domain PS-OCT system consists of three main components: a light source, a free-space Michelson interferometer, and a free-space spectrometer (Figure 3.4). The light source consists of a Ti:Sapphire laser (Griffin, KMLabs,

Inc.), which affords a tunability over a wide wavelength range between 650 nm and 1000 nm, and more importantly allows broad bandwidth operation in its modelocked configuration. As described earlier, the broad bandwidth is necessary for low coherence imaging. For our application, we use a central wavelength of 800 nm and a bandwidth of > 120 nm. Using equation (3.1), the theoretical axial resolution of the imaging system is estimated to be < 2.4 μm in free space.

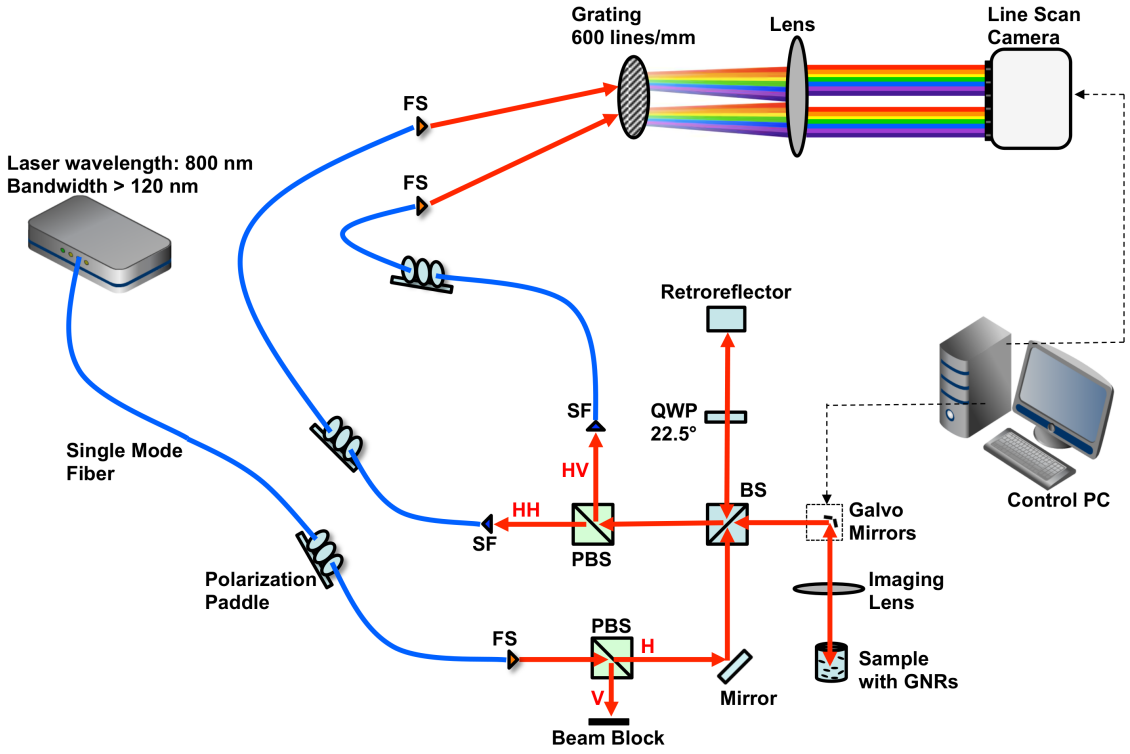

Figure 3.4: Schematic diagram of a custom-designed PS-OCT system consisting of a Ti:Sapphire laser source, a free-space Michelson interferometer, and a free space spectrometer. *HH* indicates the co-polarized component and *HV* indicates the cross-polarized component; FS: Fiber to free-space coupler, SF: Free-space to fiber coupler; QWP: Quarter wave plate; PBS: 50:50 polarizing beam splitter; BS: 50:50 beam splitter (non-polarizing).

The collimated beam from the laser is first led through a Faraday isolator, which allows transmission of light in the forward-direction only and thus protects the laser against back-reflected light. The collimated light is then launched through a single-

mode fiber (Thorlabs, 780HP FC/APC) using a free-space-to-fiber coupler consisting of a focusing lens ($f = 3.1$ mm). For a measured beam spot diameter, d, of $\sim(0.8 - 1)$ mm on the focusing lens, the NA of the imaging system is estimated to be $\sim(0.13 - 0.16)$ $\left[NA = \sin\left(\tan^{-1}\left(\frac{d}{2f}\right)\right)\right]$, which matches well with the NA (0.13) of the single-mode fiber, which is a necessary condition for efficient beam launching through the fiber. The fiber-launched beam *en route* to the free-space Michelson interferometer passes through a fiber polarization controller (Thorlabs, FPC560), the adjustment of which allows easy polarization control over the entire Poincaré sphere. The beam from the fiber is then launched through an adjustable collimator (Thorlabs, CFC-11-B-APC) into the free-space interferometer and polarized with its electric field in the horizontal direction (*i.e.,* horizontal to the surface of the optical table; H polarized) after passage through a polarizing beam splitter (Newfocus, 5812). The H polarized beam is then split by a 50:50 non-polarizing beam splitter (Thorlabs, BS011) into a stationary reference arm and a sample (imaging) arm, constituting a Michelson interferometer; the two arms are offset by a few coherence lengths as depicted in figure (3.3).

The transmitted beam from the non-polarizing beam splitter is back-reflected to within 1 arcsecond by a hollow gold retroreflector (Edmund Optics, NT46-183). The reference arm also consists of a quarter wave plate (QWP) (Thorlabs, WPQ05M-808) with its fast axis oriented at 22.5° along the beam path, so the H polarized beam upon double pass consists of equal components of H and V(vertically polarized), *i.e.,* it becomes a linearly polarized beam at 45°. The reflected portion of the beam from the non-polarizing beam splitter is directed to two galvanometer controlled steering mirrors and passes through an achromatic imaging lens *en route* to the sample. The backscattered light from the sample traverses the same optical path (achromatic lens and the galvanometer controlled mirrors) back to the non-polarizing beam splitter. The galvanometer controlled mirrors are positioned one focal length above the imaging lens,

and facilitate the $x - y$ steering of the beam over the sample during imaging.

Typically, an achromatic imaging lens of focal length 30 mm (Edmund Optics, NT45-794) is implemented in our PS-OCT imaging, which according to equation (3.8) results in a transverse resolution of $\sim$12 μm (for a beam spot on the imaging lens, d, measured to be $\sim$2.5 mm). When imaging at a slightly higher depth than that afforded by a $f = 30$ mm lens is required, a lens with a longer focal length (for instance, $f = 40$ mm achromatic lens (Edmund Optics, NT47-378)) can be used. Using a $f = 40$ mm lens in place of $f = 30$ mm lens results in a transverse resolution of $\sim$16 μm, which is a slight compromise in transverse resolution from $\sim$12 μm (a factor of 1.33), for an improvement in depth of focus by a factor of $\sim$1.78 (equation (3.9)). As the focal length of the imaging lens is changed, the optical path length in the reference arm needs to be adjusted accordingly, and thus the retroreflector in our custom setup is mounted on a lockable optical rail.

In the presence of polarization-modifying scatterers in the sample (such as GNRs, discussed in chapter 4), the backscattered sample beam consists of both H and V polarized components. Upon reaching the non-polarizing beam splitter, the H and V components interfere with their respective polarization counterparts from the reference arm. Both the interfered H and V beams traverse the same path until the reaching the interferometer exit, where a polarizing beam splitter (Newfocus, 5812) separates the two linear polarization states. The co-polarized component in which the incident and backscattered sample beams are both H polarized is represented as HH, whereas the cross-polarized component in which the incident sample beam is H and the backscattered sample beam is V is represented as HV (Figure 3.4). Again, single-mode fibers are implemented between the interferometer and the spectrometer. So, in our custom-design, the three major components operate in free-space and are connected to each other through single-mode fibers. This allows for independent optical alignment in each

component, and affords the flexibility of modifying, adding, or removing optical elements in each of the three components without compromising the beam alignment in the rest.

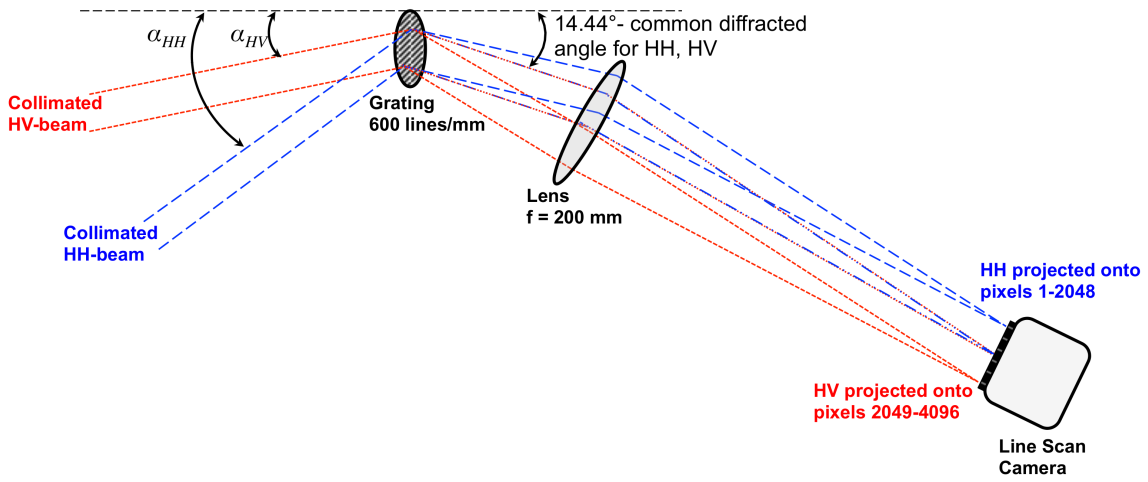

Figure 3.5: Schematic diagram of a custom-designed spectrometer consisting of a diffraction grating (600 grooves/mm), imaging lens ($f = 200$ mm), and a CCD line scan camera (Piranha, Dalsa Inc.); α_{HH}: Incident angle of collimated HH beam onto the grating; α_{HV}: Incident angle of collimated HV beam onto the grating; Blue: HH beam; Red: HV beam.

The spectrometer design employed in our PS-OCT system is similar to a single-camera design employed by Baumann *et al.* to study birefringence in human ocular tissue [55]. Since this design utilizes a single camera for acquiring both polarization states simultaneously, it eliminates synchronization issues encountered by two camera PS-OCT systems. The incoming beams in the spectrometer are first collimated by two fiber-to-free-space couplers ($f = 75$ mm). The collimated beams are then directed to the center of a transmission grating (Wasatch Photonics, 600 grooves/mm) (Figure 3.5). Adjustment of the polarization paddles between the interferometer and the spectrometer allows the maximization of the efficiency diffracted by the grating. The two orthogonal beams are incident onto the diffraction grating at angles equally offset from the grating's Littrow angle ($\alpha_L = 14.42°$) (*i.e.*, $\alpha_{HH} = 17.35°$ and $\alpha_{HV} = 11.49°$). Using the grating equation for the first-order diffraction [56], the horizontally polarized beam (incident

angle α_{HH}) is calculated to be diffracted between 8.64° to 14.44°, whereas the vertically polarized beam (incident angle α_{HV}) is calculated to be diffracted between 14.44° and 20.38° (using the CCD's spectral range for the calculation, which is chosen in our setup as [747.5, 912.5] nm). So, the choice of the two incident angles (α_{HH} and α_{HV}) allows the least diffracted HV-ray and the most diffracted HH-ray to have the same exiting angle. Thus, after the two beams pass through a camera focusing lens (Thorlabs, LB1199-B BK7, $f = 200$ mm), the two spectrally dispersed beams are imaged side by side onto 2048 pixels/each of a 4096 line scan camera (Piranha, P2-4X-04K40-10μm, Dalsa Inc.). The line scan camera operates at up to 25 kHz, and allows a maximum imaging depth z_{max} (measured) of 2.08 mm in air, whereas the theoretical z_{max} estimate according to equation (3.17) is 2.12 mm in air (given the detector's wavelength range of [747.5, 912.5] nm).

Source:	
Central wavelength of the source, λ_o	$\sim$800 nm
Source bandwidth, $\Delta\lambda$	> 120 nm
Axial resolution, l_c	Measured: 3.1 μm (Theory: < 2.4 μm)
Sample arm ($f = 30$ mm lens):	
Lateral resolution, Δx	Measured: 15 μm (Theory: $\sim$12 μm)
Depth of focus, b	283 μm
Spectrometer:	
Maximum linerate of the CCD camera	25 kHz
Spectral range of the CCD, $[\lambda_{min}, \lambda_{max}]$	[747.5, 912.5] nm
Imaging depth, z_{max} (in free space)	Measured: 2.08 mm (Theory: 2.12 mm)
Optical phase sensitivity (linerate: 1 kHz), $\Delta\phi$	Measured: 0.27 rad
SNR (HH, HV; linerate: 1 kHz)	Measured: 108 dB (Theory: 125.7 dB)

Table 3.1: Parameters of the custom-built PS-OCT system that outline the system performance.

Table 3.1 outlines various parameters that characterize the performance of the custom-

built PS-OCT system. The axial resolution was measured by imaging the surface of an attenuated mirror in the sample arm, whereas the transverse resolution was measured by imaging sparse point scatterers (silicone phantom with TiO_2 scatterers) in the sample arm. Imaging depth was measured by using the TiO_2 scatterers in the silicone phantom as fiducial markers and lowering the phantom over a known distance using a micrometer controlled sample stage. The optical phase sensitivity $\Delta\phi$ was calculated as the standard deviation of phase ϕ from an attenuated stationary mirror in the sample arm, which translates to a displacement sensitivity of 12.5 nm in free space [51]. SNR was measured with an attenuated stationary mirror in the sample arm, with a sample power of 4.90 mW and a camera linerate of 1 kHz. To measure SNR in the HV channel, an extra QWP with its fast axis oriented at 45° was inserted in the sample beam path so that the backreflected sample beam from the mirror, upon double-pass through the QWP, becomes V-polarized.

3.3 Data acquisition and image processing

OCT data acquisition is performed using 'ImageKitchen', a software package written using Visual C++ for the Windows operating system by the Photonics Systems Group at the Beckman Institute at the University of Illinois at Urbana-Champaign. ImageKitchen enables automated acquisition, processing, and visualization of the OCT data through its user-friendly GUI, and also allows additional hardware to be controlled through the same user interface. In our custom-built OCT system, ImageKitchen primarily controls image acquisition by the CCD camera via a NI-IMAQ (National Instruments Image Acquisition) driver, and imaging beam scanning across the sample by galvanometer controlled scanning mirrors via a NI-DAQ-Legacy (National Instrument Data Acquisition- Legacy) driver. Additional hardware, such as a custom-built solenoid magnet, are also integrated into and controlled by ImageKitchen for magnetomotive

OCT imaging, thereby extending the functionality of our OCT system further.

For PS-OCT imaging, as shown in figure 3.5, the *HH* beam is projected onto pixels 1-2048 of the CCD camera, whereas the *HV* beam is projected onto pixels 2049-4096 of the same camera. The collected *HH* and *HV* spectral interferograms are digitized by the line scan camera and transferred to a 32-bit PC (OS: Windows XP) by means of a high speed frame grabber board (National Instruments, PCI-1429e). The OCT frame readout and the galvanometer scanner are synchronously controlled by ImageKitchen.

After data acquisition, PS-OCT images are rendered upon post-processing of the raw data using MATLAB. The post-processing involves the following major steps:

1. Subtraction of the reference data (*i.e.,* sample blocked) from the raw data.

2. Splitting of the raw data into two halves of 2048 pixels, which represent the *HH* and *HV* spectral interferograms.

3. Performing an inverse Fourier transform (Fast Fourier Transform, FFT, in MATLAB) of the spectral interferograms to get OCT signals of the form $\tilde{S}_{HH}(z,t) = A_{HH}(z,t)e^{i\phi_{HH}(z,t)}$ and $\tilde{S}_{HV}(z,t) = A_{HV}(z,t)e^{i\phi_{HV}(z,t)}$.

In addition, an intermediary iterative algorithm is also implemented to digitally compensate for the dispersion in our high broadband SD-OCT setup [57, 58], which corrects for the following dispersions in the system: (i) camera pixel to wavenumber (k) nonlinearity, (ii) refractive index dispersion in the sample (depth-dependent dispersion), and (iii) dispersion caused by an imbalance of optical elements in the interferometric arms (fixed dispersion). The need for camera pixel to wavenumber (k) correction can be understood by the practicality of the problem: as the pixels in the CCD are equally spaced, the spectrally dispersed beam projected onto these pixels are evenly spaced in wavelength (λ) and not the wavenumber (k), *i.e.,* the collected signal is indeed $I(\lambda)$. However, the mathematical treatment in obtaining the SD-OCT signal (equation (3.16))

involves an inverse Fourier transformation of $I(k)$ and not $I(\lambda)$. Thus, it is necessary to convert the measured spectrum into an evenly sampled function in k. The employed

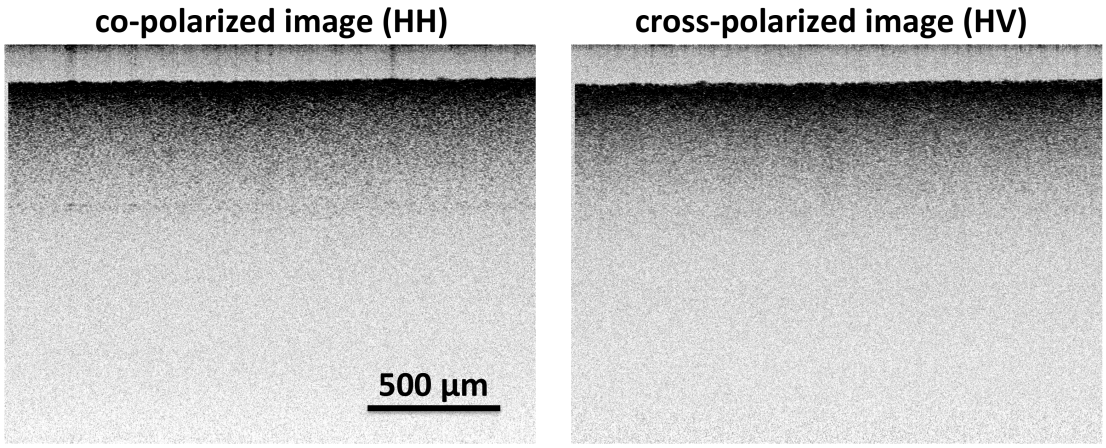

Figure 3.6: Co- and cross- polarized images of a Lambertian scatterer. Comparable signal is present in both channels suggesting that the incident polarization of the probing beam is depolarized completely upon backscattering from the lambertian surface.

algorithm also corrects the relative positioning and scaling of scatterers throughout all depths between the HH and HV images, thereby providing excellent alignment between the two polarization images.

Aligned and dispersion-compensated HH and HV polarization images of a Lambertian scattering surface is shown in figure 3.6. The Lambertian surface is observed to depolarize the incident polarized beam completely as evidenced by comparable structural contrasts seen in the HH and HV channels. On the other hand, Collagen I, which is a semi-transparent gel, is observed to be weakly backscattering and also to preserve the incident polarization of the beam as evidenced by the lack of cross-polarized (HV) signal (Figure 3.7). However, upon addition of polarization dependent scatterers (GNRs), the backscattered beam consists of both the co- and cross- polarized signals as shown in figure 3.7.

Lastly, a slight variation of our current PS-OCT setup by the insertion of a QWP with

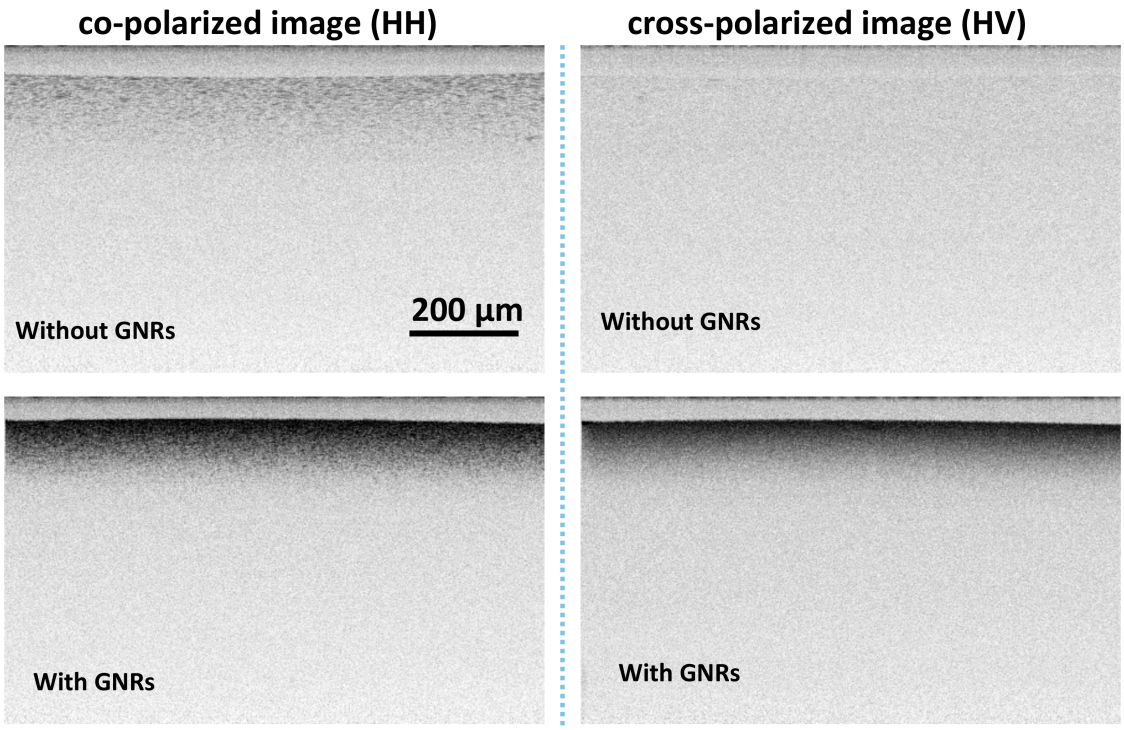

Figure 3.7: Co- and cross- polarized images of Collagen I (2 mg/ml) gel before and after addition of GNRs. Before the addition of GNRs, only the co-polarized signal is present whereas after the addition of GNRs, both the co- and cross- polarized signals are observed.

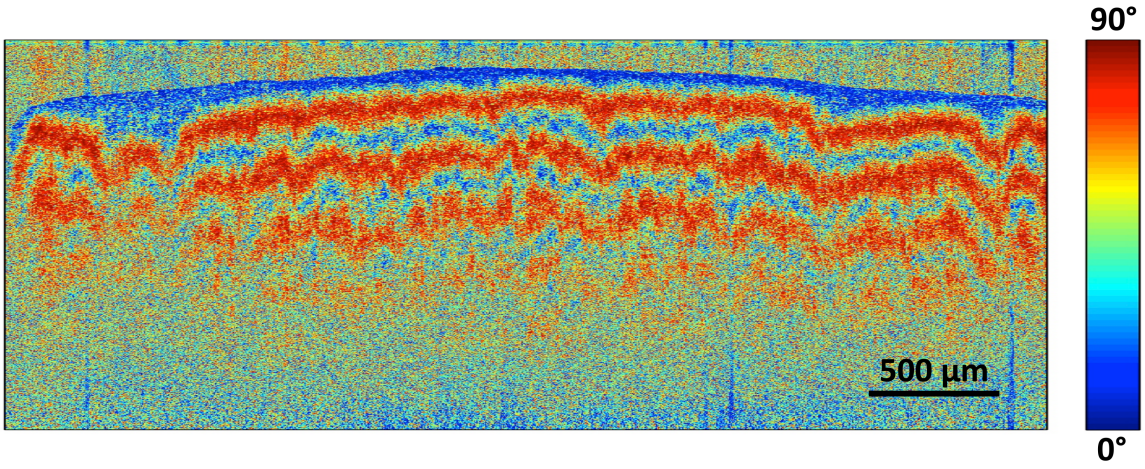

Figure 3.8: Retardance image of smooth chicken muscle showing a banding pattern owing to the sample's birefringence resulting from highly organized and aligned muscle fiber [58].

its fast axis at 45° in the sample beam path creates a circularly polarized probing beam, and thus allows measurement of retardance ($\tan^{-1}(A_V/A_H)$) in birefringent biological samples that have high order of structural organization [55]. Smooth chicken muscle has highly organized and aligned muscle fibers (organization of elongated collagen fibers) that lend to its birefringent nature. The alignment of the two polarization images becomes crucial in PS-OCT imaging to measure retardance in such samples [58]. In the retardance image (Figure 3.8), a banding pattern is observed corresponding to the birefringent smooth chicken muscle.

With the discussion of our custom-built PS-OCT system complete, in the next chapter, we'll explore the use of GNRs as polarization-dependent probes in PS-OCT imaging for micro- and nano- rheological studies.

Chapter 4

Gold Nanorods

4.1 Introduction

Metallic nanoparticles depict physical and chemical properties that are entirely different from their bulk state, which arise due to the collective oscillations of their conduction band electrons (surface plasmons) in response to external electromagnetic radiation [59, 60]. When the frequency of the impinging electromagnetic radiation matches the oscillation frequency of the surface plasmons, the oscillation attains resonance which is called the surface plasmon resonance (SPR). The optical properties of SPR nanoparticles provide a wide range of opportunities in biomedical optics, as is evident from recent applications in imaging contrast [61], biolabeling [62], and biosensing [63], among others. SPR gold nanoparticles are of particular interest due to their strong optical scattering and absorption cross-sections [64], lack of photobleaching [65], and excellent biocompability [66]. SPR gold nanoparticles, such as nanoshells [67], nanocages [68], and nanorods [69, 70], have successfully been demonstrated as contrast agents in OCT imaging as well.

Gold nanorods (GNRs) are particularly attractive for biomedical applications due to their small size and potentially improved permeation into tissue compared to larger tunable gold nanoparticles [75]. For biomedical imaging, GNRs garner additional in-

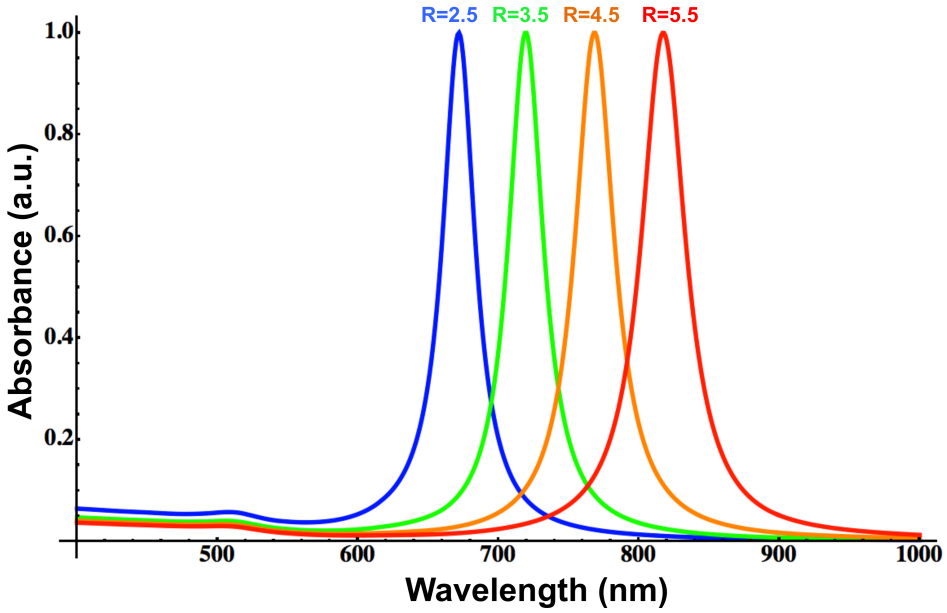

Figure 4.1: Absorbance (extinction) spectra of GNRs with various aspect ratios ($R = (L/d)$) computed using Mie-Gans theory, an electrostatic approximation for light scattering from ellipsoids [71, 72, 73, 74]; The length of the GNRs is kept fixed, $L = 80$ nm, and the width d is varied. As the aspect ratio increases, the LSPR peak is red shifted showing the tunability of the LSPR peak to various wavelengths based on the aspect ratio.

terest as their SPRs have extremely high quality factors [76] that can be tuned, by the adjustment of their aspect ratio [77], to the near-infrared "biological window" where optical absorption by the tissue is minimal [40, 41, 42]. Due to their structural anisotropy, GNRs depict plasmon resonant oscillations along the short axis (termed transverse SPR) and the long axis (termed longitudinal SPR). The LSPR (longitudinal SPR) mode has been shown to depict easy adjustability over a wide wavelength range compared to the transverse SPR as the aspect ratio of the GNRs is adjusted [77] (Figure 4.1). Tuning the shape of the gold nanoparticles from spherical to elongated rod-like structures has been shown to enhance scattering efficiency relative to absorption efficiency [78]. In addition to the aforementioned properties, light scattering from a GNR has been shown to be strongly polarized along the orientation of the its long axis, with the LSPR scattering

intensity reaching a maximum when the incident polarization of the beam is aligned with the long axis of the GNR, and becoming almost negligible when the incident polarization of the beam is aligned along the short axis of the GNR [76]. By monitoring the polarization-dependent scattering, individual GNRs under confined 2D Brownian rotation have been successfully demonstrated as local orientation sensors using a dark field microscope [79] and photothermal imaging [80].

4.2 Cross-polarized and isotropic autocorrelations

Attesting to the aforementioned polarization dependent scattering property of GNRs at the LSPR [76], the computation of $\sigma_{s,||}$ and $\sigma_{s,\perp}$, according to Mie Gans theory [71], reveals that $\sigma_{s,||} \gg \sigma_{s,\perp}$, where $\sigma_{s,||}$ and $\sigma_{s,\perp}$ are the scattering cross sections when the polarization of the incident beam is parallel and perpendicular to the long axis of the GNRs respectively. For instance, on average, $\sigma_{s,||}(\lambda)$ is 1600 times larger than $\sigma_{s,\perp}(\lambda)$ for the representative ensemble of PEGylated GNRs (size: 83 $\pm$ 7 nm by 22 $\pm$ 3 nm) over the entire detected wavelength range of the OCT system. Thus, the polarizability along the long axis of the GNRs $\alpha_{||}$ can be fairly assumed to be significantly greater than the polarizability along their short axis $\alpha_{\perp}$. Thus, the mean polarizability, $\alpha_o = \frac{\left(\alpha_{||}+2\alpha_{\perp}\right)}{3}$ and anisotropy $\beta_o = \left(\alpha_{||} - \alpha_{\perp}\right)$ can be approximated as $\beta_o \simeq 3\alpha_o$. Hence, from equation (2.34), the normalized autocorrelations evaluated from the HH and HV OCT signals at each depth z are given by:

$$g^{(1)}_{HH}(z,\tau) = \left(\frac{5}{9}\right) e^{-q^2 D_T(z)\,\tau} + \left(\frac{4}{9}\right) e^{-6D_R(z)\tau}\, e^{-q^2 D_T(z)\,\tau}$$

$$g^{(1)}_{HV}(z,\tau) = e^{-6D_R(z)\tau} e^{-q^2 D_T(z)\,\tau} \tag{4.1}$$

Now, by combining $g^{(1)}_{HH}(z,\tau)$ and $g^{(1)}_{HV}(z,\tau)$, we can isolate the rotationally invariant part as follows:

$$g^{(1)}_{ISO}(z,\tau) = \left(\frac{9}{5}\right) g^{(1)}_{HH}(z,\tau) - \left(\frac{4}{5}\right) g^{(1)}_{HV}(z,\tau) = e^{-q^2 D_T(z)\,\tau} \tag{4.2}$$

where $g^{(1)}_{ISO}(z,\tau)$ is the 'isotropic' autocorrelation and is dependent entirely on the translational diffusion of the GNRs. Additionally, D_R is inversely proportional to L^3 whereas $q^2 D_T$ scales inversely to $\lambda_o^2 L$ (equation (2.23)). For the GNRs used in this thesis, $\lambda_o \gg L$ ($L \sim 60-80$ nm, and $\lambda_o = 800$ nm). Hence, it can be assumed that $6D_R \gg q^2 D_T$, which means $g^{(1)}_{HV}(z,\tau)$ predominantly probes the fast decay due to the rotational motion of the GNRs:

$$g^{(1)}_{HV}(z,\tau) \approx e^{-6D_R(z)\tau} \tag{4.3}$$

Thus, using $g^{(1)}_{HV}(z,\tau)$ and $g^{(1)}_{ISO}(z,\tau)$ evaluated from temporal OCT data, the rotational and translational diffusion of GNRs can be estimated.

Note that equations (4.2) and (4.3) hold for a single GNR, but experimentally, light scattering within each coherence volume results from an ensemble of GNRs. Thus, the experimentally evaluated autocorrelations represent an ensemble average over the contribution from each GNR present in the coherence volume, as shown:

$$g^{(1)}_{HV}(z,\tau) = \sum_{j=1}^{N} c_j^2 e^{-6D_{R_j}(z)\tau}$$

$$g^{(1)}_{ISO}(z,\tau) = \sum_{j=1}^{N} c_j^2 e^{-q^2 D_{T_j}(z)\tau} \tag{4.4}$$

where the summation is over each GNR j in the ensemble, and c_j^2 is a factor introduced to assign higher scattering weights to larger sized, and thus more scattering GNRs in the ensemble (refer to equation 5.3 in chapter 5). The experimentally evaluated au-

tocorrelation, being a summation of exponentials, is only purely exponential when the scattering GNRs in the ensemble have no polydispersity at all. In reality, although synthesized with extreme care to have low polydispersity, GNRs indeed have some degree of polydispersity as can be seen in figures 4.2(b) and 4.2(c). However, in our OCT-based diffusion measurements, the diffusion coefficients determined represent an ensemble of GNRs and not individual GNRs. Thus, for the purpose of determining ensemble averaged diffusion coefficients of GNRs with low polydisepersity, inverse-exponential fits to the experimentally evaluated autocorrelations are performed, as discussed in section 4.4.

4.3 GNRs for OCT based diffusion imaging

GNRs used in this thesis were synthesized by modifying the seed-mediated growth method reported previously [81] at Dr. Joseph B. Tracy's laboratory in the Materials Science and Engineering Department at North Carolina State University. These nanorods have a stabilizing shell of [cetyltrimethylammonium bromide (CTAB)], which is a cationic surfactant necessary to keep the GNRs from aggregating. The actual synthesis method is detailed in the supplemental material to Chhetri *et al.* [82]. For use with ion-rich biological samples (*e.g.* Collagen I, Matrigel, and mucus studied in this thesis), it becomes necessary to passivate the GNR surface to avoid interactions between the GNRs and proteins & biopolymers present in biological samples. It has also been shown that GNRs stabilized with CTAB have strong cytotoxicity and thus lack biocompatibility [83]. For that purpose, certain batches of GNRs used in this thesis were coated with low molecular weight (1000 gm/mol) PEG (polyethylene glycol) which results in a nearly neutral surface (slightly negative zeta potential) [84], and have been been shown to adequately passivate nanoparticles for use with biological samples [85, 86].

For use with OCT, the GNRs presented in this thesis are synthesized with their LSPR

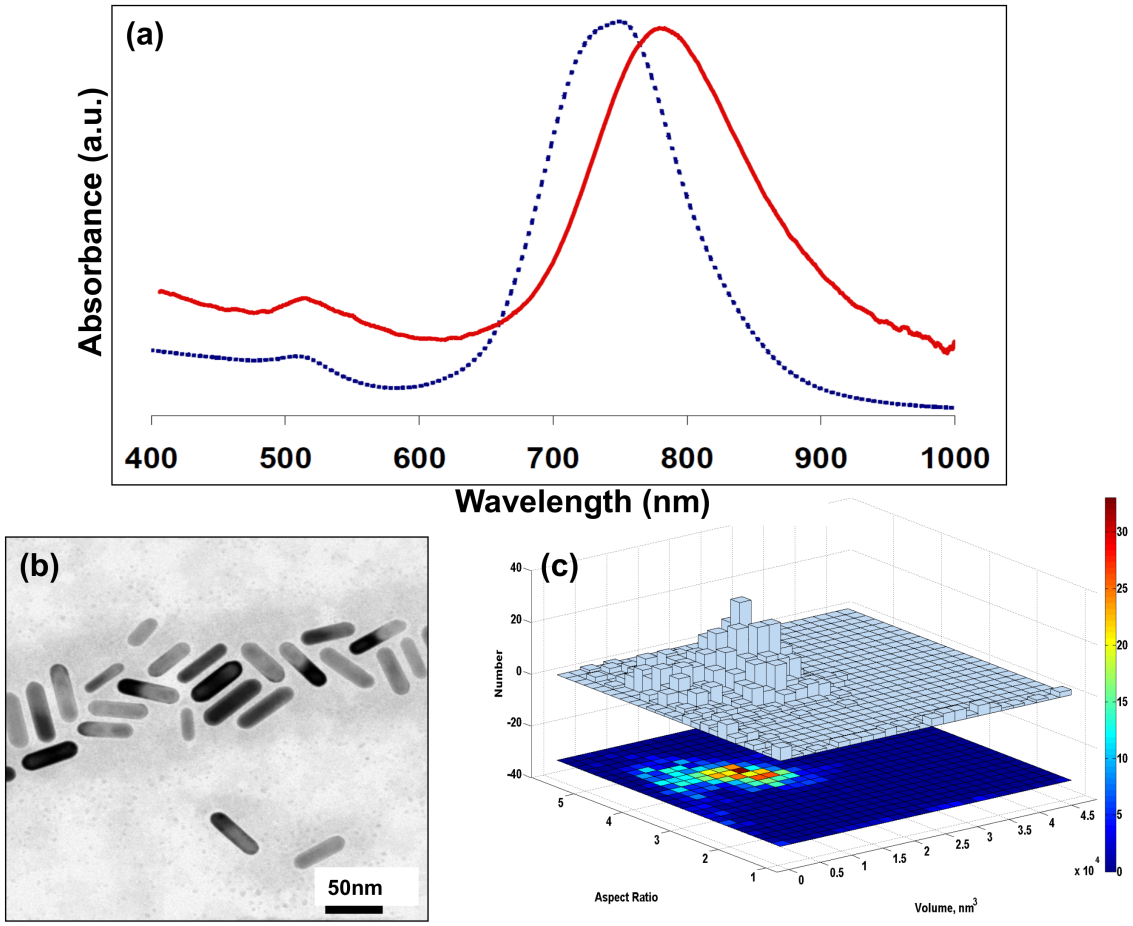

Figure 4.2: **(a)** Absorbance (extinction) spectrum measured for the dilute GNRs solution (solid red); Computed absorbance (extinction) spectrum for the measured GNR size distribution (dotted blue). **(b)** Example TEM image of the GNRs. **(c)** Size analysis ($n = 998$) of the GNRs measured using TEM which was used to compute the ensemble absorbance spectrum in (a).

to be within the OCT light source spectrum. The absorbance (extinction) spectra of a sample batch of GNRs in dilute solutions is shown in figure 4.2(a). The absorbance spectra of the colloidal aqueous solution exhibits two plasmon resonance modes, with the LSPR centered at ∼780 nm and a full-width half maximum of ∼140 nm. A representative Transmission Electron Microscopy (TEM) image for that batch of GNRs is shown in the inset of figure 4.2(b), which confirms the rod-like structure of the synthesized GNRs. For each batch of GNRs, a size analysis was performed based on the

TEM images; a representative size analysis is shown in figure 4.2(c). The measured size distribution is used to calculate the predicted absorbance according to Mie Gans theory, an electrostatic approximation for light scattering from ellipsoids [71, 72, 73, 74]. The computed ensemble absorbance spectrum for the same batch of GNRs exhibits a weak transverse mode at 520 nm and a strong longitudinal mode at 750 nm (Figure 4.2(a)).The presence of a surfactant layer of CTAB on the actual GNRs, as has been pointed out previously [69], is observed to red-shift the measured LSPR by ∼30 nm compared to the computed LSPR which doesn't account for the presence of CTAB on the GNRs.

4.4 Experimental Method

This section outlines the major experimental steps involved in using GNRs as OCT based diffusion probes.

GNRs concentration estimation:

The first step in using GNRs for OCT imaging involves the estimation of the number density of GNRs in the original solution. For this purpose, absorbance from a dilute suspension of GNRs is measured using a spectrophotometer (solution is diluted enough to allow majority of the light to pass through so that multiple scattering events of the optical beam are avoided, which would otherwise change the optical path length of the beam). The Beer-Lambert law relates the absorbance in a dilute suspension to the extinction cross-section of GNRs (σ_t), number density (N), and optical path length in the solution (l):

$$A(\lambda) = \sigma_t l N \tag{4.5}$$

Using the size distribution of GNRs measured by TEM, a prediction for absorbance is also computed using Mie Gans theory. The computed absorbance is matched with the experimental absorbance at the LSPR wavelength by adjusting N (l is known) to get an estimate for N in the dilute solution used in the spectrophotometer. Thus, using this estimate for N and the dilution factor of GNRs used during spectrophotometry, an estimate for the number density of GNRs in the original solution can be made.

Addition of GNRs to sample:

After the number density of GNRs is estimated, a small quantity of GNRs is topically added to the sample to have an ensemble of GNRs in each coherence volume (typically a few hundred; coherence volume estimated to be $\sim$375 μm^3 in air). This quantity is chosen to be of low enough concentration that the GNRs don't physically interact with each other in the sample (chosen such that the average separation between the GNRs $\gg$ maximum translational distance GNRs diffuse during the duration of the measurement). Depending on the nature of the sample, the added GNRs can be gently mixed using a pipette, left on a rotator for slow mixing, or allowed to diffuse over time without any disturbance to the sample.

PS-OCT data acquisition:

The custom-built PS-OCT system described earlier in subsection 3.2 is used to collect temporal data (M-mode) from the same region in the sample containing GNRs. To avoid unintentionally heating the GNRs in the sample, power in the sample beam is limited to 3 mW. Due to buffer size limitations in the current control PC, the maximum number of A-lines comprised of 4096 CCD array is presently limited to 12000 for each time series. Thus, using the maximum CCD linerate of 25 kHz (*i.e.,* each A-line collected in 40 μs), M-mode data can be collected for 480 ms in a single temporal frame. When

a longer observation time is necessary, sampling rates of 10 kHz, 5 kHz, 2 kHz, and 1 kHz result in an observation time of 1.2 s, 2.4 s, 6 s, and 12 s respectively, with the tradeoff being that the temporal spacing gets sparser with decreasing sampling rates. To improve the accuracy of the evaluated autocorrelations, the choice of sampling rate for each experiment is based on the following experimental criteria:

1. The fastest autocorrelation decay time to be measured must be at least twice the sampling time (Nyquist sampling criterion).

2. The total observation time (T_{obs}) must be such that $T_{obs} \gg \tau_{1/e}$, where $\tau_{1/e}$ is the 1/e decay time $g^{(1)}(\tau)$. This allows $g^{(1)}(\tau)$ sufficient time to decay off to a state of no correlation. (Note that, in this thesis, $T_{obs} > 100 \times \tau_{1/e,HV}$ and $T_{obs} > 25 \times \tau_{1/e,ISO}$ are chosen for D_R and D_T estimations respectively).

Representative B-mode and the corresponding M-mode HH, HV images of a 0.2% agarose gel with GNRs (premixed before gelation) is shown in figure 4.3. Each M-mode scan is collected at the center of the contextual B-scan, which shows temporal intensity streaks in both the co-polarized (HH) and cross-polarized (HV) channels. The intensity streaks in the co-polarized channel are observed to be longer than those in the cross-polarized channel. Qualitatively, this suggests that the temporal co-polarized signal decays over a longer timescale than the cross-polarized signal.

Diffusion coefficients estimation:

To evaluate the ensemble averaged rotational and translational diffusion coefficients from M-mode scans, the following steps are used (associated MATLAB code is included in appendix A.1):

1. Both the real and imaginary parts of the complex OCT signals $\tilde{S}_{HH}(z,t) = A_{HH}(z,t)e^{i\phi_{HH}(z,t)}$ and $\tilde{S}_{HV}(z,t) = A_{HV}(z,t)e^{i\phi_{HV}(z,t)}$ are taken as the signals to be analyzed [82, 87].

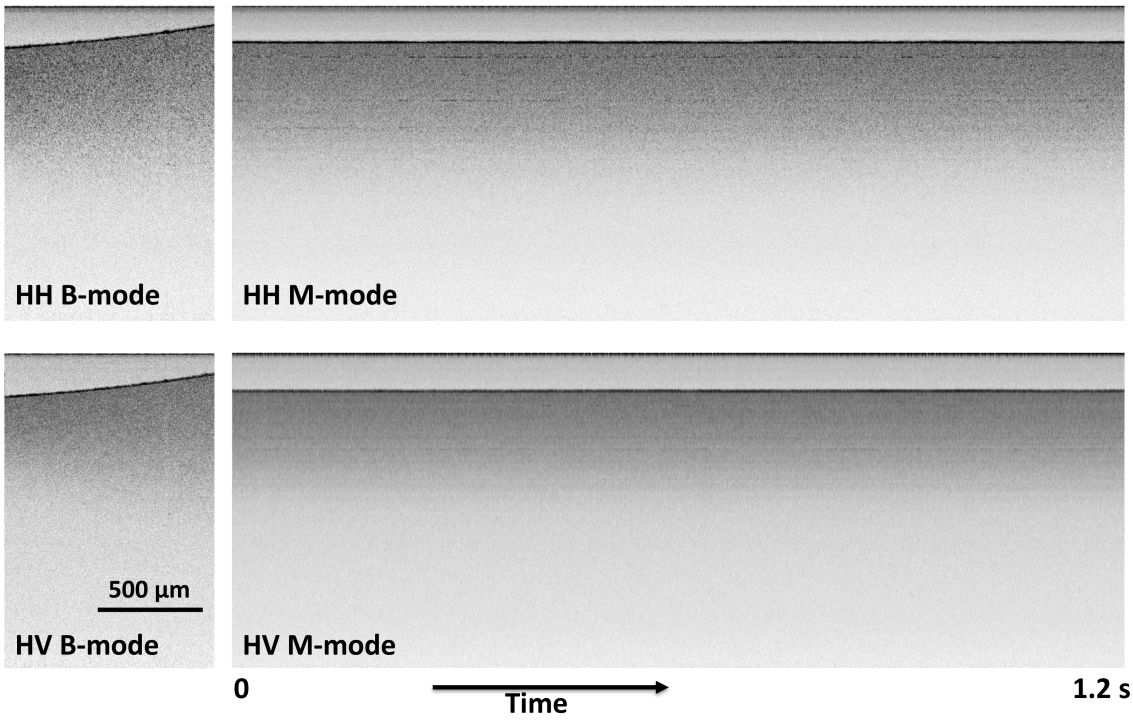

Figure 4.3: Representative *HH* and *HV* B-mode images and the corresponding M-mode images acquired with the beam temporally probing the same position in the 0.2% agarose sample premixed with GNRs. All images were acquired at a sampling rate of 10 kHz. The M-mode images consist of 12,000 A-lines and thus the temporal range extends to 1.2 seconds.

2. Fluctuations in the above signals are isolated by subtracting their average value at each depth, as in equation (2.8).

3. $G^{(1)}_{HH}(\tau)\Big|_{\mathbf{Re}}$ and $G^{(1)}_{HV}(\tau)\Big|_{\mathbf{Re}}$ are computed at each pixel in z (Note: '$|_{\mathbf{Re}}$' is added to emphasize the use of the real part of the OCT signal). The zero-lag value ($\tau = 0$) in the autocorrelations contains non-deterministic noise, and thus is replaced by a value extrapolated using the next two data points in the autocorrelation (*i.e.,* lag of τ and lag of 2τ).

4. Normalized autocorrelations $g^{(1)}_{HH}(\tau)\Big|_{\mathbf{Re}}$ and $g^{(1)}_{HV}(\tau)\Big|_{\mathbf{Re}}$ at each pixel in z are obtained by normalization of the above $G^{(1)}_{HH}(\tau)\Big|_{\mathbf{Re}}$ and $G^{(1)}_{HV}(\tau)\Big|_{\mathbf{Re}}$ by their cor-

responding maximum values (*i.e.,* $\tau = 0$ values) at each pixel in z. Normalized isotropic autocorrelation $g^{(1)}_{ISO}(\tau)\Big|_{\mathbf{Re}}$ at each pixel in z is evaluated by combining $g^{(1)}_{HH}(\tau)\Big|_{\mathbf{Re}}$ and $g^{(1)}_{HV}(\tau)\Big|_{\mathbf{Re}}$ using equation (4.2).

5. Steps (3) and (4) are repeated using the imaginary part of the OCT signals to get $g^{(1)}_{HH}(\tau)\Big|_{\mathbf{Im}}$, $g^{(1)}_{HV}(\tau)\Big|_{\mathbf{Im}}$, and $g^{(1)}_{ISO}(\tau)\Big|_{\mathbf{Im}}$.

6. For all *HH*, *HV*, and *ISO* autocorrelations, $g^{(1)}(\tau)$ at each pixel in z is obtained by adding $g^{(1)}(\tau)\big|_{\mathbf{Re}}$ and $g^{(1)}(\tau)\big|_{\mathbf{Im}}$.

7. $g^{(1)}_{HH}(\tau)$, $g^{(1)}_{HV}(\tau)$, and $g^{(1)}_{ISO}(\tau)$ at each pixel in z are averaged over 10-25 pixels in depth (corresponds to a depth-section of $\sim$15 μm to 38 μm), and this averaging is performed sequentially at multiple depth-sections in the M-mode image. The obtained autocorrelations represent the depth-resolved autocorrelations: $g^{(1)}_{HH}(z,\tau)$, $g^{(1)}_{HV}(z,\tau)$, and $g^{(1)}_{ISO}(z,\tau)$. In heterogeneous samples, the averaging is performed over depth-sections of 3 pixels only (so, each depth-section is 4.65 μm, which is comparable to the axial resolution of the OCT system).

8. To estimate $\tau_{1/e}$, the 1/e decay of $g^{(1)}(\tau)$, (unweighted) linear least-squared fittings of $\ln[g^{(1)}(\tau)]$ over a region of initial time lags (*i.e.,* from $\tau = 0$ to $\tau_{1/e}$) to $-t/\tau + c$ are carried out in each depth-section. Representative inverse-exponential fittings of the form $e^{-t/\tau+c}$ to $g^{(1)}(\tau)$ are shown in figure 5.6.

9. For the estimation of D_R and D_T in each depth-section, $\tau_{1/e}$ values of $g^{(1)}_{HV}(\tau)$ and $g^{(1)}_{ISO}(\tau)$ are used based on equation (4.3) and equation (4.2) respectively. In a homogeneous sample, the average and standard deviation of $D_R(z)$ and $D_T(z)$ computed at several depth-sections are reported.

Having outlined the experimental method in this section, the estimation of rotational and translational diffusion coefficients of GNRs in Newtonian fluids and non-Newtonian

fluids is outlined in the next chapter. More importantly, the depth-resolved autocorrelations, $g^{(1)}_{HH}(z,\tau)$ and $g^{(1)}_{HV}(z,\tau)$, offer a unique opportunity to understand the heterogeneity present in various samples, which is also shown in the following chapters. In non-Newtonian fluids, it should be noted that the autocorrelations deviate slightly from pure exponentials at longer time lags due to the elastic memory in the samples. Performing inverse-exponential fittings (as outlined above) to such autocorrelations over a region of initial time lags (*i.e.,* from $\tau = 0$ to $\tau_{1/e}$) can yet describe the short timescale dynamics of the GNRs and the outlined method lends itself as a semi-quantitive tool to understand diffusion in complex fluids. It should be noted however that the reported D_T for the ensemble of GNRs in such instances represent an "on average" estimate between the timescale of $\tau = 0$ and $\tau_{1/e}$, which assumes the viscous drag as the dominant force behind the diffusion of GNRs and thus ignores any non-viscous contributions to the autocorrelations during that duration.

Chapter 5

Diffusion of GNRs using OCT

5.1 Rotational diffusion in Newtonian fluids

5.1.1 Introduction

In the growing field of microrheology, there has been considerable interest in techniques that quantify thermal diffusion of probes within locally resolved volumes of the medium under investigation. The Stokes-Einstein relation relates diffusion measured by these passive techniques to the linear viscoelastic properties of the medium, provided that the probe is inert and the medium behaves as a near-equilibrium, homogeneous, isotropic, and incompressible continuum [88]. Optical coherence tomography (OCT) [28] provides a novel platform to study dynamic light scattering (DLS) from passively diffusing particles [87]. Using plasmon resonant gold nanorods (GNRs), DLS with OCT

enables locally resolved, passive microrheology of medium properties with microscale heterogeneities.

We investigated polarized light scattering from ensembles of GNRs using polarization-sensitive OCT (PS-OCT) to depth resolve the rotational diffusion coefficient (D_R) in media of varying viscosity. The shape anisotropy of a GNR splits the surface plasmon resonance into transverse and longitudinal modes, the latter of which provides high light scattering efficiencies due to reduced plasmon damping, and is polarized parallel to the long axis of the GNR [76]. By monitoring the polarized scattering, it has previously been shown that a GNR under two-dimensional (2D) Brownian rotation can be used as a local orientation sensor [79]. We expect GNRs in the molecular fluids in our study to obey the Stokes-Einstein relation, so that their three-dimensional (3D) Brownian diffusion can be related to the viscosity of the medium. While the translational diffusion of nanorods is complicated by coupling to rotational diffusion due to the shape anisotropy [15], rotational diffusion is independent of the state of translation, and as such, is a robust metric for local viscous properties. Furthermore, we expect GNRs to probe the viscosity of the medium at a smaller scale than that possible by using traditional microparticles.

In this study, we employ OCT to monitor D_R of ensembles of unconfined GNRs. OCT employs optical depth ranging of singly backscattered light, enabling real-time imaging in non-invasive biomedical applications. Similar to DLS techniques, OCT is an optical heterodyne method which senses ensemble-averaged scattering from scatterers within the coherence volume, providing a higher signal-to-noise ratio and speed compared to single-particle tracking methods. Unlike traditional DLS, OCT employs low-coherence light so that the coherence volume is small; as such, OCT is capable of resolving the dynamic signal from each local coherence volume over depths exceeding the mean scattering path length [26], which has implications for analyzing optically thick tissues. The localized-coherence-volume technique has previously been used with

microbeads to perform spatially resolved microrheology [24].

In this Rapid Communication, we employ PS-OCT and principles from DLS to measure the D_R of ensembles of GNRs freely suspended in media of varying viscosity. We test the validity of the Stokes-Einstein relation by comparing the observed D_R values with a model for the Stokes drag on cylinders, modified to account for the non-negligible GNR size distribution by computing the temporal statistics of a representative ensemble of GNRs. Using these validation measurements relating D_R to the viscosity of the medium, we demonstrate the capability of PS-OCT to spatially map the viscosity of a heterogeneous sample by using GNRs as rheological probes. The ability to resolve micrometer-scale heterogeneities in viscosity using GNRs with OCT may open new avenues for microrheological investigation.

5.1.2 Method and results

GNRs used in this study have an average length and width of 53 ± 10 and 15 ± 4 nm, respectively, and exhibit a strong longitudinal plasmon mode centered at 780 nm with a full width at half maximum of 140 nm, which is within the OCT source spectrum that spans 735-865 nm at half maximum for the synthesis and absorbance spectrum). Two batch solutions for the experiment were prepared by mixing 10% of the GNRs solution ($\sim 8 \times 10^8$ GNRs/μL) with glycerol (Acros Organics, 15892-0010) and water (Fisher Scientific, W5-4), respectively. Samples with varying viscosity were then prepared by mixing the two batch solutions in different proportions, and their resulting viscosities were estimated using a mixture law [89]. Although multiple GNRs populate each coherence volume, we expect them to be noninteracting, because the estimated average separation between the GNRs (minimum $\sim$1450 nm) is large compared to both the average length of a GNR ($\sim$53 nm) and the mean distance the GNRs travel over the duration of the OCT measurement (maximum $\sim$140 nm).

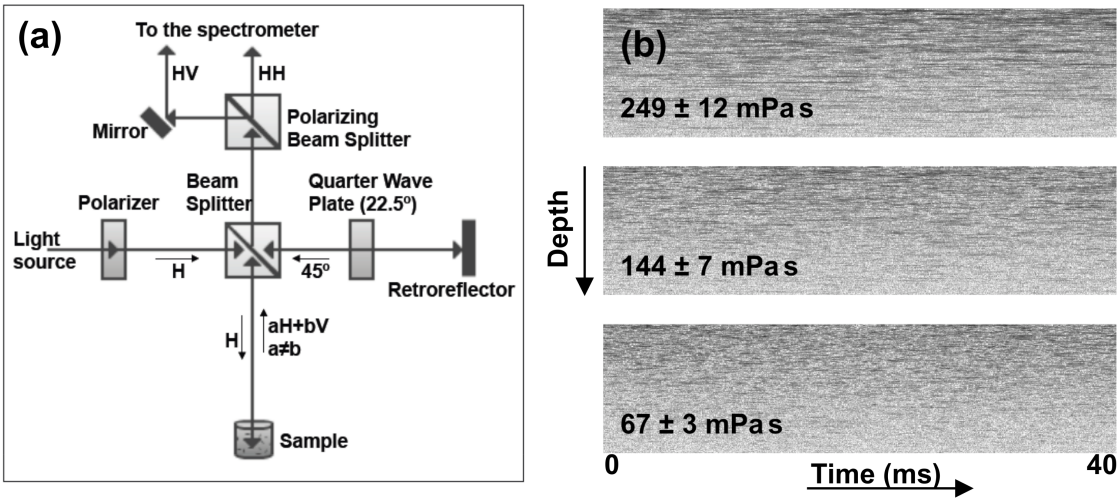

Figure 5.1: (a) PS-OCT interferometer setup. (b) Example M-mode images [using an absolute value of $\tilde{S}(z,t)$] in the HV configuration showing an increasing rate of intensity fluctuations for samples with decreasing viscosities. (Note: Intensity fluctuations only up to 40 ms shown.)

The OCT system in this study is a spectral domain, polarization-sensitive system, as shown in figure 5.1(a).The light source consists of a Ti:sapphire laser (Griffin, KM-Labs, Inc.) and provides a coherence gate of $\sim$2.6 μm in air. Light from the source is horizontally polarized and split into reference and sample arms. Imaging is performed by a lens (f = 30 mm), which provides a transverse resolution of $\sim$12 μm in air. Owing to the coherence gate and the transverse resolution, the coherence volume is estimated to be $\sim$375 μm^3 in air. Horizontally polarized light ($\sim$5 mW) incident upon the sample is backscattered into both horizontal (H) and vertical (V) polarization states, which interfere with their respective polarization states from the reference (consisting of linearly polarized light at 45°, generated after double pass through a quarter-wave plate at 22.5°). The interfered light is split into horizontal and vertical components by a polarizing beam splitter (HH and HV, respectively, where the first and second terms are the incident and backscattered polarization states from the sample, respectively), and directed to a custom spectrometer. The spectrometer is similar to a previous design

[55], and consists of a transmission grating (600 lines/mm, Wasatch Photonics), camera lens (f=200 mm), and a line scan camera (Piranha, Dalsa Inc.) operated at 25 kHz, providing an imaging depth of 2.08 mm in air.

Dynamic PS-OCT signals were recorded by acquiring depth scans from the same transverse position in the sample as a function of time (M-mode). A total of 4000 depth scans were obtained with a line rate of 25 kHz (i.e., sampled every 40 μs for an overall duration of 160 ms). Typical M-mode OCT images showing time traces of the depth-resolved intensity fluctuations for samples with different viscosities are shown in figure 5.1(b). Qualitatively, we observe that the intensity fluctuations along the horizontal (time) axis are much slower in a high viscosity sample than in a low viscosity sample. Quantitative analysis, as performed below, reveals that the time scale of these intensity fluctuations is directly related to the viscosity of the medium.

Spectral domain OCT is a heterodyne detection scheme in which the complex analytic signal $\tilde{S}(z,t)$ as a function of depth z in the sample is obtained by inverse Fourier transformation of the measured spectrum [44]. In the heterodyne experiment, the temporal autocorrelation of the real part of $\tilde{S}(z,t)$, $G^{(2)}(z,\tau)$, is relatable to the first-order correlation function of the electric field scattered from the sample, $G^{(1)}(z,\tau)$ [3]. In this study, we employ polarization-sensitive OCT to collect the cross-polarized (HV) dynamic light scattering signal because it provides direct access to D_R against a background of slow translational diffusion D_T . Specifically, (after normalization),

$$g^{(1)}_{HV}(z,\tau) = e^{-\left[6D_R(z)+q^2D_T(z)\right]\tau} \approx e^{-6D_R(z)\tau} \tag{5.1}$$

where $q = \frac{4\pi n}{\lambda_o}$ is the scattering vector in the backscattering geometry, the fast $e^{-i\omega_o t}$ term is dropped for convenience, and $6D_R \gg q^2D_T$ for the GNRs under study (by a factor of 38 for an average GNR of length 53 nm and width 15 nm, using expressions previously reported [14]). Therefore, D_R equates to $(6\tau_{1/e})^{-1}$, where $\tau_{1/e}$ is the 1/e decay

time of $g_{HV}^{(1)}$.

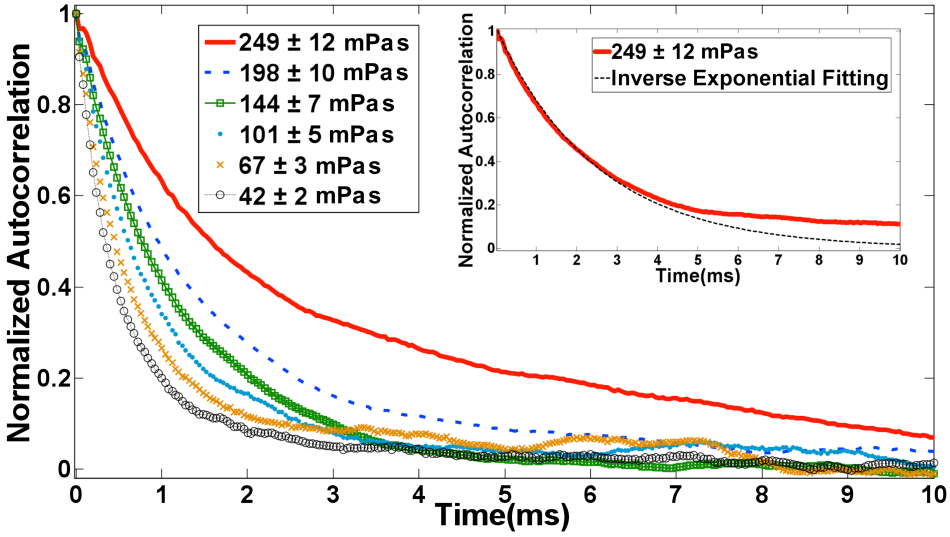

Figure 5.2: Representative $g_{HV}^{(1)}$ for samples with varying viscosity. Decay time is observed to decrease as the viscosity decreases. The inset shows a representative inverse exponential fitting to $g_{HV}^{(1)}$ (dotted line), based on equation (5.1).

Computationally, D_R at each depth z was isolated from $\tilde{S}(z,t)$ as follows: The real part of $\tilde{S}(z,t)$ was taken, and the time average was then subtracted to control for nonzero background noise and to isolate the intensity fluctuation [9]. Then, the autocorrelations were evaluated at each z and normalized to obtain $g_{HV}^{(1)}$, averaged within multiple depth intervals (N=7, with each depth interval chosen to be 35 μm), and fitted to the expected inverse-exponential of equation (5.1). A representative $g_{HV}^{(1)}$ for each sample is shown in figure 5.2, with a sample inverse-exponential fitting shown in the inset. The fittings were performed over a windowed region of $g_{HV}^{(1)}$ from $\tau = 0$ to $\sim \tau_{1/e}$. We find that the measured $g_{HV}^{(1)}$ values appear to be consistently larger than that of a pure exponential at times greater than $\tau_{1/e}$. This may be explained partially by the size distribution of GNRs giving rise to a distribution of rotational rates [as modeled in equation (5.2)], which deviates from a pure exponential in qualitatively the same manner, or it may be explained partially by the translational diffusion of the GNRs becoming more significant

at longer time scales. The rotational diffusion rate was then calculated at each depth interval according to $D_R = (6\tau_{1/e})^{-1}$. We noted that there was no significant change in D_R versus depth, which was expected because the mean scattering path length from GNRs is much longer than the depths analyzed. The D_R values averaged over multiple depth intervals are plotted in figure 5.3. As expected, an inverse relationship between D_R and viscosity is found, which suggests that the rotations of the GNRs occur over a comparatively shorter time scale as the viscosity decreases. We noted that D_R values were consistent (within 7%) when the concentration of the GNRs was decreased from 10% (at which the experiment was performed) to 2%, while maintaining the viscosity at a constant value (within 5%). Given the consistency of D_R with concentration and the invariance of measured D_R with depth, the effect of multiple scattering is believed to be negligible in our experiment.

To test the validity of the Stokes-Einstein relation for this system, the experimental D_R values were compared with a model combining the rotational diffusion of smooth cylinders [14] with the optical scattering from ellipsoids [71] while accounting for the measured size distribution of the GNRs. First, simulated autocorrelations were computed as the sum of the contribution of each GNR in a representative distribution ($n = 998$) as follows:

$$g_{HV}^{(1)}(\tau) = \sum_{j=1}^{998} c_j^2 e^{-6D_{R_j}\tau} \tag{5.2}$$

where the summation is over each nanorod j in the distribution, and c_j^2 is an optical weighing factor accounting for the maximum fluctuation in backscattering detected by the OCT system from each GNR. This is important to overcome the experimental bias for more efficient detection of larger, more slowly diffusing GNRs. The weights c_j^2 were evaluated from the optical scattering anisotropy of each GNR weighted by the incident

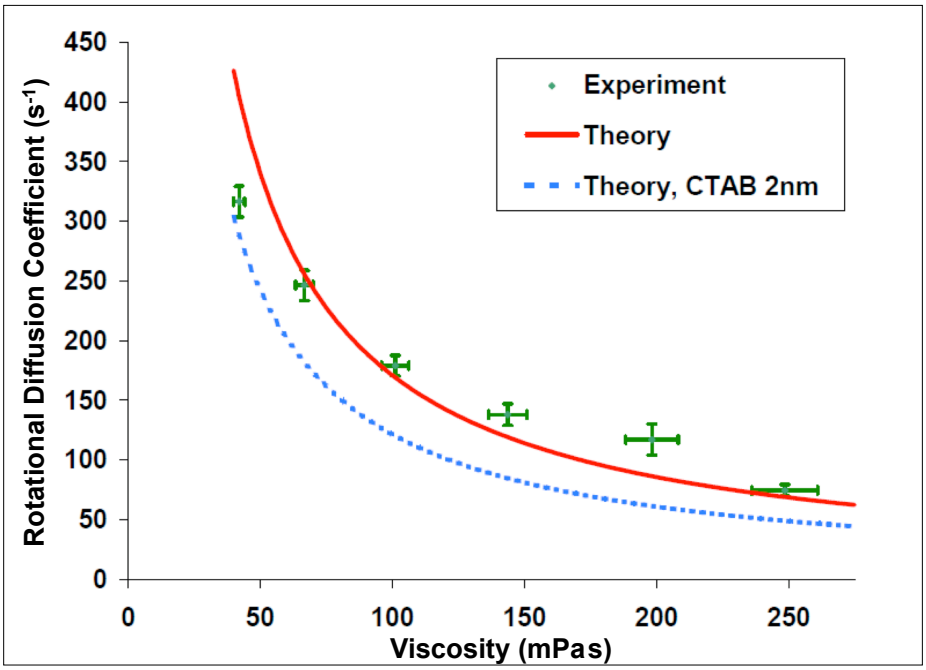

Figure 5.3: Comparison of experimental D_R with theoretical predictions assuming GNRs as smooth cylinders [14] (solid line: for the actual sizes of the GNRs, dotted line: considering an average CTAB layer of 2nm).

light spectrum, according to:

$$c_j^2 = \sum_{\lambda} \left[\sigma_{s,||}(\lambda, L_j, d_j) - \sigma_{s,\perp}(\lambda, L_j, d_j)\right] E_r^2(\lambda) \tag{5.3}$$

with L_j and d_j the length and width of the j^{th} GNR, and $\sigma_{s,||}$ and $\sigma_{s,\perp}$ the scattering cross sections, computed according to Mie Gans theory [71], of the j^{th} GNR when the incident polarization is parallel and perpendicular to the long axis, respectively. On average, we find that $\sigma_{s,||}$ is ~250 times that of $\sigma_{s,\perp}$, highlighting the high scattering anisotropy exhibited by GNRs. To compute D_{R_j} in equation (5.3) for each GNR, an expression derived for solid cylinders ($2 < L/d < 20$) was employed [14]. Theoretical D_R were then evaluated by fitting an inverse-exponential of the form shown in equation

(5.1) to the simulated autocorrelation given by equation (5.2).

Theoretical predictions were made in two ways: first, by considering the actual sizes of the GNRs measured by transmission electron microscopy (TEM), and second, by considering an average surfactant [cetyltrimethylammonium bromide (CTAB)] capping thickness of 2 nm around the GNRs. The average CTAB layer thickness was estimated from a TEM image as half of the average spacing between the GNRs when densely packed, and is consistent with previously reported values for similarly-sized GNRs, synthesized using a growth method in the presence of CTAB [90].

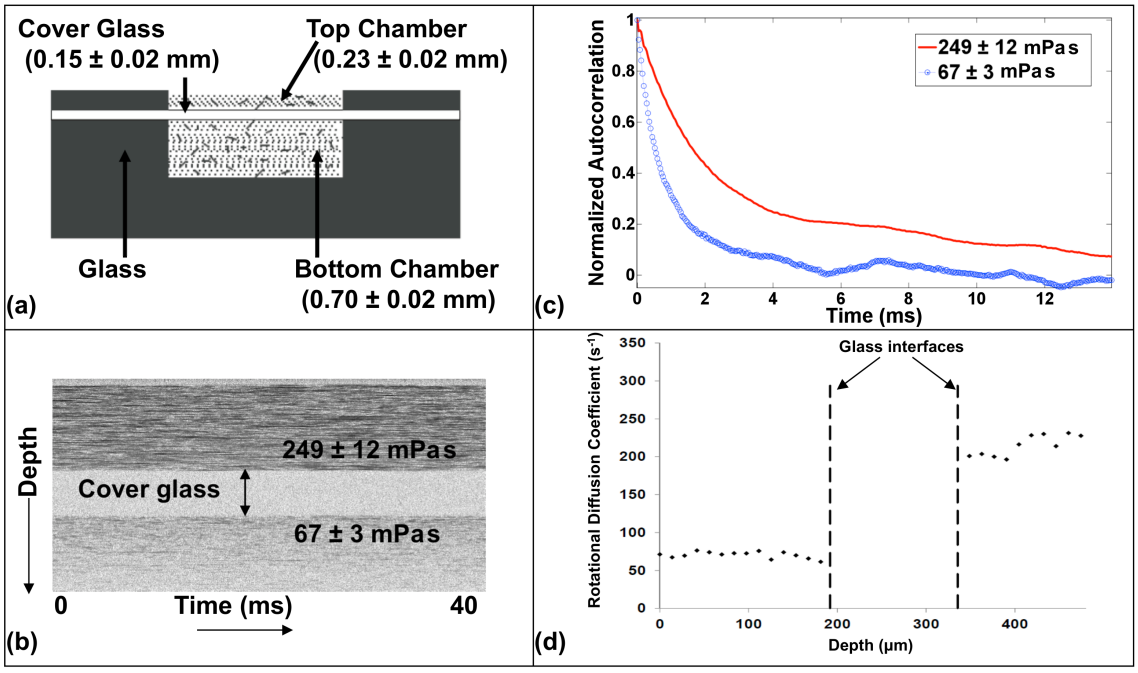

Figure 5.4: (a) Double chamber design. (b) M-mode images (using absolute value of $\tilde{S}(z,t)$ showing samples with different viscosities separated by a cover glass. (Note: Intensity fluctuations only up to 40 ms shown) (c) $g^{(1)}_{HV}(\tau)$ of the samples showing two different decay timescales. (d) D_R as a function of depth in the double chamber.

We find that the experimental D_R values correlate with the theoretical D_R computed as above for our distribution of GNRs (Figure 5.3). Agreement between experimental and theoretical D_R is obtained over a viscosity range of $42 - 249$ mPas, and the level

of agreement with theory is similar to the findings of a DLS study of similarly sized GNRs at a single viscosity [18]. In making direct comparisons between the experimental values and the theoretical predictions, it should be taken into consideration that the theoretical model is only an approximation; the GNRs are not exactly cylindrical in shape (as assumed for the rotational diffusion model), nor are they exactly ellipsoidal (as assumed for the optical scattering model).

These results demonstrate that PS-OCT can monitor viscosity using GNRs as nanoprobes within the applicability of the Stokes-Einstein relation. Next, the potential of our technique to resolve heterogeneities in viscosity was explored using a double chamber, as shown in figure 5.4(a), in which two samples with different viscosities were separated by a thin microscope cover glass. Figure 5.4(b) shows the M-mode images of the two samples in the double chamber. Figure 5.4(c) shows $g_{HV}^{(1)}$ averaged within each chamber, demonstrating two different timescales that indicate the difference in viscosity in the two chambers. By fitting $g_{HV}^{(1)}$ to the expected inverse-exponential of equation (5.1), D_R of 72 ± 5 s^{-1} and 227 ± 6 s^{-1} were found for samples in the top and bottom chamber, respectively, which are consistent with independent measurements of D_R of 74 ± 5 s^{-1} and 246 ± 13 s^{-1}, respectively, for these samples (figure 5.2). Figure 5.4(d) shows D_R as a function of depth in the double chamber, where D_R was computed within each depth interval of 35 μm, and the depth intervals were successively stepped by 14 μm through both chambers. A clear distinction between the rotational diffusion coefficients of the two samples is seen, and the D_R values measured within multiple depth intervals for the same sample are also consistent with one another. This demonstrates that DLS performed with PS-OCT using GNRs as nanoprobes is capable of resolving the microscale heterogeneities in viscosity existing at multiple depths within an object.

5.1.3 Conclusion

In conclusion, by combining the techniques of PS-OCT and DLS, we showed that polarization-dependent scattering from ensembles of GNRs provides information about D_R, and subsequently the viscosity of the medium. For the first time to the authors knowledge, we have studied the unconfined stochastic motion of plasmon resonant GNRs in 3D using OCT, and obtained agreement between experimental and theoretical D_R over a viscosity range of $42 - 249$ mPas, which is within the regime of interest in biophysical studies. Averaging over large numbers of GNRs provides a high signal-to-noise ratio for determining the viscosity within each coherence volume of the sample (in this study, $\sim$130 GNRs within each coherence volume of $\sim$375 μm^3). We also demonstrated the ability to depth-resolve the heterogeneous viscosity within a single object using this technique. Future work is needed to validate this technique in non-Newtonian fluids using the generalized Stokes-Einstein relation. Because OCT rejects multiply-scattered light, this technique has the potential to provide microrheology in optically thick samples such as biological tissues. The combination of the anisotropic and plasmon-resonant properties of GNRs with OCT provides a new tool for imaging microscale heterogeneities of rheological properties.

5.2 Calibration: Rotational and translational diffusion in Newtonian fluids

In the previous section, we discussed only the rotational diffusion of CTAB-coated GNRs, which was the first validation of rotational diffusion of GNRs measured by OCT with the Stokes-Einstein relation. In reality, both rotational and translational diffusion of GNRs in Newtonian fluids are inversely proportional to the viscosity of the medium and thus should scale proportionately with the change in viscosity. Measuring both the rotational and translation diffusion of GNRs simultaneously helps elucidate the overall

dynamics of GNRs in various media. Below we discuss rotational and translational diffusion calibrations performed on two different batches of GNRs:

5.2.1 Calibration: CTAB-coated GNRs

M-mode data for various glycerol:water solutions with dilute suspensions of CTAB-coated GNRs (size: 69 ± 17 nm by 20 ± 6 nm; size analysis based on 230 GNRs counted by TEM) were taken with 3 mW of sample beam power and at an A-line rate of 10 kHz. The GNRs number density in each sample is estimated to be $\sim 2 \times 10^8$ GNRs/μL which results in an average of ∼325 GNRs in each coherence volume with an average center to center separation between the GNRs of ∼2.1 μm.

Viscosity (mPas)	$\tau_{1/e}$ of $g^{(1)}_{HV}(\tau)$ (ms)	D_R (rad^2/s)	$\tau_{1/e}$ of $g^{(1)}_{ISO}(\tau)$ (ms)	D_T (μm^2/s)
493	3.7 ± 0.3	45 ± 4	39 ± 7	0.050 ± 0.008
329	2.72 ± 0.09	61 ± 2	28 ± 3	0.070 ± 0.007
246	2.24 ± 0.04	74 ± 1	25 ± 3	0.078 ± 0.008
166	1.64 ± 0.06	102 ± 4	19 ± 2	0.11 ± 0.01
87	1.00 ± 0.04	167 ± 7	11 ± 1	0.18 ± 0.01
43	0.61 ± 0.01	274 ± 5	5.8 ± 0.3	0.34 ±0.02
26	0.47 ± 0.01	357 ± 5	4.3 ± 0.3	0.47 ± 0.04

Table 5.1: Measured $\tau_{1/e}$ of $g^{(1)}_{HV}(\tau)$ and $g^{(1)}_{ISO}(\tau)$, and the diffusion coefficients of CTAB-coated GNRs (size: 69 ± 17 nm by 20 ± 6 nm) in Newtonian fluids

Table 5.1 lists the $\tau_{1/e}$ of the cross-polarized, isotropic autocorrelations and the corresponding diffusion coefficients in Newtonian fluids over a viscosity range of $26-493$ mPas. The measured $\tau_{1/e}$ of $g^{(1)}_{HV}(\tau)$ are observed to range between 0.47 ms to 3.7 ms. The shortest $g^{(1)}_{HV}(\tau)$ decay time of 0.47 ms is at least 4 times greater than the sampling time of 100 μs, which satisfies the Nyquist sampling criterion. Also, the overall observation time of 1.2 s is 300 times greater than the longest $g^{(1)}_{HV}(\tau)$ decay time of 3.7 ms, which allows sufficient time for $g^{(1)}_{HV}(\tau)$ to decay to 0. Similarly, the measured $\tau_{1/e}$ of

$g^{(1)}_{ISO}(\tau)$ range between 4.3 ms and 39 ms. The Nyquist criterion is satisfied as the fastest $g^{(1)}_{ISO}(\tau)$ decay of 4.3 ms is much longer than the sampling time of 100 μs. The overall observation time of 1.2 s is > 30 times the slowest $g^{(1)}_{ISO}(\tau)$ decay time of 39 ms, which again allows $g^{(1)}_{ISO}(\tau)$ sufficient time to smoothly decay off to its baseline value. Note that a longer observation time that is at least 100 times the slowest $g^{(1)}_{ISO}(\tau)$ decay time, as in the case of $g^{(1)}_{HV}(\tau)$ earlier, would allow a more accurate assessment of the $g^{(1)}_{ISO}(\tau)$ decay. However, in our present implementation, since we are limited to 12000 A-lines in an M-mode frame, the extension of the overall observation time is possible only by using a slower sampling rate, which results in a sparser sampling between A-lines and thus doesn't permit accurate co-registration of fast rotational diffusion present in $g^{(1)}_{HV}(\tau)$.

Representative experimental $g^{(1)}_{HV}(\tau)$ and $g^{(1)}_{ISO}(\tau)$ over a viscosity range of $26 - 493$ mPas are shown in figures 5.5(a) and 5.5(c) respectively. The observed autocorrelations are well-resolved between the samples, and depict a longer decay time as the viscosity increases. Note that the $g^{(1)}_{ISO}(\tau)$ autocorrelations beyond the $\sim 10 - 12$ ms mark are slightly corrupted by a wavy pattern. This is due to the $\sim 100 - 120$ Hz noise present in our current PS-OCT system, which can potentially be avoided in a future generation system by an implementation of a detector devoid of such noise. Comparing figures 5.5(a) and 5.5(c), $g^{(1)}_{HV}(\tau)$ is observed to decay faster than $g^{(1)}_{ISO}(\tau)$ for all samples, owing to the faster rotational diffusion compared to translational diffusion of the GNRs.

Figures 5.5(b) and 5.5(d) show experimental rotational and translational diffusion coefficients extracted from $g^{(1)}_{HV}(\tau)$ and $g^{(1)}_{ISO}(\tau)$ respectively for the samples in the viscosity range of $26 - 493$ mPas (data points in red). The solid blue lines represent fittings of the form $D_R = A_R/\eta + B_R$ and $D_T = A_T/\eta + B_T$ respectively to the experimental data points, whereas the dotted blue lines represent the 95% confidence interval of the fittings. The goodness of fits is estimated by R-square value, which is observed to be > 0.97 in both cases. These fittings enable the estimation of viscosity in samples once

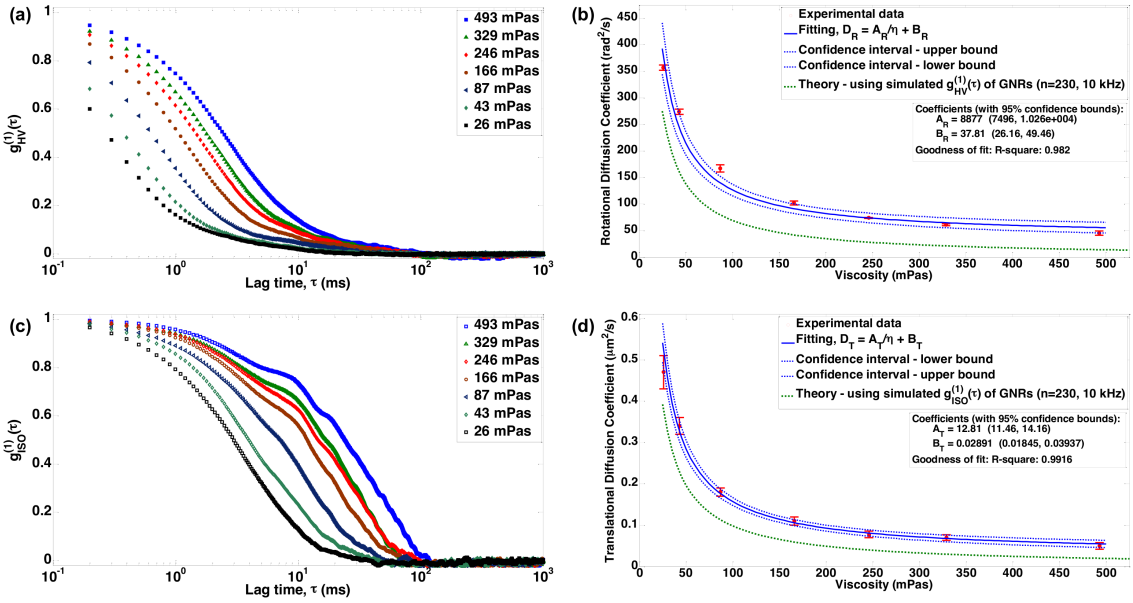

Figure 5.5: Diffusion calibration of CTAB-coated GNRs (size: 69 ± 17 nm by 20 ± 6 nm) **(a)** Representative cross-polarized autocorrelations for samples in the viscosity range of $26 - 493$ mPas. **(b)** Rotational diffusion coefficients extracted by fitting experimental $g^{(1)}_{HV}(\tau)$ to inverse-exponentials (red). **(c)** Representative isotropic autocorrelations for samples in the same viscosity range. **(d)** Translational diffusion coefficients extracted by fitting experimental $g^{(1)}_{ISO}(\tau)$ to inverse-exponentials (red). In **(b)** and **(d)**, solid blue lines are fittings of the form $D_R = A_R/\eta + B_R$ and $D_T = A_T/\eta + B_T$ to the experimental data points respectively, where η is the viscosity, and (A_R, B_R, A_T, B_T) are the fitting parameters. Dotted-blue lines represent the 95% confidence interval of the fit. In **(b)** and **(d)**, dotted green lines are the theoretical predictions of diffusion coefficients for a representative ensemble of GNRs counted by TEM ($n = 230$) assuming the GNRs as rigid cylinders and also accounting for higher backscattering from larger sized GNRs in the distribution by using optical weights (equation (5.3)).

the diffusion coefficients are measured using OCT, and thus the parameters (A_R, B_R, A_T, B_T) act as calibration parameters for the estimation of viscosity for this batch of GNRs. Note that, according to Stokes-Einstein equation, the parameters B_R and B_T should each be zero. However, we observe non-zero values for B_R and B_T in our fittings to the experimental data. B_R and B_T thus signify the noise floor in our measurements of the diffusion coefficients, and thus act as thresholds below which the estimations of D_R and D_T are inaccurate.

In figures 5.5(b) and 5.5(d), the theoretical predictions of diffusion coefficients for a representative ensemble of GNRs ($n = 230$ rods counted by TEM) are shown in dotted green. These predictions are made by fitting inverse-exponentials to the following simulated, ensemble-averaged autocorrelations:

$$g_{HV}^{(1)}(\tau) = \sum_{j=1}^{230} c_j^2 e^{-6D_{R_j}\tau} \tag{5.4}$$

$$g_{ISO}^{(1)}(\tau) = \sum_{j=1}^{230} c_j^2 e^{-q^2 D_{T_j}\tau} \tag{5.5}$$

where the summation is over each GNR j in the representative ensemble, and c_j^2 is an optical weighing factor accounting for the maximum fluctuation in backscattering detected by the OCT system from each GNR, which is evaluated as described in equation (5.3). Diffusion coefficients, D_{R_j} and D_{T_j}, for the j^{th} GNR in equations (5.4) and (5.5) are computed using the expressions derived for solid cylinders as shown in equation (2.23) [14]. The ensemble-averaged theoretical D_R and D_T over the entire viscosity range were evaluated by fitting inverse-exponentials of the form $g_{HV}^{(1)}(\tau) = e^{-6D_R\tau}$ and $g_{ISO}^{(1)}(\tau) = e^{-q^2 D_T\tau}$ to the simulated autocorrelations given by equations (5.4) and (5.5); example fittings of the autocorrelations by inverse-exponential functions are shown in figure 5.6.

In calibrating the diffusion coefficients of CTAB-coated GNRs vs viscosity (figures 5.5(b) and 5.5(d)), although the experimental diffusion coefficients are observed to correlate inversely with viscosity in accordance with Stokes-Einstein relation, both the experimental D_R and D_T are observed to be larger than the theoretical predictions evaluated from the simulated autocorrelations. The level of discrepancy between the experimental diffusion coefficients and the theoretical predictions for this batch of CTAB-coated GNRs appears to be larger than for the previous batch of CTAB-coated GNRs shown

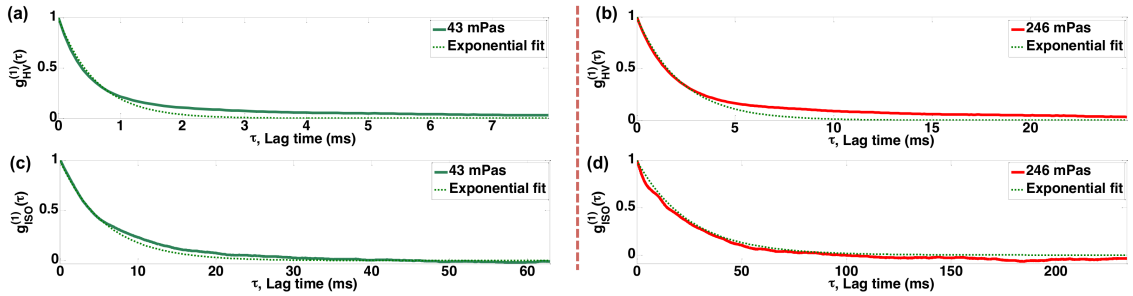

Figure 5.6: Sample inverse-exponential fittings to the experimental autocorrelations at **(a)** 43 mPas and **(b)** 246 mPas. Diffusion coefficients are obtained from the inverse-exponential functions, which are seen to fit the autocorrelation decays reasonably well (*i.e.,* linear least-square fittings of $\ln[g^{(1)}(\tau)]$ to τ with $R^2 > 0.9$). Note that the fittings to the autocorrelations are performed from $\tau = 0$ to $\tau_{1/e}$, although they are shown alongside the experimental autocorrelations at lags beyond $\tau_{1/e}$.

in figure 5.3. This can potentially be due to the presence of larger quantities of smaller sized GNRs (thus faster diffusing GNRs) in this batch of GNRs than that accounted for by the representative size analysis performed using TEM.

5.2.2 Calibration: PEGylated GNRs

Similar calibration steps were carried out for PEG-coated GNRs (PEG molecular weight: 1000 gm/mol, GNRs size: 83 ± 7 nm by 22 ± 3 nm; size analysis based on 99 GNRs counted by TEM). Dilute suspensions of PEGylated GNRs in various glycerol:water mixtures were prepared in the viscosity range of $5 - 519$ mPas. The GNRs number density in each sample is estimated to be $\sim 1.2 \times 10^8$ GNRs/μL which results in an average of ∼200 GNRs in each coherence volume with an average center to center separation between the GNRs of ∼2.5 μm. M-mode imaging was performed with 3 mW of sample-beam power and at two different sampling rates (25 kHz and 10 kHz).

Direct comparison of the evaluated diffusion coefficients at different sampling rates was possible with the collection of data at 25 kHz and 10 kHz. For the fast rotational motion of GNRs, except for the lowest viscosity sample (5 mPas), D_R estimated from

data sampled at 25 kHz and 10 kHz agreed to within 5%. For the 5 mPas sample, the D_R estimates were 12% apart. On the other hand, for the slow translational motion of GNRs, D_T estimates from 25 kHz sampling rate agreed with those from 10 kHz to within 15% for low viscosity samples ($5 - 205$ mPas), and the agreement suffered by as much as 28% at 519 mPas. This suggests that sampling at 10 kHz, which gives a longer observation time compared to 25 kHz, is important to obtain a better estimation of D_T. Moreover, except at very low viscosity (5 mPas or less), the agreement between the D_R estimates at 10 kHz and 25 kHz to within 5% suggests that a sampling rate of 10 kHz gave a reasonable estimate of D_R in the viscosity range covered.

Viscosity (mPas)	$\tau_{1/e}$ of $g^{(1)}_{HV}(\tau)$ (ms)	D_R (rad^2/s)	$\tau_{1/e}$ of $g^{(1)}_{ISO}(\tau)$ (ms)	D_T (μm^2/s)
519	5.4 ± 0.4	31 ± 2	40 ± 8	0.05 ± 0.01
334	3.4 ± 0.1	50 ± 2	29 ± 4	0.066 ± 0.009
205	2.56 ± 0.08	65 ± 2	19 ± 2	0.100 ± 0.008
104	1.64 ± 0.04	102 ± 2	13 ± 4	0.15 ± 0.04
52	0.88 ± 0.01	190 ± 3	7 ± 1	0.31 ±0.06
15	0.322 ± 0.002	517 ± 3	2.2 ± 0.2	0.97 ± 0.07
5	0.120 ± 0.002	1389 ± 18	0.93 ± 0.04	2.3 ± 0.1

Table 5.2: Measured $\tau_{1/e}$ of $g^{(1)}_{HV}(\tau)$ and $g^{(1)}_{ISO}(\tau)$, and the diffusion coefficients of PEGylated GNRs (size: 83 ± 7 nm by 22 ± 3 nm) in Newtonian fluids. Note that $g^{(1)}_{HV}(\tau)$ ware evaluated from M-mode data sampled at 25 kHz, and $g^{(1)}_{ISO}(\tau)$ were evaluated from M-mode data sampled at 10 kHz for the tabulated values.

Table 5.2 lists the $\tau_{1/e}$ of $g^{(1)}_{HV}(\tau)$ and $g^{(1)}_{ISO}(\tau)$ in Newtonian fluids over a viscosity range of $5 - 519$ mPas. $g^{(1)}_{HV}(\tau)$ was evaluated from M-mode data sampled at 25 kHz. The measured $\tau_{1/e}$ of $g^{(1)}_{HV}(\tau)$ are observed to range between 0.120 ms to 5.4 ms. The fastest $g^{(1)}_{HV}(\tau)$ decay time of 0.120 ms is thus greater than twice the sampling time of 40 μs, and the overall observation time of 480 ms is ∼89 times the slowest $g^{(1)}_{HV}(\tau)$ decay time of 5.4 ms. Similarly, $g^{(1)}_{ISO}(\tau)$ were evaluated from M-mode data sampled at 10 kHz for the tabulated values. The measured $\tau_{1/e}$ of $g^{(1)}_{ISO}(\tau)$ range between 0.93 ms and 40

ms, which when contrasted with the sampling time of 100 μs and the overall observation time of 1.2 s meet the Nyquist criterion and the long observation time criterion.

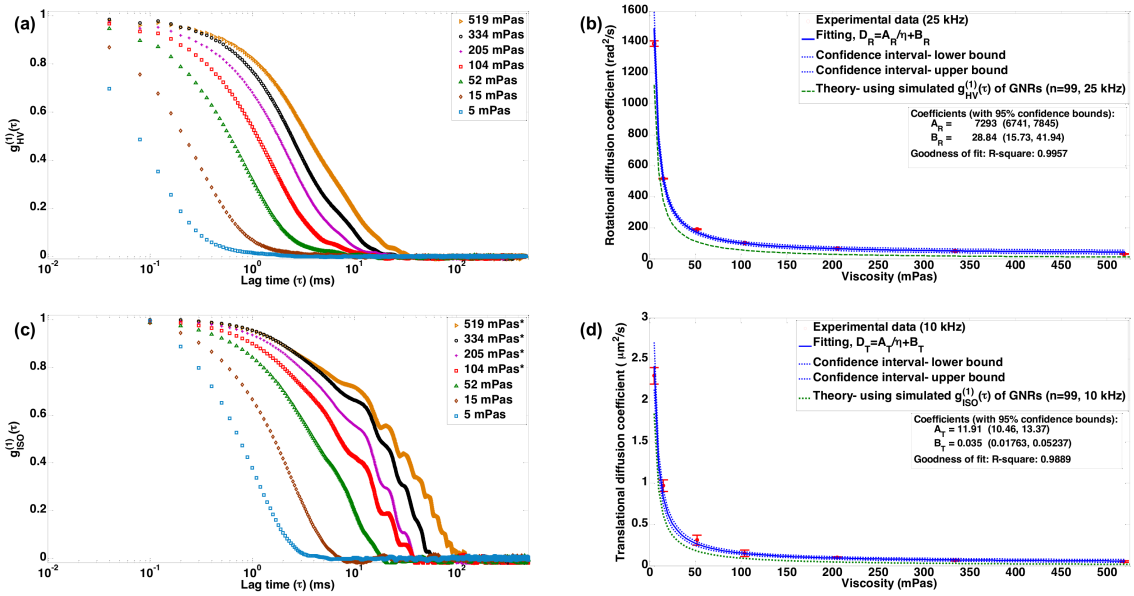

Figure 5.7: Diffusion calibration of PEGylated GNRs (size: 83 $\pm$ 7 nm by 22 $\pm$ 3 nm) **(a)** Representative $g^{(1)}_{HV}(\tau)$ for samples in the viscosity range of $5-519$ mPas. **(b)** D_R extracted by fitting experimental $g^{(1)}_{HV}(\tau)$ to inverse-exponentials (red). **(c)** Representative $g^{(1)}_{ISO}(\tau)$ for samples in the same viscosity range. **(d)** D_T extracted by fitting experimental $g^{(1)}_{ISO}(\tau)$ to inverse-exponentials (red). In **(b)** and **(d)**, solid blue lines are fittings of the form $D_R = A_R/\eta + B_R$ and $D_T = A_T/\eta + B_T$ to the experimental data points respectively, where η is the viscosity, and (A_R, B_R, A_T, B_T) are the fitting parameters. Dotted-blue lines represent the 95% confidence interval of the fit. In **(b)** and **(d)**, dotted green lines are the theoretical predictions of diffusion coefficients for a representative ensemble of GNRs counted by TEM ($n = 99$) assuming the GNRs as rigid cylinders and also accounting for higher backscattering from larger sized GNRs in the distribution by using optical weights (equation (5.3)).

Well-resolved $g^{(1)}_{HV}(\tau)$ and $g^{(1)}_{ISO}(\tau)$ over a viscosity range of $5-519$ mPas are shown in figures 5.7(a) and 5.7(c) respectively. Figures 5.7(b) and 5.7(d) respectively show D_R and D_T evaluated from $g^{(1)}_{HV}(\tau)$ and $g^{(1)}_{ISO}(\tau)$, fittings of the form $D_R = A_R/\eta + B_R$ and $D_T = A_T/\eta + B_T$, and theoretical predictions of diffusion coefficients for a representative ensemble of GNRs ($n = 99$). Compared to the calibration of CTAB-coated GNRs (figure 5.5), the experimental data and the theoretical predictions are observed to match quite

well for this batch of PEGylated GNRs.

Utility of measuring D_R and D_T:

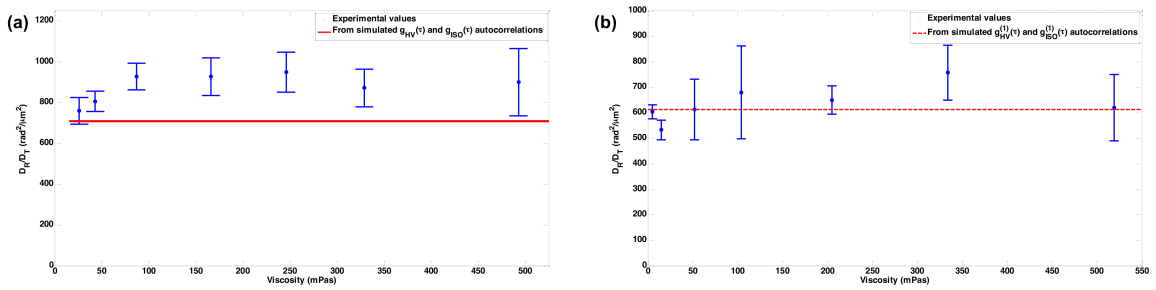

Figure 5.8: D_R/D_T of **(a)** CTAB-coated GNRs (size: 69 ± 17 nm by 20 ± 6 nm), and **(b)** PEGylated GNRs (size: 83 ± 7 nm by 22 ± 3 nm) in Newtonian fluid are observed to match within uncertainty limits at different viscosities, indicating a proportionate change in measured D_R and D_T with viscosity. The red lines are obtained from diffusion coefficients extracted from the theoretical predictions using simulated $g^{(1)}_{HV}(\tau)$ and $g^{(1)}_{ISO}(\tau)$; the simulated autocorrelations use the size distribution of GNRs measured by TEM and assume the GNRs as rigid rods to use the expressions of D_R and D_T for rigid rods (equation (2.23)).

Thus far, it has been demonstrated that both D_R and D_T of the GNRs can be simultaneously estimated using a single PS-OCT measurement. In calibrating the diffusion coefficients of two separate batches of GNRs, we've shown that the experimentally measured D_R and D_T scale inversely with the change in viscosity in accordance with the Stokes-Einstein relation. The utility of using D_R/D_T as a metric can be seen when considering the transition from Newtonian to non-Newtonian fluids. D_R/D_T for Newtonian samples of different viscosities are shown in figure 5.8 for both CTAB-coated and PEGylated GNRs. The D_R/D_T values across the samples are observed to match within their uncertainty limits for both batches of GNRs. As a reference, D_R/D_T across the entire viscosity range from simulated autocorrelation are also shown (red lines). Thus, in exploring Newtonian fluids, we can expect the two measured diffusion coefficients to scale proportionately with viscosity. However, as we venture into more complex sys-

tems such as polymer solutions, gels, biological fluids, such proportionate scaling of D_R and D_T may no longer be the case (for instance, refer to tables 5.4 and 5.5), and this can potentially be an important metric in identifying the transition from Newtonian to non-Newtonian regime based on the differentially modulated rotational vs translational motion of the GNRs in such complex systems.

Simultaneously monitoring $g^{(1)}_{HV}(\tau)$ and $g^{(1)}_{ISO}(\tau)$ also has an experimental advantage in identifying freely-diffusing GNRs from aggregated GNRs. Freely diffusing GNRs depict a distinctly faster decay in $g^{(1)}_{HV}(\tau)$ compared to $g^{(1)}_{HH}(\tau)$, whereas for aggregated GNRs, both $g^{(1)}_{HV}(\tau)$ and $g^{(1)}_{HH}(\tau)$ autocorrelation decay times are similar (since the GNR-aggregates lack the faster rotational motion depicted by freely diffusing GNRs, and thus both autocorrelations are dominated by the translational motion of the aggregated GNRs). This thus allows an experimenter to spot-check the state of GNRs in the samples before proceeding to examine the diffusion of GNRs further.

5.3 Non-Newtonian fluid: polymer solutions

Unlike Newtonian fluids discussed in the previous sections, non-Newtonian fluids (complex fluids) are characterized by a restoring elastic component and a dissipative viscous component in response to an application of a load. An example of non-Newtonian fluids is polymer solutions which exhibit elasticity on short time scales but exhibit viscous flow at long times. This time-dependent mechanical property is termed viscoelasticity, which in polymer solutions is a result of interaction, rearrangement and relaxation of polymer molecules at different times. Viscoelasticity of polymer solutions is dependent on the polymer concentration. In dilute solution, the polymers are well separated and each molecule can be considered as an isolated chain. As the concentration increases, the polymers start to overlap with neighboring polymers. The polymer mass concentration c (mass of polymer/volume of the solution) at which the polymers start overlapping is

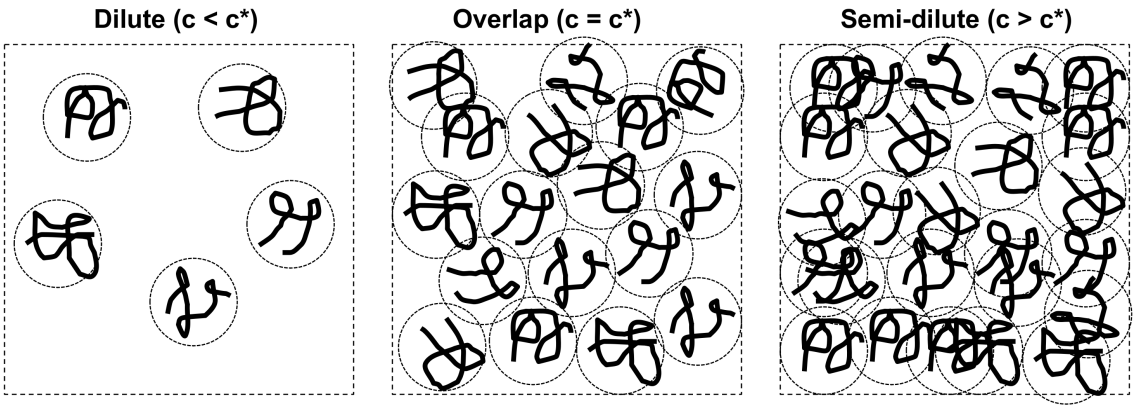

Figure 5.9: Polymer solutions in dilute ($c < c^*$), overlap ($c = c^*$), semi-dilute ($c > c^*$) regimes. In dilute polymer solutions, polymer chains are well separated and can be considered as isolated chains. At the overlap concentration ($c = c^*$), the polymers are in close proximity of one another and start overlapping. As the concentration increases beyond c^*, the pervaded volume V^* (volume of the solution spanned by each polymer at c^*) increasingly contains segments of neighboring polymers in addition to the solvent and its own polymer strand.

termed the overlap concentration c^*. Thus, polymer solutions are classified as dilute ($c < c^*$) or semi-dilute ($c > c^*$) based on the polymer mass concentration c (figure 5.9). At c^*, the average separation between polymer chains is on the order of the size of the polymer chains, whereas in semi-dilute polymer solutions, the lengthscale characterizing the average separation between polymer chains is the correlation length ξ (also known as mesh size), which is defined as the average distance from a monomer on one chain to the nearest monomer on another chain [91].

A method to characterize viscoelasticity of polymer solutions and biopolymers based on generalized Stokes-Einstein relation (GSER) was proposed in a seminal work by Mason *et. al.* [92], which relates the frequency-dependent mean squared displacement $\langle r^2(s) \rangle$ of spherical probes to the frequency-dependent complex shear modulus of the medium $G^*(s)$ as follows:

$$G^*(s) = \frac{k_B T}{s\pi a \langle \Delta r^2(s) \rangle} \tag{5.6}$$

where $\langle \Delta r^2(s) \rangle$ is the Laplace transform of the mean square displacement $\langle \Delta r^2(t) \rangle$, s is the shearing Laplace frequency, and a is the radius of the spherical probe. Using equation (5.6), the macroscopic viscoelasticity of the material can be determined from the local relaxations of the probe. The key approximation in GSER is the extension of the Stokes drag in a purely viscous medium to all frequencies (*i.e.,* all times) in treating non-Newtonian fluids. The complex shear modulus in Laplace space $G^*(s)$ is transformed to the Fourier domain by substituting $s \to i\omega$, where ω is the Fourier frequency. It should be noted that both $G^*(s)$ and $G^*(\omega)$ represent an analytic continuation of the real data (MSD of the probe) into the complex plane, and no additional information is gained by using one or the other. The elastic or storage modulus $G'(\omega)$ and viscous or loss modulus $G''(\omega)$ of the viscoelastic medium are given by the real and imaginary parts of $G^*(\omega)$ respectively. The GSER in Fourier domain is given by:

$$G^*(\omega) = \frac{k_B T}{i\omega\pi a \langle \Delta r^2(\omega) \rangle} \tag{5.7}$$

Following the implementation of Dasgupta *et. al.* [93], the complex shear modulus $G^*(\omega)$ is estimated algebraically by using a local power law to describe the MSD. The local power law is determined from the logarithmic time derivative of the MSD, given by $|\partial \ln \langle \Delta r^2(t) \rangle / \partial \ln t|$, which is equal to 1 for a probe in a purely viscous medium, 0 for a probe in a purely elastic environment, and ranges between 0 and 1 for a probe undergoing viscoelastic relaxation. This algebraic method avoids the use of numerical transforms or fitting $\langle \Delta r^2(t) \rangle$ to arbitrary functional forms, as were done during the infancy of GSER [92, 94].

For the purpose of validation of GSER using M-mode OCT imaging of diffusing probes, $G'(\omega)$ and $G''(\omega)$ were evaluated using spherical probes (polystyrene spheres of diameter 60 nm) diffused in a Newtonian fluid (water, viscosity of $\sim$1 mPas). From the M-mode signals collected from these diffusing isotropic scatterers, depth-resolved $g^{(1)}_{HH}(\tau)$

is evaluated and their mean squared displacement $\langle \Delta r^2(t) \rangle$ is extracted from $g^{(1)}_{HH}(\tau)$ as $(-6/q^2) \ln \left[g^{(1)}_{HH}(\tau) \right]$ using equation (2.29). Lastly, using the GSER for spherical probes shown in equation (5.7), $G'(\omega)$ and $G''(\omega)$ were extracted as shown in figure 5.10. As expected, the elastic modulus $G'(\omega)$ is observed to be $\sim$0 at all frequencies, whereas the viscous modulus $G''(\omega)$ scales linearly with frequency. Additionally, for a Newtonian fluid, viscosity is expected to be independent of frequency and as expected, viscosity (defined as $G''(\omega)/\omega$) shows no frequency dependence over the measured frequency range and also matches the expected bulk viscosity of $\sim$1 mPas.

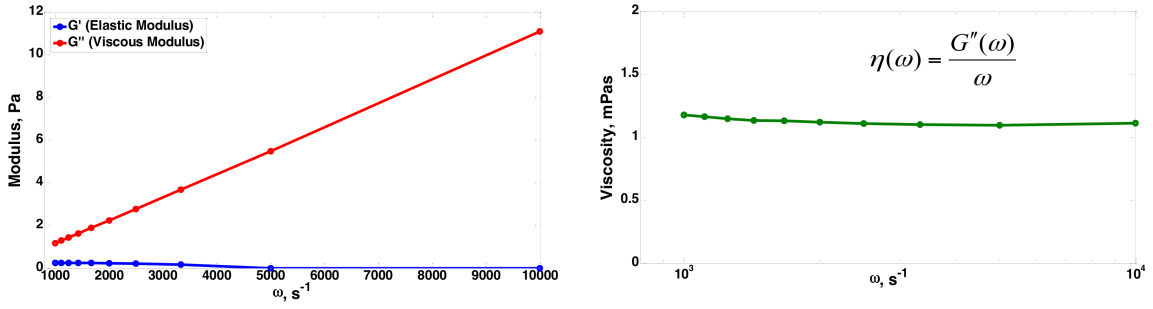

Figure 5.10: Elastic modulus G' and viscous modulus G'' for 60 nm polystyrene spheres diffused in water, and the associated viscosity estimated as $G''(\omega)/\omega$.

For GNRs, the associated GSER can be derived by taking their approximate rod-shaped geometry into consideration:

$$G^*(\omega) = \frac{k_B T}{i\omega\pi \langle \Delta r^2(\omega) \rangle} C_g \tag{5.8}$$

where C_g is a geometric constant derived using the Stokes-Einstein relation for translational diffusion of rod-shaped probes (equation 2.23). C_g also accounts for the polydispersity of GNRs in the representative ensemble, and is given by:

$$C_g = \sum_{j=1}^{n} \left(\frac{2}{L_j} \right) \left[\ln \left(\frac{L_j}{d_j} \right) + 0.312 + 0.565 \left(\frac{d_j}{L_j} \right) - 0.100 \left(\frac{d_j}{L_j} \right)^2 \right] \tag{5.9}$$

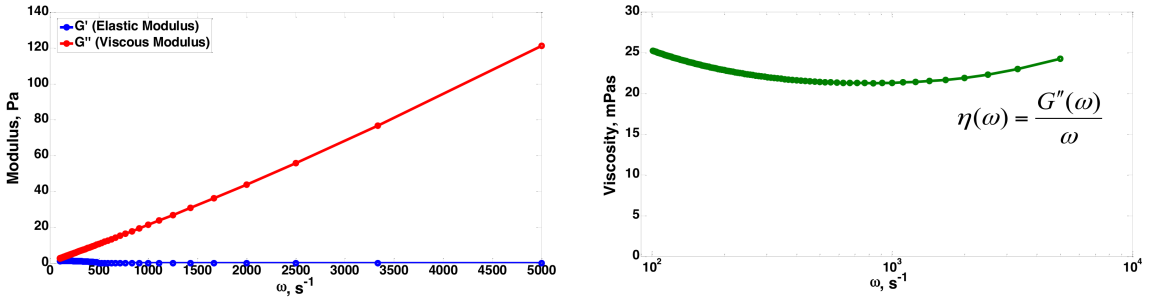

Figure 5.11: Elastic modulus G' and viscous modulus G'' for GNRs diffused in a Newtonian fluid of viscosity ∼26 mPas, and the associated viscosity estimated as $G''(\omega)/\omega$.

Again, to validate the GSER relation using M-mode PS-OCT imaging of diffusing GNRs, the simple case of GNRs diffusing in a Newtonian fluid (viscosity ∼26 mPas) is considered. From the M-mode signals collected from the diffusing GNRs, depth-resolved $g^{(1)}_{ISO}(\tau)$ is evaluated and their mean squared displacement $\langle \Delta r^2(t) \rangle$ is extracted from $g^{(1)}_{ISO}(\tau)$ as $(-6/q^2) \ln \left[g^{(1)}_{ISO}(\tau) \right]$. Using the GSER relation for GNRs shown in equation (5.8), $G'(\omega)$ and $G''(\omega)$ were extracted as shown in figure 5.11. $G'(\omega)$ and $G''(\omega)$ evaluated from the translational Brownian motion of GNRs show negligible $G'(\omega)$ at all measured frequencies, whereas $G''(\omega)$ is observed to scale linearly with viscosity as expected for a Newtonian fluid. Additionally, the frequency dependent viscosity estimated as $G''(\omega)/\omega$ matches well with the expected viscosity of ∼26 mPas. The perceived frequency dependence in the estimated viscosity is due to the local $|\partial \ln \langle \Delta r^2(t) \rangle / \partial \ln t|$ estimates not being exactly 1 at the discretely sampled times. However, observing that $G'(\omega)$ is nearly zero, while $G''(\omega)$ is nearly linear provides perspective about the ability to perform GSER.

5.3.1 Diffusion of GNRs in semi-dilute PEO solutions

To study the diffusion of GNRs in polymer solutions, aqueous solutions of polyethylene oxide (PEO) are considered in this thesis. PEO is a linear polymer of repeating monomeric units $-[(CH_2)_2O]-$. It is popular in polymer rheology experiments due to

its simple structure (linear chain of monomers), good solubility in both organic and aqueous solvents, and ease & repeatability in sample preparation. For linear polymers such as PEO, the overlap concentration c^* and mesh size ξ are given by [95]:

$$c^* = \frac{M_w}{\frac{4}{3}N_A \pi R_g^3} \tag{5.10}$$

$$\xi = R_g (c^*/c)^{0.75} \tag{5.11}$$

where M_w is the polymer molecular weight, N_A is Avogadro's number, c is the polymer mass concentration, and R_g is the radius of gyration of the polymer. The mesh size is on the order of R_g at overlap concentration. Experimentally, the dependence of R_g on M_w has been established as follows [96]:

$$R_g = 2.15 M_w^{0.583} \tag{5.12}$$

Aqueous PEO solution	Molecular weight M_w (gm/mol)	Radius of gyration R_g (nm)	Overlap concentration c^* (% w/w)	Polymer number density at c^* (polymers/μL)
PEO1M	1×10^6	68	0.13%	7.8×10^{11}
PEO4M	4×10^6	152	0.045%	6.8×10^{10}
PEO8M	8×10^6	228	0.03%	2.3×10^{10}

Table 5.3: Estimation of radius of gyration R_g, overlap concentration c^*, and the polymer number density at c^* in aqueous solutions of PEO with molecular weight M_w.

In this thesis, PEOs of three different molecular weights: 1×10^6 gm/mol, 4×10^6 gm/mol, and 8×10^6 gm/mol were used to make aqueous PEO solutions, which are labeled as PEO1M, PEO4M and PEO8M respectively. Table 5.3 outlines some of the important parameters for these PEO solutions. To study diffusion of GNRs, PEGylated

GNRs (size: 62 ± 10 nm by 18 ± 4 nm) were diffused in the aqueous PEO solutions. Comparing the polymer number density estimates at c^* with the GNRs number density in each sample ($\sim 2 \times 10^8$ GNRs/μL), the polymer chains are observed to outnumber the GNRs by ∼8000 (in PEO1M), ∼700 (in PEO4M), and ∼200 (in PEO8M).

To compare diffusion of GNRs in polymer solutions as a function of polymer concentration, aqueous PEO1M solutions at three different concentrations above c^* (1.25%, 2.5%, and 5%) with PEGylated GNRs (size: 62 ± 10 nm by 18 ± 4 nm) were imaged in M-mode using PS-OCT. The mesh size ξ is estimated to be ∼12 nm, ∼7 nm, and ∼ 4 nm in 1.25%, 2.5%, and 5% PEO1M solutions respectively. Table 5.4 outlines the measured $\tau_{1/e}$ of $g^{(1)}_{HV}(\tau)$ and $g^{(1)}_{ISO}(\tau)$ and the associated diffusion coefficients of GNRs in the PEO1M solutions. Recall that the reported diffusion coefficients for the ensemble of GNRs in PEO1M solutions represent an "on average" estimate between the timescale of $\tau = 0$ and $\tau_{1/e}$, which assumes the viscous drag as the dominant force behind the diffusion of GNRs and thus ignores any non-viscous contributions to the autocorrelations during this short duration. D_T of GNRs in all three samples are well-resolved and are observed to decrease as the polymer concentration increases. D_R of GNRs in 1.25% PEO1M sample was observed to be faster than the sampling time and was thus unresolved from the measured $g^{(1)}_{HV}(\tau)$. Rotational diffusion coefficients of GNRs in 2.5% PEO1M and 5% PEO1M solutions are well-resolved and show a decrease in rotational motion as the polymer concentration increases. With an increase in PEO concentration, the diffusing GNRs encounter increased hinderance in an increasingly compact and crowded mesh of the polymer chains, and this behavior is reflected by the measured D_R and D_T in the PEO1M solutions. Additionally, the D_R/D_T for this batch of GNRs is estimated to be 894 ± 3 rad^2/μm^2 in Newtonian fluids, whereas for the 2.5% and 5% PEO1M samples, the experimental D_R/D_T values exceed this theoretical estimate by factors of ∼2 and ∼4 respectively, which suggests disproportionate scaling of D_R and

D_T of GNRs in these PEO1M solutions.

PEO1M (% w/w)	ξ (nm)	$\tau_{1/e}$ of $g^{(1)}_{HV}(\tau)$ (ms)	D_R (rad^2/s)	$\tau_{1/e}$ of $g^{(1)}_{ISO}(\tau)$ (ms)	D_T (μm^2/s)	D_R/D_T (rad^2/μm^2)
1.25%	12	$< 2t_s$	NR	1.95 ± 0.09	1.16 ± 0.05	NR
2.5%	7	0.43 ± 0.03	394 ± 28	10 ± 1	0.23 ± 0.04	1713 ± 322
5%	4	2.4 ± 0.2	70 ± 6	117 ± 20	0.020 ± 0.004	3500 ± 762
Viscous fluids						894 ± 3

Table 5.4: Measured $\tau_{1/e}$ of $g^{(1)}_{HV}(\tau)$ and $g^{(1)}_{ISO}(\tau)$, and the diffusion coefficients of PEGylated GNRs (size: 62 ± 10 nm by 18 ± 4 nm) in PEO1M solutions of different concentrations (above c^*). $g^{(1)}_{HV}(\tau)$ for all samples and $g^{(1)}_{ISO}(\tau)$ for 1.25% PEO1M were evaluated from M-mode data sampled at 10 kHz with an overall observation time of 1.2 s. $g^{(1)}_{ISO}(\tau)$ for 2.5% PEO1M was evaluated from M-mode data sampled at 5 kHz with an overall observation time of 2.4 s, whereas $g^{(1)}_{ISO}(\tau)$ for 5% PEO1M was evaluated from M-mode data sampled at 2 kHz with an overall observation time of 6 s. Note that the D_R/D_T for this batch of GNRs is estimated to be 894 ± 3 rad^2/μm^2 in Newtonian fluids, whereas for the 2.5% and 5% PEO1M samples, the experimental D_R/D_T values exceed this theoretical estimate by factors of ∼2 and ∼4 respectively, which suggests disproportionate scaling of D_R and D_T of GNRs in these PEO1M solutions. t_s: sampling time; NR: Not resolved.

Viscoelasticity of PEO1M solutions can be qualitatively analyzed by the mean squared displacements (MSDs) of GNRs in the PEO1M solutions. Figure 5.12 shows the MSDs of GNRs in PEO1M solutions, extracted from $g^{(1)}_{ISO}(\tau)$ as $(-6/q^2)\ln\left[g^{(1)}_{ISO}(\tau)\right]$. A longer temporal stretch in MSDs is observed as the PEO1M concentration increases, suggesting a slower diffusion in solutions with higher PEO1M concentrations. MSD in 1.25% PEO1M is observed to approximately have a constant slope (in the log-log plot of MSD vs time). However, the MSDs in 2.5% and 5% PEO1M show regions where the slopes decrease in going from left to right along the x-axis, before the slopes increase again. These regions where the MSDs have reduced slopes illustrate the presence of non-negligible elastic components.

To study the contribution of viscous and elastic components in the PEO1M solutions

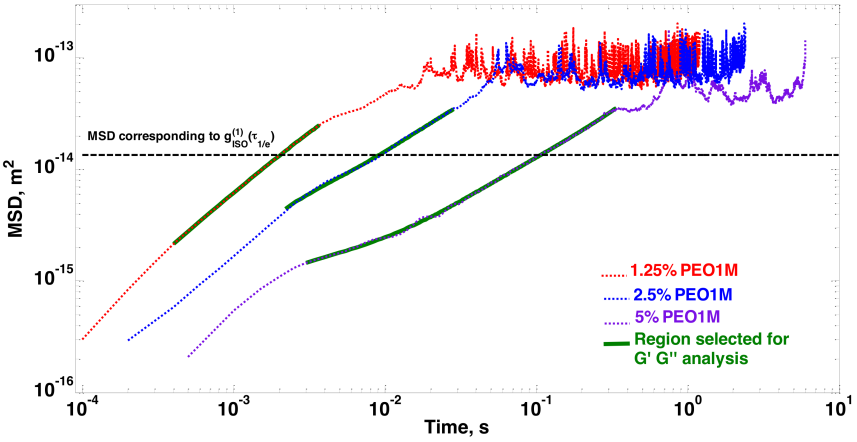

Figure 5.12: Mean square displacement (MSD) of PEGylated GNRs (size: 62 ± 10 nm by 18 ± 4 nm) vs concentration in PEO1M. MSD is extracted from $g^{(1)}_{ISO}(\tau)$ as $(-6/q^2)\ln\left[g^{(1)}_{ISO}(\tau)\right]$. Solid green lines represent the region of MSDs selected for analysis using the GSER formalism (equation (5.8)), chosen such that $|\partial \ln \langle \Delta r^2(t) \rangle / \partial \ln t| < 1$ in the selected regions.

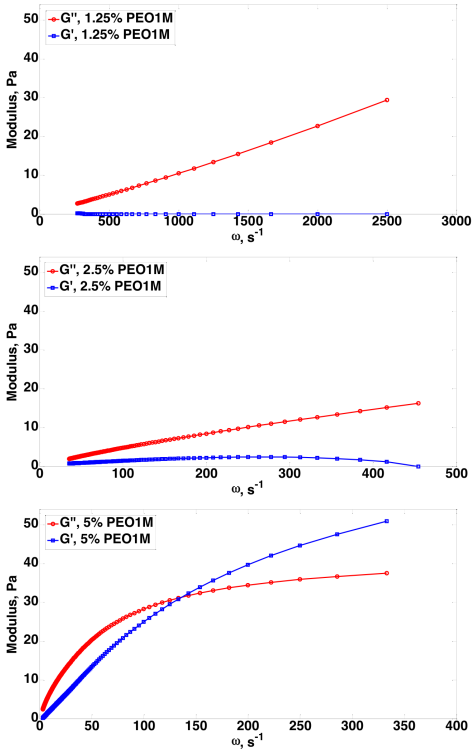

Figure 5.13: Elastic modulus G' and viscous modulus G'' for 1.25%, 2.50%, and 5% PEO1M samples. Both 1.25% PEO1M and 2.5% PEO1M solutions have dominant viscous $G''(\omega)$ components and small elastic $G'(\omega)$ components within the frequency range analyzed. The 5% PEO1M solution has a strong elastic $G'(\omega)$ component at short times (high frequencies) and a dominant viscous $G''(\omega)$ component at long times (low frequencies). Both the elastic modulus $G'(\omega)$ and viscous modulus $G''(\omega)$ increase within the measured frequency range as the PEO1M concentration increases.

further, GSER derived for translational diffusion of GNRs in equation (5.8) is implemented. Figure 5.13 shows the elastic modulus $G'(\omega)$ and viscous modulus $G''(\omega)$ of the PEO1M solutions extracted by the implementation of GSER in the selected regions of MSDs (shown in solid green). The 1.25% PEO1M solution is observed to have a dominant viscous $G''(\omega)$ component and a negligible elastic $G'(\omega)$ component which suggests that the diffusion of GNRs is dominated by viscous drag within the frequency range analyzed. The 2.5% PEO1M solution also has a dominant viscous $G''(\omega)$ component and shows a small elastic $G'(\omega)$ component within the frequency range analyzed. In contrast, within the frequency range analyzed, the 5% PEO1M solution depicts a strong elastic $G'(\omega)$ component at short times (high frequencies) and a crossover point beyond which the viscous $G''(\omega)$ component dominates. Thus, in the 5% PEO1M solution, the diffusion of GNRs are observed to be subjected to non-negligible elastic and viscous forces within the frequency range analyzed. Additionally, both the elastic modulus $G'(\omega)$ and viscous modulus $G''(\omega)$ are seen to increase within the measured frequency range as the PEO1M concentration increases, suggesting an increased viscoelasticity with an increase in the PEO1M concentration.

Viscoelasticity in PEO solutions as a function of molecular weight was also explored by using PEGylated GNRs (size: 62 $\pm$ 10 nm by 18 $\pm$ 4 nm) diffused in 2.5% PEO1M, 2.5% PEO4M, and 2.5% PEO8M. The chosen concentration is above c^* for all three solutions and the mesh size ξ is estimated to be $\sim$7-8 nm in all three cases. The notable difference between the three solutions is the overall size of the polymer molecules estimated by R_g (table 5.3). Table 5.5 outlines the measured $\tau_{1/e}$ of $g^{(1)}_{HV}(\tau)$ and $g^{(1)}_{ISO}(\tau)$ and the associated diffusion coefficients of GNRs in the PEO solutions with different molecular weights. Again, recall that the reported diffusion coefficients for the ensemble of GNRs in PEO1M solutions represent an "on average" estimate between the timescale of $\tau = 0$ and $\tau_{1/e}$, which assumes the viscous drag as the dominant force behind the

PEO sample (ξ ~7-8 nm)	$\tau_{1/e}$ of $g^{(1)}_{HV}(\tau)$ (ms)	D_R (rad^2/s)	$\tau_{1/e}$ of $g^{(1)}_{ISO}(\tau)$ (ms)	D_T (μm^2/s)	D_R/D_T (rad^2/μm^2)
2.5% PEO1M	0.43 ± 0.03	394 ± 28	10 ± 1	0.23 ± 0.04	1713 ± 322
2.5% PEO4M	0.61 ± 0.05	275 ± 20	18 ± 3	0.13 ± 0.02	2115 ± 360
2.5% PEO8M	1.1 ± 0.1	157 ± 14	44 ± 9	0.05 ± 0.01	3140 ± 688
Viscous fluids					894 ± 3

Table 5.5: Measured $\tau_{1/e}$ of $g^{(1)}_{HV}(\tau)$ and $g^{(1)}_{ISO}(\tau)$, and the diffusion coefficients of PEGylated GNRs (size: 62 ± 10 nm by 18 ± 4 nm) in PEO solutions of different molecular weight (c = 2.5% w/w). $g^{(1)}_{HV}(\tau)$ in all cases were evaluated from M-mode data sampled at 10 kHz with an overall observation time of 1.2 s, whereas $g^{(1)}_{ISO}(\tau)$ for all samples were evaluated from M-mode data sampled at 5 kHz with an overall observation time of 2.4 s. Note that the D_R/D_T for this batch of GNRs is estimated to be 894 ± 3 rad^2/μm^2 in Newtonian fluids, whereas the experimental D_R/D_T values exceed this theoretical estimate by factors of ~2, ~2.4 and ~3.5 respectively for PEO1M, PEO4M, and PEO8M samples respectively, which suggests disproportionate scaling of D_R and D_T of GNRs in these 2.5% PEO solutions.

diffusion of GNRs and thus ignores any non-viscous contributions to the autocorrelations during this short duration. Both the rotational and translational diffusion coefficients of GNRs are well-resolved in the PEO samples, and are observed to decrease as the molecular weight increases. Additionally, the D_R/D_T for this batch of GNRs is estimated to be 894 ± 3 rad^2/μm^2 in Newtonian fluids, whereas the experimental D_R/D_T values exceed this theoretical estimate by factors of ~2, ~2.4 and ~3.5 respectively for PEO1M, PEO4M, and PEO8M samples respectively, which suggests disproportionate scaling of D_R and D_T of GNRs in these 2.5% PEO solutions. Figure 5.14 shows the MSDs of GNRs in the PEO samples of constant concentration and different molecular weights. A longer temporal stretch in MSDs is observed as the molecular weight of the PEO increases, which suggests a slower diffusion of GNRs in solutions with higher molecular weight PEO. This can be explained by an increase in hinderance and obstruction to the diffusing GNRs by comparatively larger PEO molecules in the solution.

Figure 5.15 shows the elastic modulus $G'(\omega)$ and viscous modulus $G''(\omega)$ in the

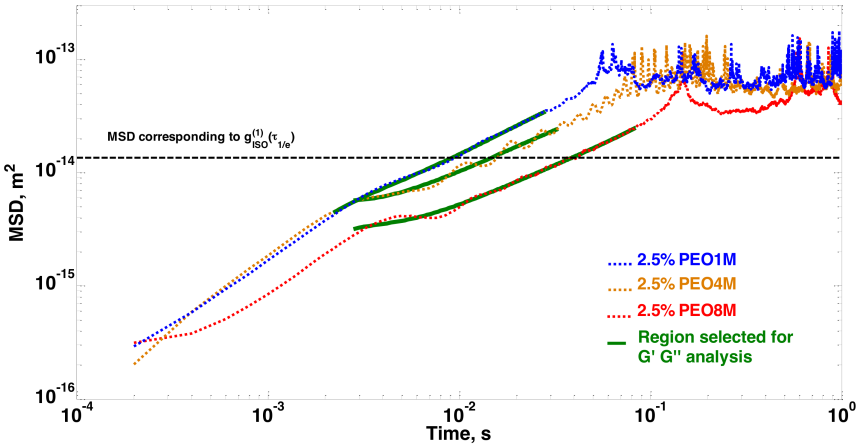

Figure 5.14: Mean square displacement (MSD) of GNRs in 2.5% PEO1M, 2.5% PEO4M and 2.5% PEO8M samples. MSD is extracted from $g^{(1)}_{ISO}(\tau)$ as $(-6/q^2)\ln\left[g^{(1)}_{ISO}(\tau)\right]$. Solid green lines represent the region of MSDs selected for analysis using the GSER formalism (equation (5.8)), chosen such that $|\partial \ln \langle \Delta r^2(t) \rangle / \partial \ln t| < 1$ in the selected regions.

PEO solutions, evaluated by an implementation of GSER for translational diffusion of GNRs to the selected regions of MSDs (solid green lines in figure 5.15). The 2.5% PEO4M and 2.5% PEO8M solutions show significant elastic components at short times and dominant viscous components at long times (low frequencies). Additionally, the elastic to viscous cross-over occurs at $\sim$100 s^{-1} in the PEO8M solution whereas similar cross-over occurs at $\sim$175 s^{-1} in the PEO4M solution. This indicates that the PEO8M solution remains dominantly elastic longer than the PEO4M solution, as expected. The observed elastic and viscous moduli also depict higher values as the molecular weight of the PEO increases, as expected.

Thus, using GNRs as diffusion probes in PEO solutions (same molecular weight but different concentrations, and same concentration but different molecular weights), we've estimated the diffusion coefficients of GNRs in the initial time window of autocorrelation decays between $\tau = 0$ to $\tau_{1/e}$ assuming viscous drag as the dominant force for the relaxation of GNRs, mapped the MSDs of GNRs (taking both viscous and elastic

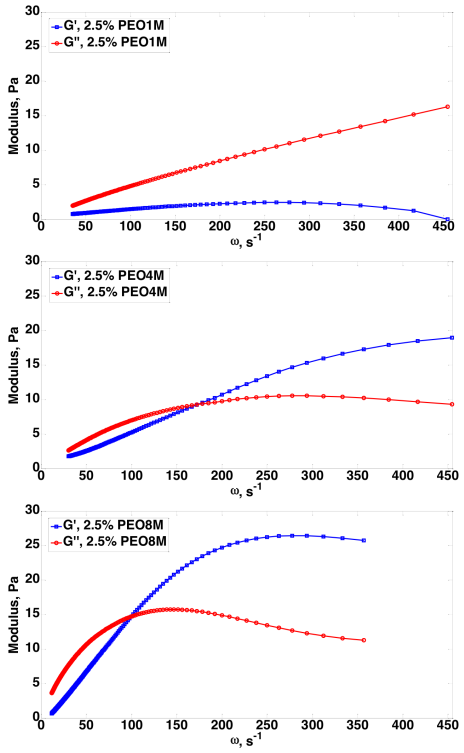

Figure 5.15: Elastic modulus G' and viscous modulus G'' for PEOs of different molecular weights (constant concentration of 2.5% w/w). PEO1M solution is observed to be dominantly viscous within the measured frequency range. Significant elastic components at high frequencies and dominant viscous components at low frequencies observed in 2.5% PEO4M and 2.5% PEO8M solutions. The elastic to viscous cross-over in PEO8M solution occurs at a comparatively lower frequency (*i.e.,* longer time). Higher elastic and viscous moduli observed as the molecular weight of the PEO increases.

forces into consideration), and additionally quantified the sample's frequency-dependent viscoelasticity (Note: the analysis of frequency-dependent viscoelasticity of PEO samples presented is semi-quantitative due to the constraints of the hardware such as the overall observation time and the sampling rate). Compared to current microrheological techniques, the frequency range covered in this study is admittedly small. A qualitative comparison with other microrheological studies of PEO samples [24, 27, 97] similarly show an increase in the overall moduli and increasing elastic contributions at shorter timescales with an increase in polymer concentration and molecular weight. With a longer observation time and a faster sampling rate in future improvements of the current PS-OCT system, the frequency range for microrheological analysis can potentially be improved, and an improved quantitative analysis of sample viscoelasticity would be possible.

5.3.2 Diffusion in "correlation length $\geq$ probe" regime

In the previous section, diffusion of GNRs was considered in solutions in which the size of the GNRs far exceeded the correlation length ξ of polymers ($\sim$7-8 nm). In such situations, the underlying complex network of polymers can be considered a continuum at the length scale of the GNRs, which is a necessary condition for the application of the GSER formalism. However, at low concentrations such that the polymer correlation length ξ is comparable to or larger than the size of the probes, GSER is no longer a valid tool to analyze the viscoelasticity of the polymer solutions. In this section, we briefly discuss the diffusion of GNRs when the polymer correlation length ξ is comparable to or larger than the size of GNRs.

To consider the diffusion of GNRs in the "correlation length $\geq$ probe" regime, PEGylated GNRs (size: 83 $\pm$ 7 nm by 22 $\pm$ 3 nm) were diffused in aqueous PEO4M solutions with polymer concentrations of 0.01% (ξ= 472 nm), 0.045% (ξ= 152 nm), and 0.1% (ξ= 85 nm), and imaged in M-mode. To put the diffusion of GNRs in these PEO4M solutions in perspective with that in the solvent (distilled water), M-mode images were acquired from the solvent with diffused GNRs as well. All M-mode images were acquired at a sampling rate of 25 kHz with in overall observation time of 480 ms.

Figure 5.16 shows well-resolved $g^{(1)}_{ISO}(\tau)$ between the solvent and the PEO4M solutions, and table 5.6 lists the corresponding $\tau_{1/e}$ of $g^{(1)}_{ISO}(\tau)$ along with the measured D_T in the solvent and the PEO4M solutions in the "correlation length $\geq$ probe" regime. A small yet distinct increase in $\tau_{1/e}$ of $g^{(1)}_{ISO}(\tau)$ is observed with an increase in PEO4M concentration. In all samples, the D_R values of the GNRs were too fast to resolve accurately at the sampling rate of 25 kHz. In the "correlation length $\geq$ probe" regime, the GNRs in the PEO4M solutions are diffusing primarily in the solvent with intermittent hinderance from the PEO4M polymers. With an increase in the polymer concentration, the diffusion of GNRs in the solvent is obstructed by the polymers at a higher

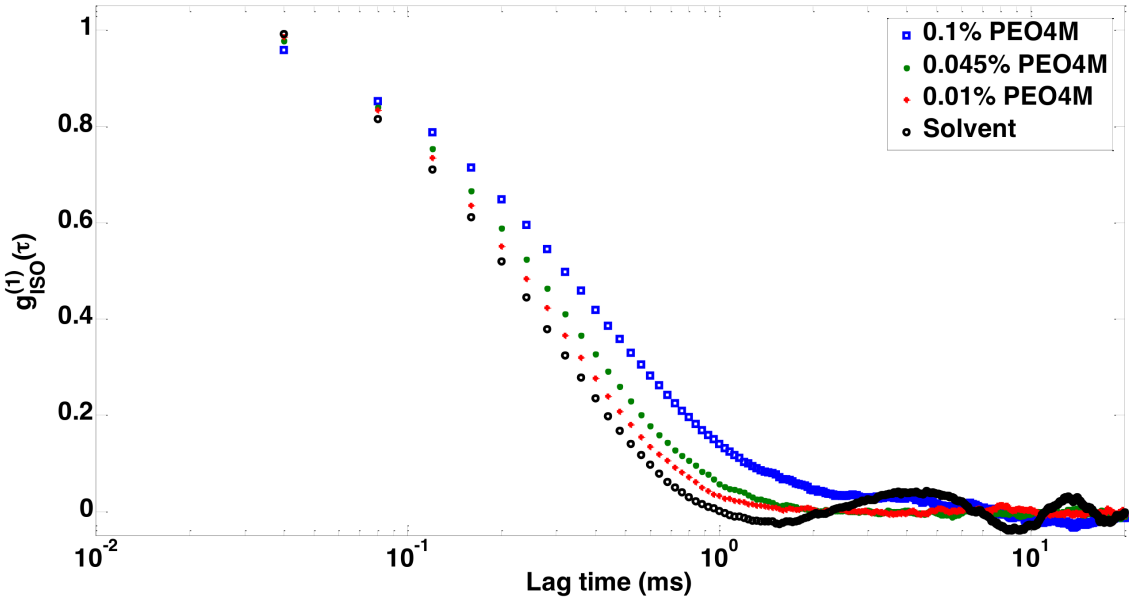

Figure 5.16: $g^{(1)}_{ISO}(\tau)$ in PEO4M in the "correlation length $\geq$ probe" regime. The decay times are observed to increase with a change in concentration of PEO4M in the solutions.

PEO4M samples	ξ (nm)	$\tau_{1/e}$, 1/e decay of $g^{(1)}_{ISO}(\tau)$ (ms)	D_T (μm^2/s)	$\eta/\eta_{solvent} = \tau_{1/e}/\tau_{1/e,solvent}$	$\eta/\eta_{solvent}$ in bulk
0.01%	472	0.29 $\pm$ 0.01	7.9 $\pm$ 0.4	1.06 $\pm$ 0.05	1.12 $\pm$ 0.05
0.045%	152	0.33 $\pm$ 0.01	6.8 $\pm$ 0.3	1.20 $\pm$ 0.05	1.56 $\pm$ 0.07
0.1%	85	0.47 $\pm$ 0.09	5.0 $\pm$ 0.8	1.7 $\pm$ 0.3	2.6 $\pm$ 0.1
Solvent		0.274 $\pm$ 0.007	8.2 $\pm$ 0.2	1.00	1.00

Table 5.6: Measured $\tau_{1/e}$ of $g^{(1)}_{ISO}(\tau)$, and the D_T of PEGylated GNRs (size: 83 $\pm$ 7 nm by 22 $\pm$ 3 nm) in the solvent (distilled water) and PEO4M solutions in the "correlation length $\geq$ probe" regime. $g^{(1)}_{HV}(\tau)$ and $g^{(1)}_{ISO}(\tau)$ were evaluated from M-mode data sampled at 25 kHz with an overall observation time of 480 ms. Rotational diffusion from $g^{(1)}_{HV}(\tau)$ was too fast to resolve in all samples (*i.e.,* Nyquist criterion not satisfied). Relative viscosity $\eta/\eta_{solvent}$ in the vicinity of the GNRs are estimated from $\tau_{1/e}/\tau_{1/e,solvent}$, and the bulk viscosities were measured using an Ubbelohde viscometer.

rate, which is reflected by a decrease in measured D_T of GNRs. Table 5.6 also lists the relative viscosity $\eta/\eta_{solvent}$ in the vicinity of the GNRs and the bulk viscosity of the solutions measured using an Ubbelohde viscometer. The bulk relative viscosity values

are observed to be slightly larger than the local relative viscosities encountered by the GNRs in the PEO4M solutions. This result highlights the mechanistic difference in measurements of bulk viscosity, which is due to the collective relaxation of polymers in the solution, and the nanoscale local viscosity encountered by the diffusing GNRs in the "correlation length $\geq$ probe" regime of polymer solutions.

The result of this section shows that the diffusion of GNRs is indicative of intermittent obstructions from the polymers in the solution even in the "correlation length $\geq$ probe" regime. Thus, understanding obstructed diffusion of GNRs can be a valuable tool in studying biological fluids at the nanoscale that have low concentrations of macromolecules (such as saliva, low concentration mucus *etc*), which are not characterized by microrheological methods based on GSER, nor by bulk rheology. Particle-tracking techniques are also capable of measuring diffusion of probes in such biological fluids. However, conventional particle-tracking involves using micron- and sub-micron- sized beads which don't portray the same obstructed diffusion encountered at the nanoscale. Thus, having a light scattering based tool using ensembles of nanoscale probes, as the one developed in this thesis, can aid as an important supplemental tool in rheological studies of various complex and biological fluids.

To summarize, in this chapter, we validated the Stokes-Einstein relation by measuring D_R of GNRs in Newtonian fluids. Secondly, validation of the Stokes-Einstein relation was extended to the measured D_T of GNRs in Newtonian fluids. In Newtonian fluids, both D_R and D_T of GNRs were observed to scale inversely proportionally with the viscosity of the sample. Next, the diffusion of GNRs in various PEO solutions which exhibit viscoleastic responses was discussed. In semi-dilute PEO solutions, the viscous and elastic moduli of the solutions were quantified using the GSER formalism based on the MSDs of the GNRs. Polymer solutions in the "correlation length $\geq$ probe" regime were also discussed, which demonstrated the merit of our outlined method in sensing

the diffusion of GNRs in the solvent with intermittent hinderance from the polymer segments. Diffusion of GNRs in the "correlation length $\geq$ probe" regime discussed in this section thus sets the stage for exploring the diffusion of GNRs in biological samples such as extracellular matrix and *in vitro* mucus, which are discussed in the next chapter.

Chapter 6

Biological studies

This chapter focuses on biological studies using GNRs as diffusion probes in 3D tissue culture models and also in *in vitro* mucus. Using the custom-built PS-OCT system to exploit the polarization sensitive scattering property of GNRs, the ability of GNRs to contrast various biological features of interest is demonstrated. Lastly, an imaging study of breast cancer 3D cultures using the OCT system is discussed in detail.

6.1 GNRs in 3D tissue culture models

Tissues *in vivo* consist of a complex, three-dimensional network comprised of the extracellular matrix (ECM) produced by stromal fibroblasts in collaboration with epithelial cells. ECM provides structural scaffolding and biochemical & biomechanical contextual information to signal appropriate cellular responses such as cellular adhesion, activation, and migration [98]. For controlled *in vitro* studies in cell biology, 3D tissue culture models comprised of proteins, such as collagen I and Matrigel®, have been successfully employed as surrogate models to mimic the structure and function of the ECM [99, 100, 101]. Collagen is the most abundant protein in mammals and is the main component of connective tissues, of which collagen I is the most abundant collagen (over 90%) in the human body and is a major structural component of ECM found in tissues and internal organs [102]. Matrigel is a gelatinous protein mixture marketed by

BD Biosciences, and is obtained from Engelbreth-Holm-Swarm (EHS) mouse sarcoma cells [103]. Tissue culture models comprised of collagen I and Matrigel have been shown to faithfully recapitulate various aspects of tissue behavior *in vivo*, which are otherwise absent in 2D cell cultures [104]. Both collagen I and Matrigel remain liquid at temperatures below 4°C, and irreversibly become gels above 4°C. This gelatinous, porous, and viscoelastic solid behaves as a scaffold for the adhesion and proliferation of the cells during *in vitro* studies. In this study, collagen I mixtures are prepared at a pH of ∼7.4, and the gelation of collagen I and collagen I:Matrigel (2 mg/ml collagen I and Matrigel mixed in equal proportion) are achieved at a temperature of 37°C in ∼30 minutes.

Studying the diffusion of GNRs in 3D tissue culture models sheds light on how nanoscopic objects navigate through the ECM pores. As will be shown, the observed diffusion of GNRs is sensitive to changes in the ECM concentration as well as the changes to the ECM due to the interplay between fibroblasts and the ECM. Diffusing GNRs in mammary epithelial 3D cultures also reveals the utility in contrasting regions with no uptake of GNRs, which sheds light on limited permeability of nanoscopic objects in regions of the 3D matrix.

6.1.1 Delivery and diffusion of GNRs

To achieve delivery of GNRs in the ECM models (collagen I, collagen I:Matrigel), addition of GNRs was carried out in two different ways: premixing the GNRs with the ECM solution before the onset of gelation, and topically adding GNRs to gelled ECM. The goal in premixing the GNRs was to study the impact on gelation by the addition of GNRs, and also to monitor the state of GNRs (trapped or freely diffusing) if gelation is achieved. Initial attempts of premixing GNRs to ECM solutions were carried out with CTAB-coated GNRs, which failed to initiate gelation due to an imbalance in pH created by the cationic CTAB-coating on the GNRs, and also resulted in aggregation of GNRs

in the ion rich ECM solution. Thus, to ensure that the GNRs remain freely diffusing and avoid adhesion in the ECM, PEGylated GNRs (PEG of molecular weight 1000 gm/mol) were used. PEGylated GNRs premixed with the ECM solutions were found to not disrupt gelation, and also resulted in an even distribution of GNRs throughout the gel without signs of aggregation. The second method of delivery (topical addition of GNRs to gelled ECM) was carried out to ensure that homogenous delivery of GNRs is possible even after the onset of gelation.

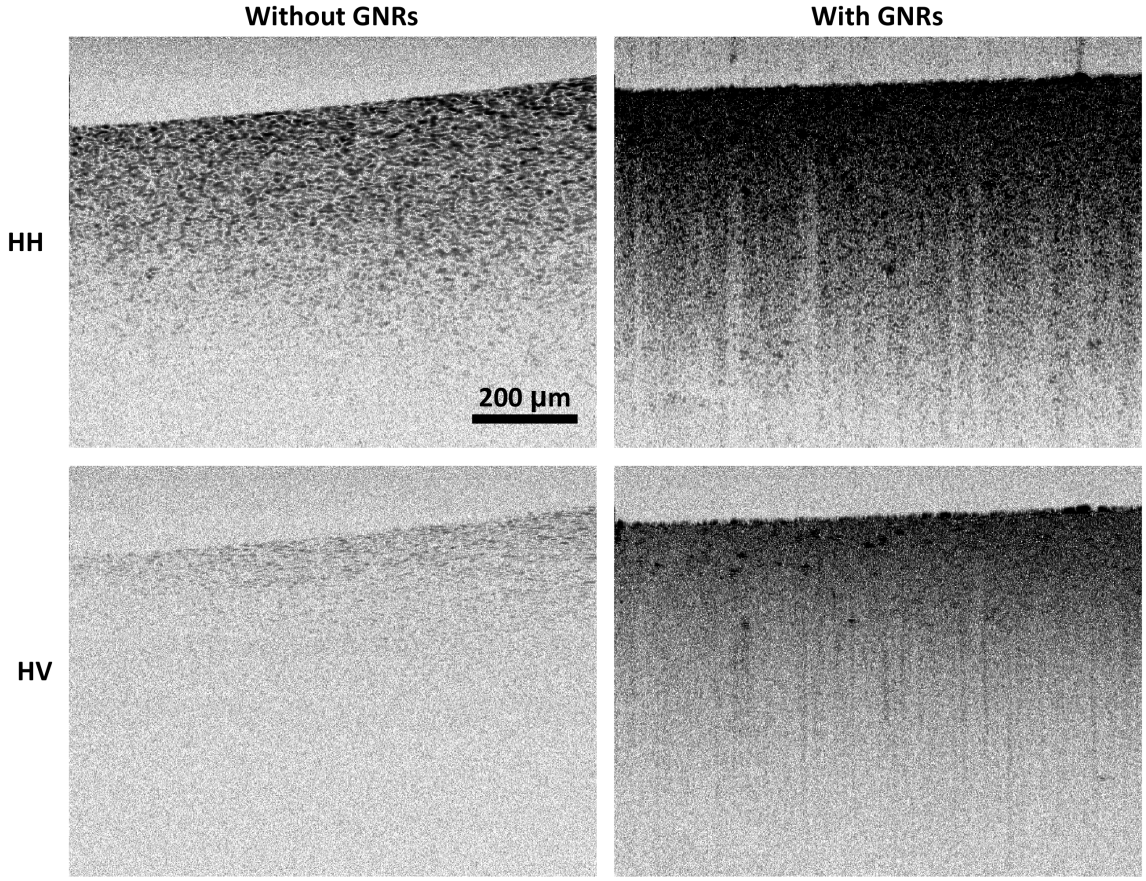

Figure 6.1: Co-polarized (HH) and cross-polarized (HV) images of collagen I:Matrigel tissue culture models before and after addition of PEGylated GNRs (83 ± 7 nm by 22 ± 3 nm). Before the addition of GNRs, the scattered light is predominantly in HH. With the addition of GNRs, HV signal is observed as well.

Collagen I:Matrigel gels imaged before and after addition of PEGylated GNRs are

shown in figure 6.1. Without the GNRs, the cross-polarized HV signal is weak compared to the co-polarized HH signal, and in presence of GNRs, strong HH and HV signals are observed indicating a homogeneous distribution of GNRs as they navigate through the gel pores. Both delivery methods (premixing and topical delivery) yielded successful

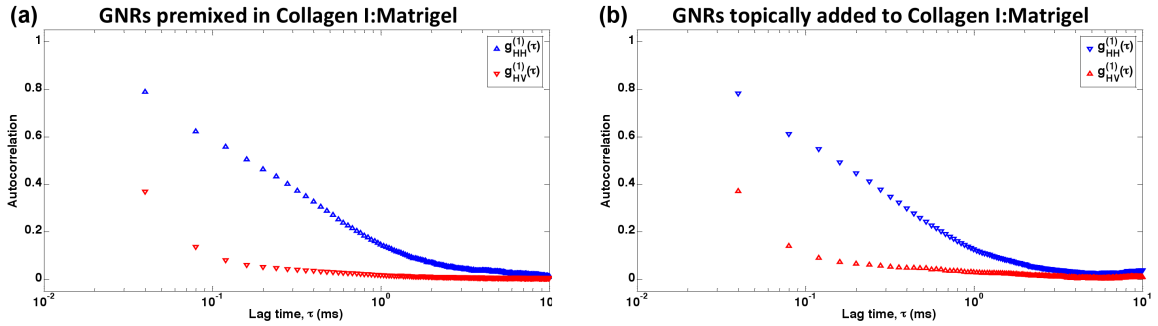

Figure 6.2: Co-polarized $g^{(1)}_{HH}(\tau)$ and cross-polarized $g^{(1)}_{HV}(\tau)$ autocorrelations evaluated from M-mode PS-OCT imaging of (a) collagen I:Matrigel premixed with GNRs, and (b) collagen I:Matrigel with topically added GNRs. A distinct rapidly decaying component (red) due to the rotational diffusion of GNRs is observed in both cases (rotational diffusion decay too fast to quantify). The slowly decaying component (blue) is due to the combination of rotational and translation of GNRs within the gel pores.

distribution of freely diffusing GNRs in collagen I:Matrigel gels. Depending on the nature of the experiment, researchers thus have the option to either premix the GNRs in the tissue culture models before gelation, or topically add GNRs at a later time. For instance, studies focusing on cellular uptake of GNRs to track cellular organization to form complex structures (which are otherwise impenetrable to topically added GNRs) might benefit from premixing the GNRs with collagen I:Matrigel during cell culture preparation. On the other hand, experiments requiring minimal intervention during cell proliferation and organization are better suited for topical delivery of GNRs into the ECM only at a later time for imaging.

With successful delivery of GNRs in the tissue culture models, M-mode PS-OCT imaging was performed to evaluate the diffusion coefficients of the GNRs. Previous studies, particularly in the context of drug delivery, have highlighted the role of pores

in the ECM for the delivery of nano-sized probes [105, 106]. The pore sizes have been estimated to be ∼500 nm for 2 mg/ml collagen I and ∼100 nm for 20 mg/ml collagen I gels [106]. In the ECM models explored in this thesis, pores larger than the size of the GNRs are expected to allow diffusion in the ECM interstitial space. The GNRs were indeed found to be freely diffusing in the solvent within the pores of the gels, as evidenced by a rapidly decaying rotational component in the cross-polarized autocorrelation $g^{(1)}_{HV}(\tau)$ and a comparatively slowly decaying co-polarized autocorrelation $g^{(1)}_{HH}(\tau)$ (figure 6.2). The presence of a distinct fast component in $g^{(1)}_{HV}(\tau)$ and a slow component in $g^{(1)}_{HH}(\tau)$ is a reliable signature to gauge free diffusion vs aggregation of GNRs in the sample as this distinct signature is absent in samples with aggregated GNRs. The fast rotational diffusion (although unresolved due to insufficient sampling speed; sampled at 25 kHz) in the ECM models suggests that the GNRs are diffusing in the pores of the matrix and probing the solvent within the pores. Isotropic autocorrelations $g^{(1)}_{ISO}(\tau)$ were evaluated from PS-OCT imaging of the solvent and the ECM models (both premixed and topical delivery of GNRs), as shown in figure 6.3. GNRs in the ECM models were observed to have a longer $\tau_{1/e}$ (0.50 ± 0.05 ms; for both topical delivery and premixing of GNRs) compared to that in the solvent (0.24 ± 0.02 ms). Thus, although the GNRs in the collagen I:Matrigel gels are primarily diffusing in the solvent within the pores, their diffusion is intermittently hindered by the pore walls resulting in a slower diffusion compared to the unhindered diffusion in solvent alone.

6.1.2 GNRs diffusion as a function of collagen I concentration

In this section, the role of collagen I concentration in the diffusion of GNRs is explored by topically delivering GNRs in collagen I gels at three different concentrations (1 mg/ml, 2 mg/ml, and 3 mg/ml). In an absence of GNRs in the collagen I gels, the OCT signal is predominantly limited to the co-polarized channel (HH), and with the delivery of

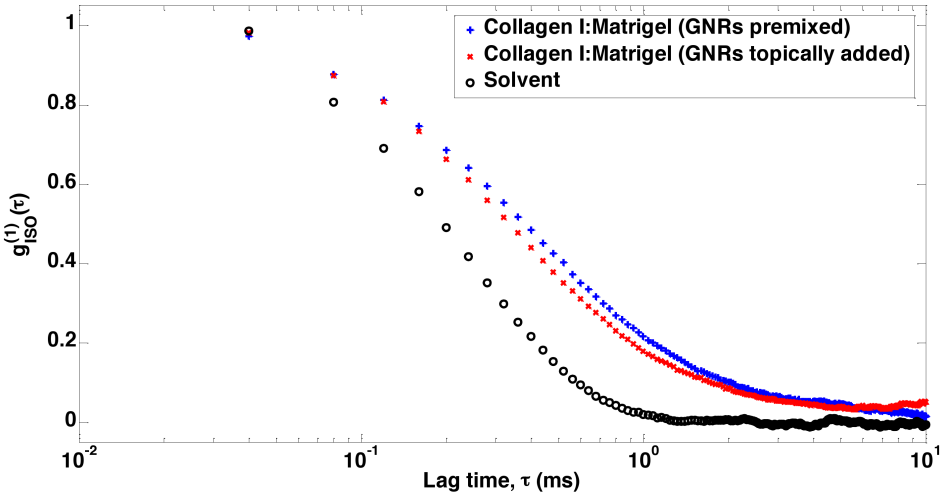

Figure 6.3: Isotropic autocorrelation $g^{(1)}_{ISO}(\tau)$ evaluated from M-mode PS-OCT imaging of solvent and collagen I:Matrigel gels. $g^{(1)}_{ISO}(\tau)$ is observed to have a longer $\tau_{1/e}$ (0.50 $\pm$ 0.05 ms) compared to that in the solvent (0.24 $\pm$ 0.02 ms). $g^{(1)}_{ISO}(\tau)$ for the two methods of GNRs delivery (premixing GNRs vs topically adding GNRs) are seen to be in agreement.

GNRs in the collagen I gels, both the co- and cross- polarized OCT signals are evident (figure 6.4). With an increase in collagen I concentration, the gels are observed to be palpably stiffer. However, in the local vicinity of the GNRs at the nanoscale, an increase in collagen concentration corresponds to a decrease in the pore size between the fibers of the ECM, and also an increase in unassembled collagen in the interstitial space [106]. Figure 6.5(a) shows $g^{(1)}_{ISO}(\tau)$ in the collagen I gels, which depicts an increase in the $\tau_{1/e}$as the concentration of collagen I increases (0.24 $\pm$ 0.02 ms in the solvent, 0.27 $\pm$ 0.02 ms for 1 mg/ml collagen I, 0.35 $\pm$ 0.04 ms for 2 mg/ml collagen I, and 0.43 $\pm$ 0.08 ms for 3 mg/ml). The corresponding translational diffusion coefficients derived from $g^{(1)}_{ISO}(\tau)$ shows that the diffusion of GNRs in the interstitial space of the collagen I gels is hindered compared to that in the solvent alone, and the diffusion is observed to decrease as the collagen I concentration increases (figure 6.5(b)). Note that the reported D_T for the ensemble of GNRs represent an "on average" estimate between the timescale of $\tau = 0$

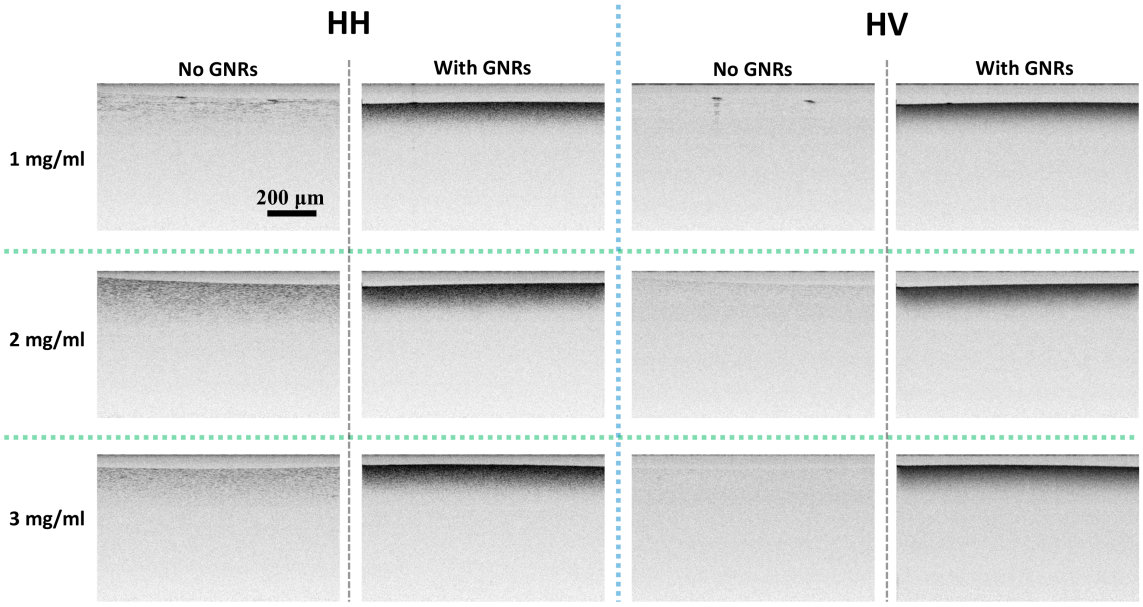

Figure 6.4: B-mode PS-OCT images of collagen I gels before and after the delivery of GNRs. Without the GNRs, the OCT signal is limited to the *HH* channel, and with the delivery of GNRs in the gels, both *HH* and *HV* channels show comparable backscattering signals.

and $\tau_{1/e}$, which assumes the viscous drag as the dominant force behind the diffusion of GNRs and thus ignores any non-viscous contributions to the autocorrelations, if any, during that duration.

The result in this section shows that M-mode PS-OCT imaging of GNRs in ECM is sensitive to changes in the ECM concentration due to the corresponding changes in the interstitial space between the matrix. This enables the possibility of monitoring changes to the ECM in non-invasive, longitudinal studies using M-mode PS-OCT imaging of GNRs as diffusion probes. Moreover, this method also has implications for drug delivery using GNRs as functionalized drug-carriers, which can potentially be translated to *in vivo* tissues.

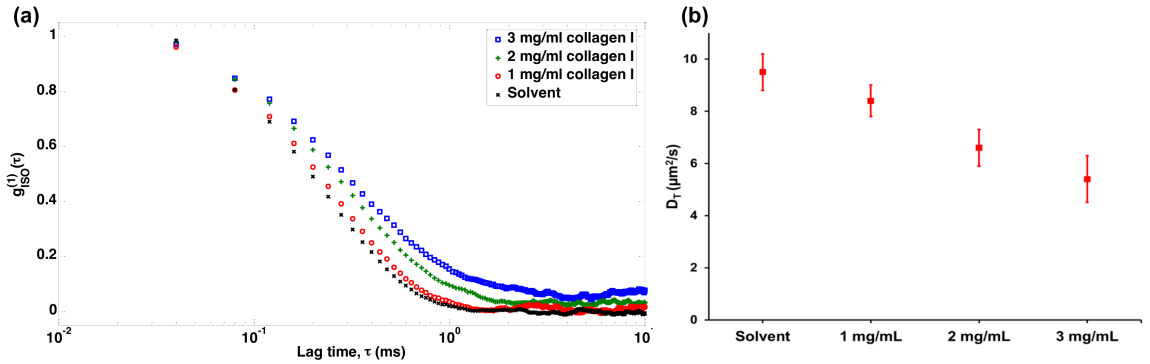

Figure 6.5: (a) Isotropic autocorrelations $g^{(1)}_{ISO}(\tau)$ in collagen I gels at different concentrations. $\tau_{1/e}$ of $g^{(1)}_{ISO}(\tau)$ increases as collagen I concentration increases (0.27 ± 0.02 ms for 1 mg/ml collagen I, 0.35 ± 0.04 ms for 2 mg/ml collagen I, and 0.43 ± 0.08 ms for 3 mg/ml). (b) Corresponding translational diffusion coefficients of GNRs show that the diffusion in the collagen I gels are slower than that in the solvent alone, and additionally, depict slower diffusion with an increase in collagen I concentration.

6.1.3 GNRs diffusion in fibroblast cultures

Fibroblasts are the principal cellular components of the connective tissues in mammals and are responsible for the synthesis of ECM, maintenance of ECM homeostasis, regulation of differentiation and homeostasis of adjacent epithelia, and wound healing through collagen deposition [107]. During the process of tissue remodeling *in vivo*, spindle-shaped fibroblasts reorganize the ECM by attaching and pulling on them [108]. In *in vitro* tissue cultures, fibroblasts similarly attach and exert tensile forces to the ECM inducing matrix modification [109]. To understand the nano- and micro- scale modifications to the ECM brought about by fibroblasts, reduction mammoplasty fibroblasts (RMFs) were seeded in collagen I:Matrigel ECM at two different concentrations (30,000 RMFs/ml, 90,000 RMFs/ml) and maintained for 2 weeks before imaging.

B-mode images of the tissue cultures acquired 24 hours after introduction of PEGylated GNRs (size: 83 ± 7 nm, 22 ± 3 nm) into the cell culture medium (~3.3×10^{11} GNRs/ml) are shown in figure 6.6. The presence of fibrillar networks of RMFs in the gels are masked by highly scattering GNRs in the *HH* image. In the *HV* images of

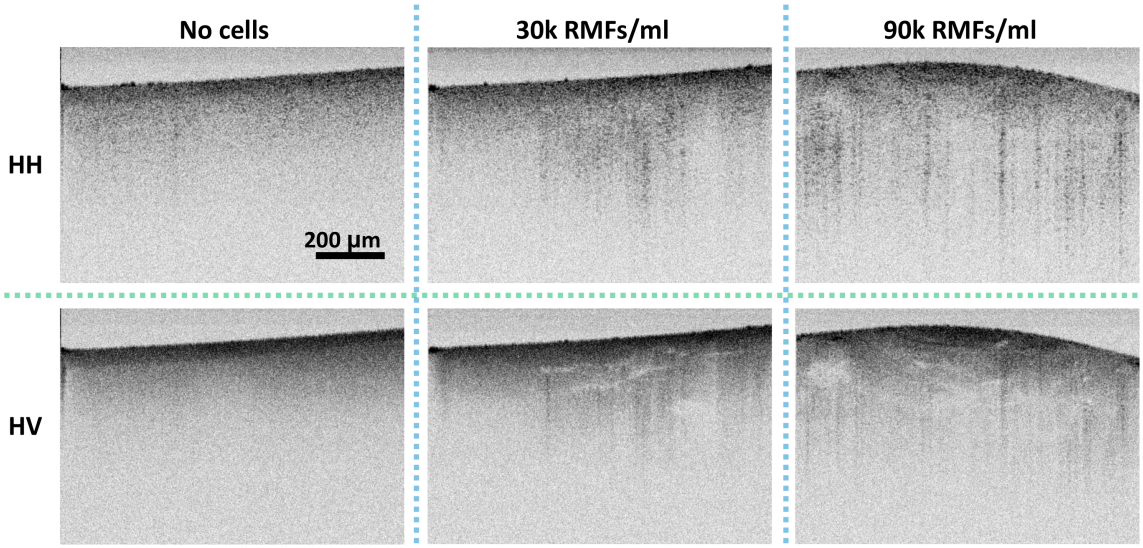

Figure 6.6: B-mode *HH* and *HV* images of collagen I:Matrigel with no cells (control), 30,000 RMFs/ml, and 90,000 RMFs/ml, imaged at 2 weeks after topical delivery of GNRs. Organizations of RMFs in the gels are evident in the *HV* images as regions of negative contrast (absence of GNRs).

the RMF cultures, regions of negative contrast (absence of GNRs) are observed which are the organizations of RMFs in the gels. M-mode PS-OCT imaging of the control gel and the RMF cultures was also performed, and the associated isotropic autocorrelations $g^{(1)}_{ISO}(\tau)$ are shown in figure 6.7(a), which show a progressive increase in the $\tau_{1/e}$ as the RMFs seeded onto the ECM increases. D_T in the control gel, RMF cultures, and the solvent (culture media), were evaluated from $g^{(1)}_{ISO}(\tau)$, and are shown in figure 6.7(b). As previously mentioned, the reported D_T for the ensemble of GNRs represent an "on average" estimate between the timescale of $\tau = 0$ and $\tau_{1/e}$, which assumes the viscous drag as the dominant force behind the diffusion of GNRs and thus ignores any non-viscous contributions to the autocorrelations, if any, during that duration. Compared to the solvent, the GNRs in both the control gel and the RMF cultures depict smaller D_T values owing to the hinderance from the ECM to their diffusion in the interstitial space. Moreover, diffusion of GNRs is observed to decrease with the concentration of RMFs

seeded into the ECM. This suggests that as RMFs proliferate in the ECM, the modified ECM results in a more constricted interstitial space between the fibril networks, which is unambiguously reflected upon the diffusion coefficients of GNRs measured by M-mode PS-OCT imaging.

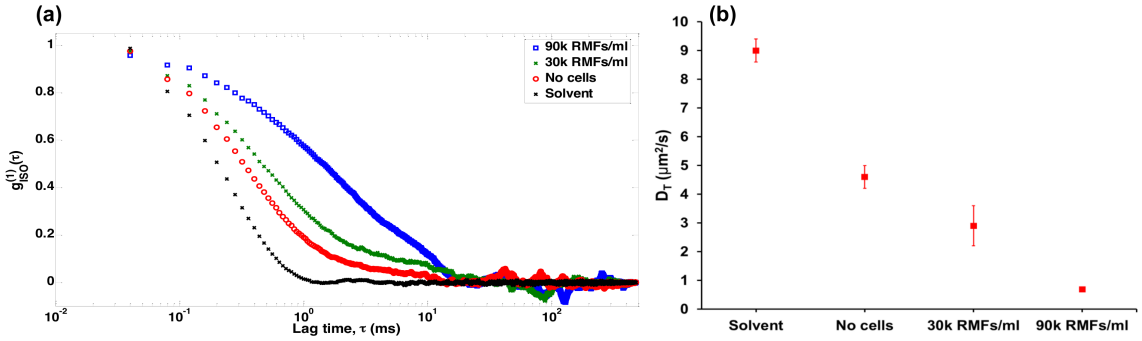

Figure 6.7: (a) Isotropic autocorrelations $g^{(1)}_{ISO}(\tau)$ in tissue cultures with RMFs. $\tau_{1/e}$ of $g^{(1)}_{ISO}(\tau)$ increases as the RMFs seeded into the ECM increases. (b) Corresponding translational diffusion coefficients of GNRs show that the diffusion in the ECM cultures are slower than that in the solvent alone, and additionally, depict slower diffusion with an increase in RMF concentration.

Recent studies have identified fibroblasts as a key cellular component of tumors and have also highlighted their potential role in cancer metastasis [110, 111]. Using the diffusion of GNRs to investigate fibroblast-induced changes to the interstitial space and the scaffold of the ECM can thus potentially aid in understanding the interplay between fibroblasts and the ECM during tumorigenesis and cancer progression.

6.1.4 GNRs in mammary epithelial cell culture

Mammary epithelial cells (MECs) form a major constituent of the human mammary gland microenvironment, and their intricate interaction with the ECM & fibroblasts is a major area of breast cancer research [112, 113]. 3D culture of MECs has been recognized as a reliable model to study morphogenesis of glandular epithelium *in vitro* [100, 104]. MCF10A (immortalized MEC, non-malignant) cultured on collagen I:Matrigel ECM

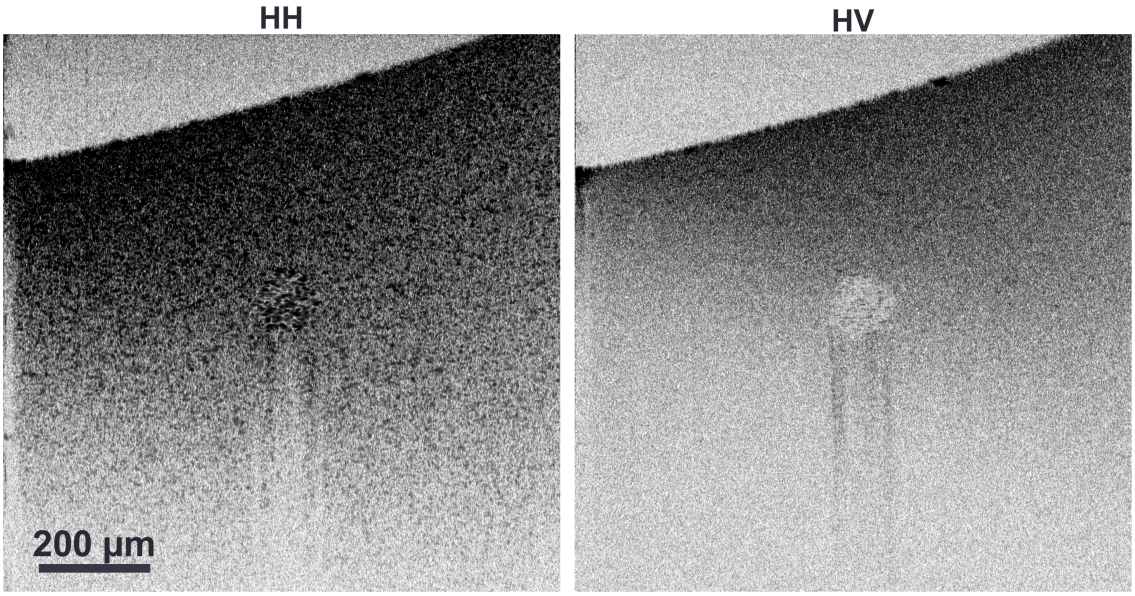

Figure 6.8: PS-OCT B-mode images of MCF10A cells cultured in collagen I:Matrigel ECM in presence of GNRs. An acinus formed by the MECs is weakly scattering in the cross-polarized channel and is seen to be negatively contrasted in the *HV* image in presence of GNRs in the surrounding ECM.

have been shown to faithfully recapitulate numerous *in vivo* features of the mammary epithelium, including the formation of spheroids with hollow lumen (called acini), and apicobasal polarity of acinar cells [99, 114]. In this section, we explore the addition of GNRs to collagen I:Matrigel, containing MCF10A cells, after the formation of acinar structures. An acinus formed by the MCF10A cells after a culture period of a week is visible in the PS-OCT B-mode images (figure 6.8). Due to the presence of GNRs in the ECM, the acinus is masked in the *HH* image, but the corresponding *HV* image shows a lack of GNRs uptake in the acinus. Thus, the location of the acinus in the gel is visible as a region of negative contrast in the *HV* image. The negative contrast in the cross-polarized PS-OCT image shows the utility of GNRs in contrasting regions of no uptake against a background of highly scattering GNRs.

The acinus and the surrounding ECM with GNRs diffusing in the gel pores constitute a heterogeneous environment to study the diffusion of GNRs. M-mode PS-OCT images

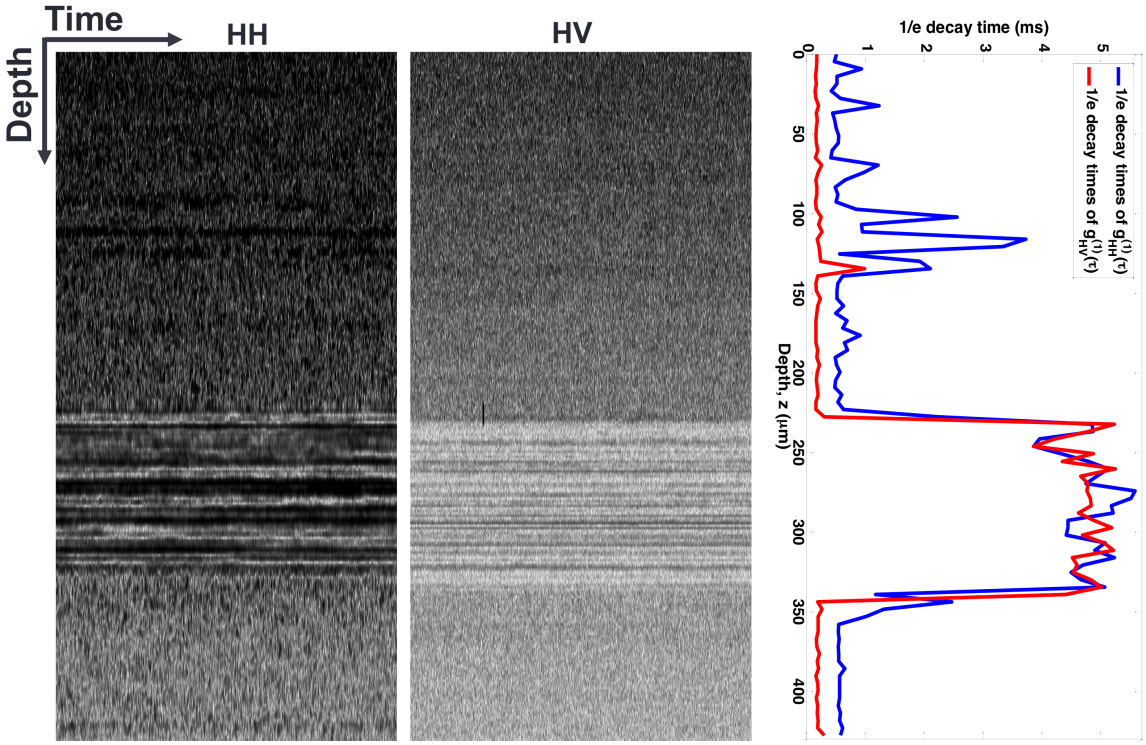

Figure 6.9: PS-OCT M-mode images of MCF10A cells cultured in collagen I:Matrigel ECM in presence of GNRs, and the depth-resolved $\tau_{1/e}$. Axial linerate of 10 kHz and an overall observation time of 1.2 s was used. Note that M-mode data up to 200 ms is shown. The lower $\tau_{1/e}$ cutoff (Nyquist) is 200 μs, whereas the upper $\tau_{1/e}$ cutoff is taken as 60 ms (at least 20 times smaller than the overall observation time). The $\tau_{1/e}$ of $g^{(1)}_{HV}(\tau)$ is at the Nyquist cutoff limit outside the acini, and the $\tau_{1/e}$ of $g^{(1)}_{HH}(\tau)$ in the acini is well below the upper $\tau_{1/e}$ cutoff of 60 ms.

were acquired over the region containing the acinus (figure 6.9), which shows shorter temporal intensity streaks in the ECM and a comparatively longer temporal intensity streaks at the location of the acinus. The intensity fluctuations in the ECM is due to the diffusion of GNRs, whereas that in the acinus is due to the endogenous scattering fluctuations from the cells and the cellular activities in the acinus. To quantify the diffusing GNRs and the endogenous scattering from the acinus, $g^{(1)}_{HH}(\tau)$ and $g^{(1)}_{HV}(\tau)$ were computed and averaged over 3 pixels in z (4.65 μm) throughout the M-mode images shown. The corresponding $\tau_{1/e}$of $g^{(1)}_{HH}(\tau)$ and $g^{(1)}_{HV}(\tau)$ plotted as a function of

depth (figure 6.9) show a clear demarcation of the acinus and the surrounding ECM. Additionally, the GNRs diffusing in the ECM pores show a distinct rapid $g^{(1)}_{HV}(\tau)$ and a comparatively slower $g^{(1)}_{HH}(\tau)$ decay (*i.e.*, $\tau_{1/e}$ of $g^{(1)}_{HV}(\tau) < \tau_{1/e}$ of $g^{(1)}_{HH}(\tau)$), whereas inside the acini, both $g^{(1)}_{HH}(\tau)$ and $g^{(1)}_{HV}(\tau)$ are observed to have comparable decay rates.

The depth-resolved $\tau_{1/e}$ also reveal a small region above the acinus where $g^{(1)}_{HH}(\tau)$ has a longer decay rate compared to the surrounding ECM. The $\tau_{1/e}$ of $g^{(1)}_{HV}(\tau)$ is also observed to be smaller than the $\tau_{1/e}$ of $g^{(1)}_{HH}(\tau)$ in this region, which is indicative of scattering as a result of diffusing GNRs. This region thus corresponds to a region in the ECM where the diffusing GNRs are under increased hinderance from the ECM scaffolds and possibly also the MCF10A cells in the vicinity. PS-OCT M-mode imaging and the depth-resolved autocorrelations are thus seen as excellent tools in probing GNRs diffusion as well as speckle fluctuations resulting from other motile activities in a biological environment.

6.2 GNRs in *in vitro* hBE mucus

Mucus is a viscoelastic gel comprised primarily of water (∼95% in healthy state) and mucins (complex glycoproteins secreted by goblet cells of the airway epithelium), as well as non-mucin proteins, cell debris, lipids, DNA, actin filaments and salts [115, 116]. Mucus plays a critical role in protecting the respiratory epithelium from inhaled pathogens, particulates, and toxic chemicals. The primary airway defense mechanism, called mucociliary clearance, involves trapping of the inhaled particles by a mucus layer lining the airways, and the continuous clearing of the trapped particles by ciliary beating [117]. Normal mucociliary clearance is hindered in respiratory diseases such as cystic fibrosis (CF) and chronic obstructive pulmonary disease (COPD) which results in more viscous, thicker-layered mucus due to reduced solvent content (in CF) and/or increased mucin content (in COPD). Lack of normal mucociliary function, more viscous & thicker-layered

mucus presents a favorable environment for bacterial growth and thus exacerbates airway infection [118], eventually resulting in bronchiectasis (anatomical changes to the bronchial airway including thickening, herniation, dilation and increased tortuosness) [119]. The anatomy of lung airways studied using OCT and corresponding histology shows corrugated inner linings in the CF airways due to the deterioration of the protective epithelial layer, which is in sharp contrast to a smooth morphology observed in normal airway (figure 6.10).

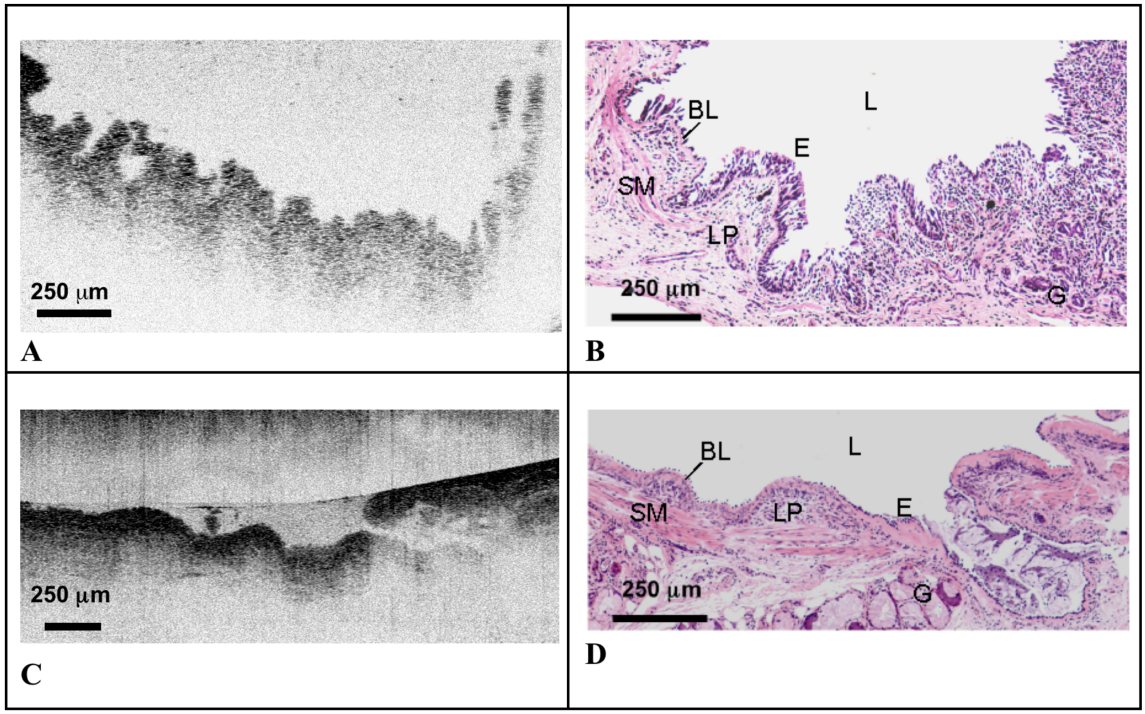

Figure 6.10: B-mode OCT images, and corresponding histological images of lung airways. **A.** CF lung bronchiole showing corrugated inner walls (the airway lumen is above); **B.** Corresponding histology of CF bronchiole using Hematoxylin and Eosin (H&E) stains; **C.** Normal lung airway with a smoother appearance (the airway lumen is above); **D.** Corresponding histology of the normal bronchiole using H&E stains. (Exposure time of 100 μs used for B-mode imaging of CF bronchiole, and 190 μs used for normal bronchiole [51].
L: Lumen, BL: Basal Lamina, E: Epithelium, LP: Lamina Propria, SM: Smooth Muscle, G: Gland.

Mucociliary clearance is an essential host defense mechanism for the maintenance of

normal function and health of lung airways. Besides trapping harmful and toxic particles, this clearance mechanism also efficiently traps and clears conventional particle-based-drug/gene delivery vehicles by steric obstruction and/or adhesion, which can pose a challenge in devising particles that can effectively deliver drugs and genes to the underlying epithelium of the airway. Recent efforts in synthesizing mucus-penetrating particles have identified low molecular weight PEG (2000 gm/mol) coatings as rendering the particles muco-inert [85, 120]. Additionally, although mucus is viscoelastic in bulk, the diffusing particles at the sub-micron- and nano- scales encounter rheological properties entirely different than that in bulk [121]. Thus, in this thesis, diffusion of muco-inert PEGylated GNRs in *in vitro* hBE (human bronchial epithelial cells) mucus is explored to shed light on nanoscale diffusion in mucus.

6.2.1 GNRs diffusion vs mucus concentration

Mucus studied in this thesis was derived from well-differentiated *in vitro* hBE cultures maintained at an air-liquid interface (ALI) [117, 122]. Diffusion of GNRs in both purified mucus (*i.e.,* accumulated mucus periodically washed to remove cellular detritus) as well as unperturbed mucus (*i.e.,* maintained at the ALI for several weeks without perturbations besides adding buffered saline) is discussed. Previous studies have correlated increased mucus concentration beyond the normal range ($\sim$2% solids) [117] with the pathogenesis of airway diseases [123, 124]. The concentration of mucus (% solid) studied in this thesis thus covers the physiological range from normal to diseased. Mucus concentration in % solid is the the ratio of the total mass of solids (including the salt content in the solvent) in mucus to the mass of mucus. To study diffusion of GNRs, PEGylated GNRs (size: 83 ± 7 nm, 22 ± 3 nm) were diffused in the mucus samples and M-mode PS-OCT was carried out at a sampling rate of 25 kHz using a sample power of $\sim$3 mW.

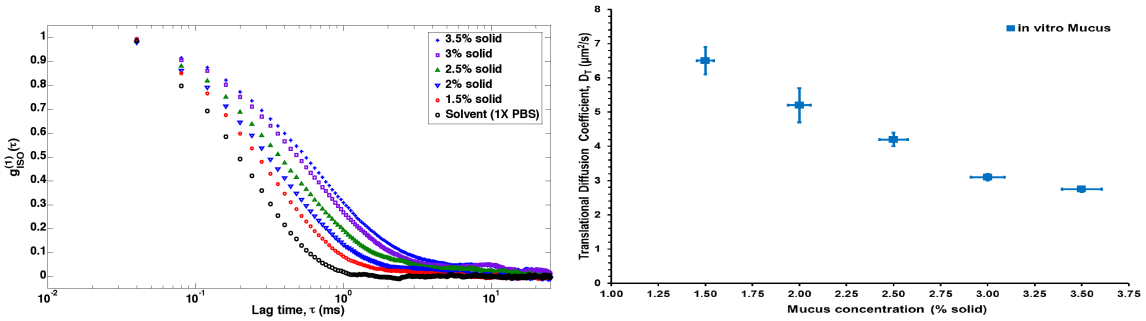

Figure 6.11: $g^{(1)}_{ISO}(\tau)$ and D_T in purified *in vitro* hBE mucus at various concentrations. D_T of GNRs decreases with mucus concentration (% solid).

$g^{(1)}_{ISO}(\tau)$ of GNRs and the corresponding D_T of GNRs in purified *in vitro* hBE mucus in the concentration range of 1.25% to 3.5% are shown in figure 6.11. As a reminder, the reported D_T for the ensemble of GNRs represent an "on average" estimate between the timescale of $\tau = 0$ and $\tau_{1/e}$, which assumes the viscous drag as the dominant force behind the diffusion of GNRs and thus ignores any non-viscous contributions to the autocorrelations, if any, during that duration. At all mucus concentrations, the rotational diffusion of GNRs was too fast to resolve at the sampling rate of 25 kHz, whereas the translational diffusion of GNRs is observed to decrease monotonically with an increase in mucus concentration over the measured concentration range. Compared to the diffusion of GNRs in the solvent (phospate buffered saline, D_T of 9.5 ± 0.2 μm^2/s), the measured diffusion rate of GNRs is only slowed less than 3-fold, which suggests that although mucus is a viscoelastic gel in bulk, at the lengthscale of the GNRs, it behaves more like a viscous fluid with the mucus macromolecules presenting intermittent hindrance to the diffusing nanoparticles. This suggests that GNRs with a non-adherent PEG surface coating are able to rapidly and efficiently percolate through the mucus barrier due to their small size. This is consistent with findings that mucus is a selectively permeable barrier whose trapping & clearance mechanism also depends on the size of the penetrating particle [125]. Rapidly mucus-penetrating particles such as the GNRs are relatively

less susceptible to rapid mucociliary clearance and thus can potentially achieve improved airway distribution and longer retention *in vivo*. GNRs thus hold tremendous potential in nanoparticle-based drug delivery applications where rapid navigation through the mucus barrier is necessary.

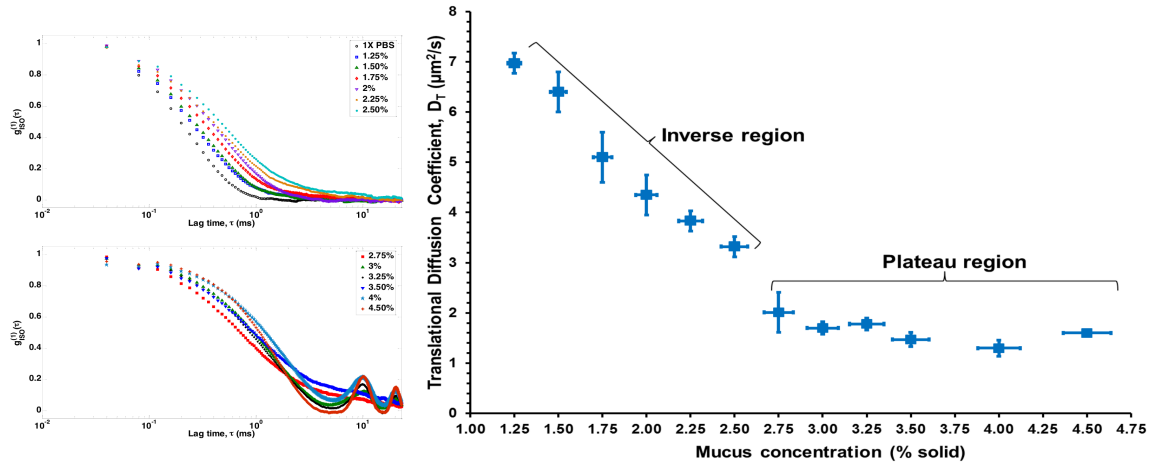

Figure 6.12: $g^{(1)}_{ISO}(\tau)$ and D_T in unperturbed *in vitro* mucus at various concentrations. D_T of GNRs scales inversely with mucus in the 1.25% - 2.5% concentration range (inverse region), whereas beyond 2.75% mucus concentration, D_T of GNRs reaches a plateau (plateau region). Note that the measured D_T values are well above the minimum measurable D_T of 0.035 μm^2/s (based on figure 5.7).

$g^{(1)}_{ISO}(\tau)$ and the corresponding D_T of GNRs were also evaluated for unperturbed mucus in the 1.25% to 4.75% concentration range (figure 6.12). Between the mucus concentrations of 1.25% and 2.50%, D_T of GNRs is observed to scale inversely with mucus concentration (Inverse region, figure 6.12). However, above a mucus concentration of 2.75%, D_T of the GNRs is observed to reach a plateau and no longer scales inversely with the mucus concentration (Plateau region, figure 6.12). In the inverse region, GNRs still suffer intermittent hindrance from the polymers in the mucus as the measured D_T are smaller than that in the solvent (9.5 $\pm$ 0.2 μm^2/s). The plateau region depicts diffusion slower than that in the solvent by ~7-fold only, so it can be inferred that the GNRs in this region are still probing the solvent in the mucus with increased hindrance

from the polymers and cellular debris in the mucus. However, the plateauing of D_T above 2.75% mucus concentration suggests the presence of mucus mesh comparable to the lengthscale of the GNRs at these concentrations. This important result sheds light on nanoscale diffusion in mucus as a function of mucus concentration, and also hints that the mucin content in purified vs unperturbed mucus might be different since no plateauing of measured D_T was observed with purified mucus (figure 6.11).

6.2.2 GNRs in *in vitro* mucus over ALI culture

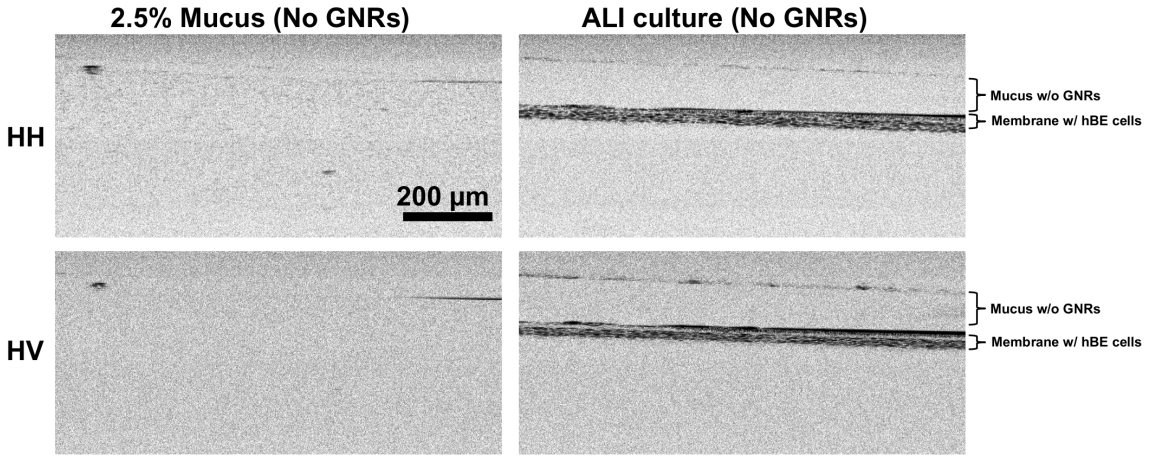

Figure 6.13: B-mode PS-OCT images of *in vitro* mucus (2.5% solids) and hBE ALI culture. Mucus shows negligible scattering in both *HH* and *HV* channels. The ALI culture is visible in both polarization channels, and a thin mucus layer is also discernible from the scattering at the top surface.

The ability to measure particle diffusion in mucus that is being cleared by underlying ciliary motion affords researchers an opportunity to probe mucus in their native state as opposed to the stationary state. To that effort, diffusion of GNRs was estimated for a mucus sample (2.5% solids) over an ALI culture. First, flow in the ALI cultures were confirmed by the directed transport of cellular debris under a microscope, and was estimated to be $\sim$20 μm/s from temporal B-mode scans using 490 nm diameter polystyrene beads as fiducial markers added to mucus. B-mode PS-OCT images of mucus without

GNRs shows negligible contrast in both co- and cross- polarized channels, whereas the layer of hBE cells in the ALI culture is visible in both polarization channels (figure 6.13). After the addition of GNRs to the mucus (2.5% solids), strong backscattering is observed in both polarization channels (figure 6.14). D_T of GNRs in the stationary state of mucus (2.5% solids) outside the ALI culture was measured (5.55 $\pm$ 0.09 μm^2/s), upon which this GNRs-loaded mucus sample was topically added to the ALI culture. Typically, the underlying ciliary motion begins transporting the mucus within a few minutes of loading, and thus D_T of GNRs in mucus (2.5% solids) over the ALI culture was measured after allowing a few minutes for mucus transport. D_T of GNRs in mucus over the ALI culture (5.6 $\pm$ 0.1 μm^2/s) was observed to match the earlier stationary state measurement (5.55 $\pm$ 0.09 μm^2/s). Mucus flow was thus observed to not affect the diffusion of GNRs measured over the transporting ALI culture which can be explained by these two factors: (i) the PS-OCT M-mode imaging was performed over an observation time of 480 ms, and the mucus flow in the ALI culture in that duration corresponds to a displacement of $\sim$10 μm in the transverse direction, which is smaller than the transverse resolution of the system ($\sim$12 μm), and (ii) the flow of the mucus was predominantly in the transverse direction and negligible in the axial direction. Also, $\tau_{1/e}$ of $g^{(1)}_{ISO}(\tau)$ was measured to be 0.406 $\pm$ 0.009 ms, and within this time the MSD of GNRs is estimated to be $\sim$2270 nm^2. Interestingly, no change in measured D_T was observed as a function of distance from the periciliary layer (PCL), suggesting that the diffusion of GNRs within the timescale of the measurement was insensitive to the ciliary activity near the PCL. Thus, it can be inferred that the GNRs at all depths were probing the solvent in the mucus pores with intermittent hinderance from the macromolecules in the mucus and with insignificant perturbation from the ciliary activity within the timescale of the measurement.

The presence of GNRs in the mucus over the ALI culture was also seen to distinctly

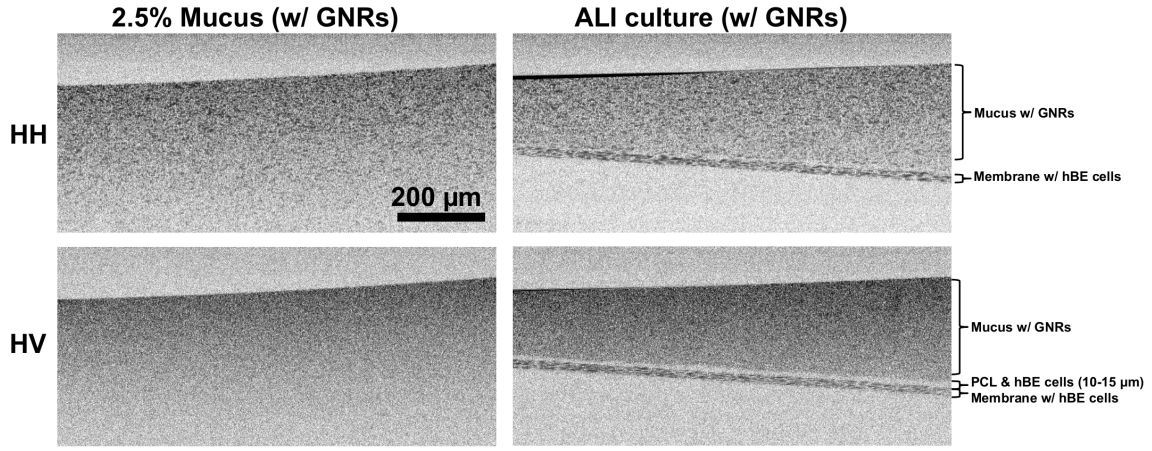

Figure 6.14: B-mode PS-OCT images of *in vitro* mucus (2.5% solids) and hBE ALI culture in presence of GNRs. Strong polarized scattering from GNRs in the mucus is visible in both *HH* and *HV* channels. A thin region above the cells in the ALI culture is also negatively contrasted in the *HV* polarization channel, which corresponds to the PCL layer. The height of the PCL layer is estimated to be ∼10-15 μm.

show a thin region of negative contrast above the hBE cells in the cross-polarized image (figure 6.14). This region corresponds to the known position of the PCL and its height is estimated from the B-mode PS-OCT image to be ∼10-15 μm, which is slightly larger than previously reported estimates [120]. The lack of cross-polarized scattering in the PCL suggests that the GNRs are excluded from this region despite their small size and elongated shape. The airway surface morphology has long been thought of as a mucus layer sitting atop a watery periciliary layer based on the gel-on-liquid model [126, 127]. However, recent evidence suggests that the PCL consists of a dense brush of macromolecules tethered to the cilia and the epithelium (gel-on-brush model) [117], which may explain the observed exclusion of GNRs from the PCL layer despite having a smaller size compared to the reported interciliary space of ∼200 nm [117].

M-mode PS-OCT images of mucus with GNRs over the ALI culture were also acquired (figure 6.15), which qualitatively shows shorter temporal intensity streaks in the mucus due to the diffusing GNRs, and a comparatively longer temporal intensity streaks

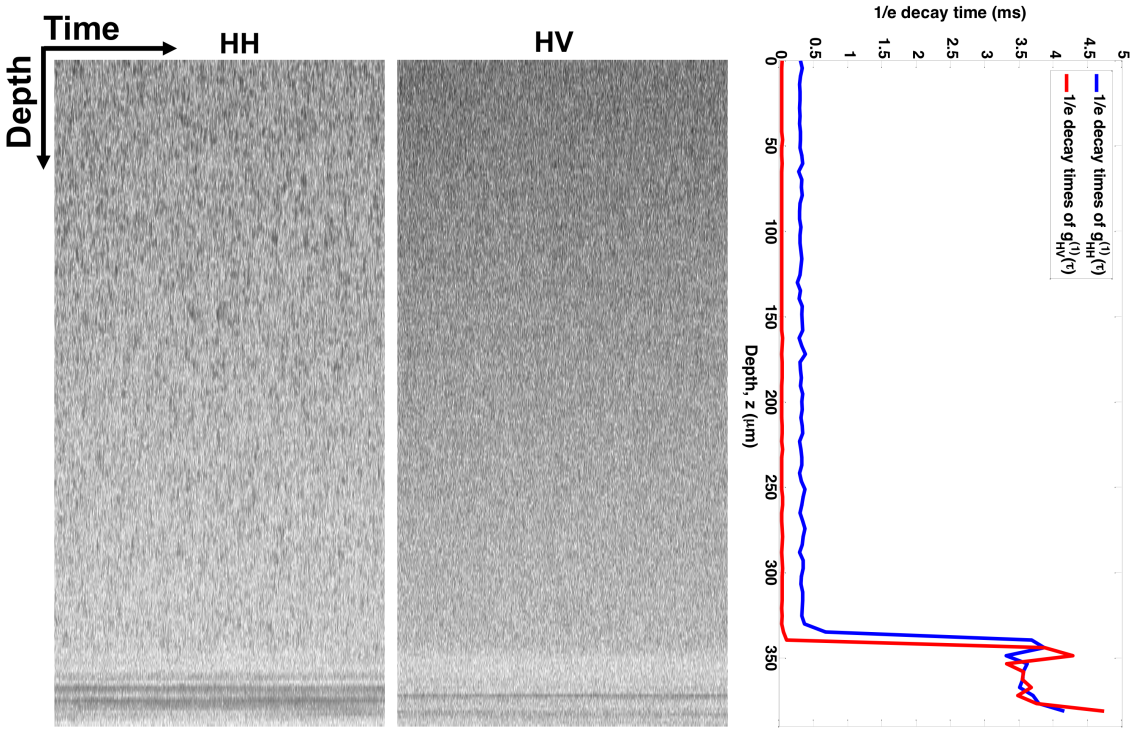

Figure 6.15: PS-OCT M-mode images of mucus with GNRs over an ALI culture, and the depth-resolved $\tau_{1/e}$. Axial linerate of 25 kHz and an overall observation time of 480 ms was used. Note that M-mode data up to 80 ms is shown. The lower $\tau_{1/e}$ cutoff (Nyquist) is 80 μs, whereas the upper $\tau_{1/e}$ cutoff is taken as 24 ms (at least 20 times smaller than the overall observation time). The $\tau_{1/e}$ of $g^{(1)}_{HV}(\tau)$ is at below the Nyquist cutoff limit in the mucus, and the $\tau_{1/e}$ of $g^{(1)}_{HH}(\tau)$ in the PCL, cell layers, and the membrane is below the upper $\tau_{1/e}$ cutoff of 12 ms.

underneath the mucus layer, which results from endogenous scattering from the ciliary activity in the PCL, the hBE cells and the membrane. To quantify the diffusion of GNRs and the endogenous scattering, $g^{(1)}_{HH}(\tau)$ and $g^{(1)}_{HV}(\tau)$ were computed and averaged over 3 pixels in z (4.65 μm) throughout the M-mode images shown. The corresponding $\tau_{1/e}$of $g^{(1)}_{HH}(\tau)$ and $g^{(1)}_{HV}(\tau)$ plotted as a function of depth (figure 6.15) show a clear demarcation of the GNRs diffusing in the mucus and the GNRs-excluded region underneath the mucus. The GNRs diffusing in the mucus show a distinct, rapid $g^{(1)}_{HV}(\tau)$ decay and a comparatively slower $g^{(1)}_{HH}(\tau)$ decay, whereas in the GNRs-excluded region, both $g^{(1)}_{HH}(\tau)$ and $g^{(1)}_{HV}(\tau)$ are observed to have similar decay rates. These results show the utility of

PS-OCT M-mode imaging and depth-resolving of autocorrelations for simultaneously probing the diffusion of GNRs and speckle fluctuations resulting from motile activities.

The study of GNRs diffusion presented in this section has implications in understanding the semi-permeable nature of mucus in trapping or allowing passage of exogenous agents (viruses, drug delivery probes). Although no comparison between the diffusion of nano-probes based on the shape has been presented in this thesis, it can be argued that GNRs, due to their shape anisotropy, might stand a better chance of percolating through the mucus mesh than a spherical shaped probe with the same hydrodynamic diameter. Current efforts in synthesizing mucus-penetrating particles have focused on surface chemistry and the size of the probes, but the shape of the probes might also play a vital role in efficient permeation through the mucus mesh. Additionally, PS-OCT imaging of GNRs in mucus over a transporting ALI culture elucidates the defense mechanism of PCL against nanoscale particles, and the observed exclusion of GNRs in the PCL lends credence to the recently proposed gel-on-brush model of airway surface.

6.3 OCT Imaging: 3D epithelial-fibroblast cultures

This section presents an imaging study of breast cancer 3D cultures using the custom-designed OCT system. The text of this section has been reprinted from the author's manuscript, "R. K. Chhetri, Z. F. Phillips, M. A. Troester, A. L. Oldenburg, Longitudinal Study of Mammary Epithelial and Fibroblast Co-Cultures Using Optical Coherence Tomography Reveals Morphological Hallmarks of Pre- Malignancy, PloS one **7**:1-7, 2012."

6.3.1 Introduction

The human mammary gland consists of a series of branching ducts, with each branch terminating as a hollow and spherical acinus. Each acinus is predominantly comprised of luminal epithelial cells surrounded by basal/myoepithelial cells, but is supported and regulated by an intricate network of other cell types. Chemical and physical interactions between epithelia and surrounding stroma are essential for the organ's development and physiological functions. This intricate network of cells is a complex microenvironment [128] that maintains normal tissue architecture (homeostasis) and suppresses malignant phenotypes in healthy individuals [129], but becomes permissive or even promotes cancer during progression [98]. Thus, interactions between mammary epithelial cells (MEC) and stromal fibroblasts are regulators of tumorigenesis [98, 113], with stroma playing a vital role in the proliferation and organization of MEC, production of extracellular matrix (ECM), and regulation of cellular adhesion and migration [98].

Fibroblasts are strongly associated with mammary epithelium, and in the vicinity of tumors, become a major cell type of the stroma [107]. These cancer-associated fibroblasts appear to promote tumor growth and facilitate the progression of breast cancer [110]. Conversely, normal fibroblasts may inhibit progression of cancer [130]. Our previous studies have illustrated that fibroblasts have distinct interactions with breast cancer subtype [131], with aggressive basal-like breast cancer cells [132] interacting with fibroblasts to produce a wide range of growth factors and cytokines that may in turn promote migration and/or proliferation of the cancer cells. However, the evolution of these interactions during breast cancer progression has not yet been well characterized. By comparing normal and pre-malignant MEC co-cultured with RMF in 3D, and by modulating the ratios of the two cell types, we aimed to elucidate how stromal-epithelial interactions modulate morphological changes in acini.

Our previous studies on interactions between breast cancer cells and fibroblasts have

relied on 2D cultures [131], but 3D co-culture models offer an interface between these studies and *in vivo* studies given their ability to recapitulate several aspects of tissue behavior [104, 99, 100]. Novel tools that image the 3D breast microenvironment can elucidate micron-scale morphological changes during the dynamic chemical and physical signaling processes between mammary cell types. To date, a majority of the studies of stromal-epithelial co-cultures have utilized imaging techniques that require sample fixation and often sectioning [133], which can perturb the native architecture and present challenges for longitudinal studies. To address these limitations, optical coherence tomography (OCT), which can assess cellular dynamics in 3D tissue models [134], was employed to non-invasively capture the 3D architecture of breast tissue models.

OCT represents an emerging medical and biological optical imaging modality [36, 135, 136, 31], that performs cross-sectional imaging of internal microstructures in tissues by measuring the magnitude and echo time delay of backscattered, near-infrared light. OCT provides micron-scale resolution for cellular imaging, and rejects multiply scattered light, unlike confocal microscopy, which enables imaging up to 2-3 millimeters in depth. This depth is ideal for assessing subsurface structures such as 3D tissue cultures [134].

Simultaneously, the non-invasive nature of OCT enables longitudinal studies in the same samples, avoiding the need to excise and process tissue specimens [137]. Recent studies have demonstrated the feasibility of OCT to provide image-guidance by scanning tumor margins during breast-sparing surgery [37, 38], and to identify invasive breast carcinomas in biopsy tissue [138]. OCT imaging has also been employed on unstained, *ex vivo* breast cancer tissues to identify morphological features, similar to histology [139, 140]. Additionally, computational methods to perform pattern analysis of OCT biopsies have been implemented to identify invasive breast carcinomas [141, 142]. Thus, OCT has translational potential with applications in basic studies and *in vivo* clinical imaging. As such, OCT imaging offers a unique platform for evaluating the architecture

of MEC grown in 3D co-cultures.

The aim of this study was to define morphological hallmarks of stromal-epithelial interactions using OCT to assess 3D *in vitro* cultures comprised of basal-like mammary epithelial cell lines (normal MCF10A, and pre-malignant MCF10DCIS.com) [143] and hTERT-immortalized fibroblasts from reduction mammoplasty (RMF). As shown below, we found distinct morphological features between acini formed by normal MCF10A cells and pre-malignant MCF10DCIS.com cells as a function of fibroblast concentration.

6.3.2 Method

Cell lines:

MCF10A and MCF10DCIS.com cells were obtained from the Barbara Ann Karamanos Cancer Institute (Detroit, MI). MCF10A cells are spontaneously immortalized MEC derived from the human breast tissue of a 36-year-old patient [144], and exhibit numerous features of normal breast epithelium including lack of tumorigenicity and dependence on growth factors and hormones for proliferation and survival [144]. Importantly, MCF10A cells in 3D cultures form stable acinar structures recapitulating the behavior of glandular epithelium seen *in vivo* [112]. MCF10DCIS.com cells are cloned from xenograft lesions of MCF10A and form DCIS-like lesions [145]. Importantly, MCF10DCIS.com cells have the same genetic background as the MCF10A, and are primed for invasive transition under key microenvironmental conditions, requiring no additional genomic changes to become invasive [145]. The MCF10A and MCF10DCIS.com cells were co-cultured with hTERT-immortalized fibroblasts from reduction mammoplasty (RMF), a gift from Charlotte Kuperwasser at Tufts University [146]. All cells used in this experiment were maintained prior to use in 2D cultures in Dulbecco's Modified Eagle Medium/Nutrient Mixture F-12 (DMEM/F12) containing 5% horse serum, 20 ng/mL Epidermal Growth Factor (EGF), 0.5 μg/mL hydrocorti-

sone, 100 ng/mL cholera toxin, 10 μg/μL insulin, and 1% penicillin-streptomycin, and kept in a humidified incubator at 37°C and 5% CO_2 [99].

3D Culture Preparation:

The 3D extracellular scaffold used in this study consisted of biologically derived collagen I and Matrigel® (BD Biosciences). Compared to collagen I gels, Matrigel-collagen I gels were found to be structurally more stable and thus less prone to loss over the duration of the study due to several cycles of media replenishments, as has been previously noted [114]. For 3D cell culture, a Matrigel-collagen I mixture was prepared on ice using a 1:1 volume ratio, with collagen I at a concentration of 1 mg/mL, according to procedures described by Johnson *et al.* [101]. Once the MEC and RMF were nearly 100% confluent in 2D, they were seeded at varying concentrations into the Matrigel-collagen I gel for growth in 3D, as follows: A total of 27 3D cultures were prepared, which included 9 co-cultures of normal MEC and RMF, 9 co-cultures of pre-malignant MEC and RMF, and 3 monocultures each of normal MEC, pre-malignant MEC, and RMF. Briefly, the following protocol was used for all co-cultures. 85 μL of Matrigel-collagen I was used to coat the bottom of 10 mm diameter tissue culture microwells, and was allowed to solidify for 30 minutes at 37°C. Then, 180 μL of Martrigel-collagen I gel was mixed with MEC and RMF according to procedures described in [131] to obtain the desired final seed concentrations. The seed concentrations of MEC and RMF in the Martigel-collagen I gels were varied as 30,000 cells/cm^3, 90,000 cells/cm^3, 270,000 cells/cm^3 and control, and were plated and allowed to solidify for 30 minutes at 37°C. After gelation, 250 μL of growth media (same as in 2D cultures above) was applied to the surface of each 3D culture. Cultures were maintained under optimum growth conditions (humidified, 37°C with 5% CO_2) for 2-4 weeks, during which the medium was changed every 2-3 days.

Although the co-cultures were maintained for 4 weeks (Figure 6.22, Table 6.1), proliferation of the cells in the co-cultures was no longer in the log-phase of growth after week 2, as evidenced by a plateau in the number of MEC per acinus (Figure 6.23). Similarly, co-cultures with higher seeded cell concentration (MEC concentration $> 90{,}000/\text{cm}^3$) also remained in log-phase for only a short time (Figure 6.23). We selected only mono-cultures and co-cultures that were still in log-phase to avoid artifacts in morphology caused by resource scarcity or cellular crowding.

OCT Imaging:

Imaging of the 3D cultures was performed using a custom, ultrahigh-resolution, spectral-domain optical coherence tomography (SD-OCT) system as described in detail previously [147]. The OCT system employed a low-coherence light source consisting of a Ti:Sapphire laser (Griffin, KMLabs, Inc.) with a central wavelength of 800 nm and a bandwidth of 125 nm. A detailed description of the OCT system and the system diagram is provided in the supplementary (subsection 6.3.5, figure 6.19). The axial (depth, z) resolution of the imaging system owing to the wavelength and the bandwidth of the light source is 3 μm in air. In the sample arm, 3D cultures were illuminated by a 10 mW beam focused by a 30 mm focal length achromatic lens, which provides a resolution of 12 μm (air) in the transverse (x and y) directions. Transverse raster-scanning over the sample was achieved using galvanometer-controlled mirrors. OCT imaging was performed on each of the live 3D cultures weekly for 4 weeks. OCT image-stacks were acquired over $3\times1.5\times1.5$ mm (in gel) into $1000\times101\times1024$ pixels (x, y, and z dimensions respectively) with an acquisition time of 40 ms per $x-z$ image. The OCT image-stacks were resampled into an isotropic pixel resolution of 1.55 μm after correcting for the refractive index of the aqueous gels, and are logarithmically scaled and displayed in a hot color map using MATLAB® (2011a, MathWorks).

Image Analysis:

2D analysis of OCT images was performed to determine the maximum acinar and lumen areas. From the color-mapped OCT images, cell clusters resembling acini were selected as shown in figure 6.16A. The OCT image containing the central position of each acinus was determined by sifting through the OCT image-stack to find the image with the largest acinus size. The overall acinus area (cells plus lumen) and lumen area were segmented within these central OCT images using ImageJ, as shown in figure 6.16B. The results were tabulated for each culture, from which the mean acini area, mean lumen area, and their associated standard errors were evaluated.

As depicted in figure 6.16C and figure 6.16D, iso-surface rendering of the OCT image stacks enables visualization of the entire 3D acinar structure. In order to quantify the 3D morphology of the acini, we computed the asphericity, that is, the deviation in acini shape from that of a perfect sphere. We defined asphericity as the ratio between the volume of a perfect sphere having the same surface area as that of the acinus, S_{acini}, and the measured volume of each acinus, V_{acini}, according to [148]:

$$\text{Asphericity} = \frac{(S_{acini})^{3/2}}{3 \times (4\pi)^{1/2} \times V_{acini}} \tag{6.1}$$

where S_{acini} is in pixels^2, and V_{acini} is in pixels^3. Asphericity is equal to 1 for a perfect sphere and increases for irregularly shaped objects. Thus, asphericity provides a size-independent measurement of how aspherical a 3D structure is, which aids in quantifying surface irregularities across renderings of various sizes.

To compute V_{acini}, OCT images were first median filtered, and a 3D mask of each acinus was obtained by thresholding the OCT image stack. Then, the 'bwboundries' command in MATLAB was applied to each 2D image in the stack to find the boundaries of thresholded objects and to "fill in" any child objects, such as the lumen. Subsequently,

stray objects that did not have any voxel overlap with the acini were removed from the 3D mask, to obtain just the acini. The volume, V_{acini}, was then computed by counting the voxels comprising the mask. Using simulated data with known geometries, it was verified that this method accurately estimated the volume of the 3D rendered object.

To compute S_{acini}, the voxels comprising the boundary of the 3D mask were counted. Due to digitization noise, a pixelation correction factor of 1.5 was needed to obtain the correct value of surface area, which corrects for pixel connectivity. This was determined in MATLAB by comparing the measured surface area to the actual surface area of spheres and ellipsoids. Above a radius of 15 pixels and for values of asphericity from 1-8, the pixelation correction factor converged to 1.5; all acini analyzed in this study had radii and asphericities within these valid ranges.

6.3.3 Results

OCT offers excellent visualization of cellular acini, as shown with representative OCT $x-z$ images of the cell cultures in 3D matrices at 1 week (Figure 6.16A). Representative images in all 3D cultures at weeks 1 and 2 can be seen in supplementary (Figures 6.20 and 6.21). At week 1, the MEC organize into spherical clusters (acini) with some clusters showing signs of a lumen at the center (Figure 6.16B, representative example). At week 2, the acini are observed to have grown in size, displaying larger and more distinct central lumens. The control gel with no cells shows a homogeneous Matrigel:collagen I structure, which was stable throughout the duration of the study. As expected, no spherical clusters were observed in RMF monocultures. Instead, RMF monocultures revealed a fibrous optical scattering pattern characteristic of fibroblasts. As the RMF concentration was increased, a higher density of fibrous structures was observed, corresponding to added rigidity of the matrix.

OCT images of co-cultures reveal a complex pattern of growth and interaction be-

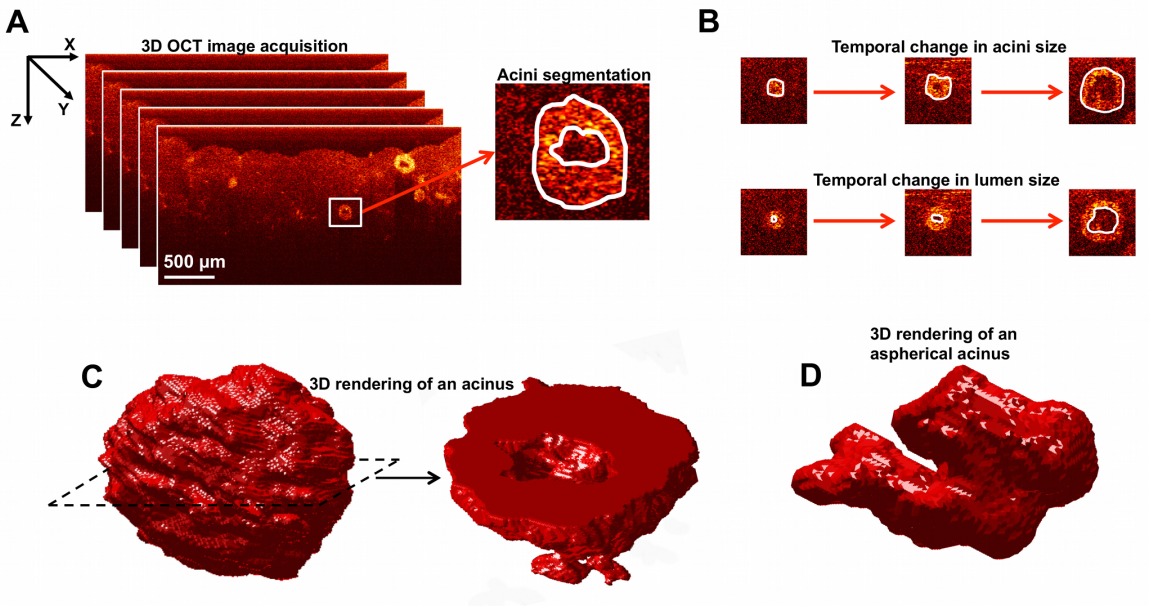

Figure 6.16: **3D-OCT image acquisition of the co-cultures, and analysis of the shape and size of acini. A.** 3D-OCT image acquistion: the surface of the gel is aligned near the top of each image, and the depth-resolved light scattering from cells beneath the gel surface is apparent at depths up to ∼1 mm; segmentation of acini to characterize the overall size and the lumen is also shown. **B.** Temporal changes in acini and lumen sizes analyzed from 3D-OCT images of the co-cultures. **C.** An example isosurface rendering of an acinus from a 3D-OCT image-stack; slicing of the rendered volume clearly shows the lumen. **D.** An example 3D rendering of an aspherical acinus.

tween RMF and the MEC, similar to *in vivo* mammary architecture. Importantly, unlike other techniques that involve slicing, fixing and staining of the gels, these images depict the unperturbed states of the live MEC and RMF *in vitro*. Thus the images were used to measure lumen size, acini size (Figure 6.16B) and to estimate the shape, characterizing cells on a continuum between spherical (*e.g.* in figure 6.16C) and aspherical (*e.g.* in figure 6.16D).

During the first two weeks of the study, both acini and lumen sizes increased (Figure 6.17). In normal MEC, the stromal:epithelial ratio did not impact acini and lumen sizes; co-cultures were seeded with 30,000 MCF10A/cm^3, and as the seed concentration of RMF was increased from 30,000 RMF/cm^3 to 90,000 RMF/cm^3, no significant

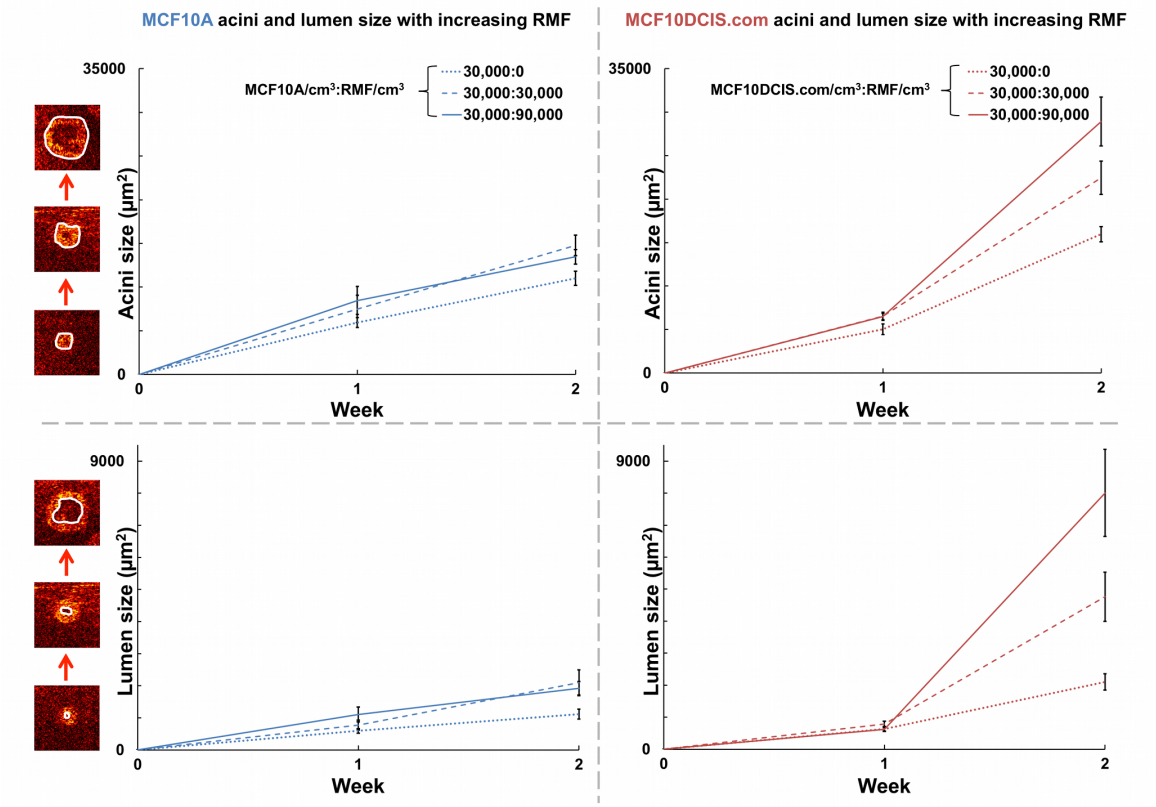

Figure 6.17: **Acini and lumen size.** Comparison of MCF10A:RMF co-cultures with MCF10DCIS.com:RMF co-cultures shows significantly larger acini and lumen sizes (Student's t-test, p-value < 0.005) at week 2. In MCF10DCIS.com:RMF co-cultures, acini and lumen size are also observed to be highly modulated by the ratio of fibroblasts.

difference was seen in acini sizes (Student's t-test, p-value $= 0.43$) or lumen sizes (Student's t-test, p-value $= 0.71$) at week 2. However, the size of pre-malignant MEC acini varied in association with stromal content. In co-cultures seeded with 30,000 MCF10DCIS.com/cm^3, as the seed concentration of RMF was increased from 30,000 RMF/cm^3 to 90,000 RMF/cm^3, statistically significant differences were seen in acini size (Student's t-test, p-value < 0.05) and lumen size (Student's t-test, p-value < 0.05) at week 2. In addition, comparing MCF10A to MCF10DCIS.com acini at week 2, MCF10DCIS.com:RMF co-cultures showed significantly larger acini and lumen sizes across the same seed concentrations (Student's t-test, p-value < 0.005). The stimulatory

effect of increased fibroblast concentration on pre-malignant MCF10DCIS.com suggests unique molecular and/or mechanical interactions that stimulate abnormal growth that are not observed in the MCF10A cells.

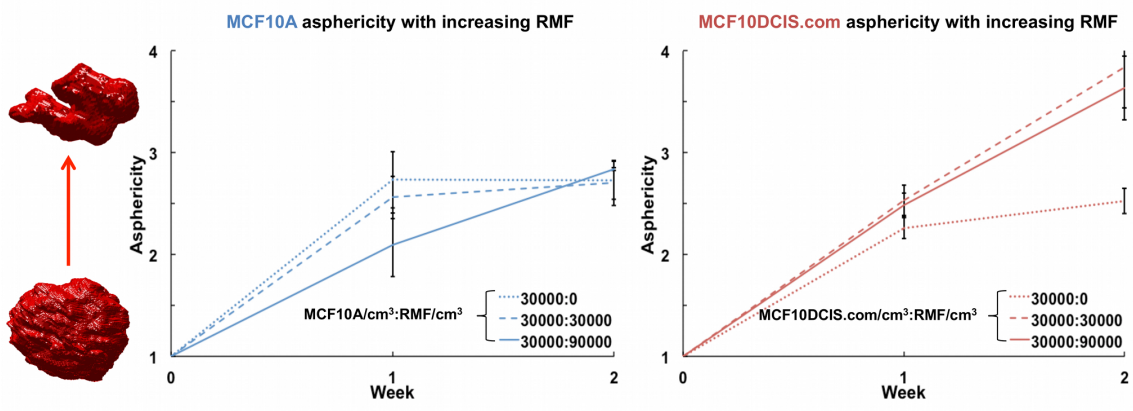

Figure 6.18: **Asphericity of acini.** The minimum asphericity value of 1 indicates a perfect sphere, while less spherical acini have higher asphericity values. Acini comprised of MCF10DCIS.com cells are seen to become increasingly aspherical in the presence of fibroblasts.

In addition to changes in acini and lumen sizes, MCF10DCIS.com cells also responded to co-culture with increasingly aspherical structures. Since asphericity is a size-independent metric, as expected, no significant correlation was found between asphericity and acini or lumen sizes in both MCF10A and MCF10DCIS.com cultures. Figure 6.18 shows the asphericity of the rendered acini in monocultures of MCF10A, MCF10DCIS.com, and co-cultures of these cells with increasing concentrations of RMF (30,000 RMF/cm^3 to 90,000 RMF/cm^3). Again, in normal cells at week 2, fibroblasts did not affect asphericity; monoculture seeded with 30,000 MCF10A/cm^3 and co-cultures seeded with 30,000 MCF10A/cm^3 had similar asphericity values. In contrast, at week 2, the MCF10DCIS.com:RMF co-cultures seeded with 30,000 MCF10DCIS.com/cm^3 had significantly increased asphericity relative to monocultures (Student's t-test, p-value < 0.005). Thus, acini formed by pre-malignant MCF10DCIS.com cells in the presence of RMF undergo a higher degree of shape difference than do acini formed by normal

MCF10A cells. The observed higher asphericity values in MCF10DCIS.com acini compared to MCF10A acini in presence of RMF highlights the role of fibroblasts in varying the morphology of the acini.

In summary, these observations show that fibroblasts differentially modulate the shape and size of acini comprised of pre-malignant and normal MEC.

6.3.4 Discussion

The application of OCT to 3D co-cultures of MEC and RMF provided excellent visualization of acinar development over time and recapitulation of *in vivo* morphologies. Acini formed by MCF10A cells in 3D co-cultures were found to be comparable in size to freshly explanted acini previously reported [112]. Observations of increased acini size, lumen size, and asphericity in pre-malignant MCF10DCIS.com co-cultures compared to normal MCF10A co-cultures, and the distinct influence of fibroblast concentration on these phenotypes, suggest that changes over time in stromal-epithelial interactions in 3D co-culture models can be detected using OCT. Interestingly, while acini morphogenesis in DCIS *in vivo* is typically envisioned as progressive invasion into the lumen by the proliferating carcinoma cells [107], our non-invasive study of live 3D co-cultures revealed no such invasion of MCF10DCIS.com into the luminal spaces. However, the formation of luminal space was expected based on *in vivo* studies, as the MCF10DCIS.com cells are comedo-type DCIS [149]. This reinforces the advantage of using OCT to non-invasively and longitudinally probe the same live co-cultures; traditional techniques require slicing, fixing and staining of repeat co-cultures at each time point, which can perturb the natural state and architecture of the organoids. A previous 3D tissue study in MEC monocultures has identified four distinct breast cell line colony morphologies: round, mass, grape-like and stellate [100]. In that study, MCF10A acini are identified as round. A comparatively gentle treatment of the 3D cultures may account for the ability of this

system to detect morphology reflective of the unique *in vivo* characteristics of comedo-type DCIS. The ability to regularly probe the same samples longitudinally also avoids problems associated with sample-to-sample variability. In addition, OCT enabled rapid collection of volumetric data with a scan time of 90 seconds per culture, which, at the time of the study, was limited by software and has recently been sped to 4 seconds per culture.

Previous research has highlighted differences between mechanical stromal-epithelial interactions (MEC and fibroblasts in physical contact), and chemical stromal-epithelial interactions (MEC and fibroblasts separated by a barrier allowing passage of soluble signals) [131]. Our results further indicated a difference in stromal-epithelial interactions between fibroblasts and normal or pre-malignant MEC, as evidenced by pronounced differences in morphological features. A number of previous studies have demonstrated that co-cultures with DCIS cells can provide interesting insights regarding signaling and phenotypes of malignant progression [150]. Indeed, our co-cultures mirrored many of the phenotypes previously observed in mammary epithelial monocultures [99, 151], while also providing fibroblast-dependent morphological change over time in the same samples. The ability to study phenotypes over time offers the opportunity to study the molecular switches that may regulate or be regulated by the mechanical changes in 3D co-cultures. Only studies of perturbations induced over time will be able to distinguish cause and effect for key molecular effectors such as HGF (hepatocyte growth factor)-signaling [150]. In such studies, the variation of matrix stiffness can be achieved by varying the collagen I concentration in the Matrigel:collagen I mixture [101, 152]. Our current study in a well-characterized, progressive 3D co-culture series, establishes OCT as a convenient platform for such future studies.

Future studies would also benefit from merging longitudinal evaluation of morphology with studies of RNA and protein expression from whole genome microarrays per-

formed using a bioinformatics approach [131]. Previous work by Kenny *et al.* correlated four distinct morphologies of MEC colonies (round, mass, grape-like, and stellate) with gene expression [100], although no data is yet available to show time- or co-cultured fibroblast-dependent morphological changes. Morphological characteristics are likely parallel to molecular phenotypic changes, and an imaging-based biomarker of shifts in molecular phenotype could allow advances in our understanding of the physical and mechanical regulation of molecular signaling. For example, previous xenograft studies have shown that MCF10DCIS.com cells are more invasive than MCF10A cells, and are enriched for expression of lymphangiogenesis markers [153]. These xenografts highlight that the breast cancer microenvironment is comprised of many cell types, and while the fibroblast is a highly abundant stromal cell type, there are many other possible contributors and mediators of the complex paracrine communication in breast tissue. However, the simplified 3D model of MEC and fibroblasts mirrors xenografts in its ability to track acini growth and asphericity, and therefore may be an *in vitro* approach to studying invasive potential.

We also note that the association between premalignant cells and high asphericity observed in this study may be related to previous studies establishing a connection between tissue structural complexity (in a mathematical sense, such as fractal dimension) and various cancers [154, 155, 156]. While asphericity is not a measure of complexity *per se*, acini with a high fractal dimension would be expected to have a high asphericity. Tying the efforts reported here in engineered tissues with OCT imaging and morphological analysis of real breast cancer tissues [38, 138, 141, 142] may lead to new mechanistic insight, and may also translate to clinical OCT imaging efforts, such as those in surgical guidance during breast cancer surgery [37].

6.3.5 Supplementary

OCT System Hardware:

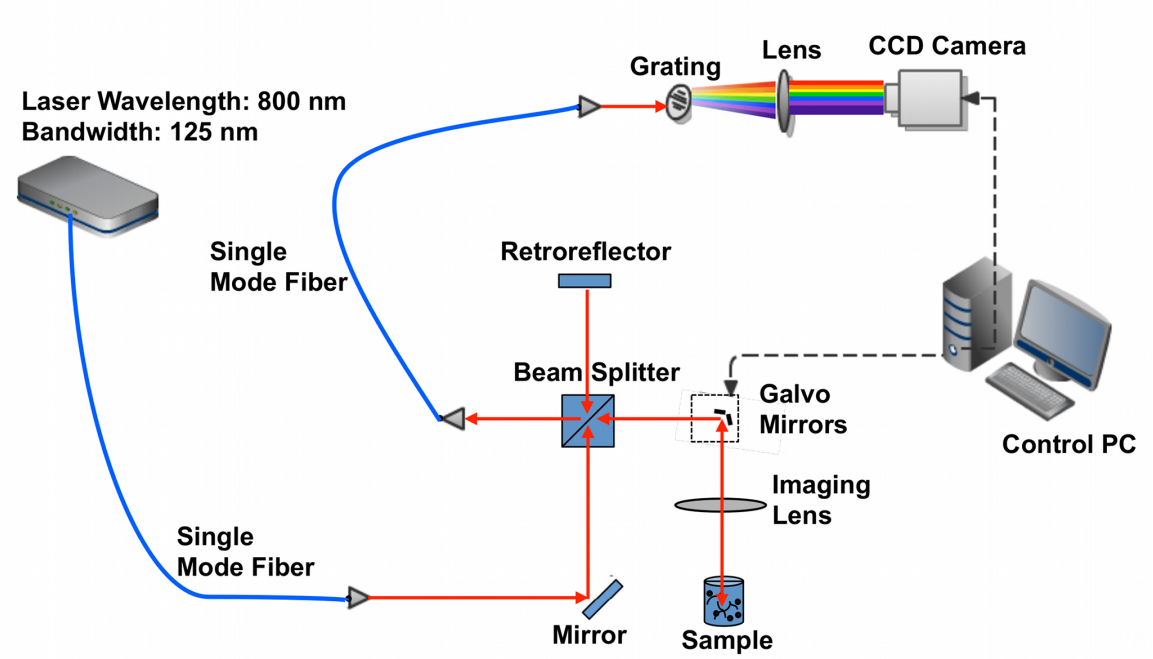

Figure 6.19: **Schematic diagram of the OCT system.** The ultrahigh resolution SD-OCT system is comprised of a Ti:Sapphire laser, a Michelson interferometer, and a high speed spectrometer (details in text). FS: fiber to free-space coupler, SF: free-space to fiber coupler.

Imaging of the 3D cultures was performed using a custom, ultrahigh-resolution, spectral-domain optical coherence tomography (SD-OCT) system which employed a low-coherence light source consisting of a Ti:Sapphire laser (Griffin, KMLabs, Inc.) with a central wavelength of 800nm and a bandwidth of 125 nm. The axial (depth, z) resolution of the imaging system owing to the wavelength and the bandwidth of the light source is 3 μm in air. Single-mode fibers were employed to simplify alignment between the components of the OCT system (laser, interferometer, and spectrometer). The light source was directed into a free-space Michelson interferometer comprised of a stationary reference arm and a sample (imaging) arm. In the sample arm, 3D cul-

tures were illuminated by a 10 mW beam focused by a 30 mm focal length achromatic lens, which provided a resolution of 12 μm (air) in the transverse (x and y) directions. Transverse raster-scanning over the sample was achieved using galvanometer-controlled mirrors. The backscattered light from the sample was collected by the same illuminating lens and interfered with the reference beam at the output of the interferometer. The interfered beam was directed into a custom-bulit spectrometer, which consists of a diffraction grating (600 lines/mm), imaging lens (focal length 200 mm), and a 25 kHz CCD linescan camera (Piranha, Dalsa Inc.). The spectral interferograms recorded by the camera are related to the depth-dependent backscattering potential of the sample via Fourier transformation, as understood for SD-OCT systems [44]. Data processing of the spectral interferogram was performed according to our previously published methods [147] to produce an OCT image with an imaging depth of 2 mm in air.

OCT Imaging results:

Representative OCT images of monocultures and co-cultures at each culture condition are shown in figure 6.20 and figure 6.21 at weeks 2 and 4, respectively. Gels that had higher seed concentrations of MEC and/or RMF were observed to have higher acini counts (Table 6.1) but smaller overall acini sizes (Figure 6.22). This suggests that the acini growth is stunted by higher seed concentrations due to resource scarcity or cellular crowding. To estimate the number of MEC per acinus, the total volume occupied by cells was approximated from the measured acini and lumen areas, A_{acini} and A_{lumen}, and compared to the volume of each MEC, V_{cell}, leading to the following relation:

$$\text{Number of MEC per acinus} = 0.74 \times \left[\frac{\left(\frac{4}{3\sqrt{\pi}}\right) \times \left(A_{acini}^{3/2} - A_{lumen}^{3/2}\right)}{V_{cell}} \right] \tag{6.2}$$

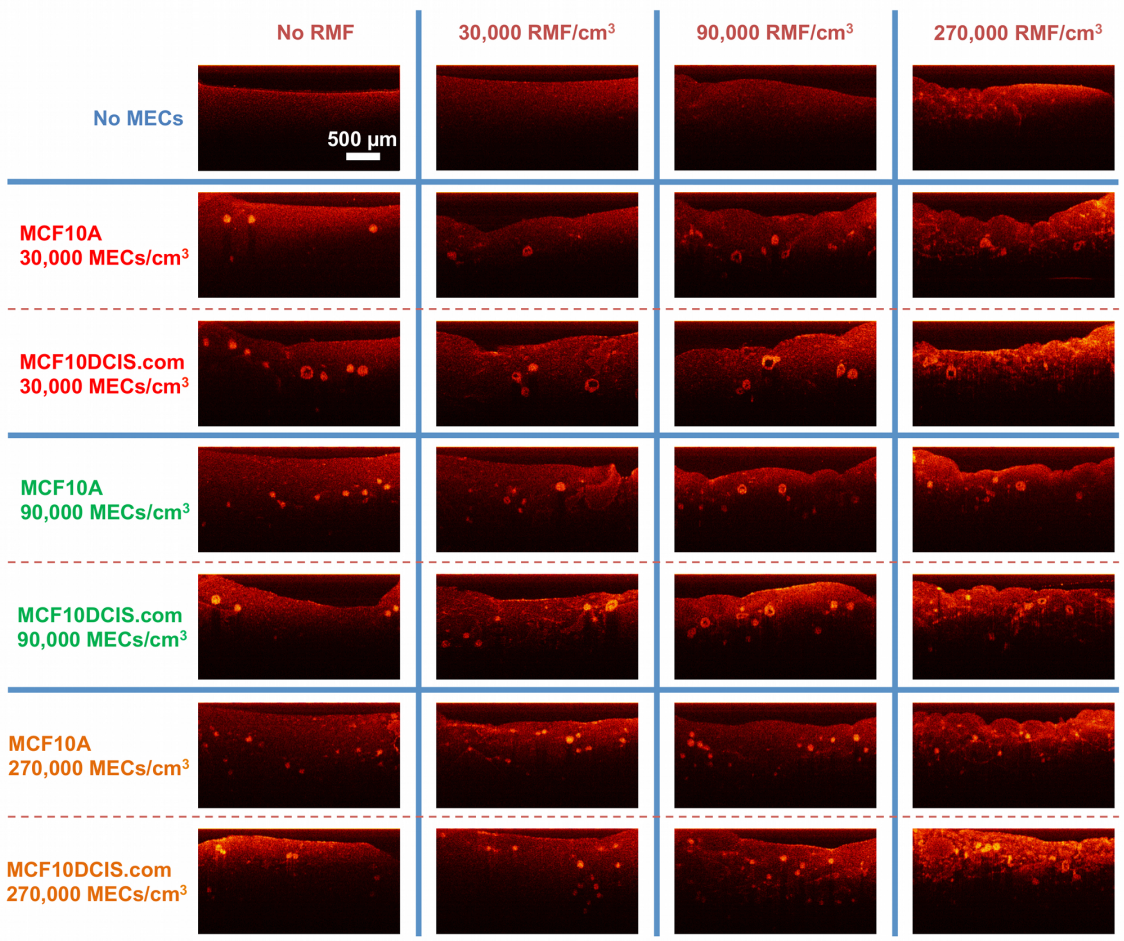

Figure 6.20: **Representative OCT $x-z$ images of 3D human mammary tissue cultures at week 2.** As indicated, the seed concentration of MEC is increasing from top to bottom, and the seed concentration of RMF is increasing from left to right.

where 0.74 is the volume packing fraction for spheres, and the MEC were approximated to be spherical. The individual MEC were found to have an average radius of 4.37 μm from fluorescent images of acini in the co-cultures, resulting in an estimation of V_{cell} as 350 μm^3. Thus the number of MEC per acinus was computed by dividing the total volume occupied by MEC by the volume of each MEC. In estimating the number of MEC per acini, we assume that acini are predominantly comprised of MECs. Figure 6.23 shows the average number of cells in acini over 4 weeks. Between week 2 and week 3, proliferation of the cells in the co-cultures was no longer in the log-phase

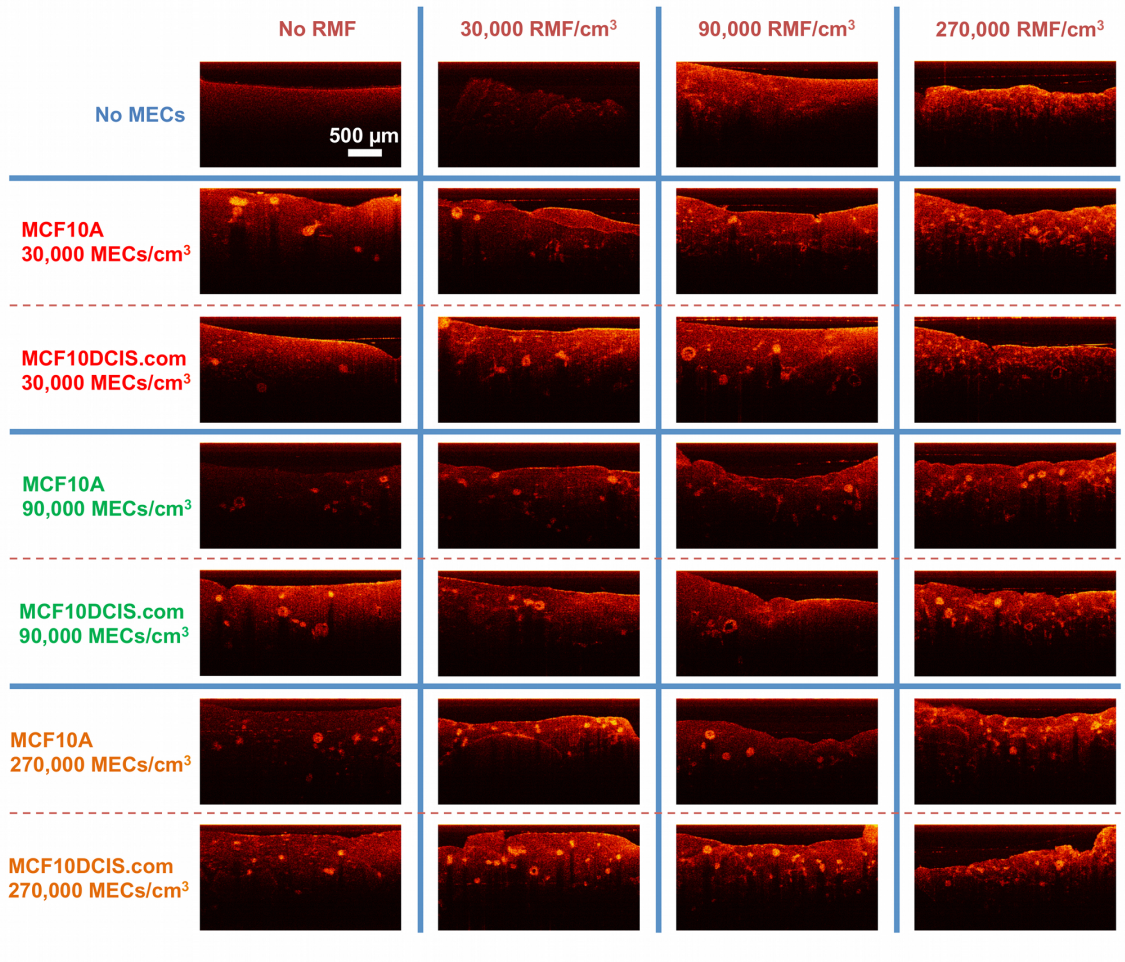

Figure 6.21: **Representative OCT $x-z$ images of 3D human mammary tissue cultures at week 4.** As indicated, the seed concentration of MEC is increasing from top to bottom, and the seed concentration of RMF is increasing from left to right.

of growth, as evidenced by a plateau in the number of MEC per acinus. Similarly, co-cultures with higher seeded cell concentration (MEC concentration $>$ 90,000/cm^3) also remained in the log-phase for only a short time (Figure 6.23) and the acini count shows numerous smaller acini interspersed in the Collagen I:Matrigel matrix (Table 6.1). Thus, monocultures seeded with 30,000 MEC/cm^3, co-cultures seeded with 30,000 MEC/cm^3:30,000 RMF/cm^3, and 30,000 MEC/cm^3:90,000 RMF/cm^3 were selected for comparison over the first two weeks only.

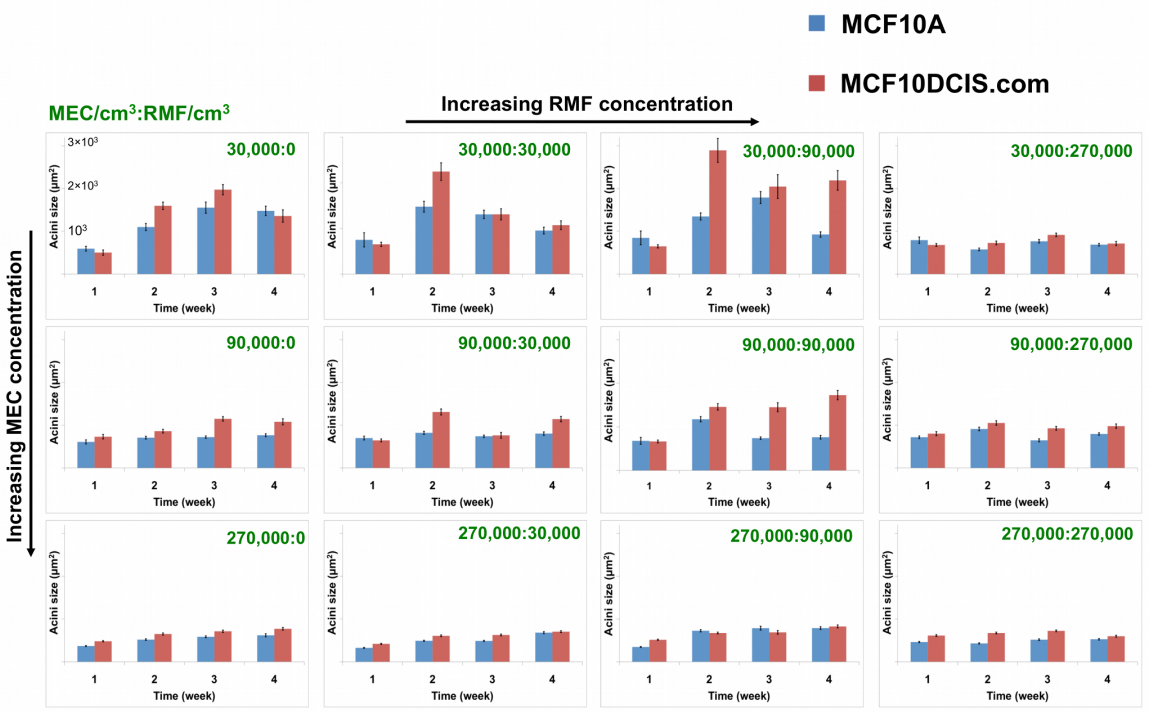

Figure 6.22: **Acini size analysis.** Histogram of average acini sizes (in μm^2) in each gel formed by the normal and pre-malignant MECs, based on the OCT images acquired weekly for 4 weeks. Error bars indicate the standard error of the measured values.

	No RMF	30,000 RMF/cm^3	90,000 RMF/cm^3	270,000 RMF/cm^3
30,000 MCF10A/cm^3	45	52	66	184
30,000 MCF10DCIS.com/cm^3	20	39	46	123
90,000 MCF10A/cm^3	119	96	66	199
90,000 MCF10DCIS.com/cm^3	75	61	56	187
270,000 MCF10A/cm^3	183	174	94	231
270,000 MCF10DCIS.com/cm^3	152	279	139	197

Table 6.1: **Number of acini in 3D cultures at week 4.** Acini count in an approximate gel volume of 4.5 mm^3 at week 4 for monocultures of MCF10A and MCF10DCIS.com, and co-cultures of MCF10A:RMF and MCF10DCIS.com:RMF.

6.3.6 Acknowledgements

The authors acknowledge the assistance of Timothy O'Brien in the Computer Integrated Systems for Microscopy and Manipulation (CISMM) at UNC-Chapel Hill, J.

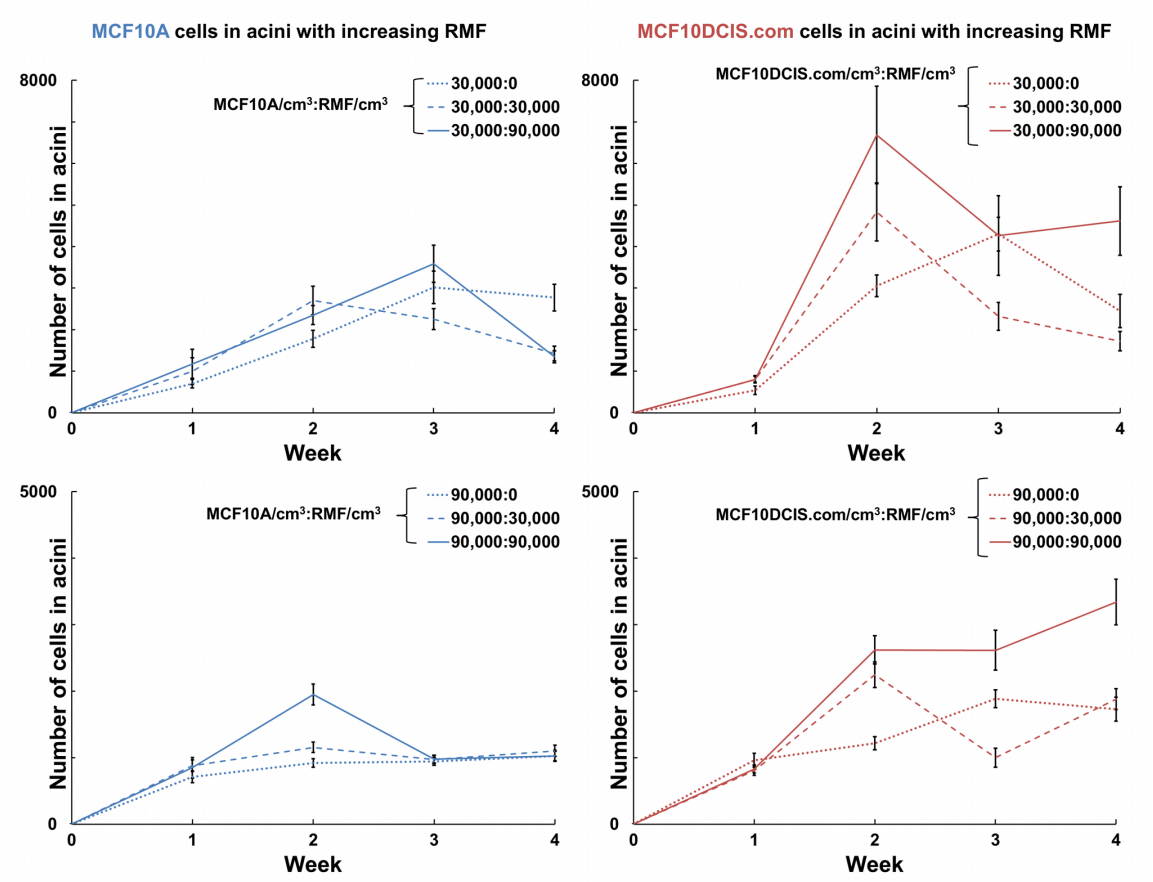

Figure 6.23: **Number of MCF10A and MCF10DCIS.com cells in acini with increasing fibroblasts.** Lack of proliferation between week 2 and week 3 is evident from the decrease in number of MEC per acinus.

Terese Camp in the Lineberger Comprehensive Cancer Center at UNC-Chapel Hill, Patricia Casbas-Hernandez in the Department of Pathology and Laboratory Medicine at UNC-Chapel Hill, and Jason M. Cooper in Applied Science - Biomedical Engineering at UNC-Chapel Hill.

Chapter 7

Conclusion

In this thesis, using a custom-built PS-OCT system, polarization-dependent scattering from plasmon-resonant GNRs was exploited to use them as diffusion probes in Newtonian fluids, non-Newtonian fluids, biologically relevant fluids such as mucus, and soft viscoelastic gels such as collagen I, Matrigel. The custom-built PS-OCT system was designed to simultaneously collect the co-polarized and cross-polarized signals from samples containing diffusing GNRs, which were synthesized to have their longitudinal plasmon resonance peak coincident with the OCT system's central wavelength.

First, the foundation for DLS using low-coherence imaging modality such as OCT was discussed, and the extension of the proposed method to use anisotropic scatterers such as GNRs was presented. Experimentally, M-mode PS-OCT imaging to depth-resolve the diffusing GNRs was performed. The translational and rotational diffusion coefficients were subsequently extracted by an inverse exponential fitting of the isotropic autocorrelation $g^{(1)}_{ISO}(\tau)$ and the cross-polarized autocorrelation $g^{(1)}_{HV}(\tau)$ respectively. The diffusion coefficients were validated with the Stokes-Einstein relation using Newtonian fluids over a range of viscosities. This validation performed for each batch of GNRs served as a diffusion calibration, which outlined the range over which the diffusion coefficients could be unambiguously resolved.

Using $g^{(1)}_{ISO}(\tau)$ and $g^{(1)}_{HV}(\tau)$ as the metrics for GNRs diffusion, the proposed method

was extended to probe non-Newtonian fluids such as PEO solutions. The MSDs of GNRs in semi-dilute ($c > c^*$) PEO solutions were evaluated from $g^{(1)}_{ISO}(\tau)$, which depicted temporal regions with elastic responses from the polymers in the solution. From the MSDs, the viscoelasticity of PEO solutions was further evaluated using GSER, which demonstrated an increasing elastic response G' with an increase in the polymer concentration as well as the polymer molecular weight. This work is thus an exploration of the nanorheology of semi-dilute PEO solutions measured by anisotropic probes using OCT. Further exploration of GNRs diffusion in the "correlation length $\geq$ probe" regime was discussed, which highlighted the diffusion of GNRs in a viscous solvent with intermittent physical obstructions from the polymer strands. An increase in the polymer correlation length within the "correlation length $\geq$ probe" regime was associated with an increase in the translational diffusion coefficients of the GNRs. Rotational diffusion coefficients of GNRs in dilute PEO solutions were found to be too fast to resolve even at the fastest sampling rate of the current OCT system. The "correlation length $\geq$ probe" regime establishes a platform for discussing the diffusion of GNRs in biological samples.

To extend the proposed method to probe biological samples, the diffusion of GNRs in ECM scaffolds (collagen I, Matrigel), and *in vitro* hBE mucus was presented. The GNRs were found to be diffusing in the solvent within the pores of the ECM with intermittent hinderance from the scaffolds, and their diffusion was determined to be sensitive to the changes in the interstitial space. Similarly, the GNRs in mucus were found to have diffusion rates less than 7-fold compared to their diffusion in the solvent, which suggests that the GNRs efficiently percolate through the mucus mesh and avoid being trapped. This result has implications in designing GNRs-based drug-delivery vehicles in diseases such as CF and COPD, where penetration of the drug carriers through the mucus barrier is important. More importantly, PS-OCT M-mode imaging of these biological samples to depth-resolve the $\tau_{1/e}$ of $g^{(1)}_{HH}(\tau)$ and $g^{(1)}_{HV}(\tau)$ was found to discriminate the diffusion

of GNRs and speckle fluctuation from cellular activities & other motile activities, and has the potential to resolve spatially heterogeneous samples.

An imaging study performed using the designed OCT system to study the architectural features formed by normal and pre-malignant MECs cultured in ECM in conjunction with mammary fibroblasts was also presented. The results of this study highlighted that fibroblasts differentially modulate the shape and size of spheroids formed by normal and pre-malignant MECs. The merit of OCT imaging in non-invasively probing 3D cultures in longitudinal studies was also demonstrated in this study.

7.1 Utility and potential impact

This thesis presents the study of diffusing GNRs carried out using a PS-OCT system. With the validation of diffusion of GNRs in Newtonian fluids, extension to non-Newtonian regimes, and eventually the extension to biological samples, this thesis presents a functional adjunction of diffusion measurements to the excellent imaging capability afforded by OCT. Additionally, the utility in using GNRs was evident in biological studies where regions lacking an uptake of GNRs showed excellent visualization in the PS-OCT images, which sheds light on the permeability of nanoscale particles within heterogeneous biological samples. Moreover, the depth-resolution of $\tau_{1/e}$ of $g^{(1)}_{HH}(\tau)$ and $g^{(1)}_{HV}(\tau)$ in biological samples also revealed simultaneous mapping of diffusing GNRs and speckle fluctuation resulting from comparatively slower activities.

With future improvements to the present PS-OCT system, such as faster sampling, longer data acquisition, and using a low-noise CCD camera, complex fluids at higher concentration than that explored in this thesis can potentially be probed using the outlined GSER formalism with a higher degree of accuracy. The study in this thesis presents a platform for extending the functional capability of OCT imaging to the growing field of microrheology and bio-rheology. Given the excellent and real-time visualization of bi-

ological features afforded by OCT, the capability to simultaneously map the rheological features using GNRs as probes shows promise to be a powerful and minimally invasive tool in biomedical research.

Appendix A

MATLAB codes

A.1 Diffusion coefficients from OCT signals

```
% Code: Rods_Diffusion.m
% Raghav K. Chhetri
%
% This code uses the HH and HV signals from spectrally processed
% PS-OCT signals and computes their autocorrelations. Exponential
% fits are performed to the autocorrelations to get the 1/e decay
% times and the diffusion coefficients of the GNRs
%------------
% NOTE: HHcomping and HVcompimg are spectrally processed PS-OCT
    signals.
Ahreal=(real(HHcompimg)); Ahimag=(imag(HHcompimg));
Avreal=(real(HVcompimg)); Avimag=(imag(HVcompimg));

RefIndx=1.34; %Refractive index
horiz=12000; % Number of Axial lines used during imaging
linerate_hz=25000; % Axial linerate (Hz)

time=(-(horiz-1)/linerate_hz:1/linerate_hz:(horiz-1)/linerate_hz)*1000;
     % in ms
time0=time(horiz:end); % in ms

roimin=100; % Region of interest
roimax=400;
stepsize=10; % Number of pixel to average the autocorrelations over
steps=(roimax-roimin)/stepsize; % Number of steps between roimin and
    roimax
%-------------------------------------------------------------------------
avg_hreal=mean(Ahreal,2); avg_himag=mean(Ahimag,2); %Average of each
    row
avg_vreal=mean(Avreal,2); avg_vimag=mean(Avimag,2); %Average of each
    row
clear HHcompimg HVcompimg;
for i=1:1024
    Ahreal(i,:)=Ahreal(i,:)-avg_hreal(i);
    Avreal(i,:)=Avreal(i,:)-avg_vreal(i);
    Ahimag(i,:)=Ahimag(i,:)-avg_himag(i);
```

```
    Avimag(i,:)=Avimag(i,:)-avg_vimag(i);
end

disp('[roimin roimax stepsize] is:');
disp([roimin roimax stepsize]);
%---HH Signals
Ah_real=Ahreal(roimin+1:roimax,:);
Ah_imag=Ahimag(roimin+1:roimax,:);
%---HV Signals
Av_real=Avreal(roimin+1:roimax,:);
Av_imag=Avimag(roimin+1:roimax,:);
clear Ahreal Ahimag Avreal Avimag1;
[gHH gHV gISON time0] = gcorr_v2(horiz,linerate_hz,steps,stepsize,
    Ah_real,Ah_imag,Av_real,Av_imag);
[Decay_Time]=Decay_v2(gHH,gHV,gISON,time0,steps,horiz,RefIndx);
%-------------------------------------------------------------------------
% Plot sample OCT signals and their corresponding frequency spectrums
NFFT = 2^nextpow2(horiz);
signal1=Ah_imag(stepsize,:);
fsignal1 = fft(signal1,NFFT)/horiz;
signal2=Av_imag(stepsize,:);
fsignal2 = fft(signal2,NFFT)/horiz;
Nyqf=linerate_hz/2; % Nyquist Frequency, in Hz
f = Nyqf*linspace(0,1,NFFT/2+1);
figure;
subplot(2,2,1); plot(time0,signal1);
xlabel('time, ms'); ylabel('Ah_imag');
subplot(2,2,2); plot(f,2*abs(fsignal1(1:NFFT/2+1)));
title('Single-Sided Amplitude Spectrum of the OCT signal (Ah-imag)');
xlabel('Frequency (Hz)'); ylabel('|F.T. of the OCT signal|');
xlim([0 200]);
subplot(2,2,3); plot(time0,signal2,'r');
xlabel('time, ms'); ylabel('Av_imag');
subplot(2,2,4); plot(f,2*abs(fsignal2(1:NFFT/2+1)),'r');
title('Single-Sided Amplitude Spectrum of the OCT signal (Av-imag)');
xlabel('Frequency (Hz)'); ylabel('|F.T. of the OCT signal|');
xlim([0 200]);
%-------------------------------------------------------------------------
% Average autocorrelation from all autocorrelations
avggHH=mean(gHH,1);
avggHV=mean(gHV,1);
avggISON=mean(gISON,1);
figure; semilogx(time0,avggHH,'xb','Linewidth',2.5);
hold on
semilogx(time0,avggHV,'or','Linewidth',2.5);
hold on
semilogx(time0,avggISON,'ok','Linewidth',2.5);
set(gca,'fontsize',18,'fontweight','bold');
xh=xlabel('log(time in ms)'); yh=ylabel('Avg Autocorrelation');
set([xh,yh],'fontweight','bold','fontsize',18); clear xh yh;
legend('gHH','gHV','gISON');
hold off
```

```
% Raghav K. Chhetri
% This function computes and plots the autocorrelations
%----------------
function [gHH gHV gISON time0] = gcorr_v2(horiz, linerate_hz, steps,
    stepsize, Ah_real, Ah_imag, Av_real, Av_imag)
auto_h=zeros(1,2*horiz-1);
auto_v=zeros(1,2*horiz-1);
gHH_real=zeros(steps,horiz);
gHH_imag=gHH_real;
gHH=gHH_real;
gHV_real=zeros(steps,horiz);
gHV_imag=gHV_real;
gHV=gHV_real;
gISON_real=zeros(steps,horiz);
gISON_imag=gHV;
gISON=gISON_real;
roiminlocal=1;
for n=1:steps;
    roimaxlocal=roiminlocal+stepsize-1;
    %---
    % REAL PART
    %---
    % AUTOCORRELATION, Signal averaged over 'stepsize' rows
    % Then, Autocorrelation evaluated as a function of depth
    auto_h=xcorr(Ah_real(roiminlocal,:),'coeff');
    auto_v=xcorr(Av_real(roiminlocal,:),'coeff');
    for i=roiminlocal+1:roimaxlocal
        auto_h=auto_h+xcorr(Ah_real(i,:),'coeff');
        auto_v=auto_v+xcorr(Av_real(i,:),'coeff');
    end
    auto_h=auto_h/(roimaxlocal-roiminlocal+1);
    auto_v=auto_v/(roimaxlocal-roiminlocal+1);
    gHH_real(n,:)=auto_h(1,horiz:end);
    gHV_real(n,:)=auto_v(1,horiz:end);
    % Extrapolate t=0 point
    gHH_real(n,1)=gHH_real(n,2)^2/gHH_real(n,3);
    gHV_real(n,1)=gHV_real(n,2)^2/gHV_real(n,3);
    % Normalize
    gHH_real(n,:)=gHH_real(n,:)/max(gHH_real(n,:));
    gHV_real(n,:)=gHV_real(n,:)/max(gHV_real(n,:));
    gISON_real(n,:)=(9/5)*gHH_real(n,:)-(4/5)*gHV_real(n,:);
    %---
    % IMAGINARY PART
    %---
    % AUTOCORRELATION, Signal averaged over 'stepsize' rows
    % Then, Autocorrelation evaluated as a function of depth
    auto_h=xcorr(Ah_imag(roiminlocal,:),'coeff');
    auto_v=xcorr(Av_imag(roiminlocal,:),'coeff');
    for i=roiminlocal+1:roimaxlocal
        auto_h=auto_h+xcorr(Ah_imag(i,:),'coeff');
        auto_v=auto_v+xcorr(Av_imag(i,:),'coeff');
    end
```

```
52      auto_h=auto_h/(roimaxlocal-roiminlocal+1);
53      auto_v=auto_v/(roimaxlocal-roiminlocal+1);
54
55      gHH_imag(n,:)=auto_h(1,horiz:end);
56      gHV_imag(n,:)=auto_v(1,horiz:end);
57      clear auto_h auto_v;
58      % Extrapolate t=0 point
59      gHH_imag(n,1)=gHH_imag(n,2)^2/gHH_imag(n,3);
60      gHV_imag(n,1)=gHV_imag(n,2)^2/gHV_imag(n,3);
61      % Normalize
62      gHH_imag(n,:)=gHH_imag(n,:)/max(gHH_imag(n,:));
63      gHV_imag(n,:)=gHV_imag(n,:)/max(gHV_imag(n,:));
64      gISON_imag(n,:)=(9/5)*gHH_imag(n,:)-(4/5)*gHV_imag(n,:);
65      %---
66      roiminlocal=roiminlocal+stepsize;
67  end
68  gHH=(gHH_real+gHH_imag)/max(max(gHH_real+gHH_imag));
69  gHV=(gHV_real+gHV_imag)/max(max(gHV_real+gHV_imag));
70  gISON=(gISON_real+gISON_imag)/max(max(gISON_real+gISON_imag));
71  % PLOTS:
72  x=ceil(sqrt(steps));
73  if x*(x-1)>=steps
74      x2=x-1;
75  else
76      x2=x;
77  end
78  time=(-(horiz-1)/linerate_hz:1/linerate_hz:(horiz-1)/linerate_hz)*1000;
79  time0=time(horiz:end);
80  % Plots autocorrelations with log x-axis
81  figure
82  for n=1:steps;
83      subplot(x,x2,n);
84      semilogx(time0,gISON(n,:),'xk','Linewidth',2.5); tmp=sprintf('Depth
            %d',n); title(tmp);
85      hold on; semilogx(time0,gHH(n,:),'xb','Linewidth',2.5);
86      hold on; semilogx(time0,gHV(n,:),'xr','Linewidth',2.5);
87      xmin=0.01; % in ms
88      xmax=(horiz/linerate_hz)*1000; % in ms
89      hold off; xlim([xmin xmax]);
90
91      set(gca,'fontsize',10,'fontweight','bold');
92      xh=xlabel('\tau, Lag time (ms)'); yh=ylabel('g^(^1^)(z,\tau)');
93      set([xh,yh],'fontweight','bold','fontsize',10); clear xh yh;
94      legend('gISON','gHH','gHV');
95      ha=axes('Position',[0 0 1 1],'Xlim',[0 1],'Ylim',[0 1],'Box','off',
            'Visible','off','Units','normalized','clipping','off');
96      tmp=sprintf('Correlator Channel: 1');
97      text(1.5, 1,tmp,'HorizontalAlignment','center','VerticalAlignment',
            'top')
98  end
99  end
```

```
% Raghav K. Chhetri
% This function performs exponential fittings to HH,HV,ISON
    autocorrelations
%----------------
function [Decay_Time]=Decay_v2(gHH,gHV,gISON,time0,steps,horiz,RefIndx)
pvalsH=zeros(steps,2); pvalsV=zeros(steps,2); pvalsISO=zeros(steps,2);
Decay_Time=zeros(steps,3);
q=4*pi*(RefIndx)./(800*10^-9); % m^-1, Including the refractive index
for n=1:steps;
    expmin=-1;
    % ----------------
    %     gHH autocorrelation
    % ----------------
    i=1; val=0;
    while val>expmin && i<horiz
        val=log(gHH(n,i));
        i=i+1;
    end
    imax1=i;
    pvalsH(n,:)=polyfit(time0(1:imax1),log(gHH(n,1:imax1)),1);
    Decay_Time(n,1)=-1/pvalsH(n,1);
    % ----------------
    %     gHV autocorrelation
    % ----------------
    i=1; val=0;
    while val>expmin && i<horiz
        val=log(gHV(n,i));
        i=i+1;
    end
    imax2=i;
    pvalsV(n,:)=polyfit(time0(1:imax2),log(gHV(n,1:imax2)),1);
    Decay_Time(n,2)=-1/pvalsV(n,1);
    % ----------------
    %     gISON autocorrelation
    % ----------------
    i=1; val=0;
    while val>expmin && i<horiz
        val=log(gISON(n,i));
        i=i+1;
    end
    imax3=i;
    pvalsISO(n,:)=polyfit(time0(1:imax3),log(gISON(n,1:imax3)),1);
    Decay_Time(n,3)=-1/pvalsISO(n,1);
end
N=250; % Number of points between time0(1)and time0(factor*imax) to use
    to estimate the exponential fit.
efitH=zeros(steps,N);
efitV=zeros(steps,N);
efitISO=zeros(steps,N);
% PLOTS:
% ----------------
% Region from which exponential fit was estimated (plotted in linear
```

```
    scale)
% ----------------
figure
for n=1:steps;
    t1=time0(1:imax1);
    t2=linspace(time0(1),time0(imax1),N);
    efitH(n,:)=polyval(pvalsH(n,:),t2);
    subplot(3,steps,n); plot(t1,log(gHH(n,1:imax1)),t2,efitH(n,:),':');
    xlabel('Time(ms)'); ylabel('Fit to log(gHH)'); xlim([0 t2(end)]);
    tt1=time0(1:imax2);
    tt2=linspace(time0(1),time0(imax2),N);
    efitV(n,:)=polyval(pvalsV(n,:),tt2);
    subplot(3,steps,steps+n); plot(tt1,log(gHV(n,1:imax2)),tt2,efitV(n
        ,:),':');
    xlabel('Time(ms)'); ylabel('Fit to log(gHV)'); xlim([0 tt2(end)]);
    ttt1=time0(1:imax3);
    ttt2=linspace(time0(1),time0(imax3),N);
    efitISO(n,:)=polyval(pvalsISO(n,:),ttt2);
    subplot(3,steps,2*steps+n); plot(ttt1,log(gISON(n,1:imax3)),ttt2,
        efitISO(n,:),':');
    xlabel('Time(ms)'); ylabel('Fit to log(gISON)'); xlim([0 ttt2(end)
        ]);
end
% ----------------
% Overlaying the exponential fit to the autocorrelations
% ----------------
factor=10; % This plots the exponential fit upto factor*imax, where
    imax is the index at which the autocorrelation reaches 1/e
if factor*imax1 > length(time0) || factor*imax2 > length(time0) ||
    factor*imax3 > length(time0)
    factor=1;
end
figure
for n=1:steps;
    t1=time0(1:factor*imax1);
    t2=linspace(time0(1),time0(factor*imax1),N);
    efitH(n,:)=polyval(pvalsH(n,:),t2);
    subplot(3,steps,n); plot(t1,gHH(n,1:factor*imax1),t2,exp(efitH(n,:)
        )./max(exp(efitH(n,:))),':');
    set(gca,'fontsize',10,'fontweight','bold');
    xh=xlabel('\tau, Lag time (ms)'); yh=ylabel('g^(^1^)_H_H(z,\tau)');
    set([xh,yh],'fontweight','bold','fontsize',10); clear xh yh;
    xlim([0 t2(end)]);
    legend('gHH','Fit to gHH');
    tt1=time0(1:factor*imax2);
    tt2=linspace(time0(1),time0(factor*imax2),N);
    efitV(n,:)=polyval(pvalsV(n,:),tt2);
    subplot(3,steps,steps+n); plot(tt1,gHV(n,1:factor*imax2),tt2,exp(
        efitV(n,:))./max(exp(efitV(n,:))),':');
    set(gca,'fontsize',10,'fontweight','bold');
    xh=xlabel('\tau, Lag time (ms)'); yh=ylabel('g^(^1^)_H_V(z,\tau)');
    set([xh,yh],'fontweight','bold','fontsize',10); clear xh yh;
```

```
95      xlim([0 tt2(end)]);
96      legend('gHV','Fit to gHV');
97      ttt1=time0(1:factor*imax3);
98      ttt2=linspace(time0(1),time0(factor*imax3),N);
99      efitISO(n,:)=polyval(pvalsISO(n,:),ttt2);
100     subplot(3,steps,2*steps+n); plot(ttt1,gISON(n,1:factor*imax3),ttt2,
            exp(efitISO(n,:))./max(exp(efitISO(n,:))),':');
101     set(gca,'fontsize',10,'fontweight','bold');
102     xh=xlabel('\tau, Lag time (ms)'); yh=ylabel('g^(^1^)_I_S_O_N(z,\tau
            )');
103     set([xh,yh],'fontweight','bold','fontsize',10); clear xh yh;
104     xlim([0 ttt2(end)]);
105     legend('gISON','Fit to gISON');
106 end
107 % ----------------
108 % TEXTS TO DISPLAY:
109 % ----------------
110 disp('Unit: ms, Decay Time exp fitting of the autocorrelation curves');
111 disp('     gHH       gHV       gISON');
112 disp(Decay_Time);
113 disp('Mean (ms)');
114 disp(mean(Decay_Time));
115 disp('Its std. deviation (ms)');
116 disp(std(Decay_Time));
117 Dr=(1/6)./(Decay_Time(:,2).*10^-3);
118 % display('Unit: rad^2/sec, Rotational Diffusion Coefficient');
119 % disp(Dr);
120 disp('Mean Rotational Diffusion Coeff.(rad^2/sec)');
121 disp(mean(Dr));
122 disp('Its std. deviation (rad^2/s)');
123 disp(std(Dr));
124 Dtt=(1/q^2)./(Decay_Time(:,3).*10^-3);
125 % display('Unit: m^2/s, Translational Diffusion Coefficient from gISON
        ');
126 % disp(Dtt);
127 disp('Mean Translational Diffusion Coeff. from gISON (m^2/s)');
128 disp(mean(Dtt));
129 disp('Its std. deviation (m^2/s)');
130 disp(std(Dtt));
```

Appendix B

Author manuscripts

The following published manuscripts adapted in this thesis are attached in the following order:

- R. K. Chhetri, K. A. Kozek, A. C. Johnston-Peck, J. B. Tracy, and A. L. Oldenburg. Imaging three-dimensional rotational diffusion of plasmon resonant gold nanorods using polarization-sensitive optical coherence tomography. Phys. Rev. E, 83(4):1-4, April 2011.

- R. K. Chhetri, Z. F. Phillips, M. A. Troester, A. L. Oldenburg. Longitudinal study of mammary epithelial and fibroblast co-cultures using optical coherence tomography reveals morphological hallmarks of pre-malignancy. PloS one, 7:1-7, 2012.

RAPID COMMUNICATIONS

PHYSICAL REVIEW E **83**, 040903(R) (2011)

Imaging three-dimensional rotational diffusion of plasmon resonant gold nanorods using polarization-sensitive optical coherence tomography

Raghav K. Chhetri,[1] Krystian A. Kozek,[2] Aaron C. Johnston-Peck,[2] Joseph B. Tracy,[2] and Amy L. Oldenburg[1,3,*]

[1]*Department of Physics and Astronomy, University of North Carolina at Chapel Hill, Chapel Hill, North Carolina 27599, USA*

[2]*Department of Materials Science and Engineering, North Carolina State University, Raleigh, North Carolina 27695, USA*

[3]*Biomedical Research Imaging Center, University of North Carolina at Chapel Hill, Chapel Hill, North Carolina 27599, USA*

(Received 22 November 2010; published 12 April 2011)

We demonstrate depth-resolved viscosity measurements within a single object using polarized optical scattering from ensembles of freely tumbling plasmon resonant gold nanorods (GNRs) monitored with polarization-sensitive optical coherence tomography. The rotational diffusion coefficient of the GNRs is shown to correlate with viscosity in molecular fluids according to the Stokes-Einstein relation. The plasmon resonant and highly anisotropic properties of GNRs are favorable for microrheological studies of nanoscale properties.

DOI: 10.1103/PhysRevE.83.040903 PACS number(s): 87.85.Rs, 42.25.Kb, 78.67.Qa, 83.85.Ei

In the growing field of microrheology, there has been considerable interest in techniques that quantify thermal diffusion of probes within locally resolved volumes of the medium under investigation. The Stokes-Einstein relation relates diffusion measured by these passive techniques to the linear viscoelastic properties of the medium, provided that the probe is inert and the medium behaves as a near-equilibrium, homogeneous, isotropic, and incompressible continuum [1]. Optical coherence tomography (OCT) [2] provides a novel platform to study dynamic light scattering (DLS) from passively diffusing particles [3]. Using plasmon resonant gold nanorods (GNRs), DLS with OCT enables locally resolved, passive microrheology of medium properties with microscale heterogeneities.

We investigated polarized light scattering from ensembles of GNRs using polarization-sensitive OCT (PS-OCT) to depth resolve the rotational diffusion coefficient (D_R) in media of varying viscosity. The shape anisotropy of a GNR splits the surface plasmon resonance into transverse and longitudinal modes, the latter of which provides high light scattering efficiencies due to reduced plasmon damping, and is polarized parallel to the long axis of the GNR [4]. By monitoring the polarized scattering, it has previously been shown that a GNR under two-dimensional (2D) Brownian rotation can be used as a local orientation sensor [5]. We expect GNRs in the molecular fluids in our study to obey the Stokes-Einstein relation, so that their three-dimensional (3D) Brownian diffusion can be related to the viscosity of the medium. While the translational diffusion of nanorods is complicated by coupling to rotational diffusion due to the shape anisotropy [6], rotational diffusion is independent of the state of translation, and as such, is a robust metric for local viscous properties. Furthermore, we expect GNRs to probe the viscosity of the medium at a smaller scale than that possible by using traditional microparticles.

In this study we employ OCT to monitor D_R of ensembles of unconfined GNRs. OCT employs optical depth ranging of singly backscattered light, enabling real-time imaging in noninvasive biomedical applications. Similar to DLS techniques, OCT is an optical heterodyne method which senses ensemble-averaged scattering from scatterers within the coherence volume, providing a higher signal-to-noise ratio and speed compared to single-particle tracking methods. Unlike traditional DLS, OCT employs low-coherence light so that the coherence volume is small; as such, OCT is capable of resolving the dynamic signal from each local coherence volume over depths exceeding the mean scattering path length [7], which has implications for analyzing optically thick tissues. The localized-coherence-volume technique has previously been used with microbeads to perform spatially resolved microrheology [8].

In this Rapid Communication, we employ PS-OCT and principles from DLS to measure the D_R of ensembles of GNRs freely suspended in media of varying viscosity. We test the validity of the Stokes-Einstein relation by comparing the observed D_R values with a model for the Stokes drag on cylinders, modified to account for the non-negligible GNR size distribution by computing the temporal statistics of a representative ensemble of GNRs. Using these validation measurements relating D_R to the viscosity of the medium, we demonstrate the capability of PS-OCT to spatially map the viscosity of a heterogeneous sample by using GNRs as rheological probes. The ability to resolve micrometer-scale heterogeneities in viscosity using GNRs with OCT may open new avenues for microrheological investigation.

GNRs used in this study have an average length and width of 53 ± 10 and 15 ± 4 nm, respectively, and exhibit a strong longitudinal plasmon mode centered at 780 nm with a full width at half maximum of 140 nm, which is within the OCT source spectrum that spans 735–865 nm at half maximum [9]. Two batch solutions for the experiment were prepared by mixing 10% of the GNRs solution ($\sim 8 \times 10^8$ GNRs/μL) with glycerol (Acros Organics, 15892-0010) and water (Fisher Scientific, W5-4), respectively. Samples with varying viscosity were then prepared by mixing the two batch solutions in different proportions, and their resulting viscosities were estimated using a mixture law [10]. Although multiple GNRs populate each coherence volume, we expect them to be noninteracting, because the estimated average separation between the GNRs (minimum $\sim$1450 nm) is large compared to both the average length of a GNR ($\sim$53 nm) and

*Author to whom correspondence should be addressed: aold@physics.unc.edu

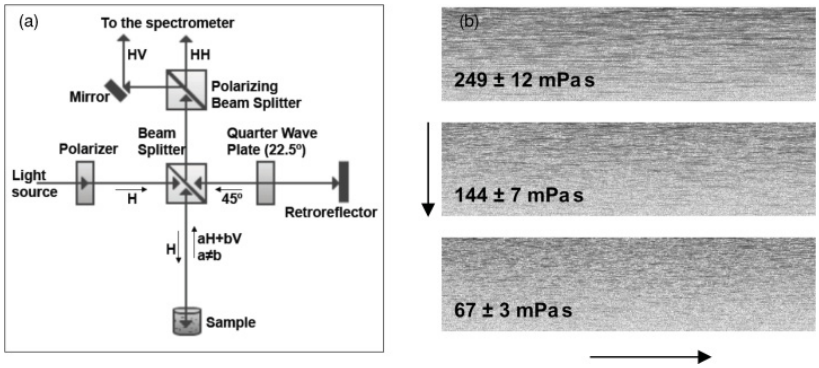

FIG. 1. (a) PS-OCT interferometer setup. (b) Example *M*-mode images [using an absolute value of $\tilde{a}(z,t)$] in the *HV* configuration showing an increasing rate of intensity fluctuations for samples with decreasing viscosities. (Note: Intensity fluctuations only up to 40 ms shown.)

the mean distance the GNRs travel over the duration of the OCT measurement (maximum ∼140 nm).

The OCT system in this study is a spectral domain, polarization-sensitive system, as shown in Fig. 1(a). The light source consists of a Ti:sapphire laser (Griffin, KMLabs, Inc.) and provides a coherence gate of ∼2.6 μm in air. Light from the source is horizontally polarized and split into reference and sample arms. Imaging is performed by a lens ($f = 30$ mm), which provides a transverse resolution of ∼12 μm in air. Owing to the coherence gate and the transverse resolution, the coherence volume is estimated to be ∼375 μm^3 in air. Horizontally polarized light (∼5 mW) incident upon the sample is backscattered into both horizontal (*H*) and vertical (*V*) polarization states, which interfere with their respective polarization states from the reference (consisting of linearly polarized light at 45°, generated after double pass through a quarter-wave plate at 22.5°). The interfered light is split into horizontal and vertical components by a polarizing beam splitter (*HH* and *HV*, respectively, where the first and second terms are the incident and backscattered polarization states from the sample, respectively), and directed to a custom spectrometer. The spectrometer is similar to a previous design [11], and consists of a transmission grating (600 lines/mm, Wasatch Photonics), camera lens ($f = 200$ mm), and a line scan camera (Piranha, Dalsa Inc.) operated at 25 kHz, providing an imaging depth of 2.08 mm in air.

Dynamic PS-OCT signals were recorded by acquiring depth scans from the same transverse position in the sample as a function of time (*M* mode). A total of 4000 depth scans were obtained with a line rate of 25 kHz (i.e., sampled every 40 μs for an overall duration of 160 ms). Typical *M*-mode OCT images showing time traces of the depth-resolved intensity fluctuations for samples with different viscosities are shown in Fig. 1(b). Qualitatively, we observe that the intensity fluctuations along the horizontal (time) axis are much slower in a high viscosity sample than in a low viscosity sample. Quantitative analysis, as performed below, reveals that the time scale of these intensity fluctuations is directly related to the viscosity of the medium.

Spectral domain OCT is a heterodyne detection scheme in which the complex analytic signal $\tilde{a}(z,t)$ as a function of depth z in the sample is obtained by inverse Fourier transformation of the measured spectrum [12]. In the heterodyne experiment, the temporal autocorrelation of the real part of $\tilde{a}(z,t)$, $G^{(2)}(z,\tau)$, is relatable to the first-order correlation function of the electric field scattered from the sample, $G^{(1)}(z,\tau)$ [13]. In this study, we employ polarization-sensitive OCT to collect the cross-polarized (*HV*) dynamic light scattering signal because it provides direct access to D_R against a background of slow translational diffusion D_T. Specifically, (after normalization),

$$g^{(1)}_{HV}(z,\tau) = e^{-[6D_R(z)+q^2D_T(z)]\tau} \approx e^{-6D_R(z)\tau}, \qquad (1)$$

where $q = 4\pi n/\lambda_0$ is the scattering vector in the backscattering geometry, the fast $e^{-i\omega_0\tau}$ term is dropped for convenience, and $6D_R \gg q^2D_T$ for the GNRs under study (by a factor of ∼38 for an average GNR of length 53 nm and width 15 nm, using expressions previously reported [14]). Therefore, D_R equates to $(6\tau_{1/e})^{-1}$, where $\tau_{1/e}$ is the $1/e$ decay time of $g^{(1)}_{HV}$.

Computationally, D_R at each depth z was isolated from $\tilde{a}_{HV}(z,t)$ as follows: The real part of $\tilde{a}_{HV}(z,t)$ was taken, and the time average was then subtracted to control for nonzero background noise and to isolate the intensity fluctuation [15]. Then, the autocorrelations were evaluated at each z and normalized to obtain $g^{(1)}_{HV}$, averaged within multiple depth intervals ($N = 7$, with each depth interval chosen to be 35 μm), and fitted to the expected inverse exponential of Eq. (1). A representative $g^{(1)}_{HV}$ for each sample is shown in Fig. 2, with a sample inverse-exponential fitting shown in the inset. The fittings were performed over a windowed region of $g^{(1)}_{HV}$ from $\tau = 0$ to $\sim \tau_{1/e}$. We find that the measured $g^{(1)}_{HV}$ values appear to be consistently larger than those of a pure exponential at times greater than $\tau_{1/e}$. This may be explained partially by the size distribution of GNRs giving rise to a distribution of rotational rates [as modeled in Eq. (2)], which deviates from a pure exponential in qualitatively the same manner, or it may be explained partially by the translational diffusion of the GNRs becoming more significant at longer time scales. The rotational diffusion rate was then calculated at each depth interval according to $D_R = (6\tau_{1/e})^{-1}$. We noted that there was no significant change in D_R versus depth, which was expected because the mean scattering path length from GNRs is much longer than the depths analyzed. The D_R values averaged over multiple depth intervals are plotted in Fig. 3. As expected, an inverse relationship between D_R and viscosity is found, which suggests that the rotations of the GNRs occur over a comparatively shorter time scale as the viscosity decreases. We noted that D_R values were consistent (within 7%) when the concentration of the GNRs was decreased from 10% (at which the experiment was performed) to 2%, while maintaining

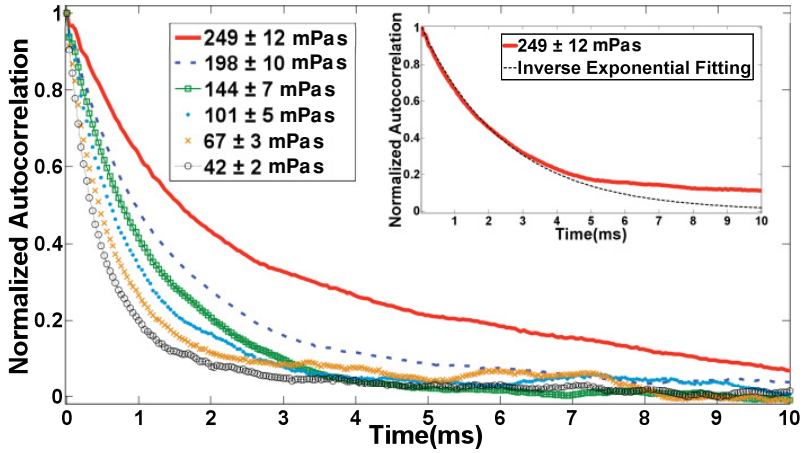

FIG. 2. (Color online) Representative $g^{(1)}_{HV}(\tau)$ for samples with varying viscosity. Decay time is observed to decrease as the viscosity decreases. The inset shows a representative inverse exponential fitting to $g^{(1)}_{HV}(\tau)$ (dotted line), based on Eq. (1).

the viscosity at a constant value (within 5%). Given the consistency of D_R with concentration and the invariance of measured D_R with depth, the effect of multiple scattering is believed to be negligible in our experiment.

To test the validity of the Stokes-Einstein relation for this system, the experimental D_R values were compared with a model combining the rotational diffusion of smooth cylinders [14] with the optical scattering from ellipsoids [16] while accounting for the measured size distribution of the GNRs. First, simulated autocorrelations were computed as the sum of the contribution of each GNR in a representative distribution ($n = 998$) as follows:

$$g^{(1)}_{HV}(\tau) = \sum_{j=1}^{998} c_j^2 e^{-6D_{Rj}\tau}, \qquad (2)$$

where the summation is over each nanorod j in the distribution, and c_j^2 is an optical weighting factor accounting for the maximum fluctuation in backscattering detected by the OCT system from each GNR. This is important to overcome the experimental bias for more efficient detection of larger, more slowly diffusing GNRs. The weights c_j^2 were evaluated from the optical scattering anisotropy of each GNR weighted by the incident light spectrum, according to

$$c_j^2 = \sum_{\lambda} [\sigma_{s,||}(\lambda, L_j, d_j) - \sigma_{s,\perp}(\lambda, L_j, d_j)] E_r^2(\lambda), \qquad (3)$$

with L_j and d_j the length and width of the jth GNR, and $\sigma_{s,||}$ and $\sigma_{s,\perp}$ the scattering cross sections, computed according to Mie Gans theory [16], of the jth GNR when the incident polarization is parallel and perpendicular to the long axis, respectively. On average, we find that $\sigma_{s,||}$ is ~250 times that of $\sigma_{s,\perp}$, highlighting the high scattering anisotropy exhibited by GNRs. To compute D_{Rj} in Eq. (2) for each GNR, an expression derived for solid cylinders ($2 < L/d < 20$) was employed [14]. Theoretical D_R were then evaluated by fitting an inverse exponential of the form shown in Eq. (1) to the simulated autocorrelation given by Eq. (2).

Theoretical predictions were made in two ways: first, by considering the actual sizes of the GNRs measured by transmission electron microscopy (TEM), and second, by considering an average surfactant [cetyltrimethylammonium bromide (CTAB)] capping thickness of 2 nm around the GNRs. The average CTAB layer thickness was estimated from a TEM image as half of the average spacing between the GNRs when densely packed, and is consistent with previously reported values for similarly sized GNRs, synthesized using a growth method in the presence of CTAB [17].

We find that the experimental D_R values correlate with the theoretical D_R computed as above for our distribution of GNRs (Fig. 3). Agreement between experimental and theoretical D_R is obtained over a viscosity range of 42–249 mPas, and the level of agreement with theory is similar to the findings of a DLS study of similarly sized GNRs at a single viscosity [18]. In making direct comparisons between the experimental values and the theoretical predictions, it should be taken into consideration that the theoretical model is only an approximation; the GNRs are not exactly cylindrical in shape (as assumed for the rotational diffusion model), nor are they exactly ellipsoidal (as assumed for the optical scattering model).

These results demonstrate that PS-OCT can monitor viscosity using GNRs as nanoprobes within the applicability of the Stokes-Einstein relation. Next, the potential of our technique to

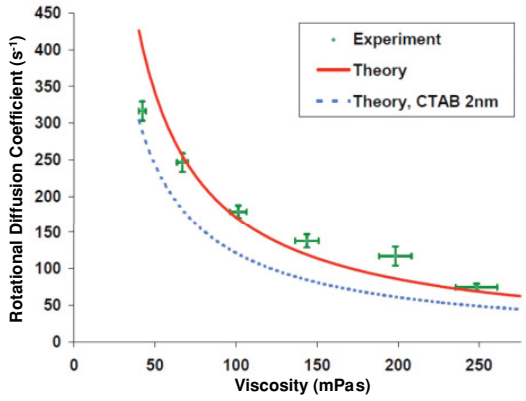

FIG. 3. (Color online) Comparison of experimental D_R with theoretical predictions assuming GNRs as smooth cylinders [14] (solid line: for the actual sizes of the GNRs; dotted line: considering an average CTAB layer of 2 nm).

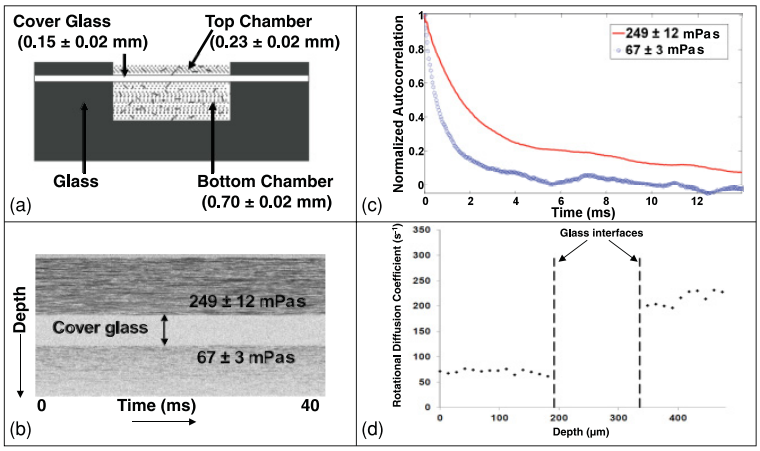

FIG. 4. (Color online) (a) Double-chamber design. (b) *M*-mode images [using an absolute value of $\tilde{a}(z,t)$] showing samples with different viscosities separated by a cover glass. (Note: Intensity fluctuations only up to 40 ms shown.) (c) $g_{HV}^{(1)}(\tau)$ of the samples showing two different decay time scales. (d) D_R as a function of depth in the double chamber.

resolve heterogeneities in viscosity was explored using a double chamber, as shown in Fig. 4(a), in which two samples with different viscosities were separated by a thin microscope cover glass. Figure 4(b) shows the *M*-mode images of the two samples in the double chamber. Figure 4(c) shows $g_{HV}^{(1)}$ averaged within each chamber, demonstrating two different time scales that indicate the difference in viscosity in the two chambers. By fitting $g_{HV}^{(1)}$ to the expected inverse exponential of Eq. (1), D_R of 72 ± 5 and $227 \pm 6\,\mathrm{s}^{-1}$ were found for samples in the top and bottom chamber, respectively, which are consistent with independent measurements of D_R of 74 ± 5 and $246 \pm 13\,\mathrm{s}^{-1}$, respectively, for these samples (Fig. 2). Figure 4(d) shows D_R as a function of depth in the double chamber, where D_R was computed within each depth interval of 35 μm, and the depth intervals were successively stepped by 14 μm through both chambers. A clear distinction between the rotational diffusion coefficients of the two samples is seen, and the D_R values measured within multiple depth intervals for the same sample are also consistent with one another. This demonstrates that DLS performed with PS-OCT using GNRs as nanoprobes is capable of resolving the microscale heterogeneities in viscosity existing at multiple depths within an object.

In conclusion, by combining the techniques of PS-OCT and DLS, we showed that polarization-dependent scattering from ensembles of GNRs provides information about D_R, and subsequently the viscosity of the medium. We have studied the unconfined stochastic motion of plasmon resonant GNRs in 3D using OCT, and obtained agreement between experimental and theoretical D_R over a viscosity range of 42–249 mPas, which is within the regime of interest in biophysical studies. Averaging over large numbers of GNRs provides a high signal-to-noise ratio for determining the viscosity within each coherence volume of the sample (in this study, ~130 GNRs within each coherence volume of ~375 $\mu\mathrm{m}^3$). We also demonstrated the ability to depth resolve the heterogeneous viscosity within a single object using this technique. Future work is needed to validate this technique in non-Newtonian fluids using the generalized Stokes-Einstein relation. Because OCT rejects multiply scattered light, this technique has the potential to provide microrheology in optically thick samples, such as biological tissues. The combination of the anisotropic and plasmon resonant properties of GNRs with OCT provides a unique tool for imaging microscale heterogeneities of rheological properties.

This work was supported by a pilot grant from the Carolina Cancer Center for Nanotechnology Excellence [C-CCNE NIH (NCI) No. U54CA119343] and by startup funds at UNC-Chapel Hill and NCSU. A.C.J.-.P acknowledges support from GAANN.

[1] T. M. Squires and Thomas G. Mason, Annu. Rev. Fluid Mech. **42**, 413 (2010).
[2] D. Huang *et al.*, Science **254**, 1178 (1991).
[3] J. Kalkman, R. Sprik, and T. G. van Leeuwen, Phys. Rev. Lett. **105**, 198302 (2010).
[4] C. Sönnichsen *et al.*, Phys. Rev. Lett. **88**, 077402 (2002).
[5] C. Sönnichsen and A. P. Alivisatos, Nano Lett. **5**, 301 (2005).
[6] Y. Han *et al.*, Science **314**, 626 (2006).
[7] D. A. Boas, K. K. Bizheva, and A. M. Siegel, Opt. Lett. **23**, 319 (1998).
[8] G. Popescu, A. Dogariu, and R. Rajagopalan, Phys. Rev. E. **65**, 041504 (2002).
[9] See supplemental material at [http://link.aps.org/supplemental/10.1103/PhysRevE.83.040903] for the synthesis and absorbance spectrum.
[10] N.-S. Cheng, Ind. Eng. Chem. Res. **47**, 3285 (2008).
[11] B. Baumann *et al.*, Opt. Express **15**, 1054 (2007).
[12] A. F. Fercher *et al.*, Opt. Commun. **117**, 43 (1995).
[13] C. S. Johnson Jr. and D. A. Gabriel, *Laser Light Scattering* (Dover, New York, 1994).
[14] A. Ortega and J. García de la Torre, J. Chem. Phys. **119**, 9914 (2003).
[15] B. J. Berne and R. Pecora, *Dynamic Light Scattering: With Applications to Chemistry, Biology, and Physics* (Dover, New York, 2000).
[16] C. F. Bohren and D. R. Huffman, *Absorption and Scattering of Light by Small Particles* (Wiley, New York, 1983).
[17] Y. Abate *et al.*, Chem. Phys. Lett. **474**, 146 (2009).
[18] J. Rodríguez-Fernández *et al.*, J. Phys. Chem. C **111**, 5020 (2007).

OPEN ACCESS Freely available online

PLOS ONE

Longitudinal Study of Mammary Epithelial and Fibroblast Co-Cultures Using Optical Coherence Tomography Reveals Morphological Hallmarks of Pre-Malignancy

Raghav K. Chhetri[1], Zachary F. Phillips[2], Melissa A. Troester[3], Amy L. Oldenburg[1,4]*

1 Department of Physics and Astronomy, University of North Carolina at Chapel Hill, Chapel Hill, North Carolina, United States of America, **2** Curriculum in Applied Sciences and Engineering, University of North Carolina at Chapel Hill, Chapel Hill, North Carolina, United States of America, **3** Lineberger Comprehensive Cancer Center/Department of Epidemiology, University of North Carolina at Chapel Hill, Chapel Hill, North Carolina, United States of America, **4** Biomedical Research Imaging Center, University of North Carolina at Chapel Hill, Chapel Hill, North Carolina, United States of America

Abstract

The human mammary gland is a complex and heterogeneous organ, where the interactions between mammary epithelial cells (MEC) and stromal fibroblasts are known to regulate normal biology and tumorigenesis. We aimed to longitudinally evaluate morphology and size of organoids in 3D co-cultures of normal (MCF10A) or pre-malignant (MCF10DCIS.com) MEC and hTERT-immortalized fibroblasts from reduction mammoplasty (RMF). This co-culture model, based on an isogenic panel of cell lines, can yield insights to understand breast cancer progression. However, 3D cultures pose challenges for quantitative assessment and imaging, especially when the goal is to measure the same organoid structures over time. Using optical coherence tomography (OCT) as a non-invasive method to longitudinally quantify morphological changes, we found that OCT provides excellent visualization of MEC-fibroblast co-cultures as they form ductal acini and remodel over time. Different concentrations of fibroblasts and MEC reflecting reported physiological ratios [1] were evaluated, and we found that larger, hollower, and more aspherical acini were formed only by pre-malignant MEC (MCF10DCIS.com) in the presence of fibroblasts, whereas in comparable conditions, normal MEC (MCF10A) acini remained smaller and less aspherical. The ratio of fibroblast to MEC was also influential in determining organoid phenotypes, with higher concentrations of fibroblasts producing more aspherical structures in MCF10DCIS.com. These findings suggest that stromal-epithelial interactions between fibroblasts and MEC can be modeled *in vitro*, with OCT imaging as a convenient means of assaying time dependent changes, with the potential for yielding important biological insights about the differences between benign and pre-malignant cells.

Citation: Chhetri RK, Phillips ZF, Troester MA, Oldenburg AL (2012) Longitudinal Study of Mammary Epithelial and Fibroblast Co-Cultures Using Optical Coherence Tomography Reveals Morphological Hallmarks of Pre-Malignancy. PLoS ONE 7(11): e49148. doi:10.1371/journal.pone.0049148

Editor: Edna Cukierman, Fox Chase Cancer Center, United States of America

Received May 10, 2012; **Accepted** October 9, 2012; **Published** November 12, 2012

Funding: This research was supported by a grant from the Carolina Cancer Center for Nanotechnology Excellence (C-CCNE NIH (National Cancer Institute) #U54CA119343) and by startup funds at UNC-Chapel Hill. M.A.T. lab was supported in the development of the co-culture model system by grants from National Cancer Institute and National Institute of Environmental Health Sciences (U01019472 and R01- CA138255). The funders had no role in study design, data collection and analysis, decision to publish, or preparation of the manuscript.

Competing Interests: The authors have declared that no competing interests exist.

* E-mail: aold@physics.unc.edu

Introduction

The human mammary gland consists of a series of branching ducts, with each branch terminating as a hollow and spherical acinus. Each acinus is predominantly comprised of luminal epithelial cells surrounded by basal/myoepithelial cells, but is supported and regulated by an intricate network of other cell types. Chemical and physical interactions between epithelia and surrounding stroma are essential for the organ's development and physiological functions. This intricate network of cells is a complex microenvironment [2] that maintains normal tissue architecture (homeostasis) and suppresses malignant phenotypes in healthy individuals [3], but becomes permissive or even promotes cancer during progression [4]. Thus, interactions between mammary epithelial cells (MEC) and stromal fibroblasts are regulators of tumorigenesis [4,5], with stroma playing a vital role in the proliferation and organization of MEC, production of extracellular matrix (ECM), and regulation of cellular adhesion and migration [4].

Fibroblasts are strongly associated with mammary epithelium, and in the vicinity of tumors, become a major cell type of the stroma [6]. These cancer-associated fibroblasts appear to promote tumor growth and facilitate the progression of breast cancer [7]. Conversely, normal fibroblasts may inhibit progression of cancer [8]. Our previous studies have illustrated that fibroblasts have distinct interactions with breast cancer subtype [9], with aggressive basal-like breast cancer cells [10] interacting with fibroblasts to produce a wide range of growth factors and cytokines that may in turn promote migration and/or proliferation of the cancer cells. However, the evolution of these interactions during breast cancer progression has not yet been well characterized. By comparing normal and pre-malignant MEC co-cultured with RMF in 3D,

and by modulating the ratios of the two cell types, we aimed to elucidate how stromal-epithelial interactions modulate morphological changes in acini.

Our previous studies on interactions between breast cancer cells and fibroblasts have relied on 2D cultures [9], but 3D co-culture models offer an interface between these studies and *in vivo* studies given their ability to recapitulate several aspects of tissue behavior [11–13]. Novel tools that image the 3D breast microenvironment can elucidate micron-scale morphological changes during the dynamic chemical and physical signaling processes between mammary cell types. To date, a majority of the studies of stromal-epithelial co-cultures have utilized imaging techniques that require sample fixation and often sectioning [14], which can perturb the native architecture and present challenges for longitudinal studies. To address these limitations, optical coherence tomography (OCT), which can assess cellular dynamics in 3D tissue models [15], was employed to non-invasively capture the 3D architecture of breast tissue models.

OCT represents an emerging medical and biological optical imaging modality [16–19], that performs cross-sectional imaging of internal microstructures in tissues by measuring the magnitude and echo time delay of backscattered, near-infrared light. OCT provides micron-scale resolution for cellular imaging, and rejects multiply scattered light, unlike confocal microscopy, which enables imaging up to 2–3 millimeters in depth. This depth is ideal for assessing subsurface structures such as 3D tissue cultures [15]. Simultaneously, the non-invasive nature of OCT enables longitudinal studies in the same samples, avoiding the need to excise and process tissue specimens [20]. Recent studies have demonstrated the feasibility of OCT to provide image-guidance by scanning tumor margins during breast-sparing surgery [21,22], and to identify invasive breast carcinomas in biopsy tissue [23]. OCT imaging has also been employed on unstained, *ex vivo* breast cancer tissues to identify morphological features, similar to histology [24,25]. Additionally, computational methods to perform pattern analysis of OCT biopsies have been implemented to identify invasive breast carcinomas [26,27]. Thus, OCT has translational potential with applications in basic studies and *in vivo* clinical imaging. As such, OCT imaging offers a unique platform for evaluating the architecture of MEC grown in 3D co-cultures.

The aim of this study was to define morphological hallmarks of stromal-epithelial interactions using OCT to assess 3D *in vitro* cultures comprised of basal-like mammary epithelial cell lines (normal MCF10A, and pre-malignant MCF10DCIS.com) [28] and hTERT-immortalized fibroblasts from reduction mammoplasty (RMF). As shown below, we found distinct morphological features between acini formed by normal MCF10A cells and pre-malignant MCF10DCIS.com cells as a function of fibroblast concentration.

Methods

Cell Lines

MCF10A and MCF10DCIS.com cells were obtained from the Barbara Ann Karamanos Cancer Institute (Detroit, MI). MCF10A cells are spontaneously immortalized MEC derived from the human breast tissue of a 36-year-old patient [29], and exhibit numerous features of normal breast epithelium including lack of tumorigenicity and dependence on growth factors and hormones for proliferation and survival [29]. Importantly, MCF10A cells in 3D cultures form stable acinar structures recapitulating the behavior of glandular epithelium seen *in vivo* [30]. MCF10DCIS. -com cells are cloned from xenograft lesions of MCF10A and form DCIS-like lesions [31]. Importantly, MCF10DCIS.com cells have the same genetic background as the MCF10A, and are primed for invasive transition under key microenvironmental conditions, requiring no additional genomic changes to become invasive [31]. The MCF10A and MCF10DCIS.com cells were co-cultured with hTERT-immortalized fibroblasts from reduction mammoplasty (RMF), a gift from Charlotte Kuperwasser at Tufts University [32]. All cells used in this experiment were maintained prior to use in 2D cultures in Dulbecco's Modified Eagle Medium/Nutrient Mixture F-12 (DMEM/F12) containing 5% horse serum, 20 ng/mL Epidermal Growth Factor (EGF), 0.5 μg/mL hydrocortisone, 100 ng/mL cholera toxin, 10 μg/μL insulin, and 1% penicillin-streptomycin, and kept in a humidified incubator at 37°C and 5% CO_2 [12].

3D Culture Preparation

The 3D extracellular scaffold used in this study consisted of biologically derived collagen I and Matrigel® (BD Biosciences). Compared to collagen I gels, Matrigel-collagen I gels were found to be structurally more stable and thus less prone to loss over the duration of the study due to several cycles of media replenishments, as has been previously noted [33]. For 3D cell culture, a Matrigel-collagen I mixture was prepared on ice using a 1:1volume ratio, with collagen I at a concentration of 1 mg/mL, according to procedures described by Johnson *et. al.* [34]. Once the MEC and RMF were nearly 100% confluent in 2D, they were seeded at varying concentrations into the Matrigel-collagen I gel for growth in 3D, as follows: A total of 27 3D cultures were prepared, which included 9 co-cultures of normal MEC and RMF, 9 co-cultures of pre-malignant MEC and RMF, and 3 monocultures each of normal MEC, pre-malignant MEC, and RMF. Briefly, the following protocol was used for all co-cultures. 85 μL of Matrigel-collagen I was used to coat the bottom of 10 mm diameter tissue culture microwells, and was allowed to solidify for 30 minutes at 37°C. Then, 180 μL of Martrigel-collagen I gel was mixed with MEC and RMF according to procedures described in [9] to obtain the desired final seed concentrations. The seed concentrations of MEC and RMF in the Martigel-collagen I gels were varied as 30,000 cells/cm^3, 90,000 cells/cm^3, 270,000 cells/cm^3 and control, and were plated and allowed to solidify for 30 minutes at 37°C. After gelation, 250 μL of growth media (same as in 2D cultures above) was applied to the surface of each 3D culture. Cultures were maintained under optimum growth conditions (humidified, 37°C with 5% CO_2) for 2–4 weeks, during which the medium was changed every 2–3 days.

Although the co-cultures were maintained for 4 weeks (Figure S4, Table S1), proliferation of the cells in the co-cultures was no longer in the log-phase of growth after week 2, as evidenced by a plateau in the number of MEC per acinus (Figure S5). Similarly, co-cultures with higher seeded cell concentration (MEC concentration >90,000/cm^3) also remained in log-phase for only a short time (Figure S5). We selected only monocultures and co-cultures that were still in log-phase to avoid artifacts in morphology caused by resource scarcity or cellular crowding.

OCT Imaging

Imaging of the 3D cultures was performed using a custom, ultrahigh-resolution, spectral-domain optical coherence tomography (SD-OCT) system as described in detail previously [35]. The OCT system employed a low-coherence light source consisting of a Ti:Sapphire laser (Griffin, KMLabs, Inc.) with a central wavelength of 800 nm and a bandwidth of 125 nm. A detailed description of the OCT system and the system diagram is provided in the supplementary (Figure S1). The axial (depth, *z*) resolution of the imaging system owing to the wavelength and the bandwidth of

the light source is 3 μm in air. In the sample arm, 3D cultures were illuminated by a 10 mW beam focused by a 30 mm focal length achromatic lens, which provides a resolution of 12 μm (air) in the transverse (*x* and *y*) directions. Transverse raster-scanning over the sample was achieved using galvanometer-controlled mirrors. OCT imaging was performed on each of the live 3D cultures weekly for 4 weeks. OCT image-stacks were acquired over 3×1.5×1.5 mm (in gel) into 1000×101×1024 pixels (*x*, *y*, and *z* dimensions respectively) with an acquisition time of 40 ms per *x*-*z* image. The OCT image-stacks were resampled into an isotropic pixel resolution of 1.55 μm after correcting for the refractive index of the aqueous gels, and are logarithmically scaled and displayed in a "hot" color map using MATLAB® (2011a, MathWorks).

Image Analysis

2D analysis of OCT images was performed to determine the maximum acinar and lumen areas. From the color-mapped OCT images, cell clusters resembling acini were selected as shown in Figure 1A. The OCT image containing the central position of each acinus was determined by sifting through the OCT image-stack to find the image with the largest acinus size. The overall acinus area (cells plus lumen) and lumen area were segmented within these central OCT images using ImageJ, as shown in Figure 1B. The results were tabulated for each culture, from which the mean acini area, mean lumen area, and their associated standard errors were evaluated.

As depicted in Figures 1C and 1D, iso-surface rendering of the OCT image stacks enables visualization of the entire 3D acinar structure. In order to quantify the 3D morphology of the acini, we computed the asphericity, that is, the deviation in acini shape from that of a perfect sphere. We defined asphericity as the ratio between the volume of a perfect sphere having the same surface area as that of the acinus, S_{acini}, and the measured volume of each acinus, V_{acini}, according to [36]:

$$Asphericity = \frac{(S_{acini})^{3/2}}{3 \times (4\pi)^{1/2} \times V_{acini}} \quad (1)$$

where S_{acini} is in pixels^2, and V_{acini} is in pixels^3. Asphericity is equal to 1 for a perfect sphere and increases for irregularly shaped objects. Thus, asphericity provides a size-independent measurement of how aspherical a 3D structure is, which aids in quantifying surface irregularities across renderings of various sizes.

To compute V_{acini}, OCT images were first median filtered, and a 3D mask of each acinus was obtained by thresholding the OCT image stack. Then, the 'bwboundries' command in MATLAB was applied to each 2D image in the stack to find the boundaries of thresholded objects and to "fill in" any child objects, such as the lumen. Subsequently, stray objects that did not have any voxel overlap with the acini were removed from the 3D mask, to obtain just the acini. The volume, V_{acini}, was then computed by counting the voxels comprising the mask. Using simulated data with known geometries, it was verified that this method accurately estimated the volume of the 3D rendered object.

To compute S_{acini}, the voxels comprising the boundary of the 3D mask were counted. Due to digitization noise, a pixelation correction factor of 1.5 was needed to obtain the correct value of surface area, which corrects for pixel connectivity. This was determined in MATLAB by comparing the measured surface area to the actual surface area of spheres and ellipsoids. Above a radius of 15 pixels and for values of asphericity from 1–8, the pixelation correction factor converged to 1.5; all acini analyzed in this study had radii and asphericities within these valid ranges.

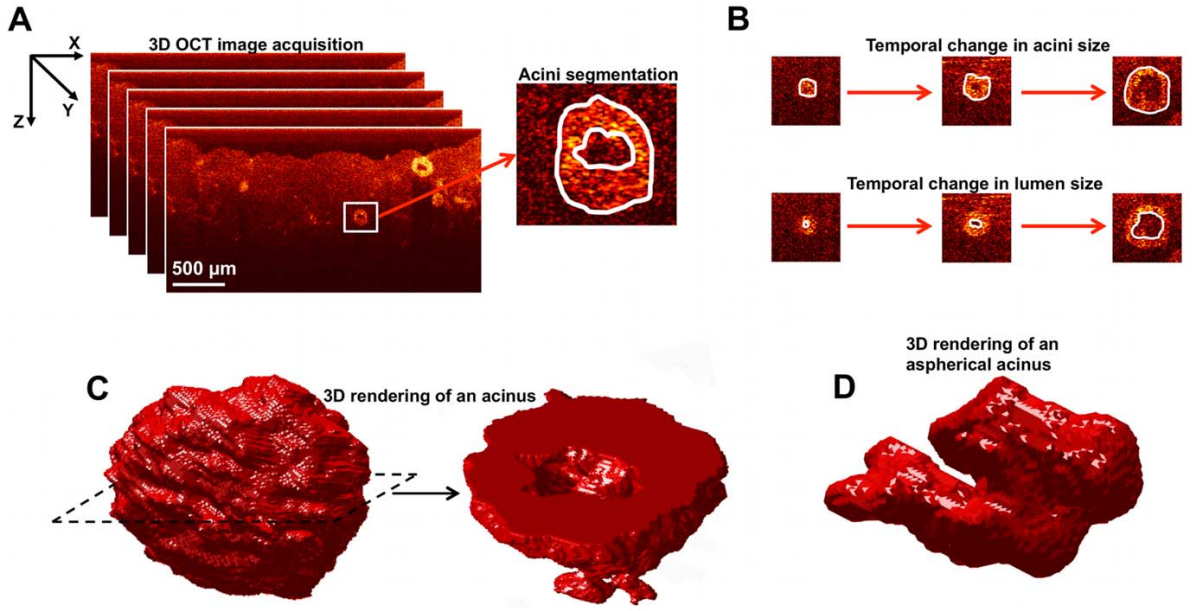

Figure 1. 3D-OCT image acquisition of the co-cultures, and analysis of the shape and size of acini. A. 3D-OCT image acquistion: the surface of the gel is aligned near the top of each image, and the depth-resolved light scattering from cells beneath the gel surface is apparent at depths up to ~1 mm; segmentation of acini to characterize the overall size and the lumen is also shown. B. Temporal changes in acini and lumen sizes analyzed from 3D-OCT images of the co-cultures. C. An example isosurface rendering of an acinus from a 3D-OCT image-stack; slicing of the rendered volume clearly shows the lumen. D. An example 3D rendering of an aspherical acinus.
doi:10.1371/journal.pone.0049148.g001

Results

OCT offers excellent visualization of cellular acini, as shown with representative OCT *x-z* images of the cell cultures in 3D matrices at 1 week (Figure 1A). Representative images in all 3D cultures at weeks 1 and 2 can be seen in supplementary (Figure S2 and S3). At week 1, the MEC organize into spherical clusters (acini) with some clusters showing signs of a lumen at the center (Figure 1B, representative example). At week 2, the acini are observed to have grown in size, displaying larger and more distinct central lumens. The control gel with no cells shows a homogeneous Matrigel:collagen I structure, which was stable throughout the duration of the study. As expected, no spherical clusters were observed in RMF monocultures. Instead, RMF monocultures revealed a fibrous optical scattering pattern characteristic of fibroblasts. As the RMF concentration was increased, a higher density of fibrous structures was observed, corresponding to added rigidity of the matrix.

OCT images of co-cultures reveal a complex pattern of growth and interaction between RMF and the MEC, similar to *in vivo* mammary architecture. Importantly, unlike other techniques that involve slicing, fixing and staining of the gels, these images depict the unperturbed states of the live MEC and RMF *in vitro*. Thus the images were used to measure lumen size, acini size (Figure 1B) and to estimate the shape, characterizing cells on a continuum between spherical (*e.g.* in Figure 1C) and aspherical (*e.g.* in Figure 1D).

During the first two weeks of the study, both acini and lumen sizes increased (Figure 2). In normal MEC, the stromal:epithelial ratio did not impact acini and lumen sizes; co-cultures were seeded with 30,000 MCF10A/cm^3, and as the seed concentration of RMF was increased from 30,000 RMF/cm^3 to 90,000 RMF/cm^3, no significant difference was seen in acini sizes (Student's t-test, p-value = 0.43) or lumen sizes (Student's t-test, p-value = 0.71) at week 2. However, the size of pre-malignant MEC acini varied in association with stromal content. In co-cultures seeded with 30,000 MCF10DCIS.com/cm^3, as the seed concentration of RMF was increased from 30,000 RMF/cm^3 to 90,000 RMF/cm^3, statistically significant differences were seen in acini size (Student's t-test, p-value <0.05) and lumen size (Student's t-test, p-value <0.05) at week 2. In addition, comparing MCF10A to MCF10DCIS acini at week 2, MCF10DCIS.com:RMF co-cultures showed significantly larger acini and lumen sizes across the same seed concentrations (Student's t-test, p-value <0.005). The stimulatory effect of increased fibroblast concentration on pre-malignant MCF10DCIS.com suggests unique molecular and/or mechanical interactions that stimulate abnormal growth that are not observed in the MCF10A cells.

In addition to changes in acini and lumen sizes, MCF10DCIS.com cells also responded to co-culture with increasingly aspherical structures. Since asphericity is a size-independent metric, as expected, no significant correlation was found between asphericity and acini or lumen sizes in both MCF10A and MCF10DCIS.com cultures. Figure 3 shows the asphericity of the rendered acini in monocultures of MCF10A, MCF10DCIS.com, and co-cultures of these cells with increasing concentrations of RMF (30,000 RMF/cm^3 to 90,000 RMF/cm^3). Again, in normal cells at week 2, fibroblasts did not affect asphericity; monoculture seeded with 30,000 MCF10A/cm^3 and co-cultures seeded with 30,000 MCF10A/cm^3 had similar asphericity values. In contrast, at week 2, the MCF10DCIS.com:RMF co-cultures seeded with 30,000 MCF10DCIS/cm^3 had significantly increased asphericity relative to monocultures (Student's t-test, p-value <0.005). Thus, acini formed by pre-malignant MCF10DCIS.com cells in the presence of RMF undergo a higher degree of shape difference than do acini formed by normal MCF10A cells. The observed higher asphericity values in MCF10DCIS.com acini compared to MCF10A acini in presence of RMF highlights the role of fibroblasts in varying the morphology of the acini.

In summary, these observations show that fibroblasts differentially modulate the shape and size of acini comprised of pre-malignant and normal MEC.

Discussion

The application of OCT to 3D co-cultures of MEC and RMF provided excellent visualization of acinar development over time and recapitulation of *in vivo* morphologies. Acini formed by MCF10A cells in 3D co-cultures were found to be comparable in size to freshly explanted acini previously reported [30]. Observations of increased acini size, lumen size, and asphericity in pre-malignant MCF10DCIS.com co-cultures compared to normal MCF10A co-cultures, and the distinct influence of fibroblast concentration on these phenotypes, suggest that changes over time in stromal-epithelial interactions in 3D co-culture models can be detected using OCT. Interestingly, while acini morphogenesis in DCIS *in vivo* is typically envisioned as progressive invasion into the lumen by the proliferating carcinoma cells [6], our non-invasive study of live 3D co-cultures revealed no such invasion of MCF10DCIS.com into the luminal spaces. However, the formation of luminal space was expected based on *in vivo* studies, as the MCF10DCIS.com cells are comedo-type DCIS [37]. This reinforces the advantage of using OCT to non-invasively and longitudinally probe the same live co-cultures; traditional techniques require slicing, fixing and staining of repeat co-cultures at each time point, which can perturb the natural state and architecture of the organoids. A previous 3D tissue study in MEC monocultures has identified four distinct breast cell line colony morphologies: round, mass, grape-like and stellate [13]. In that study, MCF10A acini are identified as round. A comparatively gentle treatment of the 3D cultures may account for the ability of this system to detect morphology reflective of the unique *in vivo* characteristics of comedo-type DCIS. The ability to regularly probe the same samples longitudinally also avoids problems associated with sample-to-sample variability. In addition, OCT enabled rapid collection of volumetric data with a scan time of 90 seconds per culture, which, at the time of the study, was limited by software and has recently been sped to 4 seconds per culture.

Previous research has highlighted differences between mechanical stromal-epithelial interactions (MEC and fibroblasts in physical contact), and chemical stromal-epithelial interactions (MEC and fibroblasts separated by a barrier allowing passage of soluble signals) [9]. Our results further indicated a difference in stromal-epithelial interactions between fibroblasts and normal or pre-malignant MEC, as evidenced by pronounced differences in morphological features. A number of previous studies have demonstrated that co-cultures with DCIS cells can provide interesting insights regarding signaling and phenotypes of malignant progression [38]. Indeed, our co-cultures mirrored many of the phenotypes previously observed in mammary epithelial monocultures [12,39], while also providing fibroblast-dependent morphological change over time in the same samples. The ability to study phenotypes over time offers the opportunity to study the molecular switches that may regulate or be regulated by the mechanical changes in 3D co-cultures. Only studies of perturbations induced over time will be able to distinguish cause and effect for key molecular effectors such as HGF (hepatocyte growth factor)-signaling [38]. In such studies, the variation of matrix

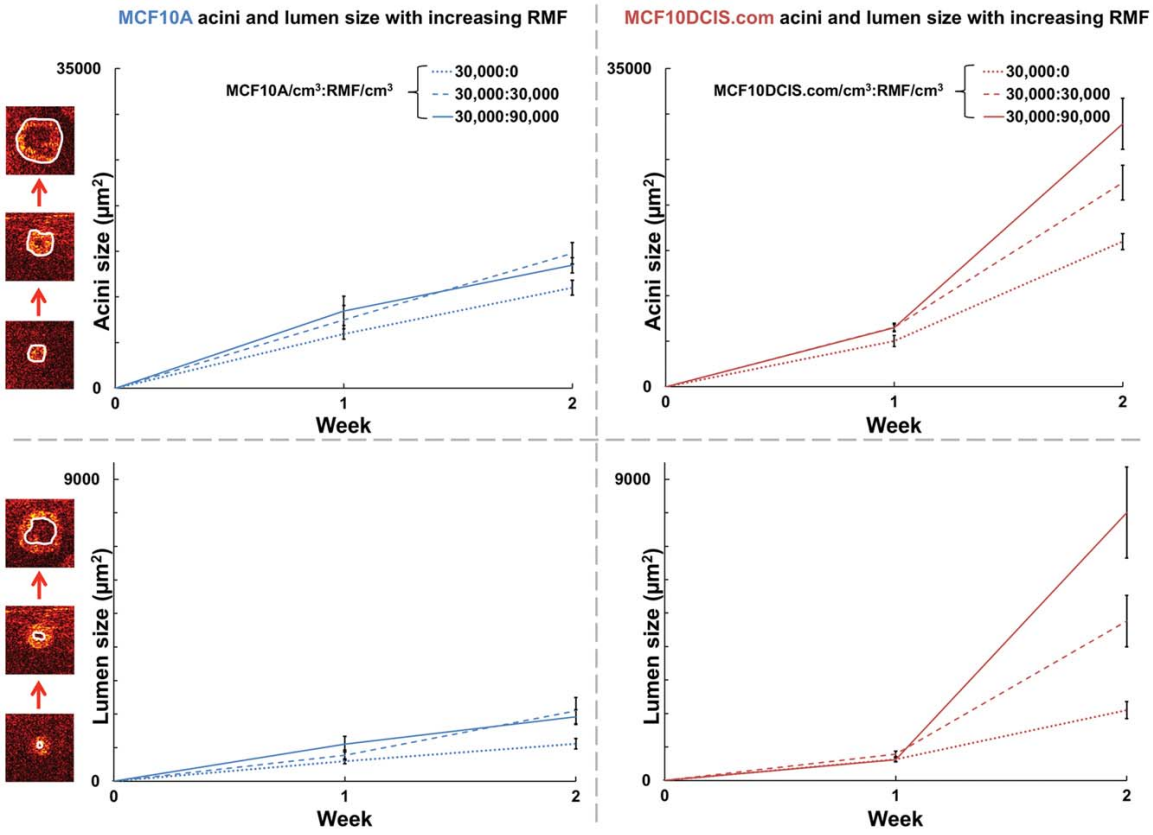

Figure 2. Acini and lumen size. Comparison of MCF10A:RMF co-cultures with MCF10DCIS.com:RMF co-cultures shows significantly larger acini and lumen sizes (Student's t-test, p-value <0.005) at week 2. In MCF10DCIS.com:RMF co-cultures, acini and lumen size are also observed to be highly modulated by the ratio of fibroblasts.
doi:10.1371/journal.pone.0049148.g002

stiffness can be achieved by varying the collagen I concentration in the Matrigel:collagen I mixture [34,40]. Our current study in a well-characterized, progressive 3D co-culture series, establishes OCT as a convenient platform for such future studies.

Future studies would also benefit from merging longitudinal evaluation of morphology with studies of RNA and protein expression from whole genome microarrays performed using a bioinformatics approach [9]. Previous work by Kenny, *et al*,

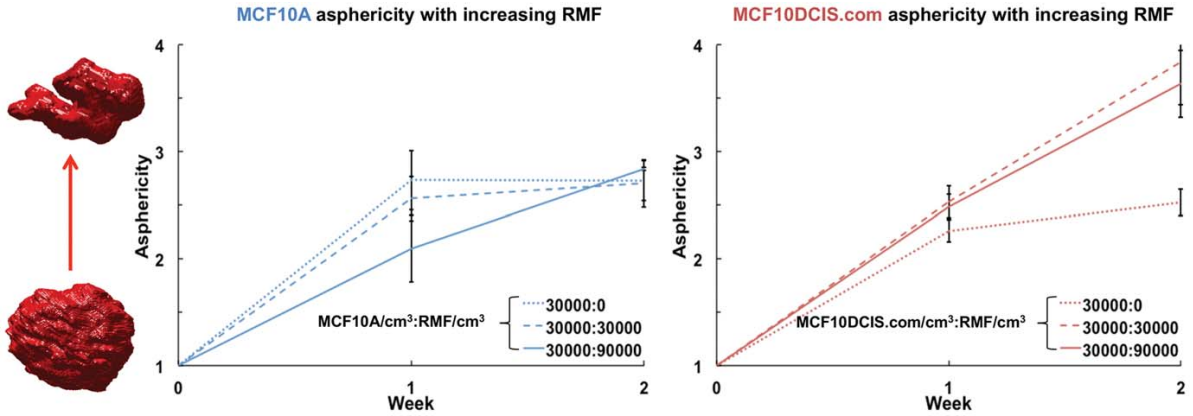

Figure 3. Asphericity of acini. The minimum asphericity value of 1 indicates a perfect sphere, while less spherical acini have higher asphericity values. Acini comprised of MCF10DCIS.com cells are seen to become increasingly aspherical in the presence of fibroblasts.
doi:10.1371/journal.pone.0049148.g003

correlated four distinct morphologies of MEC colonies (round, mass, grape-like, and stellate) with gene expression [13], although no data is yet available to show time- or co-cultured fibroblast-dependent morphological changes. Morphological characteristics are likely parallel to molecular phenotypic changes, and an imaging-based biomarker of shifts in molecular phenotype could allow advances in our understanding of the physical and mechanical regulation of molecular signaling. For example, previous xenograft studies have shown that MCF10DCIS.com cells are more invasive than MCF10A cells, and are enriched for expression of lymphangiogenesis markers [41]. These xenografts highlight that the breast cancer microenvironment is comprised of many cell types, and while the fibroblast is a highly abundant stromal cell type, there are many other possible contributors and mediators of the complex paracrine communication in breast tissue. However, the simplified 3D model of MEC and fibroblasts mirrors xenografts in its ability to track acini growth and asphericity, and therefore may be an *in vitro* approach to studying invasive potential.

We also note that the association between premalignant cells and high asphericity observed in this study may be related to previous studies establishing a connection between tissue structural complexity (in a mathematical sense, such as fractal dimension) and various cancers [42–44]. While asphericity is not a measure of complexity *per se*, acini with a high fractal dimension would be expected to have a high asphericity. Tying the efforts reported here in engineered tissues with OCT imaging and morphological analysis of real breast cancer tissues [22,23,26,27] may lead to new mechanistic insight, and may also translate to clinical OCT imaging efforts, such as those in surgical guidance during breast cancer surgery [21].

Supporting Information

Figure S1 Schematic diagram of the OCT system. The ultrahigh resolution SD-OCT system is comprised of a Ti:Sapphire laser, a Michelson interferometer, and a high speed spectrometer (details in text). FS: fiber to free-space coupler, SF: free-space to fiber coupler.
(TIF)

Figure S2 Representative OCT x-z images of 3D human mammary tissue cultures at week 2. As indicated, the seed concentration of MEC is increasing from top to bottom, and the seed concentration of RMF is increasing from left to right.
(TIF)

Figure S3 Representative OCT x-z images of 3D human mammary tissue cultures at week 4. As indicated, the seed concentration of MEC is increasing from top to bottom, and the seed concentration of RMF is increasing from left to right.
(TIF)

Figure S4 Acini size analysis. Histogram of average acini sizes (in μm^2) in each gel formed by the normal and pre-malignant MECs, based on the OCT images acquired weekly for 4 weeks. Error bars indicate the standard error of the measured values.
(TIF)

Figure S5 Number of MCF10A and MCF10DCIS.com cells in acini with increasing fibroblasts. Lack of proliferation between week 2 and week 3 is evident from the decrease in number of MEC per acinus.
(TIF)

Table S1 Number of acini in 3D cultures at week 4. Acini count in an approximate gel volume of 4.5 mm^3 at week 4 for monocultures of MCF10A and MCF10DCIS.com, and co-cultures of MCF10A:RMF and MCF10DCIS.com:RMF.
(DOC)

File S1 Supplementary.
(DOC)

Acknowledgments

The authors acknowledge the assistance of Timothy O' Brien in the Computer Integrated Systems for Microscopy and Manipulation (CISMM) at UNC-Chapel Hill, J. Terese Camp in the Lineberger Comprehensive Cancer Center at UNC-Chapel Hill, Patricia Casbas-Hernandez in the Department of Pathology and Laboratory Medicine at UNC-Chapel Hill, and Jason M. Cooper in Applied Science - Biomedical Engineering at UNC-Chapel Hill.

Author Contributions

Conceived and designed the experiments: RKC ZFP MAT ALO. Performed the experiments: RKC ZFP MAT ALO. Analyzed the data: RKC ZFP MAT ALO. Contributed reagents/materials/analysis tools: RKC ZFP MAT ALO. Wrote the paper: RKC ZFP MAT ALO.

References

1. Sadlonova A, Novak Z, Johnson MR, Bowe DB, Gault SR, et al. (2005) Breast fibroblasts modulate epithelial cell proliferation in three-dimensional in vitro co-culture. Breast cancer research: BCR 7: R46–59.
2. Gefen A, Dilmoney B (2007) Mechanics of the normal woman's breast. Technology and health care: official journal of the European Society for Engineering and Medicine 15: 259–271.
3. Nelson CM, Bissell MJ (2006) Of extracellular matrix, scaffolds, and signaling: tissue architecture regulates development, homeostasis, and cancer. Annual review of cell and developmental biology 22: 287–309.
4. Bissell MJ, Radisky D (2001) Putting tumours in context. Nature reviews Cancer 1: 46–54.
5. Maller O, Martinson H, Schedin P (2010) Extracellular matrix composition reveals complex and dynamic stromal-epithelial interactions in the mammary gland. Journal of mammary gland biology and neoplasia 15: 301–318.
6. Kalluri R, Zeisberg M (2006) Fibroblasts in cancer. Nature reviews Cancer 6: 392–401.
7. Orimo A, Gupta PB, Sgroi DC, Arenzana-Seisdedos F, Delaunay T, et al. (2005) Stromal fibroblasts present in invasive human breast carcinomas promote tumor growth and angiogenesis through elevated SDF-1/CXCL12 secretion. Cell 121: 335–348.
8. Dong-Le Bourhis X, Berthois Y, Millot G, Degeorges A, Sylvi M, et al. (1997) Effect of stromal and epithelial cells derived from normal and tumorous breast tissue on the proliferation of human breast cancer cell lines in co-culture. International journal of cancer Journal international du cancer 71: 42–48.
9. Camp JT, Elloumi F, Roman-Perez E, Rein J, Stewart DA, et al. (2011) Interactions with fibroblasts are distinct in Basal-like and luminal breast cancers. Molecular cancer research: MCR 9: 3–13.
10. Perou CM, Sørlie T, Eisen MB, van de Rijn M, Jeffrey SS, et al. (2000) Molecular portraits of human breast tumours. Nature 406: 747–752.
11. Weaver VM, Lelièvre S, Lakins JN, Chrenek M a, Jones JCR, et al. (2002) Beta4 Integrin-Dependent Formation of Polarized Three-Dimensional Architecture Confers Resistance To Apoptosis in Normal and Malignant Mammary Epithelium. Cancer cell 2: 205–216.
12. Debnath J, Muthuswamy SK, Brugge JS (2003) Morphogenesis and oncogenesis of MCF-10A mammary epithelial acini grown in three-dimensional basement membrane cultures. Methods 30: 256–268.
13. Kenny P a, Lee GY, Myers C a, Neve RM, Semeiks JR, et al. (2007) The morphologies of breast cancer cell lines in three-dimensional assays correlate with their profiles of gene expression. Molecular oncology 1: 84–96.
14. Krause S, Maffini MV, Soto AM, Sonnenschein C (2010) The microenvironment determines the breast cancer cells' phenotype: organization of MCF7 cells in 3D cultures. BMC cancer 10: 263.
15. Tan W, Oldenburg AL, Norman JJ, Desai TA, Boppart SA (2006) Optical coherence tomography of cell dynamics in three-dimensional tissue models. Optics Express 14: 7159.
16. Tearney GJ, Brezinski ME, Bouma BE, Boppart SA, Pitris C, et al. (1997) In Vivo Endoscopic Optical Biopsy with Optical Coherence Tomography. Science 276: 2037–2039.

17. Boppart SA, Bouma BE, Pitris C, Tearney GJ, Southern JF, et al. (1998) Intraoperative assessment of microsurgery with three-dimensional optical coherence tomography. Radiology 208: 81–86.
18. Fujimoto JG, Drexler W, Schuman JS, Hitzenberger CK (2009) Optical Coherence Tomography (OCT) in ophthalmology: introduction. Optics Express 17: 3978–3979.
19. Brezinski ME, Tearney GJ, Bouma BE, Boppart SA, Hee MR, et al. (1996) Imaging of coronary artery microstructure (in vitro) with optical coherence tomography. The American journal of cardiology 77: 92–93.
20. Boppart SA, Bouma BE, Pitris C, Southern JF, Brezinski ME, et al. (1998) In vivo cellular optical coherence tomography imaging. Nature Medicine 4: 861–865.
21. Boppart SA, Luo W, Marks DL, Singletary KW (2004) Optical coherence tomography: feasibility for basic research and image-guided surgery of breast cancer. Breast cancer research and treatment 84: 85–97.
22. Nguyen FT, Zysk AM, Chaney EJ, Kotynek JG, Oliphant UJ, et al. (2009) Intraoperative evaluation of breast tumor margins with optical coherence tomography. Cancer research 69: 8790–8796.
23. Zysk AM, Nguyen FT, Chaney EJ, Kotynek JG, Oliphant UJ, et al. (2009) Clinical feasibility of microscopically-guided breast needle biopsy using a fiber-optic probe with computer-aided detection. Technology in cancer research & treatment 8: 315–321.
24. Latrive A, Boccara AC (2011) In vivo and in situ cellular imaging full-field optical coherence tomography with a rigid endoscopic probe. Biomedical Optics Express 2: 2897.
25. McLaughlin R a, Scolaro L, Robbins P, Hamza S, Saunders C, et al. (2010) Imaging of human lymph nodes using optical coherence tomography: potential for staging cancer. Cancer research 70: 2579–2584.
26. Zysk AM, Boppart SA (2006) Computational methods for analysis of human breast tumor tissue in optical coherence tomography images. Journal of biomedical optics 11: 054015.
27. Sullivan AC, Hunt JP, Oldenburg AL (2011) Fractal analysis for classification of breast carcinoma in optical coherence tomography. Journal of biomedical optics 16: 066010.
28. Neve RM, Chin K, Fridlyand J, Yeh J, Baehner FL, et al. (2006) A collection of breast cancer cell lines for the study of functionally distinct cancer subtypes. Cancer cell 10: 515–527.
29. Soule HD, Maloney TM, Wolman SR, Peterson WD, Brenz R, et al. (1990) Isolation and characterization of a spontaneously immortalized human breast epithelial cell line, MCF-10. Cancer research 50: 6075–6086.
30. Petersen OW, Rønnov-Jessen L, Howlett a R, Bissell MJ (1992) Interaction with basement membrane serves to rapidly distinguish growth and differentiation pattern of normal and malignant human breast epithelial cells. Proceedings of the National Academy of Sciences of the United States of America 89: 9064–9068.
31. Miller FR, Santner SJ, Tait L, Dawson PJ (2000) MCF10DCIS.com xenograft model of human comedo ductal carcinoma in situ. Journal of the National Cancer Institute 92: 1185–1186.
32. Proia D a, Kuperwasser C (2006) Reconstruction of human mammary tissues in a mouse model. Nature protocols 1: 206–214.
33. Krause S, Maffini MV, Soto AM, Sonnenschein C (2008) A novel 3D in vitro culture model to study stromal-epithelial interactions in the mammary gland. Tissue engineering Part C, Methods 14: 261–271.
34. Johnson KR, Leight JL, Weaver VM (2007) Demystifying the effects of a three-dimensional microenvironment in tissue morphogenesis. Methods in cell biology 83: 547–583.
35. Oldenburg AL, Gallippi CM, Tsui F, Nichols TC, Beicker KN, et al. (2010) Magnetic and contrast properties of labeled platelets for magnetomotive optical coherence tomography. Biophysical journal 99: 2374–2383.
36. Tang J, Enderling H, Becker-Weimann S, Pham C, Polyzos A, et al. (2011) Phenotypic transition maps of 3D breast acini obtained by imaging-guided agent-based modeling. Integrative biology: quantitative biosciences from nano to macro 3: 408–421.
37. Shekhar MPV, Tait L, Pauley RJ, Wu GS, Santner SJ, et al. (2008) Comedo-ductal carcinoma in situ: A paradoxical role for programmed cell death. Cancer biology & therapy 7: 1774–1782.
38. Jedeszko C, Victor BC, Podgorski I, Sloane BF (2009) Fibroblast hepatocyte growth factor promotes invasion of human mammary ductal carcinoma in situ. Cancer research 69: 9148–9155.
39. Debnath J, Brugge JS (2005) Modelling glandular epithelial cancers in three-dimensional cultures. Nature reviews Cancer 5: 675–688.
40. Paszek MJ, Zahir N, Johnson KR, Lakins JN, Rozenberg GI, et al. (2005) Tensional homeostasis and the malignant phenotype. Cancer cell 8: 241–254.
41. Yu M, Tang Z, Alousi S, Berk RS, Miller F, et al. (2007) Expression patterns of lymphangiogenic and angiogenic factors in a model of breast ductal carcinoma in situ. American journal of surgery 194: 594–599.
42. Baish JW, Jain RK (2000) Fractals and cancer. Cancer research 60: 3683–3688.
43. Backman V, Roy HK (2011) Light-scattering technologies for field carcinogenesis detection: a modality for endoscopic prescreening. Gastroenterology 140: 35–41.
44. Tambasco M, Eliasziw M, Magliocco AM (2010) Morphologic complexity of epithelial architecture for predicting invasive breast cancer survival. Journal of translational medicine 8: 140.

References

[1] W. Brown. Light Scattering: Principles and Development. Oxford University Press, USA, 1996.

[2] C. C. Han and A. Z. Akcasu. Scattering and Dynamics of Polymers. Wiley, 2011.

[3] C. S. Johnson Jr. and D. A. Gabriel. Laser Light Scattering. Dover Publications, 1995.

[4] N. A. Clark, J. H. Lunacek, and G. B. Benedek. A Study of Brownian Motion Using Light Scattering. American Journal of Physics, 38(5):575, 1970.

[5] N. Wax. Selected Papers on Noise and Stochastic Processes. Dover Publications, 1954.

[6] D. Magde, E. Elson, and W. Webb. Thermodynamic Fluctuations in a Reacting System Measurement by Fluorescence Correlation Spectroscopy. Physical Review Letters, 29(11):705–708, September 1972.

[7] K. M. Berland, P. T. So, and E. Gratton. Two-photon fluorescence correlation spectroscopy: method and application to the intracellular environment. Biophysical journal, 68(2):694–701, February 1995.

[8] B. E. A. Saleh and M. C. Teich. Fundamentals of Photonics. Wiley-Interscience, 2007.

[9] B. J. Berne and R. Pecora. Dynamic Light Scattering. Dover Publications, 2000.

[10] T. Tanaka and G. B. Benedek. Measurement of the Velocity of Blood Flow (in vivo) Using a Fiber Optic Catheter and Optical Mixing Spectroscopy. Applied optics, 14(1):189–96, January 1975.

[11] B. R. Ware. Electrophoretic light scattering. Advances in Colloid and Interface Science, 4(1):1–44, February 1974.

[12] B. R. Ware and W. H. Flygare. Light scattering in mixtures of BSA, BSA dimers,

and fibrinogen under the influence of electric fields. Journal of Colloid and Interface Science, 39(3):670–675, June 1972.

[13] M. Doi and S. F. Edwards. The Theory of Polymer Dynamics. Oxford University Press, USA, 1988.

[14] A. Ortega and J. Garcia de la Torre. Hydrodynamic properties of rodlike and disklike particles in dilute solution. The Journal of Chemical Physics, 119(18):9914, November 2003.

[15] Y. Han, A. M. Alsayed, M. Nobili, J. Zhang, T. C. Lubensky, and A. G. Yodh. Brownian motion of an ellipsoid. Science, 314(5799):626–30, October 2006.

[16] E. Andablo-Reyes, P. Díaz-Leyva, and J. Arauz-Lara. Microrheology from Rotational Diffusion of Colloidal Particles. Physical Review Letters, 94(10):1–4, March 2005.

[17] W. Brown. Dynamic Light Scattering: The Method and Some Applications. Oxford University Press, USA, 1993.

[18] J. Rodriguez-Fernandez, J. Perez-Juste, L. M. Liz-Marzan, and P. R. Lang. Dynamic Light Scattering of Short Au Rods with Low Aspect Ratios. Journal of Physical Chemistry C, 111(13):5020–5025, April 2007.

[19] D. Mukhija and M. J. Solomon. Translational and rotational dynamics of colloidal rods by direct visualization with confocal microscopy. Journal of colloid and interface science, 314(1):98–106, October 2007.

[20] B. D. Marshall, V. A. Davis, D. C. Lee, and B. A. Korgel. Rotational and translational diffusivities of germanium nanowires. Rheologica Acta, 48(5):589–596, May 2009.

[21] F. C. Cheong and D. G. Grier. Rotational and translational diffusion of copper oxide nanorods measured with holographic video microscopy. Optics Express, 18(7):6555, March 2010.

[22] D. Pine, D. Weitz, P. Chaikin, and E. Herbolzheimer. Diffusing wave spectroscopy. Physical Review Letters, 60(12):1134–1137, March 1988.

[23] A. Wax, C. Yang, R. R. Dasari, and M. S. Feld. Path-length-resolved dynamic light scattering: modeling the transition from single to diffusive scattering. Applied

optics, 40(24):4222–7, August 2001.

[24] G. Popescu, A. Dogariu, and R. Rajagopalan. Spatially resolved microrheology using localized coherence volumes. Physical Review E, 65(4):1–8, April 2002.

[25] G. Popescu and A. Dogariu. Scattering of low coherence radiation and applications. The European Physical Journal Applied Physics, 32(2):73–93, December 2005.

[26] D. A. Boas, K. K. Bizheva, and A. M. Siegel. Using dynamic low-coherence interferometry to image Brownian motion within highly scattering media. Optics Letters, 23(5):319, March 1998.

[27] I. Sohn. Spatially resolved microrheology through a liquid/liquid interface. Journal of Colloid and Interface Science, 269(2):503–513, January 2004.

[28] D. Huang, E. Swanson, C. Lin, J. Schuman, W. Stinson, W Chang, M. Hee, T Flotte, K Gregory, C. Puliafito, and Al. Et. Optical coherence tomography. Science, 254(5035):1178–1181, November 1991.

[29] B. C. Quirk, R. A. McLaughlin, A. Curatolo, R. W. Kirk, P. B. Noble, and D. D. Sampson. In situ imaging of lung alveoli with an optical coherence tomography needle probe. Journal of biomedical optics, 16(3):036009, March 2011.

[30] W. Drexler, U. Morgner, R. K. Ghanta, F. X. Kärtner, J. S. Schuman, and J. G. Fujimoto. Ultrahigh-resolution ophthalmic optical coherence tomography. Nature medicine, 7(4):502–7, April 2001.

[31] M. E. Brezinski, G. J. Tearney, B. E. Bouma, S. A. Boppart, M. R. Hee, E. A. Swanson, J. F. Southern, and J. G. Fujimoto. Imaging of coronary artery microstructure (in vitro) with optical coherence tomography. The American journal of cardiology, 77(1):92–3, January 1996.

[32] C. Pitris, M. E. Brezinski, B. E. Bouma, G. J. Tearney, J. F. Southern, and J. G. Fujimoto. High resolution imaging of the upper respiratory tract with optical coherence tomography: a feasibility study. American Journal of Respiratory and Critical Care Medicine, 157(5 Pt 1):1640–1644, 1998.

[33] G. J. Tearney, M. E. Brezinski, J. F. Southern, B. E. Bouma, S. A. Boppart, and J. G. Fujimoto. Optical biopsy in human urologic tissue using optical coherence tomography. The Journal of urology, 157(5):1915–9, May 1997.

[34] S. A. Boppart, M. E. Brezinski, C. Pitris, and J. G. Fujimoto. Optical coherence tomography for neurosurgical imaging of human intracortical melanoma. Neurosurgery, 43(4):834–41, October 1998.

[35] J. A. Izatt, M. D. Kulkarni, K. Kobayashi, and M. V. Sivak. Optical coherence tomography and microscopy in gastrointestinal tissues. IEEE Journal of Selected Topics in Quantum Electronics, 2(4):1017–1028, 1996.

[36] G. J. Tearney, M. E. Brezinski, B. E. Bouma, S. A. Boppart, C. Pitris, J. F. Southern, and J. G. Fujimoto. In vivo endoscopic optical biopsy with optical coherence tomography. Science, 276(5321):2037–9, June 1997.

[37] S. A. Boppart, W. Luo, D. L. Marks, and K. W. Singletary. Optical coherence tomography: feasibility for basic research and image-guided surgery of breast cancer. Breast cancer research and treatment, 84(2):85–97, March 2004.

[38] F. T. Nguyen, A. M. Zysk, E. J. Chaney, J. G. Kotynek, U. J. Oliphant, F. J. Bellafiore, K. M. Rowland, P. A. Johnson, and S. A. Boppart. Intraoperative evaluation of breast tumor margins with optical coherence tomography. Cancer research, 69(22):8790–6, November 2009.

[39] W. Drexler and J. G. Fujimoto. OCT: Technology and Applications. Springer, 2008.

[40] R. R. Anderson and J. A. Parrish. The optics of human skin. The Journal of investigative dermatology, 77(1):13–9, July 1981.

[41] R. Weissleder. A clearer vision for in vivo imaging. Nature biotechnology, 19(4):316–7, April 2001.

[42] A. F. Fercher, W. Drexler, C. K. Hitzenberger, and T. Lasser. Optical coherence tomography - principles and applications. Reports on Progress in Physics, 66(2):239–303, 2003.

[43] A. Wax and V. Backman. Biomedical Applications of Light Scattering. McGraw-Hill Professional, 2009.

[44] A. F. Fercher, C. K. Hitzenberger, G. Kamp, and S. Y. El-Zaiat. Measurement of intraocular distances by backscattering spectral interferometry. Optics Communications, 117(1-2):43–48, 1995.

[45] G. Hausler and M. W. Lindner. Coherence Radar and Spectral Radar- New Tools for Dermatological Diagnosis. Journal of Biomedical Optics, 3(1):21, January 1998.

[46] M. Wojtkowski, A. Kowalczyk, R. Leitgeb, and A. F. Fercher. Full range complex spectral optical coherence tomography technique in eye imaging. Optics letters, 27(16):1415–7, August 2002.

[47] B. Golubovic, B. E. Bouma, G. J. Tearney, and J. G. Fujimoto. Optical frequency-domain reflectometry using rapid wavelength tuning of a Cr4+:forsterite laser. Optics letters, 22(22):1704–6, November 1997.

[48] F. Lexer, C. K. Hitzenberger, A. F. Fercher, and M. Kulhavy. Wavelength-tuning interferometry of intraocular distances. Applied Optics, 36(25):6548, September 1997.

[49] Y. Zhao, Z. Chen, C. Saxer, S. Xiang, J. F. de Boer, and J. S. Nelson. Phase-resolved optical coherence tomography and optical Doppler tomography for imaging blood flow in human skin with fast scanning speed and high velocity sensitivity. Optics letters, 25(2):114–6, January 2000.

[50] L. Mandel and E. Wolf. Optical Coherence and Quantum Optics. Cambridge University Press, 1995.

[51] R. K. Chhetri, J. Carpenter, R. Superfine, S. H. Randell, and A. L. Oldenburg. Magnetomotive optical coherence elastography for relating lung structure and function in cystic fibrosis. In Proceedings of SPIE, volume 7554, pages 755420–1–755420–10, 2010.

[52] M. A. Bail, G. Hausler, J. M. Hermann, M. W. Lindner, and R. Ringler. Optical coherence tomography with the "spectral radar": fast optical analysis in volume scatterers by short-coherence interferometry. In Proceedings of SPIE, volume 2925, pages 298–303, 1996.

[53] E. A. Swanson, D. Huang, M. R. Hee, J. G. Fujimoto, C. P. Lin, and C. A. Puliafito. High-speed optical coherence domain reflectometry. Optics letters, 17(7):547, April 1992.

[54] M. Choma, M. Sarunic, C. Yang, and J. Izatt. Sensitivity advantage of swept source and Fourier domain optical coherence tomography. Optics express, 11(18):2183–9, September 2003.

[55] B. Baumann, E. Götzinger, M. Pircher, and C. K. Hitzenberger. Single camera based spectral domain polarization sensitive optical coherence tomography. Optics Express, 15(3):1054, February 2007.

[56] C. A. Palmer. Diffraction grating handbook. Richardson Grating Laboratory, 2000.

[57] D. L. Marks, A. L. Oldenburg, J. J. Reynolds, and S. A. Boppart. Digital Algorithm for Dispersion Correction in Optical Coherence Tomography for Homogeneous and Stratified Media. Applied Optics, 42(2):204, 2003.

[58] A. L. Oldenburg and R. K. Chhetri. Digital dispersion compensation for ultrabroad-bandwidth single-camera spectral-domain polarization-sensitive OCT. In Proceedings of SPIE, volume 7889, pages 78891V–78891V–6, 2011.

[59] R. H. Doremus. Optical Properties of Small Gold Particles. The Journal of Chemical Physics, 40(8):2389, 1964.

[60] U. Kreibig and P. Zacharias. Surface plasma resonances in small spherical silver and gold particles. Zeitschrift fur Physik, 231(2):128–143, April 1970.

[61] J. Yguerabide and E. E. Yguerabide. Light-scattering submicroscopic particles as highly fluorescent analogs and their use as tracer labels in clinical and biological applications. Analytical biochemistry, 262(2):157–76, September 1998.

[62] D. I. Gittins and F. Caruso. Biological and physical applications of water-based metal nanoparticles synthesised in organic solution. Chemphyschem : a European journal of chemical physics and physical chemistry, 3(1):110–3, January 2002.

[63] K. S. Lee and M. A. El-Sayed. Gold and silver nanoparticles in sensing and imaging: sensitivity of plasmon response to size, shape, and metal composition. The journal of physical chemistry. B, 110(39):19220–5, October 2006.

[64] M. A. Van Dijk, A. L. Tchebotareva, M. Orrit, M. Lippitz, S. Berciaud, D. Lasne, L. Cognet, and B. Lounis. Absorption and scattering microscopy of single metal nanoparticles. Physical chemistry chemical physics : PCCP, 8(30):3486–95, August 2006.

[65] R. A. Sperling, P. R. Gil, F. Zhang, M. Zanella, and W. J. Parak. Biological applications of gold nanoparticles. Chemical Society Reviews, 37(9):1896–908,

September 2008.

[66] C. J. Murphy, A. M. Gole, J. W. Stone, P. N. Sisco, A. M. Alkilany, E. C. Goldsmith, and S. C. Baxter. Gold nanoparticles in biology: beyond toxicity to cellular imaging. Accounts of chemical research, 41(12):1721–30, December 2008.

[67] C. Loo, A. Lin, L. Hirsch, M. H. Lee, J. Barton, N. Halas, J. West, and R. Drezek. Nanoshell-enabled photonics-based imaging and therapy of cancer. Technology in cancer research & treatment, 3(1):33–40, February 2004.

[68] H. Cang, T. Sun, Z. Y. Li, J. Chen, B. J. Wiley, Y. Xia, and X. Li. Gold nanocages as contrast agents for spectroscopic optical coherence tomography. Optics letters, 30(22):3048–50, November 2005.

[69] A. L. Oldenburg, M. N. Hansen, D. A. Zweifel, A. Wei, and S. A. Boppart. Plasmon-resonant gold nanorods as low backscattering albedo contrast agents for optical coherence tomography. Optics express, 14(15):6724–38, July 2006.

[70] T. S. Troutman, J. K. Barton, and M. Romanowski. Optical coherence tomography with plasmon resonant nanorods of gold. Optics letters, 32(11):1438–40, June 2007.

[71] C. Bohren and D. Huffman. Absorption and scattering of light by small particles. Wiley-VCH, 1983.

[72] P. B. Johnson and R. W. Christy. Optical Constants of the Noble Metals. Physical Review B, 6(12):4370–4379, December 1972.

[73] S. Link and M. A. El-Sayed. Size and Temperature Dependence of the Plasmon Absorption of Colloidal Gold Nanoparticles. The Journal of Physical Chemistry B, 103(21):4212–4217, May 1999.

[74] A. L. Oldenburg, M. N. Hansen, A. Wei, and S. A. Boppart. Plasmon-resonant gold nanorods provide spectroscopic OCT contrast in excised human breast tumors. In Samuel Achilefu, Darryl J. Bornhop, and Ramesh Raghavachari, editors, Proceedings of SPIE, volume 6867, pages 68670E–68670E–10, February 2008.

[75] B. C. Rostro-Kohanloo, L. R. Bickford, C. M. Payne, E. S. Day, L. J. E. Anderson, M. Zhong, S. Lee, K. M. Mayer, T. Zal, L. Adam, C. P. N. Dinney, Rebekah a Drezek, Jennifer L West, and Jason H Hafner. The stabilization and targeting of

surfactant-synthesized gold nanorods. Nanotechnology, 20(43):434005, October 2009.

[76] C. Sönnichsen, T. Franzl, T. Wilk, G. von Plessen, and J. Feldmann. Drastic Reduction of Plasmon Damping in Gold Nanorods. Physical Review Letters, 88(7), January 2002.

[77] S. Link and M. A. El-Sayed. Spectral Properties and Relaxation Dynamics of Surface Plasmon Electronic Oscillations in Gold and Silver Nanodots and Nanorods. The Journal of Physical Chemistry B, 103(40):8410–8426, October 1999.

[78] K. S. Lee and M. A. El-Sayed. Dependence of the enhanced optical scattering efficiency relative to that of absorption for gold metal nanorods on aspect ratio, size, end-cap shape, and medium refractive index. The journal of physical chemistry. B, 109(43):20331–8, November 2005.

[79] C. Sönnichsen and A. P. Alivisatos. Gold nanorods as novel nonbleaching plasmon-based orientation sensors for polarized single-particle microscopy. Nano letters, 5(2):301–4, February 2005.

[80] W. S. Chang, J. W. Ha, L. S. Slaughter, and S. Link. Plasmonic nanorod absorbers as orientation sensors. Proceedings of the National Academy of Sciences, 107(7):2781–6, February 2010.

[81] B. Nikoobakht and M. A. El-Sayed. Preparation and Growth Mechanism of Gold Nanorods (NRs) Using Seed-Mediated Growth Method. Chemistry of Materials, 15(10):1957–1962, May 2003.

[82] R. K. Chhetri, K. A. Kozek, A. C. Johnston-Peck, J. B. Tracy, and A. L. Oldenburg. Imaging three-dimensional rotational diffusion of plasmon resonant gold nanorods using polarization-sensitive optical coherence tomography. Physical Review E, 83(4):1–4, April 2011.

[83] A. V. Liopo, A. Conjusteau, O. V. Chumakova, S. A. Ermilov, R. Su, and A. A. Oraevsky. Highly purified biocompatible gold nanorods for contrasted optoacoustic imaging of small animal models. Nanoscience and nanotechnology letters (Print), 4(7):681–686, July 2012.

[84] T. Niidome, M. Yamagata, Y. Okamoto, Y. Akiyama, H. Takahashi, T. Kawano, Y. Katayama, and Y. Niidome. PEG-modified gold nanorods with a stealth character for in vivo applications. Journal of controlled release : official journal

of the Controlled Release Society, 114(3):343–7, September 2006.

[85] S. K. Lai, D. E. O'Hanlon, S. Harrold, S. T. Man, Y. Y. Wang, R. Cone, and J. Hanes. Rapid transport of large polymeric nanoparticles in fresh undiluted human mucus. Proceedings of the National Academy of Sciences of the United States of America, 104(5):1482–7, January 2007.

[86] J. V. Jokerst, T. Lobovkina, R. N. Zare, and S. S. Gambhir. Nanoparticle PEGylation for imaging and therapy. Nanomedicine (London, England), 6(4):715–28, June 2011.

[87] J. Kalkman, R. Sprik, and T. G. van Leeuwen. Path-Length-Resolved Diffusive Particle Dynamics in Spectral-Domain Optical Coherence Tomography. Physical Review Letters, 105(19):198302, November 2010.

[88] T. M. Squires and T. G. Mason. Fluid Mechanics of Microrheology. Annual Review of Fluid Mechanics, 42(1):413–438, January 2010.

[89] N. S. Cheng. Formula for the Viscosity of a GlycerolWater Mixture. Industrial & Engineering Chemistry Research, 47(9):3285–3288, May 2008.

[90] Y. Abate, A. Schwartzberg, D. Strasser, and S. R. Leone. Nanometer-scale size dependent imaging of cetyl trimethyl ammonium bromide (CTAB) capped and uncapped gold nanoparticles by apertureless near-field optical microscopy. Chemical Physics Letters, 474(1-3):146–152, May 2009.

[91] M. Rubinstein and R. H. Colby. Polymer Physics. Oxford University Press, USA, 2003.

[92] T. G. Mason and D. A. Weitz. Optical measurements of frequency-dependent linear viscoelastic moduli of complex fluids. Physical review letters, 74(7):1250–1253, February 1995.

[93] Bivash Dasgupta, Shang-you Tee, John Crocker, B. Frisken, and D. Weitz. Microrheology of polyethylene oxide using diffusing wave spectroscopy and single scattering. Physical Review E, 65(5):1–10, May 2002.

[94] T. G. Mason, H. Gang, and D. A. Weitz. Rheology of complex fluids measured by dynamic light scattering. Journal of Molecular Structure, 383(1-3):81–90, September 1996.

[95] E. C. Cooper, P. Johnson, and A. M. Donald. Probe diffusion in polymer solutions in the dilute/semi-dilute crossover regime: 1. Poly(ethylene oxide). Polymer, 32(15):2815–2822, January 1991.

[96] K. Devanand and J. C. Selser. Asymptotic behavior and long-range interactions in aqueous solutions of poly(ethylene oxide). Macromolecules, 24(22):5943–5947, October 1991.

[97] S. Rathgeber, H. J. Beauvisage, H. Chevreau, N. Willenbacher, and C. Oelschlaeger. Microrheology with fluorescence correlation spectroscopy. Langmuir : the ACS journal of surfaces and colloids, 25(11):6368–76, June 2009.

[98] M. J. Bissell and D. Radisky. Putting tumours in context. Nature reviews. Cancer, 1(1):46–54, October 2001.

[99] J. Debnath, S. K. Muthuswamy, and J. S. Brugge. Morphogenesis and oncogenesis of MCF-10A mammary epithelial acini grown in three-dimensional basement membrane cultures. Methods, 30(3):256–268, July 2003.

[100] P. A. Kenny, G. Y. Lee, C. A. Myers, R. M. Neve, J. R. Semeiks, P. T. Spellman, K. Lorenz, E. H. Lee, M. H. Barcellos-Hoff, O. W. Petersen, J. W. Gray, and M. J. Bissell. The morphologies of breast cancer cell lines in three-dimensional assays correlate with their profiles of gene expression. Molecular oncology, 1(1):84–96, June 2007.

[101] K. R. Johnson, J. L. Leight, and V. M. Weaver. Demystifying the effects of a three-dimensional microenvironment in tissue morphogenesis. Methods in cell biology, 83(07):547–83, January 2007.

[102] Y. Yang, L. M. Leone, and L. J. Kaufman. Elastic Moduli of Collagen Gels Can Be Predicted from Two-Dimensional Confocal Microscopy. Biophysical Journal, 97(7):2051–2060, October 2009.

[103] C. S. Hughes, L. M. Postovit, and G. A. Lajoie. Matrigel: a complex protein mixture required for optimal growth of cell culture. Proteomics, 10(9):1886–90, May 2010.

[104] V. M. Weaver, S. Lelièvre, J. N. Lakins, M. A. Chrenek, J. C. R. Jones, F. Giancotti, Z. Werb, and M. J. Bissell. Beta4 Integrin-Dependent Formation of Polarized Three-Dimensional Architecture Confers Resistance To Apoptosis in

Normal and Malignant Mammary Epithelium. Cancer cell, 2(3):205–16, September 2002.

[105] S. Ramanujan, A. Pluen, T. D. McKee, E. B. Brown, Y. Boucher, and R. K. Jain. Diffusion and convection in collagen gels: implications for transport in the tumor interstitium. Biophysical journal, 83(3):1650–60, September 2002.

[106] A. Erikson, H. N. Andersen, S. N. Naess, P. Sikorski, and C. de L. Davies. Physical and chemical modifications of collagen gels: impact on diffusion. Biopolymers, 89(2):135–43, February 2008.

[107] R. Kalluri and M. Zeisberg. Fibroblasts in cancer. Nature reviews. Cancer, 6(5):392–401, May 2006.

[108] A. Desmoulière, C. Chaponnier, and G. Gabbiani. Tissue repair, contraction, and the myofibroblast. Wound repair and regeneration, 13(1):7–12, 2005.

[109] F. Grinnell. Fibroblast biology in three-dimensional collagen matrices. Trends in cell biology, 13(5):264–9, May 2003.

[110] A. Orimo, P. B. Gupta, D. C. Sgroi, F. Arenzana-Seisdedos, T. Delaunay, R. Naeem, V. J. Carey, A. L. Richardson, and R. A. Weinberg. Stromal fibroblasts present in invasive human breast carcinomas promote tumor growth and angiogenesis through elevated SDF-1/CXCL12 secretion. Cell, 121(3):335–348, 2005.

[111] C. J. Olsen, J. Moreira, E. M. Lukanidin, and N. S. Ambartsumian. Human mammary fibroblasts stimulate invasion of breast cancer cells in a three-dimensional culture and increase stroma development in mouse xenografts. BMC cancer, 10:444, January 2010.

[112] O. W. Petersen, L. Ronnov-Jessen, A. R. Howlett, and M. J. Bissell. Interaction with basement membrane serves to rapidly distinguish growth and differentiation pattern of normal and malignant human breast epithelial cells. Proceedings of the National Academy of Sciences, 89(19):9064–9068, October 1992.

[113] O. Maller, H. Martinson, and P. Schedin. Extracellular matrix composition reveals complex and dynamic stromal-epithelial interactions in the mammary gland. Journal of mammary gland biology and neoplasia, 15(3):301–18, September 2010.

[114] S. Krause, M. V. Maffini, A. M. Soto, and C. Sonnenschein. A novel 3D in vitro culture model to study stromal-epithelial interactions in the mammary gland. Tissue engineering. Part C, Methods, 14(3):261–71, September 2008.

[115] R. Bansil and B. S. Turner. Mucin structure, aggregation, physiological functions and biomedical applications. Current Opinion in Colloid & Interface Science, 11(2-3):164–170, June 2006.

[116] J. V. Fahy and B. F. Dickey. Airway mucus function and dysfunction. The New England journal of medicine, 363(23):2233–47, December 2010.

[117] B. Button, L.-H. Cai, C. Ehre, M. Kesimer, D. B. Hill, J. K. Sheehan, R. C. Boucher, and M. Rubinstein. A Periciliary Brush Promotes the Lung Health by Separating the Mucus Layer from Airway Epithelia. Science, 337(6097):937–941, August 2012.

[118] R. C. Boucher. Molecular insights into the physiology of the 'thin film' of airway surface liquid. The Journal of Physiology, 516(3):631–638, May 1999.

[119] B. M. Morrissey. Pathogenesis of bronchiectasis. Clinics in chest medicine, 28(2):289–96, June 2007.

[120] S. K. Lai, Y.-Y. Wang, and J. Hanes. Mucus-penetrating nanoparticles for drug and gene delivery to mucosal tissues. Advanced drug delivery reviews, 61(2):158–71, February 2009.

[121] B. S. Schuster, J. S. Suk, G. F. Woodworth, and J. Hanes. Nanoparticle diffusion in respiratory mucus from humans without lung disease. Biomaterials, pages 1–8, February 2013.

[122] M. L. Fulcher, S. Gabriel, K. A. Burns, J. R. Yankaskas, and S. H. Randell. Well-differentiated human airway epithelial cell cultures. Methods in molecular medicine, 107:183–206, January 2005.

[123] M. Mall, B. R. Grubb, J. R. Harkema, W. K. O'Neal, and R. C. Boucher. Increased airway epithelial Na+ absorption produces cystic fibrosis-like lung disease in mice. Nature medicine, 10(5):487–93, May 2004.

[124] H. Matsui, V. E. Wagner, D. B. Hill, U. E. Schwab, T. D. Rogers, B. Button, R. M. Taylor, R. Superfine, M. Rubinstein, B. H. Iglewski, and R. C. Boucher. A physical linkage between cystic fibrosis airway surface dehydration and Pseu-

domonas aeruginosa biofilms. Proceedings of the National Academy of Sciences of the United States of America, 103(48):18131–6, November 2006.

[125] S. K. Lai, Y. Y. Wang, R. Cone, D. Wirtz, and J. Hanes. Altering mucus rheology to "solidify" human mucus at the nanoscale. PloS one, 4(1):e4294, January 2009.

[126] H. Matsui, S. H. Randell, S. W. Peretti, C. W. Davis, and R. C. Boucher. Coordinated clearance of periciliary liquid and mucus from airway surfaces. The Journal of clinical investigation, 102(6):1125–31, September 1998.

[127] D. J. Smith, E. A. Gaffney, and J. R. Blake. Modelling mucociliary clearance. Respiratory physiology & neurobiology, 163(1-3):178–88, November 2008.

[128] A. Gefen and B. Dilmoney. Mechanics of the normal woman's breast. Technology and Health Care, 15(4):259–71, January 2007.

[129] C. M. Nelson and M. J. Bissell. Of extracellular matrix, scaffolds, and signaling: tissue architecture regulates development, homeostasis, and cancer. Annual review of cell and developmental biology, 22:287–309, January 2006.

[130] X. Dong-Le Bourhis, Y. Berthois, G. Millot, A. Degeorges, M. Sylvi, P. M. Martin, and F. Calvo. Effect of stromal and epithelial cells derived from normal and tumorous breast tissue on the proliferation of human breast cancer cell lines in co-culture. International Journal of Cancer., 71(1):42–8, March 1997.

[131] J. T. Camp, F. Elloumi, E. Roman-Perez, J. Rein, D. A. Stewart, J. C. Harrell, C. M. Perou, and M. A. Troester. Interactions with fibroblasts are distinct in Basal-like and luminal breast cancers. Molecular cancer research : MCR, 9(1):3–13, January 2011.

[132] C. M. Perou, T. Sorlie, M. B. Eisen, M. van de Rijn, S. S. Jeffrey, C. A. Rees, J. R. Pollack, D. T. Ross, H. Johnsen, L. A. Akslen, O. Fluge, A. Pergamenschikov, C. Williams, S. X. Zhu, P. E. Lonning, A. L. Borresen-Dale, P. O. Brown, and D. Botstein. Molecular portraits of human breast tumours. Nature, 406(6797):747–52, August 2000.

[133] S. Krause, M. V. Maffini, A. M. Soto, and C. Sonnenschein. The microenvironment determines the breast cancer cells' phenotype: organization of MCF7 cells in 3D cultures. BMC cancer, 10:263, January 2010.

[134] W. Tan, A. L. Oldenburg, J. J. Norman, T. A. Desai, and S. A. Boppart. Optical coherence tomography of cell dynamics in three-dimensional tissue models. Optics Express, 14(16):7159, 2006.

[135] S. A. Boppart, B. E. Bouma, C. Pitris, G. J. Tearney, J. F. Southern, M. E. Brezinski, and J. G. Fujimoto. Intraoperative assessment of microsurgery with three-dimensional optical coherence tomography. Radiology, 208(1):81–86, 1998.

[136] J. G. Fujimoto, W. Drexler, J. S. Schuman, and C. K. Hitzenberger. Optical Coherence Tomography (OCT) in ophthalmology: introduction. Optics Express, 17(5):3978–3979, 2009.

[137] S. A. Boppart, B. E. Bouma, C. Pitris, J. F. Southern, M. E. Brezinski, and J. G. Fujimoto. In vivo cellular optical coherence tomography imaging. Nature Medicine, 4(7):861–865, July 1998.

[138] A. M. Zysk, F. T. Nguyen, E. J. Chaney, J. G. Kotynek, U. J. Oliphant, F. J. Bellafiore, P. A. Johnson, K. M. Rowland, and S. A. Boppart. Clinical feasibility of microscopically-guided breast needle biopsy using a fiber-optic probe with computer-aided detection. Technology in cancer research & treatment, 8(5):315–21, October 2009.

[139] A. Latrive and A. C. Boccara. In vivo and in situ cellular imaging full-field optical coherence tomography with a rigid endoscopic probe. Biomedical Optics Express, 2(10):2897, September 2011.

[140] R. A. McLaughlin, L. Scolaro, P. Robbins, S. Hamza, C. Saunders, and D. D. Sampson. Imaging of human lymph nodes using optical coherence tomography: potential for staging cancer. Cancer research, 70(7):2579–84, April 2010.

[141] A. M. Zysk and S. A. Boppart. Computational methods for analysis of human breast tumor tissue in optical coherence tomography images. Journal of biomedical optics, 11(5):054015, 2006.

[142] A. C. Sullivan, J. P. Hunt, and A. L. Oldenburg. Fractal analysis for classification of breast carcinoma in optical coherence tomography. Journal of biomedical optics, 16(6):066010, June 2011.

[143] R. M. Neve, K. Chin, J. Fridlyand, J. Yeh, F. L. Baehner, T. Fevr, L. Clark, N. Bayani, J. P. Coppe, F. Tong, T. Speed, P. T. Spellman, S. DeVries, A. Lapuk, N. J. Wang, W. L. Kuo, J. L. Stilwell, D. Pinkel, D. G. Albertson, F. M.

Waldman, F. McCormick, R. B. Dickson, M. D. Johnson, M. Lippman, S. Ethier, A. Gazdar, and J. W. Gray. A collection of breast cancer cell lines for the study of functionally distinct cancer subtypes. Cancer cell, 10(6):515–27, December 2006.

[144] H. D. Soule, T. M. Maloney, S. R. Wolman, W. D. Peterson, R. Brenz, C. M. McGrath, J. Russo, R. J. Pauley, R. F. Jones, and S. C. Brooks. Isolation and characterization of a spontaneously immortalized human breast epithelial cell line, MCF-10. Cancer research, 50(18):6075–86, September 1990.

[145] F. R. Miller, S. J. Santner, L. Tait, and P. J. Dawson. MCF10DCIS.com xenograft model of human comedo ductal carcinoma in situ. Journal of the National Cancer Institute, 92(14):1185–6, July 2000.

[146] D. A. Proia and C. Kuperwasser. Reconstruction of human mammary tissues in a mouse model. Nature protocols, 1(1):206–14, January 2006.

[147] A. L. Oldenburg, C. M. Gallippi, F. Tsui, T. C. Nichols, K. N. Beicker, R. K. Chhetri, D. Spivak, A. Richardson, and T. H. Fischer. Magnetic and contrast properties of labeled platelets for magnetomotive optical coherence tomography. Biophysical journal, 99(7):2374–83, October 2010.

[148] J. Tang, H. Enderling, S. Becker-Weimann, C. Pham, A. Polyzos, C. Y. Chen, and S. V. Costes. Phenotypic transition maps of 3D breast acini obtained by imaging-guided agent-based modeling. Integrative biology : quantitative biosciences from nano to macro, 3(4):408–21, April 2011.

[149] M. P. V. Shekhar, L. Tait, R. J. Pauley, G. S. Wu, S. J. Santner, P. Nangia-Makker, V. Shekhar, H. Nassar, D. W. Visscher, G. H. Heppner, and F. R. Miller. Comedo-ductal carcinoma in situ: A paradoxical role for programmed cell death. Cancer biology & therapy, 7(11):1774–82, November 2008.

[150] C. Jedeszko, B. C. Victor, I. Podgorski, and B. F. Sloane. Fibroblast hepatocyte growth factor promotes invasion of human mammary ductal carcinoma in situ. Cancer research, 69(23):9148–55, December 2009.

[151] J. Debnath and J. S. Brugge. Modelling glandular epithelial cancers in three-dimensional cultures. Nature reviews. Cancer, 5(9):675–88, September 2005.

[152] M. J. Paszek, N. Zahir, K. R. Johnson, J. N. Lakins, G. I. Rozenberg, A. Gefen, C. A. Reinhart-King, S. S. Margulies, M. Dembo, D. Boettiger, D. A. Hammer,

and V. M. Weaver. Tensional homeostasis and the malignant phenotype. Cancer cell, 8(3):241–54, September 2005.

[153] M. Yu, Z. Tang, S. Alousi, R. S. Berk, F. Miller, and M. A. Kosir. Expression patterns of lymphangiogenic and angiogenic factors in a model of breast ductal carcinoma in situ. American journal of surgery, 194(5):594–9, November 2007.

[154] J. W. Baish and R. K. Jain. Fractals and cancer. Cancer research, 60(14):3683–8, July 2000.

[155] V. Backman and H. K. Roy. Light-scattering technologies for field carcinogenesis detection: a modality for endoscopic prescreening. Gastroenterology, 140(1):35–41, January 2011.

[156] M. Tambasco, M. Eliasziw, and A. M. Magliocco. Morphologic complexity of epithelial architecture for predicting invasive breast cancer survival. Journal of translational medicine, 8(1):140, January 2010.